NAVAL POSTGRADUATE SCHOOL
Monterey, California

AD-A244 372



DTIC
ELECTE
JAN 15 1992
S B D

THESIS

HEAT TRANSFER, ADIABATIC EFFECTIVENESS AND INJECTANT DISTRIBUTIONS DOWNSTREAM OF SINGLE ROWS AND TWO STAGGERED ROWS OF FILM-COOLING HOLES WITH SIMPLE AND COMPOUND ANGLES

by

Stephen Mark Jackson

DECEMBER 1991

Thesis Advisor: Phillip Ligrani

92-01241

Approved for public release: Distribution is unlimited

92 1 14 0[illegible]

SECURITY CLASSIFICATION OF THIS PAGE

REPORT DOCUMENTATION PAGE

Form Approved
OMB No 0704-0188

1a. REPORT SECURITY CLASSIFICATION Unclassified	1b. RESTRICTIVE MARKINGS
2a. SECURITY CLASSIFICATION AUTHORITY	3. DISTRIBUTION/AVAILABILITY OF REPORT Approved for public release: Distribution is unlimited
2b. DECLASSIFICATION/DOWNGRADING SCHEDULE	
4. PERFORMING ORGANIZATION REPORT NUMBER(S)	5. MONITORING ORGANIZATION REPORT NUMBER(S)
6a. NAME OF PERFORMING ORGANIZATION Naval Postgraduate School 6b. OFFICE SYMBOL (If applicable) ME	7a. NAME OF MONITORING ORGANIZATION Naval Postgraduate School
6c. ADDRESS (City, State and ZIP Code) Monterey, CA 93943-5000	7b. ADDRESS (City, State, and ZIP Code) Monterey, CA 93943-5000
8a. NAME OF FUNDING/SPONSORING ORGANIZATION Naval Sea Systems Command 8b. OFFICE SYMBOL (If applicable) 56X3	9. PROCUREMENT INSTRUMENT IDENTIFICATION NUMBER RGPLG
8c. ADDRESS (City, State, and ZIP Code) Dr. Dan. Groghan Naval Sea Systems Command Code 56X3 Washington, D.C. 20352	10. SOURCE OF FUNDING NUMBER PROGRAM ELEMENT NO.: LG2LG PROJECT NO.: TASK NO.: WORK UNIT ACCESSION NO.:

11. TITLE (Include Security Classification)
HEAT TRANSFER, ADIABATIC EFFECTIVENESS AND INJECTANT DISTRIBUTIONS DOWNSTREAM OF SINGLE ROWS AND TWO STAGGERED ROWS OF FILM-COOLING HOLES WITH SIMPLE AND COMPOUND ANGLES

12. PERSONAL AUTHORS
STEPHEN MARK JACKSON

13a. TYPE OF REPORT	13b. TIME COVERED	14. DATE OF REPORT (Year, Month, Day)	15. PAGE COUNT
Master's Thesis	FROM_____ TO_____	DECEMBER 1991	243

16. SUPPLEMENTARY NOTATION
The views expressed are those of the author and do not reflect the official policy or position of the Department of Defense or the U.S. Government

17. COSATI CODES			18. SUBJECT TERMS (Continue on reverse if necessary and identify by block numbers)
FIELD	GROUP	SUB-GROUP	compound angle injection, simple angle injection, film-cooling, turbulent boundary layer

19. ABSTRACT (Continue on reverse if necessary and identify by block numbers)

Experimental results for two compound angle injection systems (configurations 1 and 3), and for a simple injection system (configuration 2) are compared in this thesis. The effects of blowing ratio, spanwise hole spacing, hole angle orientation, and streamwise position (x/d) are discussed in reference to measurements of spanwise-averaged adiabatic effectiveness, iso-energetic Stanton number, and Stanton number θ approximately equal to 1.5 obtained downstream of both one row of holes and two staggered rows of holes. Results indicate that effectiveness depends mostly on four parameters: simple or compound angle injection, spanwise hole spacing, one or two rows of holes, and blowing ratio. Results show that for a specified blowing ratio, for all configurations tested to date, spanwise-averaged adiabatic effectiveness is greatest at lower x/d values but decreases with streamwise development as the injectant is convected downstream. The rate of spanwise-averaged adiabatic effectiveness decrease is dependent on the blowing ratio, and mostly a result of lift-off of the injectant from the test surface at x/d values less than about 20. At larger x/d, spanwise-averaged adiabatic effectiveness values generally increase with blowing ratio mostly because of greater amounts of injectant along the test surface. Results also show that the iso-energetic Stanton number ratio lies between 1 and 1.35 for all cases studied and generally increases with blowing ratio for a given x/d.

20. DISTRIBUTION/AVAILABILITY OF ABSTRACT	21. ABSTRACT SECURITY CLASSIFICATION	
XX UNCLASSIFIED/UNLIMITED _ SAME AS RPT _ DTIC USERS	unclassified	
22a. NAME OF RESPONSIBLE INDIVIDUAL Phillip Ligrani	22b. TELEPHONE (Include Area Code) (408) 646-3382	22c. OFFICE SYMBOL ME/Li

DD Form 1473, JUN 86 — Previous editions are obsolete.

S/N 0102-LF-014-6603

SECURITY CLASSIFICATION OF THIS PAGE
Unclassified

Approved for public release: Distribution is unlimited

Heat Transfer, Adiabatic Effectiveness and Injectant Distributions
Downstream of Single Rows and Two Staggered Rows of
Film-Cooling Holes with Simple and Compound Angles

by

Stephen Mark Jackson
Lieutenant, United States Navy
B.S., United States Naval Academy, 1983

Submitted in partial fulfillment of the
requirements for the degree of

MASTER OF SCIENCE
IN MECHANICAL ENGINEERING

from the

NAVAL POSTGRADUATE SCHOOL

DECEMBER 1991

Author: Steph Jackson LT, USN
Stephen Mark Jackson

Approved by: Phillip M. Ligrani
Phillip Ligrani, Thesis Advisor

A.J. Healey, Chairman
Department of Mechanical Engineering

ABSTRACT

Experimental results for two compound angle injection systems (configurations 1 and 3), and for a simple injection system (configuration 2) are compared in this thesis. The effects of blowing ratio, spanwise hole spacing, hole angle orientation, and streamwise position (x/d) are discussed in reference to measurements of spanwise-averaged adiabatic effectiveness, iso-energetic Stanton number, and Stanton number for θ approximately equal to 1.5 obtained downstream of both one row of holes and two staggered rows of holes. Results indicate that effectiveness depends mostly on four parameters: simple or compound angle injection, spanwise hole spacing, one or two rows of holes, and blowing ratio. Results show that for a specified blowing ratio, for all configurations tested to date, spanwise-averaged adiabatic effectiveness is greatest at lower x/d values but decreases with streamwise development as the injectant is convected downstream. The rate of spanwise-averaged adiabatic effectiveness decrease is dependent on the blowing ratio, and mostly a result of lift-off of the injectant from the test surface at x/d values less than about 20. At larger x/d, spanwise-averaged adiabatic effectiveness values generally increase with blowing ratio mostly because of greater amounts of injectant along the test surface. Results also show that the iso-energetic Stanton number ratio lies between 1 and 1.35 for all cases studied and generally increases with blowing ratio for a given x/d.



Accession For
NTIS GRA&I
DTIC TAB
Unannounced
Justification
By
Distribution/
Availability Codes
Dist | Avail and/or Special
A-1

TABLE OF CONTENTS

I. INTRODUCTION 1
A. BACKGROUND/THEORY 1
B. PRESENT STUDY 7
C. EXPERIMENTAL OUTLINE 8
D. THESIS ORGANIZATION 9
II. EXPERIMENTAL APPARATUS AND PROCEDURES 10
A. WIND TUNNEL AND COORDINATE SYSTEM 10
B. INJECTION SYSTEM AND INJECTION CONFIGURATIONS 11
1. Injection System 11
2. Injection Configuration 12
C. STREAMWISE MEAN VELOCITY MEASUREMENTS 13
D. STANTON NUMBER MEASUREMENTS 13
E. MEAN TEMPERATURE MEASUREMENTS 14
F. BASELINE DATA CHECKS 15
III. EXPERIMENTAL RESULTS 16
A. CONFIGURATION TWO, SIMPLE ANGLE RESULTS 16
1. Heat Transfer Measurements Downstream of Two Rows Of Film-Cooling Holes With m=0.5 16
2. Heat Transfer Measurements Downstream Of Two Rows Of Film-Cooling Holes With m=1.05 17
3. Heat Transfer Measurements Downstream Of Two Rows Of Film-Cooling Holes With m=1.5 18

B. CONFIGURATION THREE, COMPOUND ANGLE RESULTS 18
1. Two Rows Of Film-Cooling Holes With m=0.5 18
a. Heat Transfer Measurements 18
b. Velocity and Pressure Surveys 19
c. Injectant Distributions 20
2. Two Rows Of Film-Cooling Holes With m=1.0 20
a. Heat Transfer Measurements 20
b. Velocity and Pressure Surveys 21
c. Injectant Distributions 22
3. Two Rows Of Film-Cooling Holes With m=1.5 22
a. Heat Transfer Measurements 22
b. Velocity and Pressure Surveys 23
c. Injectant Distributions 23
4. One Row Of Film-Cooling Holes With m=0.5 24
a. Heat Transfer Measurements 24
b. Velocity and Pressure Surveys 24
c. Injectant Distributions 25
5. One Row Of Film-Cooling Holes With m=1.0 25
a. Heat Transfer Measurements 25
b. Velocity and Pressure Surveys 26
c. Injectant Distributions 26
6. Heat Transfer Measurements Downstream Of One Row of Film-Cooling Holes With m=1.5 27
C. COMPARISON OF RESULTS FROM THE SIMPLE ANGLE AND COMPOUND ANGLE FILM-COOLING HOLE CONFIGURATIONS 28
IV. SUMMARY AND CONCLUSIONS 31
APPENDIX A: FIGURES 33
APPENDIX B: UNCERTAINTY ANALYSIS 201
APPENDIX C: DATA ACQUISITION, PROCESSING AND PLOTTING PROGRAMS 202

APPENDIX D: DATA FILE DIRECTORY 207
LIST OF REFERENCES 221
INITIAL DISTRIBUTION LIST 223

LIST OF FIGURES

Figure 1. Test Section Coordinate System, Configuration 2, Simple Angle 34
Figure 2. Test Section Coordinate System, Configuration 3, Compound Angle 35
Figure 3. Top View Schematic of Wind Tunnel Test Section, Configuration 2, Simple Angle 36
Figure 4. Top View Schematic of Wind Tunnel Test Section, Configuration 3, Compound Angle 37
Figure 5. Injection Hole Configuration, Simple Angle 38
Figure 6. Injection Hold Configuration, Compound Angle 39
Figure 7. Coefficient of Discharge (C_d) Versus Reynolds Number (Re) for Injection System 40
Figure 8. Injectant Temperature Versus Plenum Temperature, Bishop [Ref. 6] 41
Figure 9. Baseline Stanton Number Comparison Between Exact Solution and Experimental Measurements, Configuration 2 42
Figure 10. Baseline Stanton Number Comparison Between Exact Solution and Experimental Measurements, Configuration 3 43
Figure 11. St/Sto Versus x/d for Various θ Values with m=0.5, [Ref. Ligrani, Bishop, Ciriello] 44
Figure 12. St/Sto Versus θ, Simple Angle, 2 Rows, m=0.5, x/d=17.4, z/d=0.0 45
Figure 13. St/Sto Versus θ Simple Angle, 2 Rows, m=0.5, x/d=17.4, z/d=0.0 46
Figure 14. St/Sto Versus θ, Simple Angle, 2 Rows, m=0.5, x/d=33.2, z/d=0.0 47

Figure 15. St/Sto Versus θ, Simple Angle, 2 Rows, m=0.5, x/d=54.4, z/d=0.0 48
Figure 16. St/Sto Versus θ, Simple Angle, 2 Rows, m=0.5, x/d=75.6, z/d=0.0 49
Figure 17. St/Sto Versus θ, Simple Angle, 2 Rows, m=0.5, x/d=96.7, z/d-0.0 50
Figure 18. η Versus x/d, Simple Angle, 2 Rows, m=0.5, Spanwise Average 51
Figure 19. Stf/Sto Versus x/d, Simple Angle, 2 Rows, m=0.5, Spanwise Average 52
Figure 20. Spanwise Variation of η Simple Angle, 2 Rows, m=0.5 53
Figure 21. Spanwise Variation of Stf/Sto, Simple Angle, 2 Rows, m=0.5 54
Figure 22. Spanwise Variation of St/Sto, Simple Angle, 2 Rows, m=0.5, θ=1.59 55
Figure 23. St/Sto Versus θ, Simple Angle, 2 Rows, m=1.0, x/d=6.8, z/d=0.0 56
Figure 24. St/Sto Versus θ, Simple Angle, 2 Rows, m=1.0, x/d=17.4, z/d=0.0 57
Figure 25. St/Sto Versus θ, Simple Angle, 2 Rows, m=1.0, x/d=33.2, z/d=0.0 58
Figure 26. St/Sto Versus θ, Simple Angle, 2 Rows, m=1.0, x/d=54.4, z/d=0.0 59
Figure 27. St/Sto Versus θ, Simple Angle, 2 Rows, m=1.0, x/d=75.6, z/d=0.0 60
Figure 28. St/Sto Versus θ, Simple Angle, 2 Rows, m=1.0, x/d=96.7, z/d=0.0 61
Figure 29. η Versus x/d, Simple Angle, 2 Rows, m=1.0, Spanwise Average 62
Figure 30. Stf/Sto Versus x/d, Simple Angle, 2 Rows, m=1.0, Spanwise Average 63

Figure 31. Spanwise Variation of η, Simple Angle, 2 Rows, m=1.0 64
Figure 32. Spanwise Variation of Stf/Sto, Simple Angle, 2 Rows, m=1.0 65
Figure 33. Spanwise Variation of St/Sto, Simple Angle, 2 Rows, m=1.0, θ=1.66 66
Figure 34. St/Sto Versus θ, Simple Angle, 2 Rows, m=1.5, x/d=6.8, z/d=0.0 67
Figure 35. St/Sto Versus θ, Simple Angle, 2 Rows, m=1.5, x/d=17.4, z/d=0.00 68
Figure 36. St/Sto Versus θ, Simple Angle, 2 Rows, m=1.5, x/d=33.2, z/d=0.0 69
Figure 37. St/Sto Versus θ, Simple Angle, 2 Rows, m=1.5, x/d=54.4, z/d=0.0 70
Figure 38. St/Sto Versus θ, Simple Angle, 2 Rows, m=1.5, x/d=75.6, z/d=0.0 71
Figure 39. St/Sto Versus θ, Simple Angle, 2 Rows, m=1.5, x/d=96.7, z/d=0.0 72
Figure 40. η Versus x/d, Simple Angle, 2 Rows, m=1.5, Spanwise Average 73
Figure 41. Stf/Sto Versus x/d, Simple Angle, 2 Rows, m=1.5, Spanwise Average 74
Figure 42. Spanwise Variation of η, Simple Angle, 2 Rows, m=1.5 75
Figure 43. Spanwise Variation of Stf/Sto, Simple Angle, 2 Rows, m=1.5 76
Figure 44. Spanwise Variation of St/Sto, Simple Angle, 2 Rows, m=1.5, θ=1.66 77
Figure 45. St/Sto Versus θ, Compound Angle, 2 rows, m=0.5, x/d=6.8, z/d=0.0 78
Figure 46. St/Sto Versus θ Compound Angle, 2 Rows, m=0.5, x/d=17.6, z/d=0.0 79

Figure 47. St/Sto Versus θ, compound Angle, 2 Rows, m=0.5, x/d=33.8, z/d=0.0 80
Figure 48. St/Sto Versus θ, Compound Angle, 2 Rows, m=0.5, x/d=55.5, z/d=0.0 81
Figure 49. St/Sto Versus θ, Compound Angle, 2 Rows, m=0.5, x/d=77.1, z/d=0.0 82
Figure 50. St/Sto Versus θ, Compound Angle, 2 Rows, m=0.5, x/d=98.7, z/d=0.0 83
Figure 51. η Versus x/d, Compound Angle, 2 Rows, m=0.5, Spanwise Average 84
Figure 52. Stf/Sto Versus x/d, Compound Angle, 2 Rows, m=0.5, Spanwise Average 85
Figure 53. Spanwise Variation of η, Compound Angle, 2 Rows, m=0.5 86
Figure 54. Spanwise Variation of Stf/Sto, Compound Angle, 2 Rows, m=0.5 87
Figure 55. Spanwise Variation of St/Sto, Compound Angle, 2 Rows, m=0.5, θ=1.54 88
Figure 56. Streamwise Velocity Field, Compound Angle, 2 Rows, m=0.5, x/d=9.9 89
Figure 57. Streamwise Pressure Field, Compound Angle, 2 Rows, m=0.5, x/d=9.9 90
Figure 58. Streamwise Velocity Field, Compound Angle, 2 Rows, m=0.5, x/d=44.3 91
Figure 59. Streamwise Pressure Field, Compound Angle, 2 Rows, m=0.5, x/d=44.3 92
Figure 60. Streamwise Velocity Field, Compound Angle, 2 Rows, m=0.5, x/d=86.3 93
Figure 61. Streamwise Pressure Field, Compound Angle, 2 Rows, m=0.5, x/d=86.3 94
Figure 62. Streamwise Injectant Distribution, Compound Angle, 2 Row, m=0.5, x/d=9.9 95

Figure 63. Streamwise Injectant Distribution, Compound Angle, 2 Rows, m=0.5, x/d=44.3 96
Figure 64. Streamwise Injectant Distribution, Compound Angle, 2 Rows, m=0.5, x/d=86.3 97
Figure 65. St/Sto Versus θ, Compound Angle, 2 Rows, m=1.0, x/d=6.8, z/d=0.0 98
Figure 66. St/Sto Versus θ Compound Angle, 2 Rows, m=1.0, x/d=17.6, z/d=0.0 99
Figure 67. St/Sto Versus θ, Compound Angle, 2 rows, m=1.0, x/d=33.8, z/d=0.0 100
Figure 68. St/Sto Versus θ, Compound Angle, 2 Rows, m=1.0, x/d=55.5, z/d=0.0 101
Figure 69. St/Sto Versus θ, Compound Angle, 2 Rows, m=1.0, x/d=77.1, z/d=0.0 102
Figure 70. St/Sto Versus θ Compound Angle, 2 Rows, m=1.0, x/d=98.7, z/d=0.0 103
Figure 71. η Versus x/d, Compound Angle, 2 Rows, m=1.0, Spanwise Average 104
Figure 72. Stf/Sto Versus x/d, Compound Angle, 2 Rows, m=1.0, Spanwise Average 105
Figure 73. Spanwise Variation of η, Compound Angle, 2 Rows, m=1.0 106
Figure 74. Spanwise Variation of Stf/Sto, Compound Angle, 2 Rows, m=1.0 107
Figure 75. Spanwise Variation of St/Sto, Compound Angle, 2 Rows, m=1.00, θ=1.72 108
Figure 76. Streamwise Velocity Field, Compound Angle, 2 Rows, m=1.0, x/d=9.9 109
Figure 77. Streamwise Pressure Field, Compound Angle, 2 Rows, m=1.0, x/d=9.9 110
Figure 78. Streamwise Velocity Field, Compound Angle, 2 Rows, m=1.0, x/d=44.3 111

Figure 79. Streamwise Pressure Field, Compound Angle, 2 Rows, m=1.0, x/d=44.3 112
Figure 80. Streamwise Velocity Field, Compound Angle, 2 Rows, m=1.0, x/d=86.3 113
Figure 81. Streamwise Pressure Field, Compound Angle, 2 Rows, m=1.0, x/d=86.3 114
Figure 82. Streamwise Injectant Distribution, Compound Angle, 2 Rows, m=1.0, x/d=9.9 115
Figure 83. Streamwise Injectant Distribution, Compound Angle, 2 Rows, m=1.0, x/d=44.3 116
Figure 84. Streamwise Injectant Distribution, Compound Angle, 2 Rows, m=1.0, x/d=86.3 117
Figure 85. St/Sto Versus θ, Compound Angle, 2 Rows, m=1.5, x/d=6.8, z/d=0.0 118
Figure 86. St/Sto Versus θ Compound Angle, 2 Rows, m=1.5, x/d=17.6, z/d=0/0 119
Figure 87. St/Sto Versus θ, Compound Angle, 2 Rows, m=1.5, x/d=33.8, z/d=0.0 120
Figure 88. St/Sto Versus θ, Compound Angle, 2 Rows, m=1.5, x/d=55.5, z/d=0.0 121
Figure 89. St/Sto Versus θ, Compound Angle, 2 Rows, m=1.5, x/d=77.1, z/d=0.0 122
Figure 90. St/Sto Versus θ, Compound Angle, 2 Rows, m=1.5, x/d=98.7, z/d=0.0 123
Figure 91. η Versus x/d, Compound Angle, 2 Rows, m=1.5, Spanwise Average 124
Figure 92. Stf/Sto Versus x/d, Compound Angle, 2 Rows, m=1.5, Spanwise Average 125
Figure 93. Spanwise Variation of η, Compound Angle, 2 Rows, m=1.5 126
Figure 94. Spanwise Variation of Stf/Sto, Compound Angle, 2 Rows, m=1.5 127

Figure 95. Spanwise Variation of St/Sto, Compound Angle, 2 Rows, m=1.5, θ=1.24 128
Figure 96. Streamwise Velocity Field, Compound Angle, 2 Rows, m=1.5, x/d=9.9 129
Figure 97. Streamwise Pressure Field, Compound Angle, 2 Rows, m=1.5, x/d=9.9 130
Figure 98. Streamwise Velocity Field, Compound Angle, 2 Rows, m=1.5, x/d=44.3 131
Figure 99. Streamwise Pressure Field, Compound Angle, 2 Rows, m=1.5, x/d=44.3 132
Figure 100. Streamwise Velocity Field, Compound Angle, 2 Rows, m=1.5, x/d=86.3 133
Figure 101. Streamwise Pressure Field, Compound Angle, 2 Rows, m=1.5, x/d=86.3 134
Figure 102. Streamwise Injectant Distribution, Compound Angle, 2 Rows, m=1.5, x/d=9.9 135
Figure 103. Streamwise Injectant Distribution, Compound Angle, 2 rows, m=0.5, x/d=44.3 136
Figure 104. Streamwise Injectant Distribution, Compound Angle, 2 Rows, m=0.5, x/d=44.3 137
Figure 105. St/Sto Versus θ, Compound Angle, 1 Row, m=0.5, x/d=6.8 138
Figure 106. St/Sto Versus θ, Compound Angle, 1 Row, m=0.5, x/d=17.6 139
Figure 107. St/Sto Versus θ, Compound Angle, 1 row, m=0.5, x/d=33.8, z/d=-1.27 140
Figure 108. St/Sto Versus θ, Compound Angle, 1 Row, m=0.5, x/d=55.5, z/d=-1..27 141
Figure 109. St/Sto Versus θ, Compound Angle, 1 Row, m=0.5, x/d=77.1, z/d=-1.27 142
Figure 110. St/Sto Versus θ, Compound Angle, 1 Row, m=0.5, x/d=98..7, z/d=-1.27 143

Figure 111. η Versus x/d, Compound Angle, 1 Row, m=0.5, Spanwise Average 144
Figure 112. Stf/Sto Versus x/d, Compound Angle, 1 Row, m=0.5, Spanwise Average 145
Figure 113. Spanwise Variation of η, Compound Angle, 1 Row, m=0.5 146
Figure 114. Spanwise Variation of Stf/Sto, Compound Angle, 1 Row, m=0.5 147
Figure 115. Spanwise Variation of St/Sto, Compound Angle, 1 Row, m=0.5, θ=1.37 148
Figure 116. Streamwise Velocity Field, Compound Angle, 1 Row, m=0.5, x/d=9.9 149
Figure 117. Streamwise Pressure Field, Compound Angle, 1 Row, m=0.5, x/d=9.9 150
Figure 118. Streamwise Velocity Field, Compound Angle, 1 Row, m=0.5, x/d=44.3 151
Figure 119. Streamwise Pressure Field, Compound Angle, 1 Row, m=0.5, x/d=44.3 152
Figure 120. Streamwise Velocity Field, Compound Angle, 1 Row, m=0.5, x/d=86.3 153
Figure 121. Streamwise Pressure Field, Compound Angle, 1 Row, m=0.5, x/d=86.3 154
Figure 122. Streamwise Injectant Distribution, Compound Angle, 1 Row, m=0.5, x/d=9.9 155
Figure 123. Streamwise Injectant Distribution, Compound Angle, 1 Row, m=0.5, x/d=44.3 156
Figure 124. Streamwise Injectant Distribution, Compound Angle, 1 Row, x=0.5, x/d=86.3 157
Figure 125. St/Sto Versus θ, Compound Angle, 1 Row, m=1.0, x/d=6.8, z/d=-1.27 158
Figure 126. St/Sto Versus θ, Compound Angle, 1 Row, m=1.0, x/d=17.6, z/d=-1.27 159

Figure 127. St/Sto Versus θ, Compound Angle, 1 Row, m=1.0, x/d=33.8, z/d=-1.27 160
Figure 128. St/Sto Versus θ, Compound Angle, 1 Row, m=1.0, x/d=55.5, z/d=-1.27 161
Figure 129. St/Sto Versus θ, Compound Angle, 1 Row, m=1.0, x/d=77.1, z/d=-1.27 162
Figure 130. St/Sto Versus θ, Compound Angle, 1 Row, m=1.0, x/d=98.7, z/d=-1.27 163
Figure 131. η Versus x/d, Compound Angle, 1 Row, m=1.0, Spanwise Average 164
Figure 132. Stf/Sto Versus x/d, Compound Angle, 1 Row, m=1.0, Spanwise Average 165
Figure 133. Spanwise Variation of η, Compound Angle, 1 Row, m=1.0 166
Figure 134. Spanwise Variation of Stf/Sto, Compound Angle, 1 Row, m=1.0 167
Figure 135. Spanwise Variation of St/Sto, Compound Angle, 1 Row, m=1.0, θ=1.89 168
Figure 136. Streamwise Velocity Field, Compound Angle, 1 Row, m=1.0, x/d=9.9 169
Figure 137. Streamwise Pressure Field, Compound Angle, 1 Row, m=1.0, x/d=9.9 170
Figure 138. Streamwise Velocity Field, Compound Angle, 1 Row, m=1.0, xx/d=44.3 171
Figure 139. Streamwise Pressure Field, Compound Angle, 1 Row, m=1.0, x/d=44.3 172
Figure 140. Streamwise Velocity Field, Compound Angle, 1 Row, m=1.0, x/d=86.3 173
Figure 141. Streamwise Pressure Field, Compound Angle, 1 Row, m=1.0, x/d=86.3 174
Figure 142. Streamwise Injectant Distribution, Compound Angle, 1 Row, m=1.0, x/d=9.9 175

Figure 143. Streamwise Injectant Distribution, Compound Angle, 1 Row, m=1.0, x/d=44.3 176
Figure 144. Streamwise Injectant Distribution, Compound Angle, 1 Row, m=1.0, x/d=86.3 177
Figure 145. St/Sto Versus θ, Compound Angle, 1 Row, m=1.5, x/d=6.8, z/d=-1.27 178
Figure 146. St/Sto Versus θ, Compound Angle, 1 Row, m=1.5, x/d=17.6, z/d=-1.27 179
Figure 147. St/Sto Versus θ, Compound Angle, 1 Row, m=1.5, x/d=33.8, z/d=-1.27 180
Figure 148. St/Sto Versus θ, Compound Angle, 1 Row, m=1.5, x/d=55.5, z/d=-1.27 181
Figure 149. St/Sto Versus θ, Compound Angle, 1 Row, m=1.5, x/d=77.1, z/d=-1.27 182
Figure 150. St/Sto Versus θ, Compound Angle, 1 Row, m=1.5, x/d=98.7, z/d=-1.27 183
Figure 151. η Versus x/d, Compound Angle, 1 Row, m=1.5, Spanwise Average 184
Figure 152. Stf/Sto Versus x/d, Compound Angle, 1 Row, m=1.5, Spanwise Average 185
Figure 153. Spanwise Variation of η, Compound Angle, 1 Row, m=1.5 186
Figure 154. Spanwise Variation of Stf/Sto, Compound Angle, 1 Row, m=1.5 187
Figure 155. Spanwise Variation of St/Sto, Compound Angle, 1 Row, m=1.5, θ=1.5 188
Figure 156. Comparison of Two Row Adiabatic Effectiveness as Dependent Upon x/d, for Compound and Simple Angle Configurations 189
Figure 157. Comparison of Two Row Stf/Sto as Dependent Upon x/d for Compound and Simple Angle Configurations 190

Figure 158. Comparisons of Two Row Adiabatic Effectiveness as Dependent Upon x/d for Configuration 2 (Simple Angle), and Configuration 3 (Compound Angle) 191
Figure 159. Comparisons of Two Row Stf/Sto as Dependent Upon x/d for Configuration 2 (Simple Angle), and Configuration 3 (Compound Angle) 192
Figure 160. Comparisons of Two Row Adiabatic Effectiveness as Dependent Upon x/d for Configuration 1 (Compound Angle), and Configuration 3 (Compound Angle) 193
Figure 161. Comparisons of Two Row Stf/Sto as Dependent Upon x/d for Configuration 1 (Compound Angle), and Configuration 3 (Compound Angle) 194
Figure 162. Comparison of One Row Adiabatic Effectiveness as Dependent Upon x/d for Compound and Simple Angle Configurations 195
Figure 163. Comparison of One Row Stf/Sto as Dependent Upon x/d for Compound and Simple Angle Configurations 196
Figure 164. Comparisons of One Row Adiabatic Effectiveness as Dependent Upon x/d for Configuration 2 (Simple Angle), and Configuration 3 (Compound Angle) 197
Figure 165. Comparisons of One Row Stf/Sto as Dependent Upon x/d for Configuration 2 (Simple Angle), and Configuration 3 (Compound Angle) 198
Figure 166. Comparisons of One Row Adiabatic Effectiveness as Dependent Upon x/d for Configuration 1 (Compound Angle), and Configuration 3 (Compound Angle) 199
Figure 167. Comparisons of One Row Stf/Sto as Dependent Upon x/d for Configuration 1 (Compound Angle), and Configuration 3 (Compound Angle) 200

I. INTRODUCTION

A. BACKGROUND/THEORY

Current inlet temperatures of gas turbines are approaching 2000 K. Such temperatures are required to achieve high performance levels. However, the same temperatures, in combination with the high rotational speeds, also put extraordinary stress on component materials, especially on the blades of the first turbine stage. For long, safe, and reliable operation, an efficient means of cooling these blades is thus a necessity to avoid excessive thermal stresses. Film cooling is one method of thermal protection for gas turbine surfaces which is extensively used in commercial and military applications. Of the different film injection configurations, simple angle injection has been the method employed frequently on turbine blades, turbine endwalls, combustion chamber linings, and afterburner linings in the past. Simple angle injection refers to situations in which the film is injected with holes inclined to the test surface such that injectant is issued approximately in the direction of the mainstream flow when viewed in the streamwise/spanwise plane.

More recently, gas turbine components include film holes with compound angle orientations. Compound angle holes produce injectant which often provides better protection and higher film effectiveness than injectant from holes with simple angle orientations. Holes with compound angle orientations are inclined to the test surface such that the injectant is issued with a spanwise velocity component relative to the mainstream flow. Although compound angle film-cooling is now a common means of turbine blade protection, there are little data

in the archival literature on heat transfer and boundary layer behavior downstream of film cooling holes with compound angle orientations. One objective of the present test program is to provide new information on the local heat transfer and injectant distributions in boundary layers which develop downstream of film-cooling holes with compound angle orientations.

References 1 through 9 present film-cooling results measured downstream of single and multiple film-cooling holes. Of these References, 2, 3, 4, 5, 7, and 8 present results on the influences of embedded, longitudinal vortices on film-cooling. More recently, Mitchell [Ref. 7], Bishop [Ref. 8], and Cirellio [Ref. 9], present results measured downstream of injection holes with compound angle orientations without embedded vortices.

In the present study, new Stanton number, iso-energetic Stanton number, adiabatic film effectiveness, mean velocity, mean total pressure, and injectant distribution data are presented and analyzed for the same simple angle configuration used by Cirellio [Ref. 9], as well as for a new compound angle injection hole configuration. Adiabatic film cooling effectiveness values are determined using linear superposition theory applied to Stanton number ratios measured at different injection temperatures. This is possible since the three-dimensional energy equation which describes the flow field is linear and homogeneous in its dependent variable, temperature. This equation is of the form :

$$\alpha\left(\frac{\partial^2 T}{\partial x^2}+\frac{\partial^2 T}{\partial y^2}+\frac{\partial^2 T}{\partial z^2}\right)=u\frac{\partial T}{\partial x}+v\frac{\partial T}{\partial y}+w\frac{\partial T}{\partial z} \qquad \text{(Equation 1.1)}$$

where $\alpha = \frac{k}{\rho c}$. (Equation 1.2)

The technique of superposition was first applied to film cooling by Metzger, Carper and Swank [Ref. 1]. They examined the effect of secondary fluid injection through nontangential slots on the heat transfer in regions near the injection site. They described differences due to the various tangential injection geometries employed as reflected by rather large variations of the adiabatic wall temperature. To facilitate comparisons of various film-cooling schemes, the parameter Φ is employed, which depends on temperature parameter θ and blowing ratio m. The parameter Φ is defined as :

$$\Phi = \frac{h_{\text{with film injection}}}{h_{\text{without film injection}}} = \frac{h}{h_o} \qquad \text{(Equation 1.3)}$$

The parameter (m) is defined as:

$$m = \frac{\rho_c u_c}{\rho_\infty u_\infty} \qquad \text{(Equation 1.4)}$$

The parameter (θ) is defined as:

$$\theta = \frac{T_c - T_\infty}{T_w - T_\infty} \qquad \text{(Equation 1.5)}$$

In a comment on the Metzger, Carper and Swank paper, E.R.G. Eckert relates Φ to the adiabatic wall temperature (T_{aw}). The adiabatic wall temperature (T_{aw}), is defined as the temperature which the film-cooled wall assumes when the heat flux $\dot{q}$ in the following equation is zero.

$$\dot{q} = h_f A(T_w - T_{aw}) \qquad \text{(Equation 1.7)}$$

Equation 1.4 relates heat transfer to the difference between the actual wall temperature and the adiabatic wall temperature with the iso-energetic heat transfer coefficient hf. With an adiabatic condition, $\dot{q} = 0$ and $T_w = T_{aw}$. The adiabatic film-cooling effectiveness is given by:

$$\eta_{aw} = \frac{T_{aw} - T_\infty}{T_w - T_\infty} \qquad \text{(Equation 1.8)}$$

The heat flux given by equation 1.7 may also be expressed in terms of the difference between the actual wall temperature and the freestream temperature using the equation given by:

$$\dot{q} = hA(T_w - T_\infty) \qquad \text{(Equation 1.9)}$$

Setting Equations 1.7 and 1.9 equal then yields:

$$h = h_f \frac{T_w - T_{aw}}{T_w - T_\infty} \qquad \text{(Equation 1.10)}$$

The temperature term may also be given by :

$$\frac{T_w - T_{aw}}{T_w - T_\infty} = \frac{(T_w - T_\infty) - (T_{aw} - T_\infty)}{(T_w - T_\infty)} = 1 - \frac{(T_{aw} - T_\infty)}{(T_w - T_\infty)}$$

(Equation 1.11)

or alternatively;

$$\frac{T_w - T_{aw}}{T_w - T_\infty} = (1 - \eta_{aw}\theta) \qquad \text{(Equation 1.12)}$$

Substituting equation 1.12 into equation 1.10 finally yields:

$$h = h_f(1 - \theta\eta_{aw}) \qquad \text{(Equation 1.13)}$$

In this study, heat transfer data is normalized with baseline heat transfer coefficients, h_O, measured when no film-cooling is employed. Dividing Equation

1.13 by h_o, and then expressing h, hf, and h_o in terms of St, Stf, and St_o, equation 1.13 finally becomes:

$$\frac{St}{St_o} = \frac{St_f}{St_0}(1 - \theta\eta_{aw}) \qquad \text{(Equation 1.14)}$$

Equation 1.14 gives a linear relation between St/Sto and θ. A plot of St/Sto versus θ gives a line with a vertical axis intercept of Stf/Sto, and a horizontal axis intercept of $1/\eta_{aw}$. If temperature variations are small enough that fluid properties are invariant over the range of θ considered and with respect to all three coordinate directions, then this line is straight, [Ref. 10]. St/St_o measurements at different θ can thus be extrapolated to the axis intercepts, to determine the iso-energetic Stanton number ratio, Stf/Sto, and the adiabatic film cooling effectiveness , η_{aw}.

Figure 11 shows St/Sto experimental data obtained at different θ obtained downstream of two rows of film cooling holes with simple angle orientations producing injectant at a blowing ratio of 0.5, [Ref. 9]. As θ is varied from 0.0 to values near 3.0, the blowing ratio is maintained constant and the density ratio changes from 1.0 to about 0.9. In spite of these variations, the linearity of data in figure 11 is evident for all six values of x/d along the spanwise centerline of the test surface (Z/d=0.0). Lines through each set of data also illustrate some of the horizontal axis intercepts and vertical axis intercepts which give $1/\eta_{aw}$ and Stf/Sto respectively. To obtain local variations of these quantities, the method of linear superposition is applied for each measurement location. In most cases, no

extrapolation is needed to determine Stf/Sto because St/Sto is measured directly at θ =0.

B. PRESENT STUDY

The objective of the present work is to determine Stanton numbers at θ values ranging from 0 to 3.0, at x/d ratios of 6.8, 17.4, 33.2, 54.4, 75.6 and 96.7 for a simple angle injection system, configuration 2, and at x/d values of 6.8, 17.6, 33.8, 55.5, 77.1, and 98.7 for a compound angle injection system, configuration 3. With the simple angle configuration, configuration 2, holes are inclined at 35 degrees with respect to the test surface in the streamwise/normal plane. With the compound angle configuration, configuration 3, holes are inclined at 35 degrees with respect to the test surface when projected into the streamwise/normal plane, and 30 degrees with respect to the test surface when projected into the spanwise/normal plane. With each configuration, two staggered rows of holes are used. Within each row for both configurations, holes are spaced 6 hole diameters apart. Results presented include distributions of Stanton number ratios, adiabatic film cooling effectiveness values deduced from using linear superposition, and injectant distributions. Also presented are plots showing the streamwise development of distributions of mean velocity and mean temperature.

C. EXPERIMENTAL OUTLINE

Three different types of measurements are made in the present study which are described as follows:

1. Stanton numbers, Stanton number ratios , iso-energetic Stanton number ratios and adiabatic film cooling effectiveness at 21 spanwise locations at x/d ratios of 6.8, 17.4, 33.2, 54.4, 75.6 and 96.7 for configuration 2 and at x/d ratios of 6.8, 17.6, 33.8, 55.5, 77.1, and 98.7 for configuration 3.

2. Mean velocity and total pressure surveys in (Y-Z) planes at x/d of 9.9, 44.3, and 86.3 for configuration 3.

3. Mean temperature (T- T_{∞}) surveys in (Y-Z) planes at x/d of 9.9, 44.3, and 86.3 for configuration 3.

Data was obtained with no film-cooling to obtain a baseline set of measurements, as well as for 9 film-cooling arrangements. Results for the following configurations are presented: (1) two staggered rows of configuration 3 compound angle film-cooling holes with a blowing ratio of m=0.5; (2) two staggered rows of configuration 3 compound angle film-cooling holes with a blowing ratio of m=1.0; (3) two staggered rows of configuration 3 compound angle film-cooling holes with a blowing ratio of m=1.5; and (4) one row of configuration 3 compound angle film-cooling holes with a blowing ratio of m=0.5; (5) one row of configuration 3 compound angle film-cooling holes with a blowing ratio of m=1.0; (6) one row of configuration 3 compound angle film-cooling holes with a blowing ratio of m=1.5; (7) two staggered rows of configuration 2 simple angle film-cooling holes with a blowing ratio of m=0.5; (8) two staggered rows of configuration 2 simple angle film-cooling holes with

a blowing ratio of m=1.0; and (9) two staggered rows of configuration 2 simple angle film-cooling holes with a blowing ratio of m=1.5.

D. THESIS ORGANIZATION

The remainder of this thesis is organized as follows. The experimental apparatus and procedures are discussed in Chapter II. The experimental results are presented in Chapter III. A summary of the results and conclusions is presented in Chapter IV. Appendix A contains all of the figures. Appendix B gives the experimental uncertainty magnitudes from Schwartz [Ref. 8]. Data acquisition, processing, and plotting programs are described in Appendix C. Finally, a data file directory listing the names of all data files contained on micro floppy disks is presented in Appendix D.

II. EXPERIMENTAL APPARATUS AND PROCEDURES

A. WIND TUNNEL AND COORDINATE SYSTEM.

The wind tunnel is the same one used in the experiments of Ligrani, et al. (1989, 1991). The facility, located in the laboratories of the Department of Mechanical Engineering of the Naval Postgraduate School, is open-circuit and subsonic. A centrifugal blower is located at the upstream end, followed by a diffuser, a header containing a honeycomb and three screens, and then a 16 to1 contraction ratio nozzle. The nozzle leads to the test section which is a rectangular duct 3.05 m long and 0.61 m wide, with a topwall having adjustable height to permit a zero pressure gradient to be set along the length of the test section (without the film cooling) to within 0.01 inches of water differential pressure. The initial duct height at the nozzle exit is 0.203 m. The freestream velocity is 10 m/s and the freestream turbulence intensity is approximately 0.13 percent based on the same velocity. The boundary layer is tripped using a 2 mm high spanwise uniform strip of tape near the nozzle exit. This trip is located 1.072 m upstream of the surface used to measure local Stanton number distributions.

Schematics showing the test section and coordinate system are presented in Figures 1, 2 for film injection configurations 2 and 3, respectively. Locations of the boundary layer trip, film cooling holes, heat transfer test surface, and thermocouple rows along the test surface are evident. Dimensional values of distances labelled in Figures 1 and 2 and are also given in Figures 3 and 4. With both configurations 2 and 3, an unheated starting length exists upstream of the

heat transfer surface when it is elevated in temperature. In regard to the coordinate system, Z is the spanwise coordinate measured from the test section spanwise centerline; X is measured from the upstream edge of the boundary layer trip; and Y is measured normal to the test surface. x is measured from the downstream edge of the injection holes and generally presented as x/d.

B. INJECTION SYSTEM AND INJECTION CONFIGURATIONS.

1. Injection System

The injection system was described by Ligrani, et al (1991). Air for the injection system originates in two 1.5 horsepower DR513 Rotron Blowers capable of producing 30 cfm at 2.5 psig. From the blowers, air flows through a regulating valve, a Fisher and Porter rotometer, a diffuser, and then into the injection heat exchanger and plenum chamber. The exchanger provides the means to heat the injectant above ambient temperature. With this system and test plate heating, the non-dimensional injection temperature parameter θ is maintained at values ranging from 0.0 to 3.0, which includes values within the range of gas turbine component operation. The upper surface of the plenum chamber is connected to the injection tubes for either injection configuration. With configuration 2, each tube is 7.6 cm long. This gives a length to diameter ratio of about 8. With configuration 3, the tube length is 9.4 cm which gives a length to diameter ratio of approximately 10.

Injection system performance was checked by measuring discharge coefficients at different Reynolds numbers based on injection hole diameter and mean injectant velocity. These values compare favorably with earlier measurements (Ligrani, et al, 1989). Procedures to measure discharge

coefficients and blowing ratios are described by Ligrani, et al (1989). The results of these performance checks are presented in Figure 7.

2. Injection Configuration

A schematic showing the simple angle film hole geometry (configuration 2) along the test surface is shown on Figure 5. A schematic showing the compound angle film hole geometry (configuration 3) along the test surface is shown in Figure 6. In both cases, holes are arranged in two rows which are staggered with respect to each other with spanwise spacings between adjacent holes of 3.0d. Centerlines of holes in separate rows are separated by 3.9d- 4.0 d in the streamwise direction. When only one row of holes is employed, it is the downstream row located closest to the heat flux surface. With this arrangement, spanwise hole spacing is 6.0d. Each row of holes contains five injection cooling holes with a nominal inside diameter of 0.945 cm for configuration 2 and 0.925 cm for configuration 3. The centerline of the middle hole of the downstream row is located on the spanwise centerline (Z=0.0 cm) of the test surface. The compound angle holes are employed with Ω=35 degrees and ß=30 degrees, where Ω is the angle of the injection holes with respect to the test surface as projected into the streamwise/normal plane, and ß is the angle of the injection holes with respect to the test surface as projected into the spanwise/normal plane. Thus, as shown in Figure6, holes are oriented so that the spanwise components of injectant velocity are directed in the negative-Z direction. The plane of each injection hole is angled at 50.5 degrees from the streamwise/normal (X-Y) plane. Within the plane of each hole, hole centerlines are oriented at angles of 24 degrees from the plane of the test surface (X-Z).

With the simple angle arrangement, Ω=35 degrees and ß=90 degrees. Thus, the plane of each injection hole is within the streamwise/normal (X-Y) plane and holes are inclined at an angle of 35 degrees with respect to the test surface.

C. STREAMWISE MEAN VELOCITY MEASUREMENTS.

The streamwise mean velocity was measured using a five-hole pressure probe with a conical tip manufactured by United Sensors Corporation. Celesco transducers and Carrier Demodulators are used to sense pressures when connected to probe output ports. The same automated traverse used for injectant surveys was used to obtain these surveys. With this device, the pressure probe was traversed over 10.2 cm by 20.3 cm spanwise/normal planes at 800 locations spaced 0.51 cm apart in each direction. At each location, 50 samples of the output from each of the five pressure ports are aquisitioned for later processing. These devices, measurement procedures employed, as well as data acquisition equipment and procedures used are further detailed by Ligrani, et al (1989, 1991), Bishop (1990), and Ciriello (1991).

D. STANTON NUMBER MEASUREMENTS.

The heat transfer surface is designed to provide a constant heat flux over its area. The surface next to the airstream is stainless steel foil painted flat black. Immediately beneath this is a liner containing 126 thermocouples, which is just above an Electrofilm Corp., etched foil heater rated at 120 volts, and 1500 watts. Located below the heater are several layers of insulating materials including Lexan sheets, foam insulation, styrofoam and balsa wood. Surface

temperature levels and convective heat transfer rates are controlled by adjusting power into the heater using a Standard Electric Co. Variac, type 3000B. To determine the heat loss by conduction, an energy balance was performed. This was accomplished by insulating the top of the test surface (which is nominally exposed to the airstream) and measuring conduction loss from the bottom as it is dependent upon the difference in temperature between the test surface and the surrounding ambient air. Radiation losses from the top of the test surface were analytically estimated. The thermal contact resistance between thermocouples and the foil top surface was estimated on the basis of outputs of the thermocouples and measurements from calibrated liquid crystals on the surface of the foil. This difference was then correlated as a function of heat flux through the foil.

After the surface was completed, a variety of qualification tests were conducted to check the performance of the heat transfer test surface. These were described in detail by Ligrani, et al (1989), Bishop (1990) and Ciriello (1991), along with additional details on the measurement of local Stanton numbers.

E. MEAN TEMPERATURE MEASUREMENTS.

Copper-constantan thermocouples were used to measure temperatures along the surface of the test plate, the freestream temperature, and temperature distributions which were correlated to injection distributions. For the distributions, a thermocouple was traversed over spanwise/normal planes (800 probe locations) using an automated two-dimensional traversing system which could be placed at different streamwise locations. Voltages from thermocouples and the Carrier Demodulators (used for the mean velocity measurements) are digitally sampled and read using a Hewlett-Packard 3497A Data Acquisition

Control Unit with a 3498A Extender. These units are controlled by a Hewlett-Packard Series 9153C computer.

F. BASELINE DATA CHECKS.

Repeated measurements of spanwise-averaged Stanton numbers show good agreement (maximum deviation is 4 percent) with the correlation from Kays and Crawford (1980) for turbulent heat transfer to a flat plate with unheated starting length and constant heat flux boundary condition. Figures 9 and 10 present baseline data for configurations 2 and 3, respectively. Figure 9 presents baseline data for two separate conditions. Condition 1, with $(T_{plate}-T_{\infty})=9.66$, was obtained with 4 amps applied to the plate heaters. A higher power level of 6 amps was utilized to obtain condition 2 with $(T_{plate}-T_{\infty})=20.08$. Both sets of data show good agreement with the Kays and Crawfords' unheated starting length constant heat flux correlation, with a maximum deviation of approximately 10%. Similar conclusions may be drawn in regard to the baseline data for configuration 3 shown in Figure 10.

III. EXPERIMENTAL RESULTS

Experimental results are presented in two parts. Results for the simple angle injection system, configuration 2, are given first. These results are then followed by ones for the compound angle injection system, configuration 3. For configuration 2, surface heat transfer data are presented from measurements downstream of two staggered rows of holes. For configuration 3, surface heat transfer data, injectant distributions, surveys of mean velocity, and surveys of total pressure are presented from measurements downstream of both one row of holes and two staggered rows of film-cooling holes. In both cases (configurations 2 and 3), data are presented for blowing ratios of 0.5, 1.0, and 1.5.

A. CONFIGURATION TWO, SIMPLE ANGLE RESULTS

1. Heat Transfer Measurements Downstream of Two Rows Of Film-Cooling Holes With m=0.5

Figures 12-17 present St/Sto vs. θ results for x/d=6.8, 17.4, 33.2, 54.4, 75.6, and 96.7 at z/d=0.0 for m=0.5. Figures 18 and 19 then present spanwise-averaged adiabatic effectivenesses and spanwise-averaged Stf/Sto as dependent on x/d, repectively. Figures 20, 21, and 22 show streamwise and spanwise varations of spanwise-averaged adiabatic effectiveness, iso-energetic Stanton number ratio, and Stanton number ratio, respectively. Spatially resolved plots of effectiveness in Figure 20 show that spanwise periodicity, evident at x/d=6.8, is less pronounced as the flow develops in the streamwise direction. The spanwise

variations of St_f/St_o and St/St_o in Figures 21 and 22 show similar spanwise periodicity which is most evident at x/d=6.8, and not particularly evident at x/d greater than 54.3. The Stanton number ratio data in Figure 22 are given for θ = 1.59.

2. Heat Transfer Measurements Downstream Of Two Rows Of Film-Cooling Holes With m=1.05

Figures 23-28 present St/Sto vs. Θ for x/d=6.8, 17.4, 33.2, 54.4, 75.6, and 96.7 at z/d=0.0 for m=1.05. Figures 29 and 30 then present spanwise-averaged adiabatic effectivenesses and spanwise-averaged iso-energetic Stanton number ratios as dependent upon x/d, respectively. Figures 31, 32, and 33 show streamwise and spanwise variations of spanwise-averaged adiabatic effectiveness, iso-energetic Stanton number ratio, and Stanton number ratio, respectively. The Stanton number ratio data in Figure 33 are for θ=1.66. Spatially resolved plots of spanwise-averaged adiabatic effectiveness in Figure 31 again show spanwise periodicity at low x/d values which becomes less pronounced with streamwise development. Compared to results for m=0.5, effectiveness values are lower at x/d values below about 50 due to lift-off effects. At higher x/d values, effectiveness values are greater because larger amounts of film injectant are present next to the test surface. Figures 32 and 33 show similar spanwise periodicity for iso-energetic Stanton number ratio and Stanton number ratio which are similar to the variations in Figures 21 and 22 for m=0.5.

3. Heat Transfer Measurements Downstream Of Two Rows Of Film-Cooling Holes With m=1.5

Figures 34-39 present St/Sto vs θ for x/d=6.8, 17.4, 33.2, 54.4, 75.6, and 96.7 at z/d=0.0 for m=1.5. Figures 40 and 41 then present spanwise-averaged adiabatic effectivenesses and spanwise-averaged iso-energetic stanton number ratios as dependent upon x/d, respectively. Figures 42, 43, and 44 show the streamwise and spanwise variations of spanwise-averaged adiabatic effectiveness, Stanton number ratio and iso-energetic Stanton number ratio, respectively. Spatially resolved plots of spanwise-averaged adiabatic effectiveness in Figure 42 show spanwise periodicity which becomes less pronounced with streamwise development. The amplitude and frequency of effectiveness peaks are smaller than the effectiveness peaks measured for m=0.5 and m=1.05. In addition, spanwise-averaged magnitudes of the adiabatic effectiveness for m=1.5 are lower than ones for m=0.5 and m=1.05 at x/d less than 33.2 due to increased lift-off as the blowing ratio increases. At x/d values greater than 33.2, spanwise-averaged effectiveness values are higher for m=1.5 because greater amounts of injectant are present near the test surface.

B. CONFIGURATION THREE, COMPOUND ANGLE RESULTS

1. Two Rows Of Film-Cooling Holes With m=0.5

a. Heat Transfer Measurements

Figures 45-50 present St/Sto vs. Θ results measured at z/d=0.0, for x/d=6.8, 17.6, 33.8, 55.5, 77.1, and 98.7 and for m=0.5. These figures illustrate

the linearity of St/Sto vs. θ data at each x/d presented. Similar linearity is present for the entire range of locations along the test plate, which supports the use of linear superposition theory for determination of adiabatic effectiveness and iso-energetic Stanton number ratio, even though the flow field is highly three dimensional. Figures 51 and 52 then present spanwise-averaged adiabatic effectivenesses and spanwise-averaged iso-energetic Stanton number ratios, respectively, as dependent upon x/d. Figures 53, 54, and 55 then show streamwise and spanwise variations of adiabatic effectiveness, iso-energetic Stanton number ratio, and Stanton number ratio for θ=1.54, respectively.

Figure 51 shows that spanwise-averaged adiabatic effectiveness is greatest at x/d=6.8, and decreases with streamwise distance. Figure 52 shows that iso-energetic Stanton number ratio is relatively constant at about 1.1 for x/d greater than approximately 15. Such behavior is consistent with earlier results, [Ref. 7 and 8] which show that iso-energetic Stanton number is strongly dependent on blowing ratio and/or momentum flux ratio and very weakly dependent on x/d. Figures 53, 54, and 55 show that spatially resolved plots of effectiveness, iso-energetic Stanton number ratio, and Stanton number ratio for θ=1.54, respectively, are fairly spanwise uniform for all x/d.

b. Velocity And Pressure Surveys

Surveys of total pressure and streamwise velocity in spanwise-normal planes at x/d=9.9, 44.3, and 86.3 are shown in Figures 56-61. For each x/d, total pressure and velocity distributions are qualitatively similar. Total pressure and velocity results in Figures 56 and 57 for x/d= 9.9 are spanwise periodic, with deficits separated by 2.5-3 cm near the wall which is the same as the spanwise hole spacing. Less spanwise periodicity is evident at x/d =44.3 in Figures 58 and

59, and at x/d=86.3 in Figures 60 and 61. Fairly uniform distributions of streamwise velocity and total pressure across the span of the measurement plane are present at x/d=86.3 where local boundary layer thicknesses are about 30 percent larger than values at x/d=9.9.

c. Injectant Distributions

Figures 62, 63, and 64 show surveys of temperature in spanwise/normal planes at x/d=9.9, 44.3, and 86.3, respectively. According to Ligrani et al. [Ref. 9], these surveys provide information on distributions of the injectant. At x/d=9.9, individual injectant concentrations are spanwise periodic and non-circular near the wall across the span of the measurement plane. Distributions for x/d=44.3 and x/d=86.3 in Figures 63 and 64 show less spanwise periodicity. In fact, the results in Figure 64 are fairly spanwise uniform.

2. Two Rows Of Film-Cooling Holes With m=1.0

a. Heat Transfer Measurements

Figures 65-70 present St/Sto vs. θ results measured at z/d=0.0. for x/d=6.8, 17.6, 33.8, 55.5, 77.1, and 98.7, and for m=1.0. Figures 71 and 72 then present results of spanwise-averaged adiabatic effectivenesses and spanwise-averaged iso-energetic Stanton number ratios as dependent upon x/d, respectively. Figures 73, 74, and 75 show streamwise and spanwise variations of adiabatic effectiveness, Stf/Sto and St/Sto for θ=1.72, respectively.

Figures 65-70 illustrate the linearity of St/St_o as dependent upon θ for the entire range of locations along the test surface, which again supports the use of linear superposition theory for determination of spanwise-averaged adiabatic effectivenesses and spanwise averaged iso-energetic Stanton number

ratios. Figure 71 shows that spanwise averaged adiabatic effectiveness values are greatest at low x/d and decrease linearly after x/d=15. Figure 72 shows that iso-energetic Stanton number ratio increases slightly over the first quarter of the test plate and remains fairly constant at about 1.1 as x/d varies. Such behavior is consistent with earlier results, Ligrani et al. [Ref. 9], which show weak dependence of iso-energetic Stanton number ratio on x/d. Figure 73 shows that spatially resolved plots of effectiveness are spanwise periodic at x/d=6.8 and x/d=17.6, while the spanwise distribution of adiabatic effectiveness is fairly uniform for x/d greater than 33.8. Figures 74, and 75 show that the spanwise and streamwise variations of iso-energetic Stanton number ratio and Stanton number ratio are spanwise periodic for all x/d along the test plane.

b. Velocity And Pressure Surveys

Figures 76-81 present surveys of total pressure and streamwise velocity in spanwise-normal planes for x/d=9.9, 44.3, and 86.3. For each x/d, the total pressure and velocity distributions are qualitatively similar. The total pressure and velocity results in Figures 76 and 77 for x/d=9.9 are spanwise periodic. The separation between deficits increases in the spanwise direction at further downstream locations indicating that injectant from upstream holes merges with injectant from downstream holes. The distance between the deficits is as large as 3.5cm near the wall. When compared to similar data for m=0.5 (Figures 56-61), near wall deficits for m=1.0 are larger near the wall and separated by slightly larger spanwise distances. Figures 78-81 show that total pressure and velocity distributions are fairly spanwise uniform for x/d greater than 44.3. These figures also show increases in local boundary layer thickness of approximately 10% compared to results in Figures 76 and 77 for m=0.5.

c. Injectant Distributions

Figures 82, 83, and 84 show surveys of temperature in spanwise/normal planes at x/d=9.9, 44.3, and 86.3, respectively. According to Ligrani et al. [Ref. 9], these surveys provide information on distributions of the injectant. At x/d=9.9, individual injectant concentrations are spanwise periodic and non-circular near the wall across the span of the measurement plane. Distributions for x/d=44.3 and x/d=86.3 in Figures 83 and 84 show less spanwise periodicity. In fact, the results in Figure 84 are fairly spanwise uniform.

3. Two Rows Of Film-Cooling Holes With m=1.5

a. Heat Transfer Measurements

Figures 85-90 present St/Sto vs. θ results for x/d=6.8, 17.6, 33.8, 55.5, 77.1, and 98.7 at z/d=0.0 for m=1.5. The linearity of the data provides added support for the linear superposition technique. Figures 91 and 92 present spanwise-averaged adiabatic effectivenesses and spanwise-averaged iso-energetic Stanton number ratios as dependent upon x/d, respectively. Figures 93, 94, and 95 show streamwise and spanwise variations of adiabatic effectiveness, Stf/Sto, and St/Sto for θ=1.24.

Figures 91 shows spanwise-averaged adiabatic effectiveness values are greatest at low x/d and decrease with x/d for values greater than 15. Figure 92 shows that iso-energetic Stanton number ratios decrease for x/d values between 5 and 35. At x/d values greater than 35, iso-energetic Stanton number ratios are fairly constant at about 1.2. Figures 93, 94, and 95 show spatially resolved plots of adiabatic effectiveness, iso-energetic Stanton number ratio, and

Stanton number ratio for θ=1.24, which are spanwise periodic at x/d=6.8 and x/d=17.6. At x/d values greater than 33.8, the distributions are fairly uniform. W'.en compared toFigures 73-75, the data inFigures 93-95 suggest that lift-off effects are increasingly important at higher blowing ratios.

b. Velocity And Pressure Surveys

Figures 96-101 present surveys of total pressure and streamwise velocity in spanwise-normal planes for x/d=9.9, 44.3, and 86.3. For each x/d, the total pressure and velocity distributions are qualitatively similar. Total pressure and velocity results in Figures 96 and 97 for x/d= 9.9 are spanwise periodic, with deficits separated by 4-5 cm near the wall. When compared to data for m=0.5 and m=1.0, (Figures 56, 57, 76, and 77), the near-wall deficits are larger with greater separation. Figures 98-101 show that the distributions of total pressure and velocity are spanwise uniform for x/d values greater than 44.3.

c. Injectant Distributions

Figures 102-104 show surveys of temperature in spanwise/normal planes at x/d=9.9, 44.3, and 86.3, respectively, which provide information on distributions of the injectant . At x/d=9.9, individual injectant concentrations are non-circular and spanwise periodic near the wall. Distributions for x/d=44.3 and x/d=86.3 in Figures 103 and 104 show less spanwise periodicity and greater spanwise uniformity.

4. One Row Of Film-Cooling Holes With m=0.5

a. Heat Transfer Measurements

Figures 105-110 present St/Sto vs. θ results measured at z/d= -1.27, for x/d=6.8, 17.6, 33.8, 55.5, 77.1, and 98.7, for m=0.5. These figures illustrate the linearity of St/Sto vs. θ data at each x/d. Figures 111 and 112 present spanwise-averaged adiabatic effectivenesses and spanwise-averaged iso-energetic Stanton number ratios as dependent upon x/d, respectively. Figures 113, 114, and 115 then show streamwise and spanwise variations of adiabatic effectiveness, iso-energetic Stanton number ratio, and Stanton number ratio for θ=1.37.

Figure 111 shows that spanwise-averaged adiabatic effectiveness is greatest at x/d=6.8 and decreases as x/d increases. Figure 112 shows that iso-energetic Stanton number ratio is relatively constant at 1.0 for all x/d. Such behavior is consistent with earlier results, [Ref. 7, and 8], which show that the iso-energetic Stanton number ratio is strongly dependent on blowing ratio and/or momentum flux ratio, and very weakly dependent on x/d. Figures 113, 114, and 115 show spatially resolved plots of adiabatic effectiveness, iso-energetic Stanton number ratio, and Stanton number ratio for θ=1.37, respectively. In all cases these data are fairly spanwise uniform for all x/d.

b. Velocity And Pressure Surveys

Surveys of total pressure and streamwise velocity in spanwise-normal planes at x/d=9.9, 44.3, and 86.3 are shown in Figures 116-121. For each x/d, total presssure and velocity distributions are qualitatively similar. Total pressure and velocity results in Figures 116 and 117 for x/d= 9.9 are spanwise periodic,

periodic, with deficits separated by 5.5-6 cm near the wall which is the same as the spanwise hole spacing. Figures 98-101 show fairly uniform distributions of streamwise velocity and total pressure across the span of the measurement plane for x/d values greater than 44.3.

c. Injectant Distributions

Figures 122, 123, and 124 show surveys of temperature in spanwise/normal planes at x/d=9.9, 44.3, and 86.3, respectively, which provide information on distributions of the injectant. At x/d=9.9, the injectant distributions are semi-circular and spanwise periodic near the wall. Distributions for x/d=44.3 and x/d=86.3 in Figures 123 and 124 show less spanwise periodicity and greater spanwise uniformity.

5. One Row Of Film-Cooling Holes With m=1.0

a. Heat Transfer Measurements

Figures 125-130 present St/Sto vs. θ results measured at z/d= -1.27, for x/d=6.8, 17.6, 33.8, 55.5, 77.1, and 98.7, and for m=1.0. These figures illustrate the linearity of St/Sto vs. θ data at each x/d presented. Figures 131 and 132 then present spanwise-averaged adiabatic effectivenesses and spanwise-averaged iso-energetic Stanton number ratios as dependent upon x/d, respectively. Figures 133, 134, and 135 show streamwise and spanwise variations of the adiabatic effectiveness, iso-energetic Stanton number ratio, and Stanton number ratio for θ=1.37, respectively.

Figure 131 shows that spanwise-averaged adiabatic effectiveness is greatest at x/d=6.8 and decreases with streamwise development. Figure 132

shows that the iso-energetic Stanton number ratio is relatively constant at about 1.0 for all x/d. Such behavior is consistent with earlier results, [Ref. 7 and 8], which show that the iso-energetic Stanton number ratio is strongly dependent on blowing ratio and/or momentum flux ratio and very weakly dependent on x/d. Figure 133 shows that spatially resolved plots of adiabatic effectiveness are spanwise-periodic for x/d=6.8 and x/d=17.6, while the adiabatic effectiveness is fairly spanwise uniform. for x/d values greater than 33.8. Spacially resolved plots of iso-energetic Stanton number ratio, and Stanton number ratio for θ=1.89, in Figures 134 and 135, respectively, show spanwise periodicity tfor all x/d. Results for m=0.5 in Figures 114 and 115 do not show as much periodicity.

b. Velocity and Pressure Surveys

Surveys of total pressure and streamwise velocity in spanwise-normal planes at x/d=9.9, 44.3, and 86.3 are shown in Figures 136-141. For each x/d, total presssure and velocity distributions are qualitatively similar. Total pressure and velocity results in Figures 136 and 137 for x/d= 9 9 are non-circular and spanwise periodic. The separation of the deficits is approximately 6cm near the wall which is the same as the spanwise hole spacing. Figures 138-141 show fairly uniform distributions for streamwise velocity and total pressure across the span of the measurement plane for x/d values greater than 44.3.

c. Injectant Distributions

Figures 142, 143, and 144 show surveys of temperature in spanwise/normal planes at x/d=9.9, 44.3, and 86.3, which provide information on distributions of the injectant . At x/d=9.9, individual injectant concentrations are spanwise periodic and circular near the wall. Distributions for

x/d=44.3 and x/d=86.3 in Figures 143 and 144 show less spanwise periodicity and more spanwise uniformity.

6. Heat Transfer Measurements Downstream Of One Row Of Film-Cooling Holes With m=1.5

Figures 145-150 present St/Sto vs. θ results measured at z/d= -1.27, for x/d=6.8, 17.6, 33.8, 55.5, 77.1, and 98.7 and for m=1.5. These figures illustrate the linearity of St/Sto vs. θ at each x/d. Simililar linearity is present for the entire range of locations along the test plate. Such behavior once again supports the use of linear superposition theory for determination of adiabatic effectiveness and iso-energetic Stanton number ratio. Figures 151 and 152 then present spanwise-averaged adiabatic effectivenesses and spanwise-averaged iso-energetic Stanton number ratios as dependent upon x/d, respectively. Figures 153, 154, and 155 then show streamwise and spanwise variations of adiabatic effectiveness, iso-energetic Stanton number ratio and Stanton number ratio for θ=1.29.

Figure 151 shows that spanwise averaged adiabatic effectiveness is greatest at x/d=6.8, and then decreases with streamwise development. Figure 152 shows that iso-energetic Stanton number ratio is relatively constant at about 1.1 for all x/d. Figure 153 shows that spatially resolved plots of spanwise-averaged adiabatic effectiveness are spanwise-periodic for x/d=6.8 and x/d=17.6, while adiabatic effectiveness is fairly spanwise uniformfor x/d values greater than 33.8. Spacially resolved plots of iso-energetic Stanton number ratio, and Stanton number ratio for θ=1.29 in respective figures 154 and 155 show spanwise periodicity for the entire range of x/d.

C. COMPARISON OF RESULTS FROM THE SIMPLE ANGLE AND COMPOUND ANGLE FILM-COOLING HOLE CONFIGURATIONS.

Experimental results for two compound angle injection systems (configurations 1 and 3), and for a simple angle injection system (configuration 2) are compared in this section. The effects of blowing ratio, spanwise hole spacing, hole angle orientation, and streamwise position are discussed in reference to measurements obtained downstream of both one row of holes and downstream of two staggered rows of holes. The hole diameter for configurations 1 and 2 is 0.945cm. The hole diameter for configuration 3 is 0.925cm. When two staggered rows are employed, the spanwise hole spacing is 3.9d for configuration 1, and 3.0d for configurations 2 and 3. When one row of holes is employed, the spanwise hole spacing is 7.8d for configuration 1, and 6.0d for configurations 2 and 3.

Results are first presented for two staggered rows of film-cooling injection holes. Figures 156 and 157 show spanwise-averaged adiabatic effectivenesses and iso-energetic Stanton number ratios as dependent upon x/d , respectively, for all 3 film hole configurations. Figures 158 and 159 then present spanwise-averaged adiabatic effectivenesses and spanwise-averaged iso-energetic Stanton number ratios as dependent upon x/d for configurations 1 and 3. Figures 160 and 161 then present spanwise-averaged adiabatic effectivenesses and spanwise-averaged iso-energetic Stanton number ratios as dependent upon x/d, for configurations 2 and 3.

Results are now presented for one row of film-cooling holes. Figure 162 and 163 present spanwise-averaged adiabatic effectivenesses and iso-energetic Stanton number ratios as dependent upon x/d for all 3 film hole configurations. Figures 164 and 165 present spanwise-averaged adiabatic effectivenesses and iso-energetic Stanton number ratios, respectively, for configurations 1 and 3. Figures 166 and 167 present similar data for configurations 2 and 3.

Results in Figures 156 and 161 show that spanwise-averaged adiabatic effectiveness values are greatest at lower x/d and decrease with streamwise development as the injectant is convected downstream. For a specified blowing ratio and for all three film hole configurations, the rate of spanwise-averaged adiabatic effectiveness decrease is dependent on the blowing ratio, and mostly a result of lift-off of the injectant from the test surface at x/d values less than about 20. At larger x/d, spanwise-averaged adiabatic effectiveness values generally increase with blowing ratio mostly because of greater amounts of injectant along the test surface.

Results in Figures 160 and 164 show that spanwise averaged magnitudes of the adiabatic film-cooling effectiveness downstream of compound angle injection configurations are generally higher than ones downstream of simple angle configurations when compared for the same blowing ratio (m), streamwise location (x/d), and streamwise hole spacing (s/d).

Results in Figures 157, 159, 161, 163, 165, and 167 show that the iso-energetic Stanton number ratio lies between 1 and 1.35 for all cases studied and generally increases with blowing ratio for a given x/d and a given injection hole configuration.

Results in Figures 156 and 161 show spanwise-averaged adiabatic effectiveness values measured downstream of two rows of holes are approximately 30-70% higher than values obtained downstream of a single row of holes, due to greater amounts of injectant along the test surface.

IV. SUMMARY AND CONCLUSIONS

Experimental results are presented which describe the development and structure of flow downstream of a single row, and downstream of two staggered rows of film-cooling holes with simple and compound angle orientations. Two configurations are investigated, a simple angle injection system in which the injectant is introduced into the freestream parallel to the main flow (as viewed in the streamwise/spanwise planes), and a compound angle injection system in which the injectant is introduced with spanwise velocity components. The effects of blowing ratio, spanwise hole spacing, hole angle orientation, and streamwise position are determined from measurements of adiabatic effectivenesses, iso-energetic Stanton number ratios, and Stanton number ratios for θ values approximately equal to 1.5.

For configuration 2, measurements are made downstream of three injection arrangements: (1) two staggered rows of film-cooling holes with a blowing ratio of m=0.5, (2) two staggered rows of film-cooling holes with a blowing ratio of m=1.05, and (3) two staggered rows of film-cooling holes with a blowing ratio of m=1.5.

For configuration 3, measurements are made downstream of six injection arrangements: (1) two staggered rows of film-cooling holes with a blowing ratio of m=0.5, (2) two staggered rows of film-cooling holes with a blowing ratio of m=1.0, (3) two staggered rows of film-cooling holes with a blowing ratio of m=1.5, (4) one row of film-cooling holes with blowing ratio of m=0.5, (5) one row of film-cooling holes with blowing ratio of m=1.0, and (6) one row of film-cooling holes with blowing ratio of m=1.5.

Results indicate that effectiveness depends mostly on four parameters: simple or compound angle injection, spanwise hole spacing, one or two rows of holes, and blowing ratio. Results show show that for a specified blowing ratio, for all configurations tested to date, spanwise-averaged adiabatic effectiveness is greatest at lower x/d values but decreases with streamwise development as the injectant is convected downstream. The rate of spanwise-averaged adiabatic effectiveness decrease is dependent on the blowing ratio, and mostly a result of lift-off of the injectant from the test surface at x/d values less than about 20. At larger x/d, spanwise-averaged adiabatic effectiveness values generally increase with blowing ratio mostly because of greater amounts of injectant along the test surface. Results further show that show that the iso-energetic Stanton number ratio lies between 1 and 1.35 for all cases studied and generally increases with blowing ratio for a given x/d and a given injection hole configuration.

Spanwise averaged magnitudes of the adiabatic film-cooling effectiveness downstream of compound angle injection configurations are generally higher than ones downstream of simple angle configurations at x/d less than 20-30 when compared for the same blowing ratio (m), streamwise location (x/d), and streamwise hole spacing (s/d). Finally, spanwise-averaged adiabatic effectiveness values measured downstream of two rows of holes are approximately 30-70% higher than values obtained downstream of a single row of holes due to greater amounts of injectant along the test surface.

APPENDIX A: FIGURES

Appendix A contains all of the figures generated for this thesis. The figures presented include: test set-up; injection hole configurations; plots of Stanton number ratios as dependent upon position; plots of spanwise-averaged adiabatic effectiveness and iso-energetic Stanton number ratios as dependent upon position; spatially resolved plots of spanwise-averaged adiabatic effectiveness, iso-energetic Stanton number ratio, and Stanton number ratio for θ values near 1.5; and spanwise plots of velocity, pressure and temperature for the nine configurations.

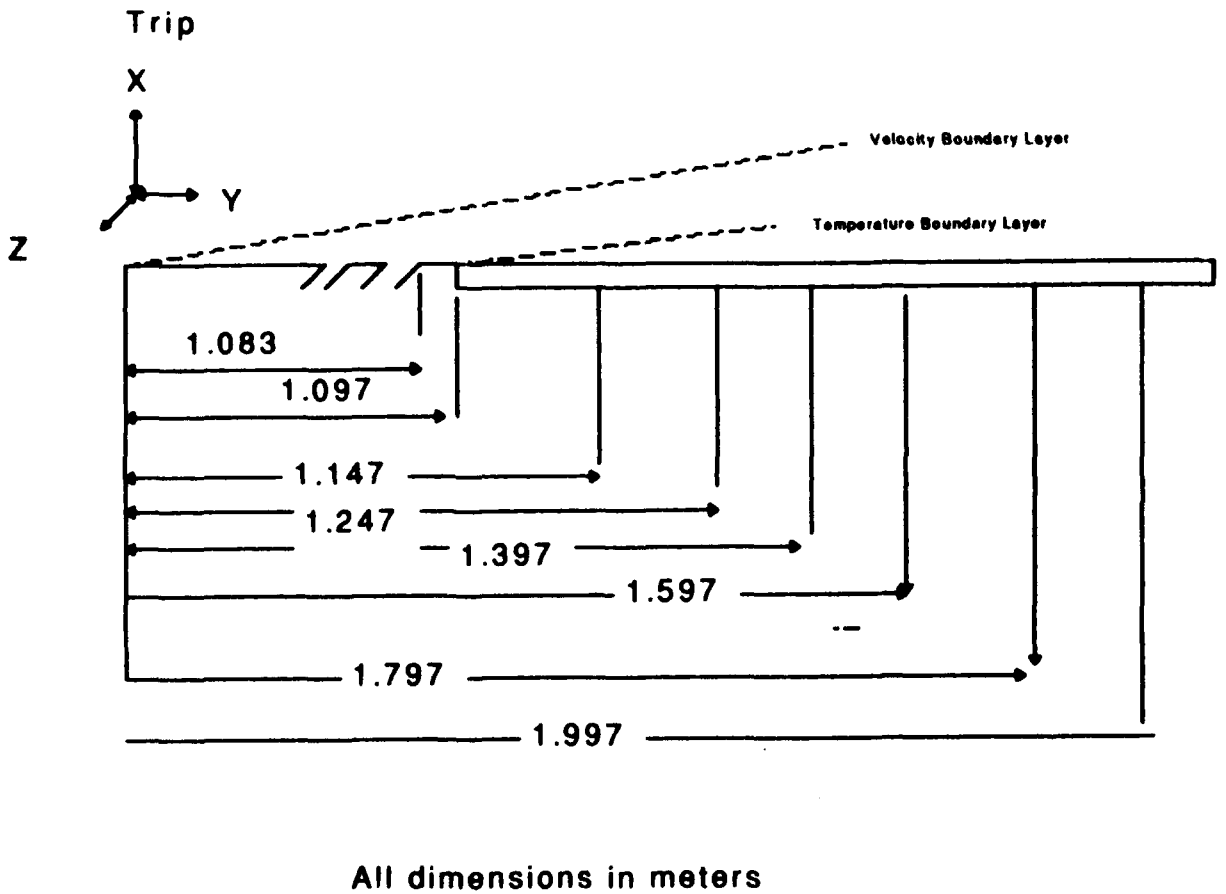


Figure 1. Test Section Coordinate System, Configuration 2, Simple Angle

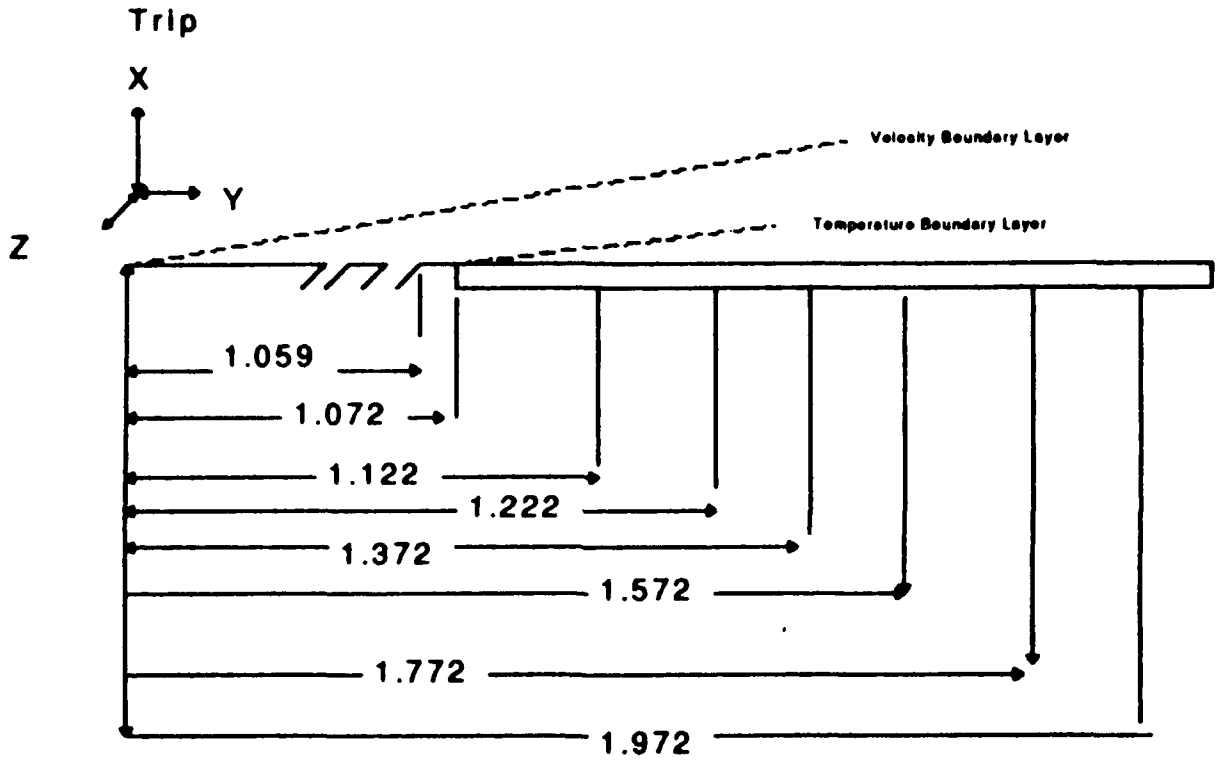


Figure 2. Test Section Coordinate System, Configuration 3, Compound Angle

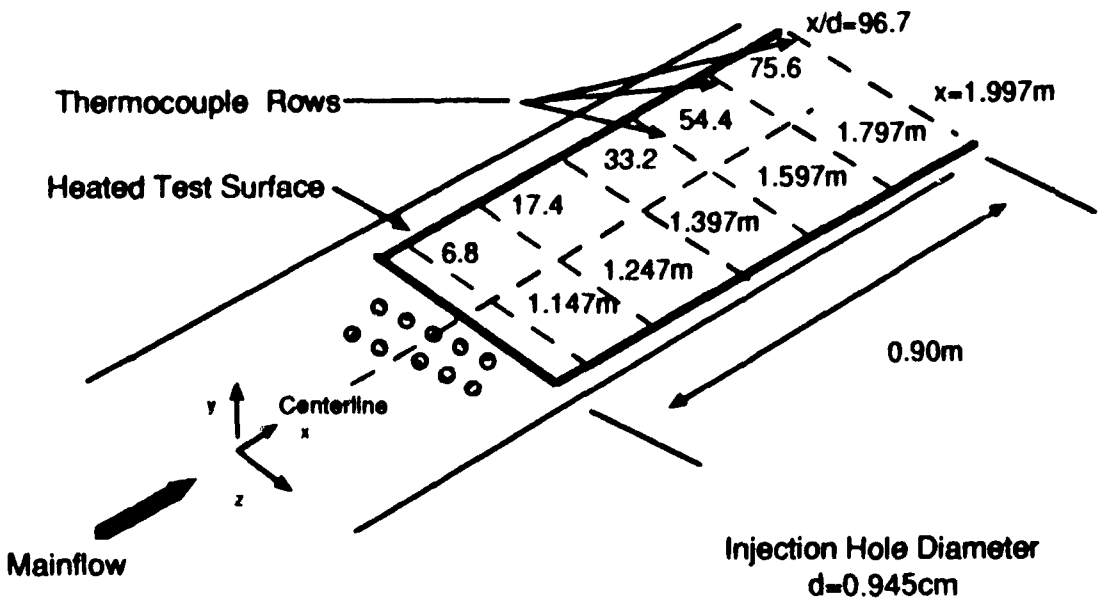


Figure 3. Top View Schematic of Wind Tunnel Test Section, Configuration 2, Simple Angle

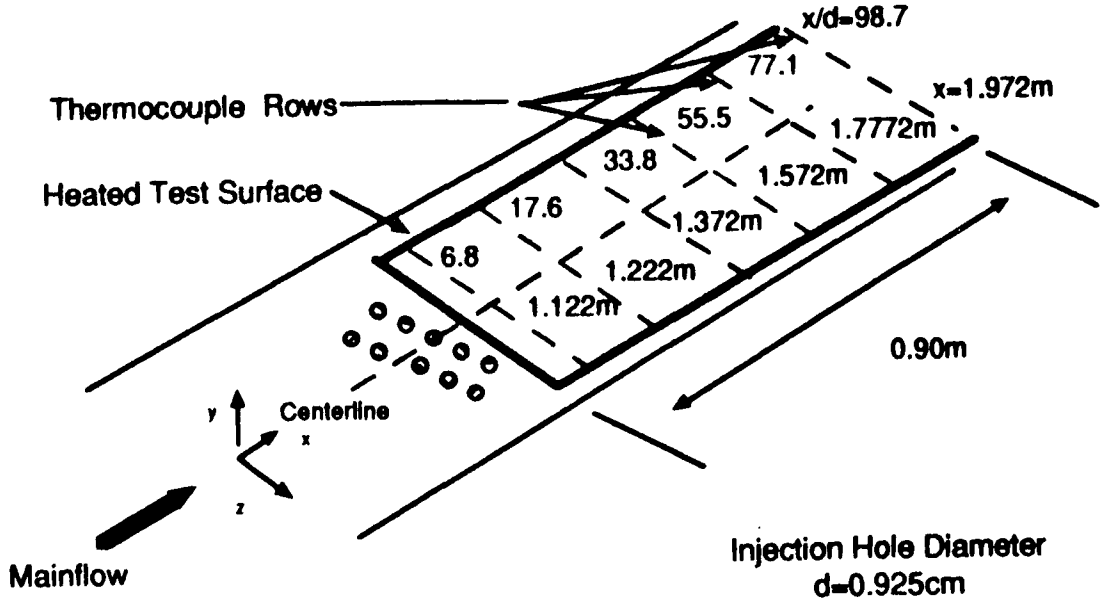


Figure 4. Top View Schematic of Wind Tunnel Test Section, Configuration 3, Compound Angle

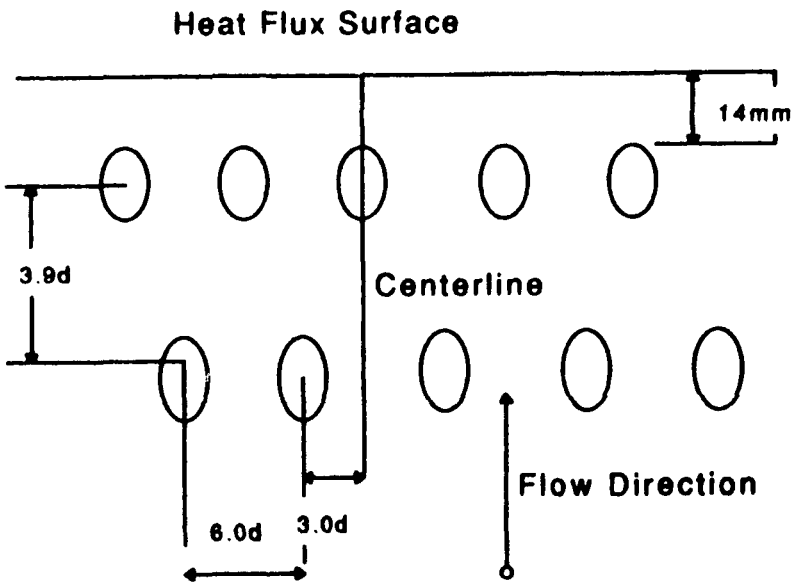


Figure 5. Injection Hole Configuration, Simple Angle

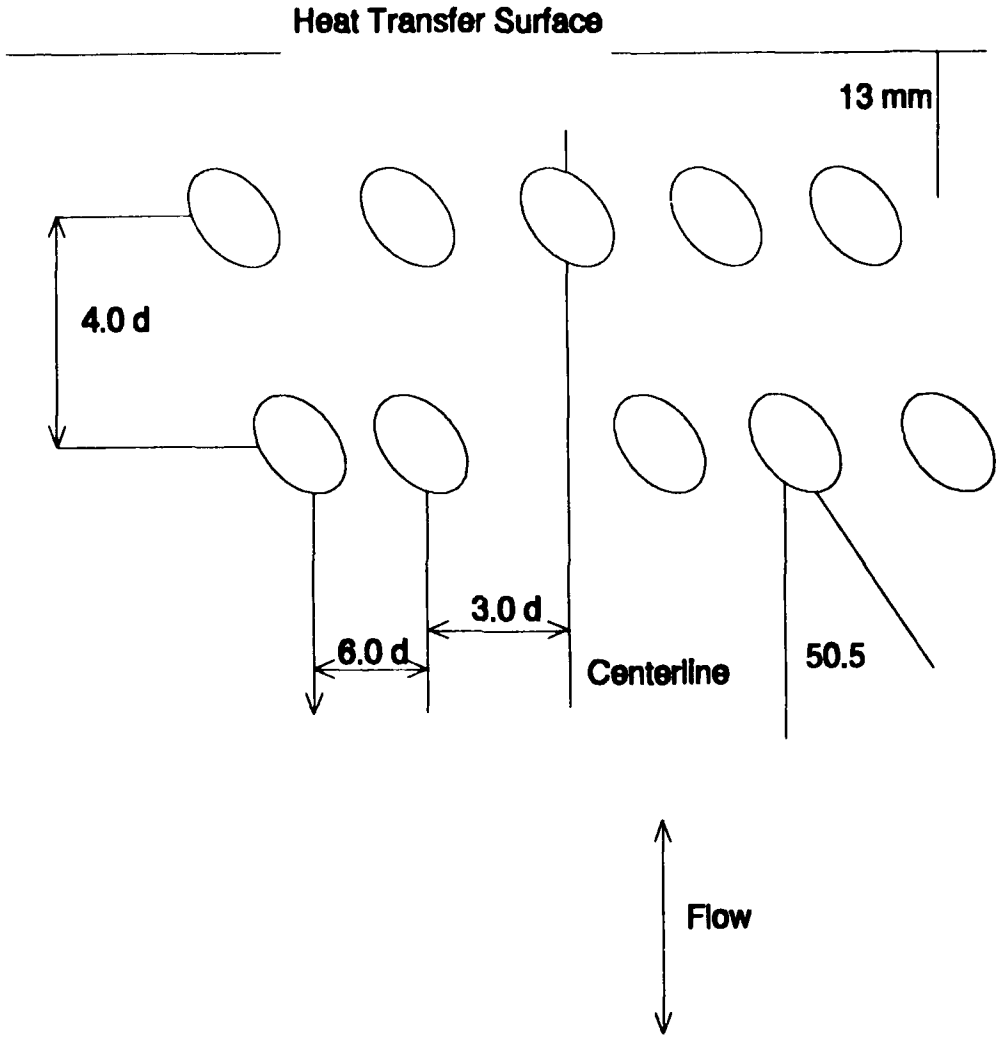


Figure 6. Injection Hold Configuration, Compound Angle

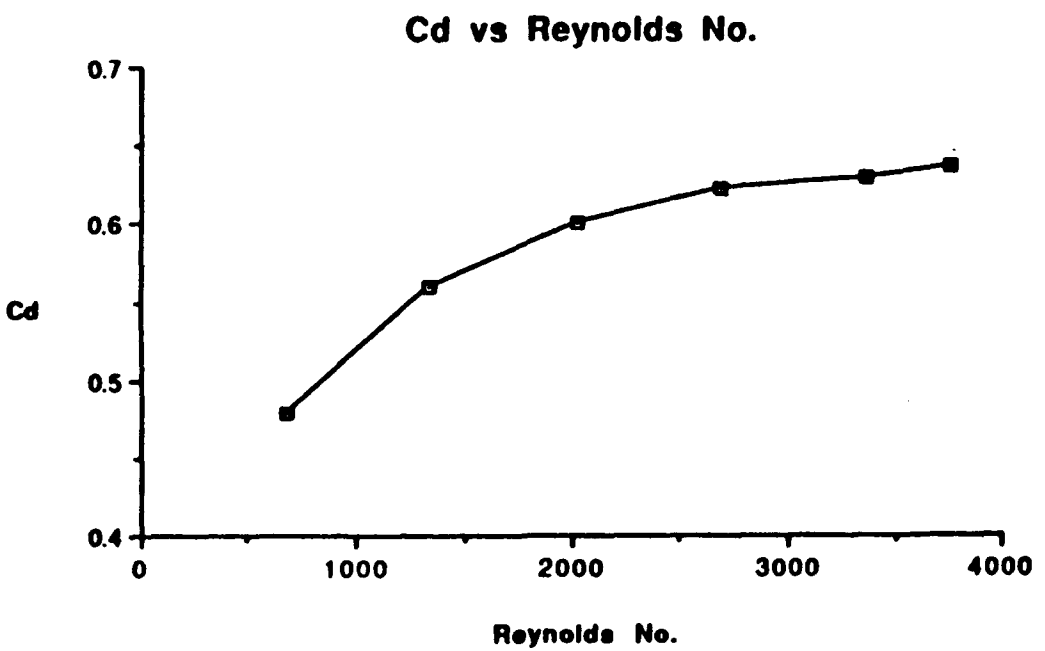


Figure 7. Coefficient of Discharge (C_d) Versus Reynolds Number (Re) for Injection System

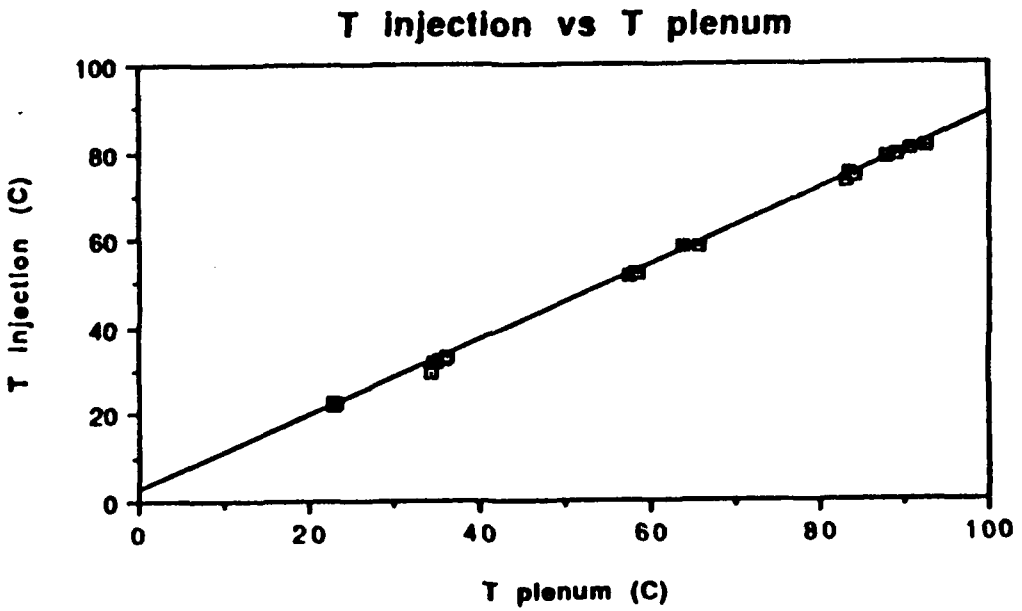


Figure 8. Injectant Temperature Versus Plenum Temperature, Bishop [Ref. 6]

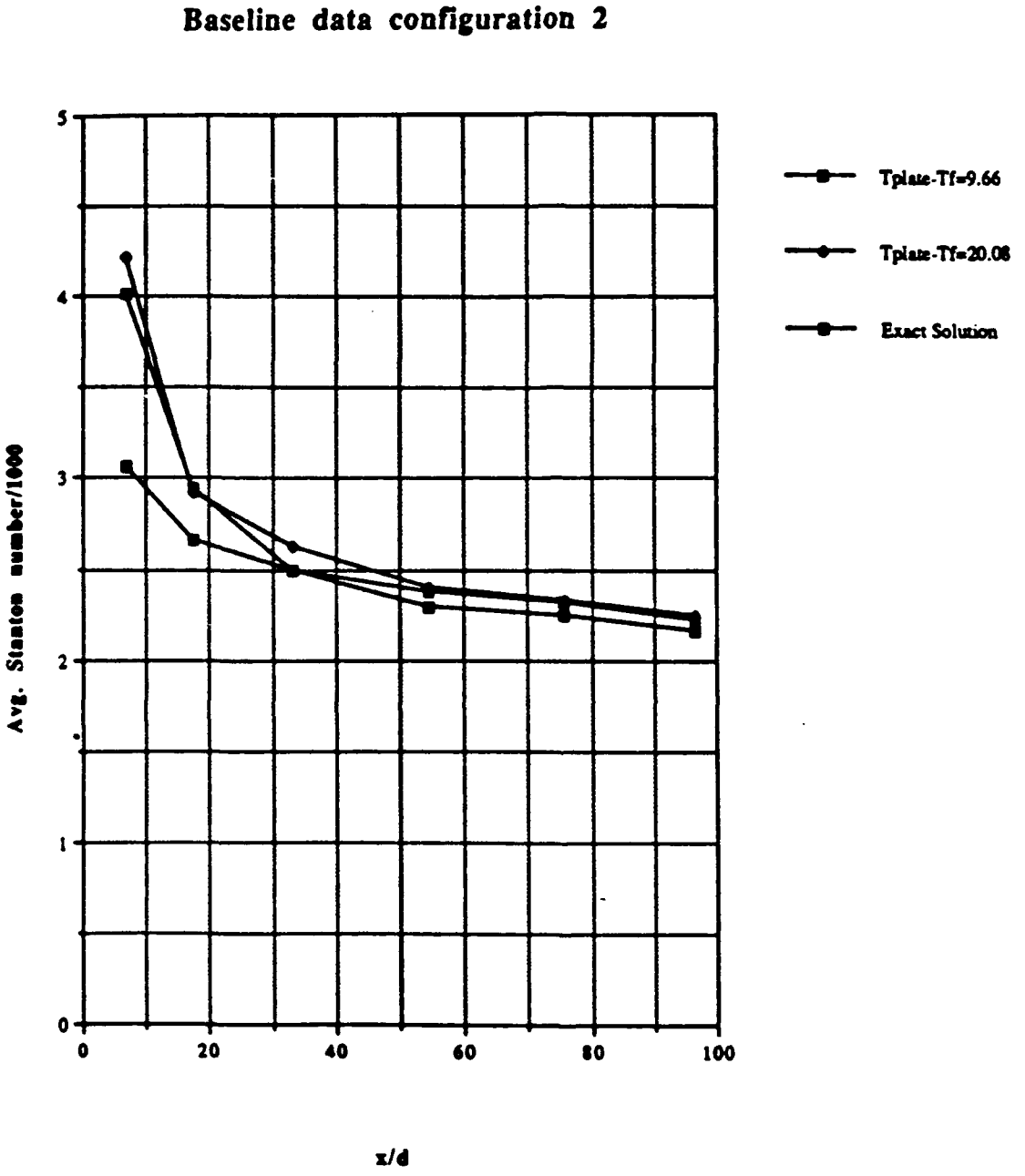


Figure 9. Baseline Stanton Number Comparison Between Exact Solution and Experimental Measurements, Configuration 2

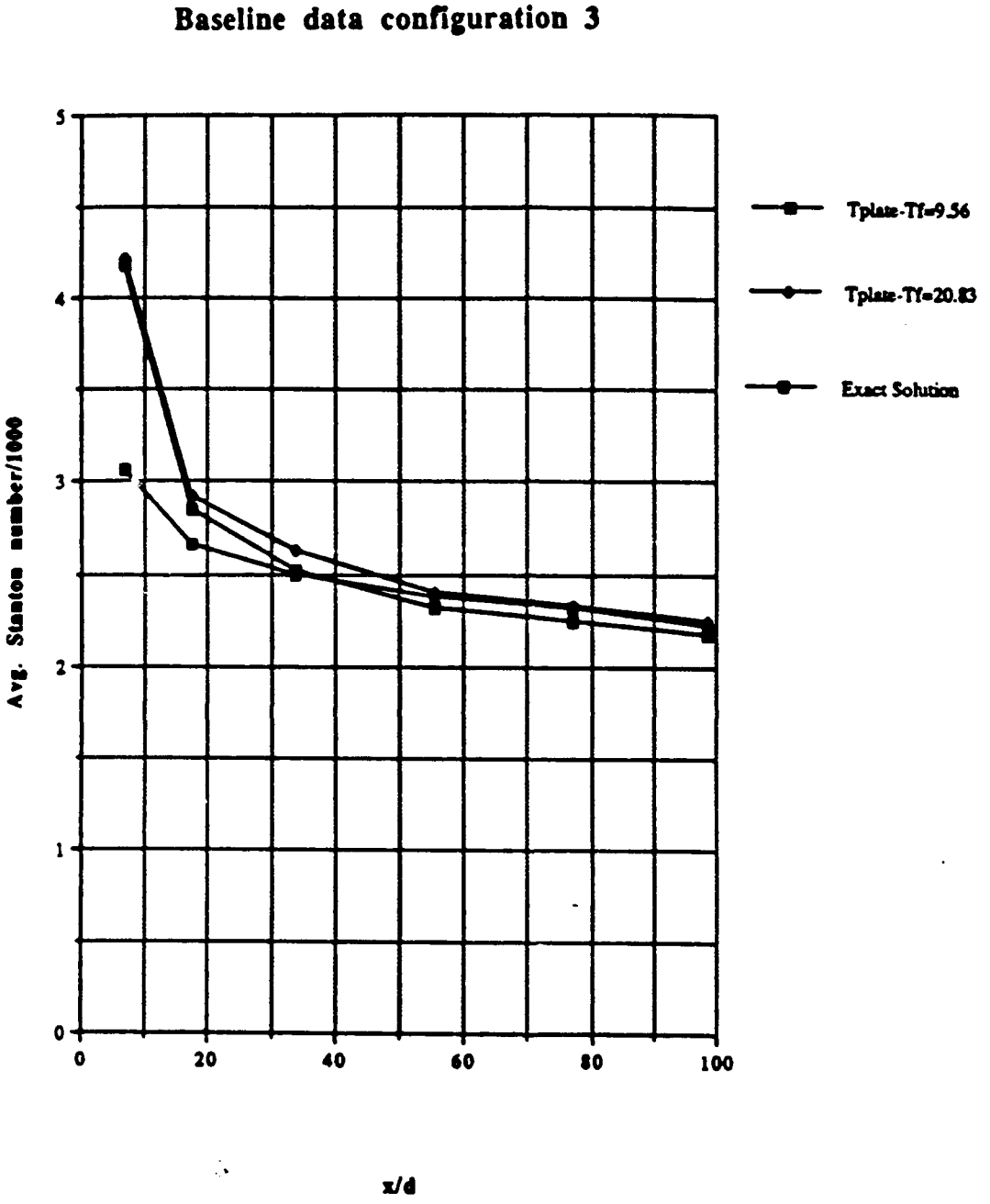


Figure 10. Baseline Stanton Number Comparison Between Exact Solution and Experimental Measurements, Configuration 3

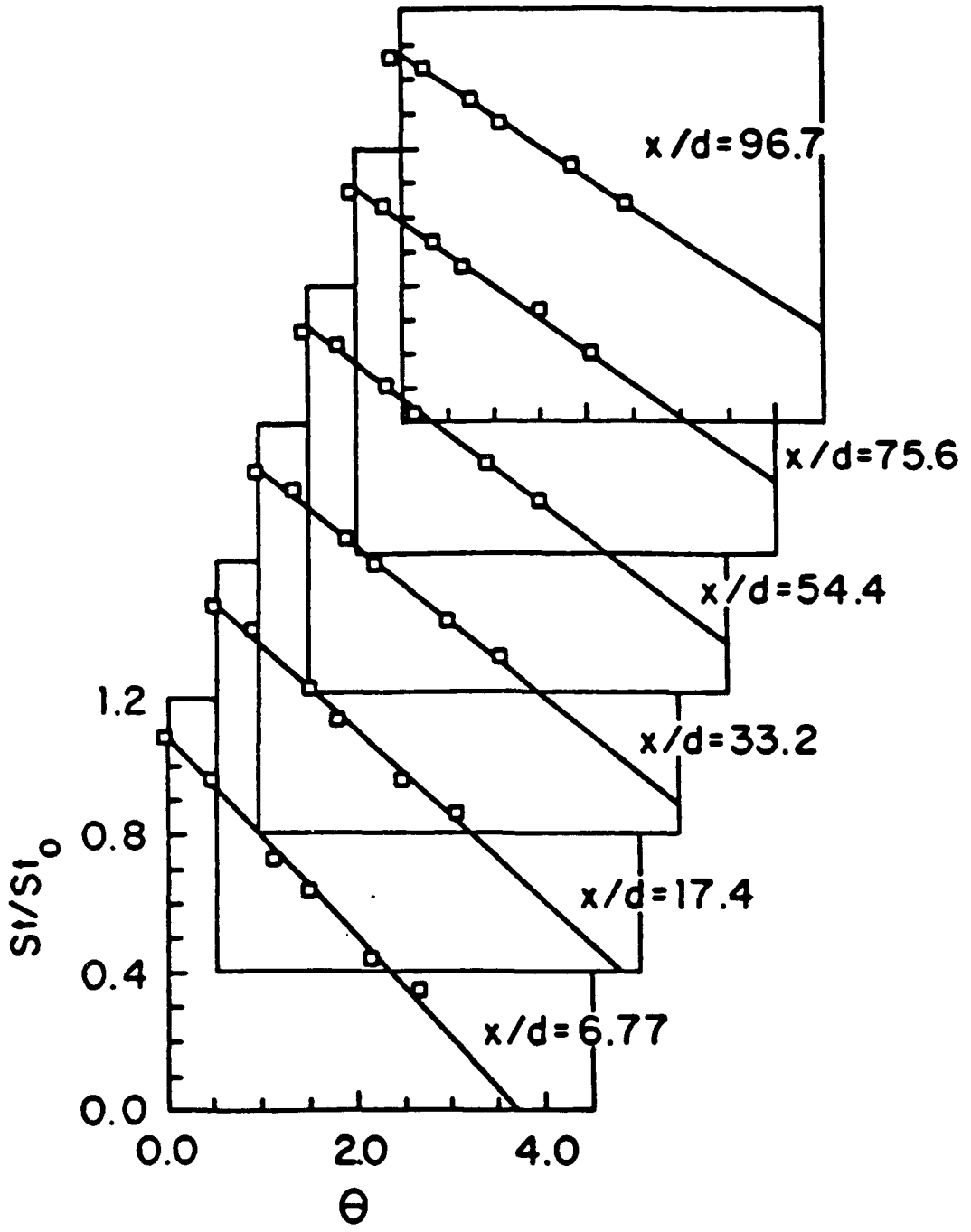


Figure 11. St/Sto Versus x/d for Various θ Values with m=0.5, [Ref. Ligrani, Bishop, Ciriello]

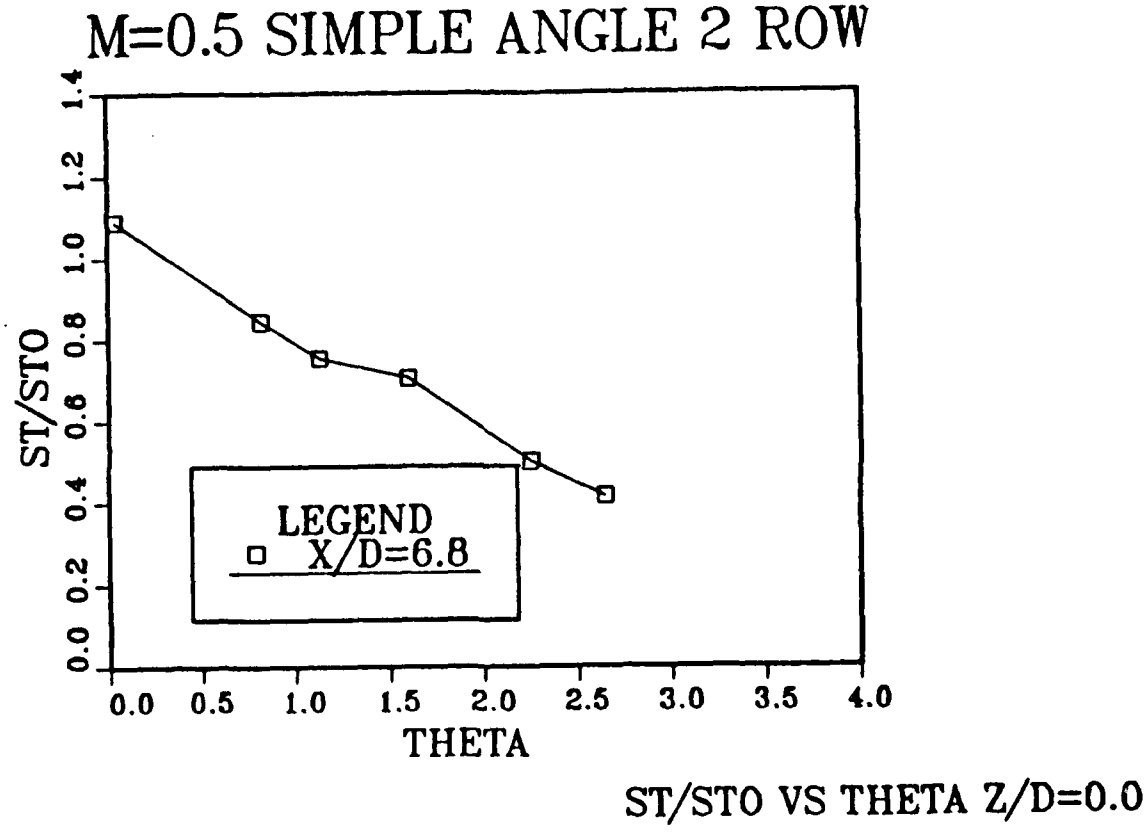


Figure 12. St/Sto Versus θ, Simple Angle, 2 Rows, m=0.5, x/d=17.4, z/d=0.0

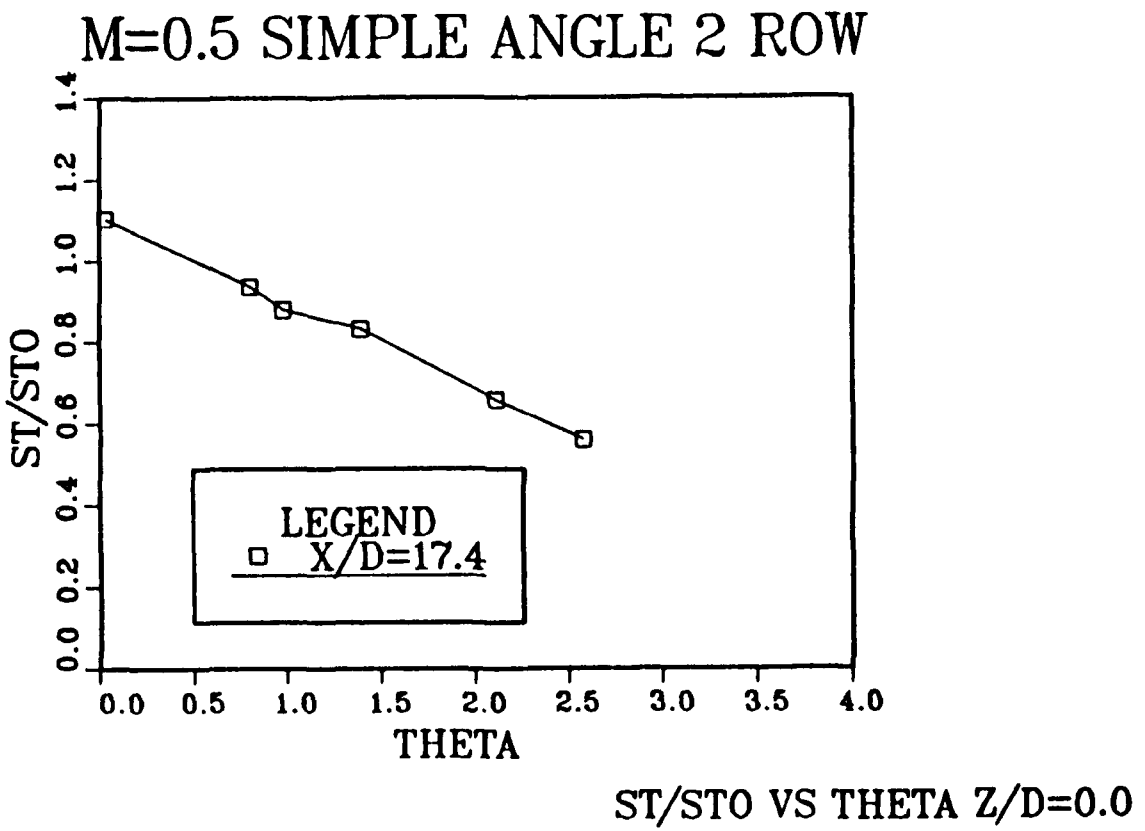


Figure 13. St/Sto Versus θ Simple Angle, 2 Rows, m=0.5, x/d=17.4, z/d=0.0

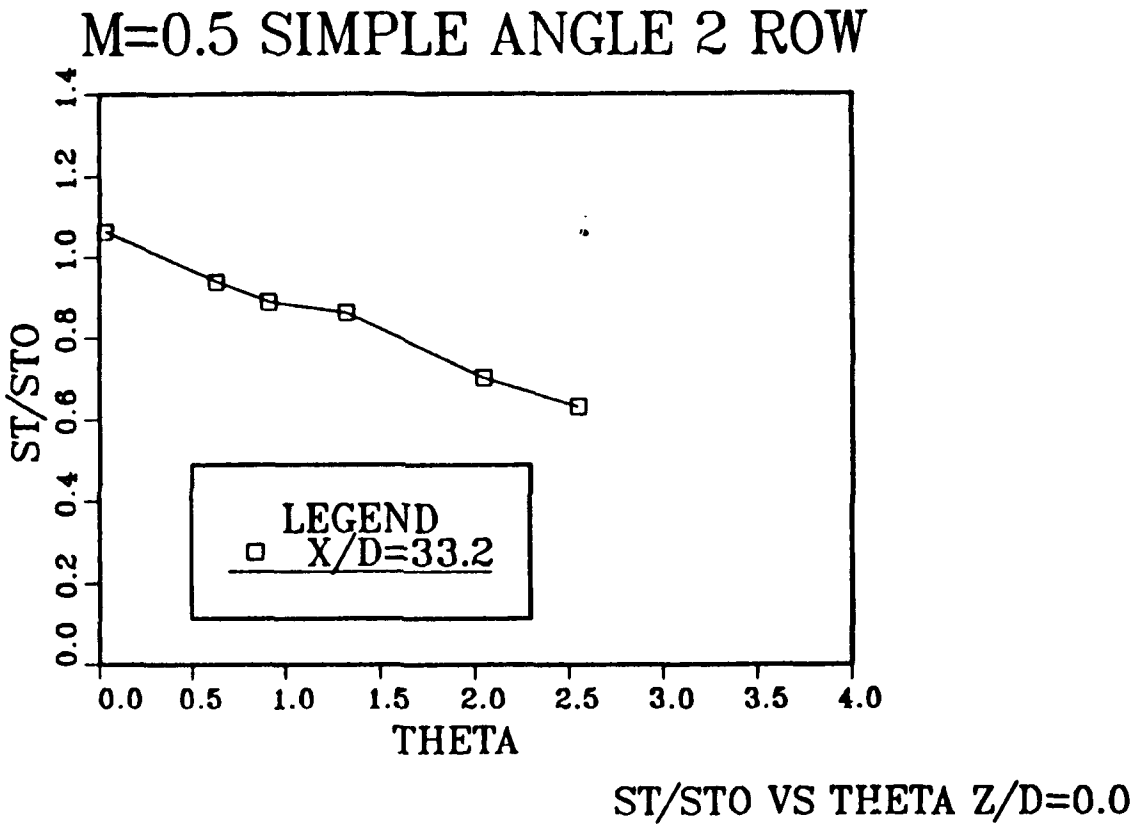


Figure 14. St/Sto Versus θ, Simple Angle, 2 Rows, m=0.5, x/d=33.2, z/d=0.0

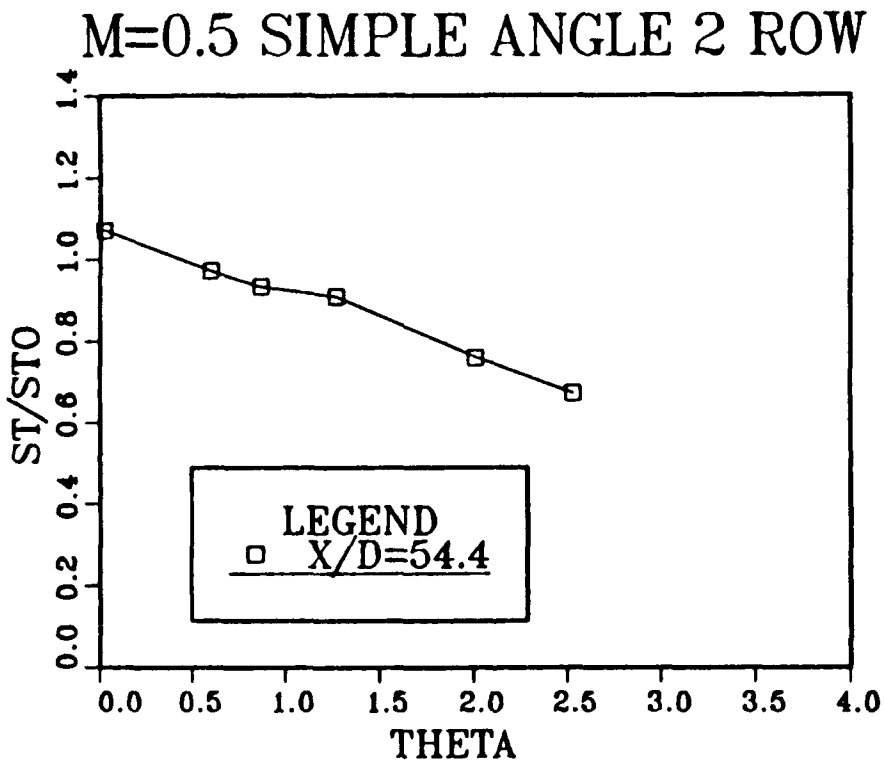


Figure 15. St/Sto Versus θ, Simple Angle, 2 Rows, m=0.5, x/d=54.4, z/d=0.0

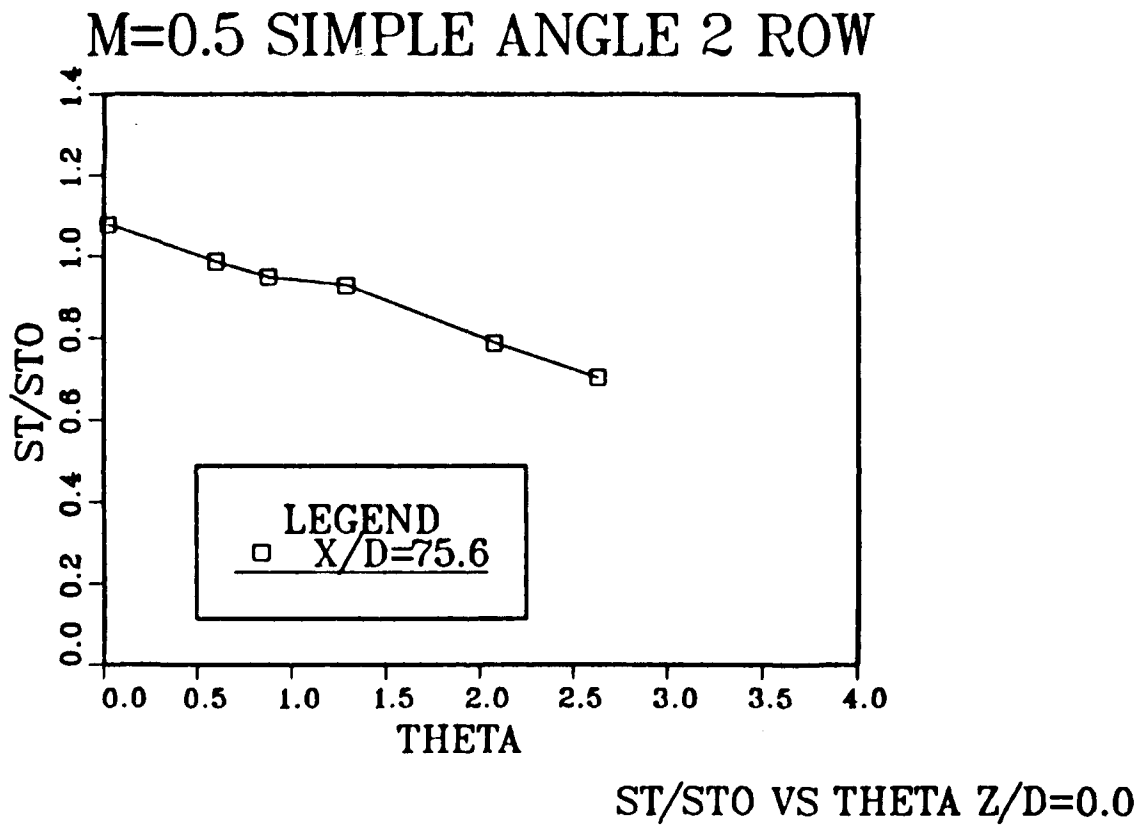


Figure 16. St/Sto, Versus θ, Simple Angle, 2 Rows, m=0.5, x/d=75.6, z/d=0.0

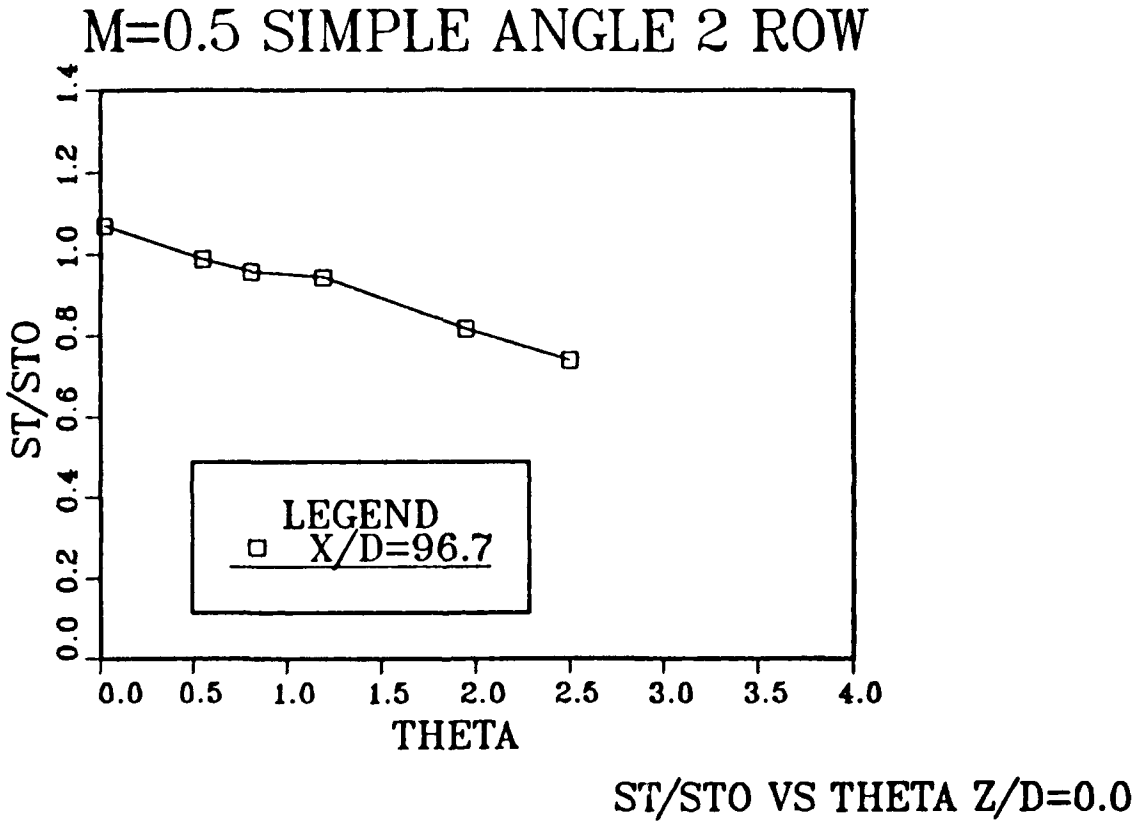


Figure 17. St/Sto Versus θ, Simple Angle, 2 Rows, m=0.5, x/d=96.7, z/d-0.0

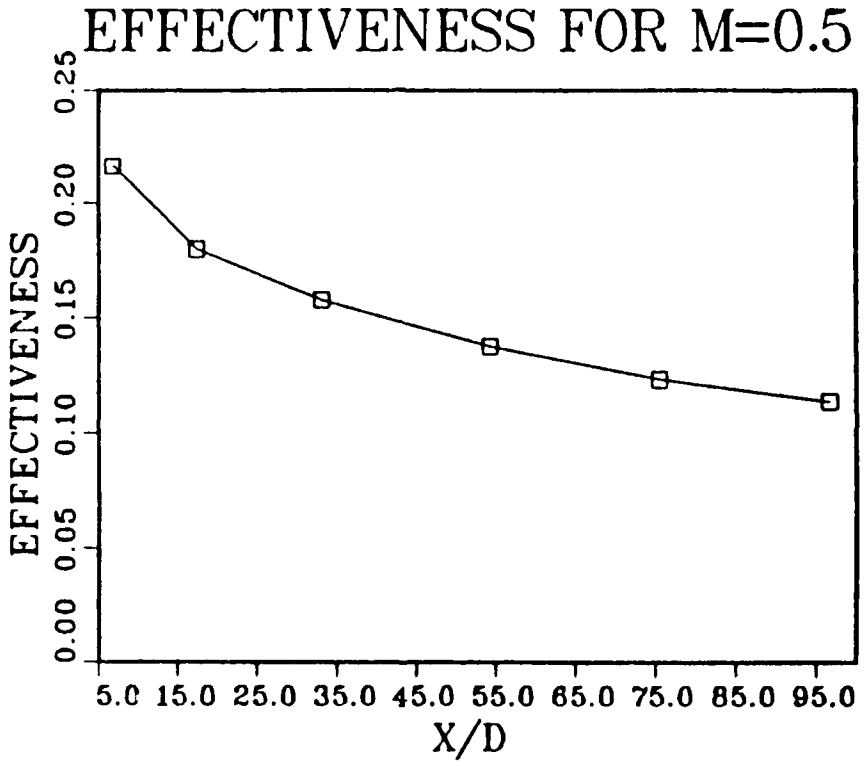


Figure 18. η **Versus x/d, Simple Angle, 2 Rows, m=0.5, Spanwise Average**

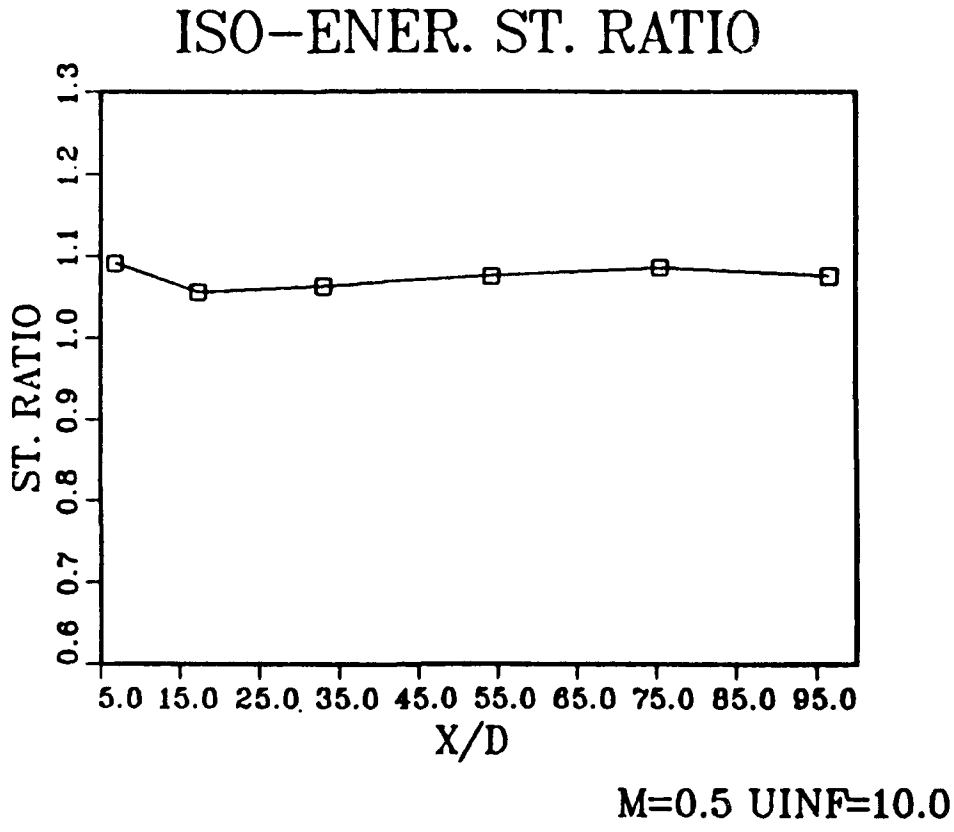


Figure 19. Stf/Sto Versus x/d, Simple Angle, 2 Rows, m=0.5, Spanwise Average

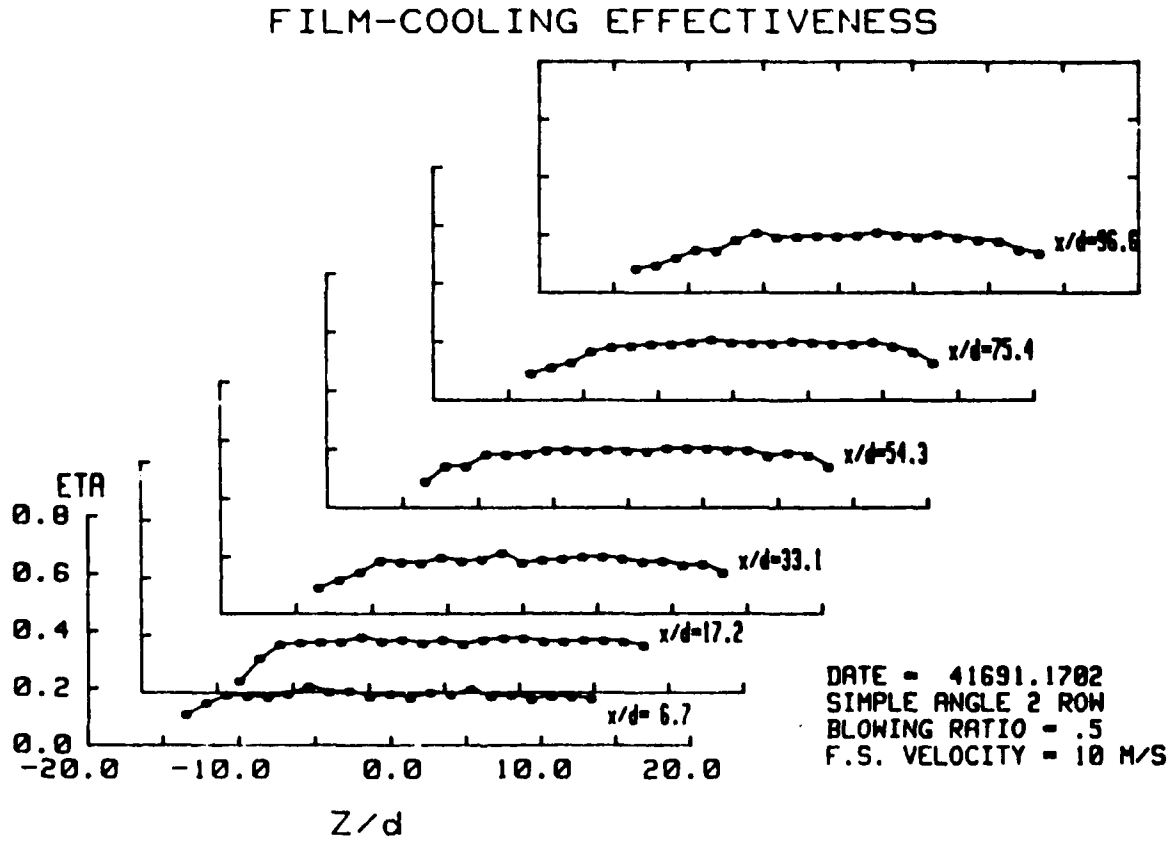


Figure 20. Spanwise Variation of η Simple Angle, 2 Rows, m=0.5

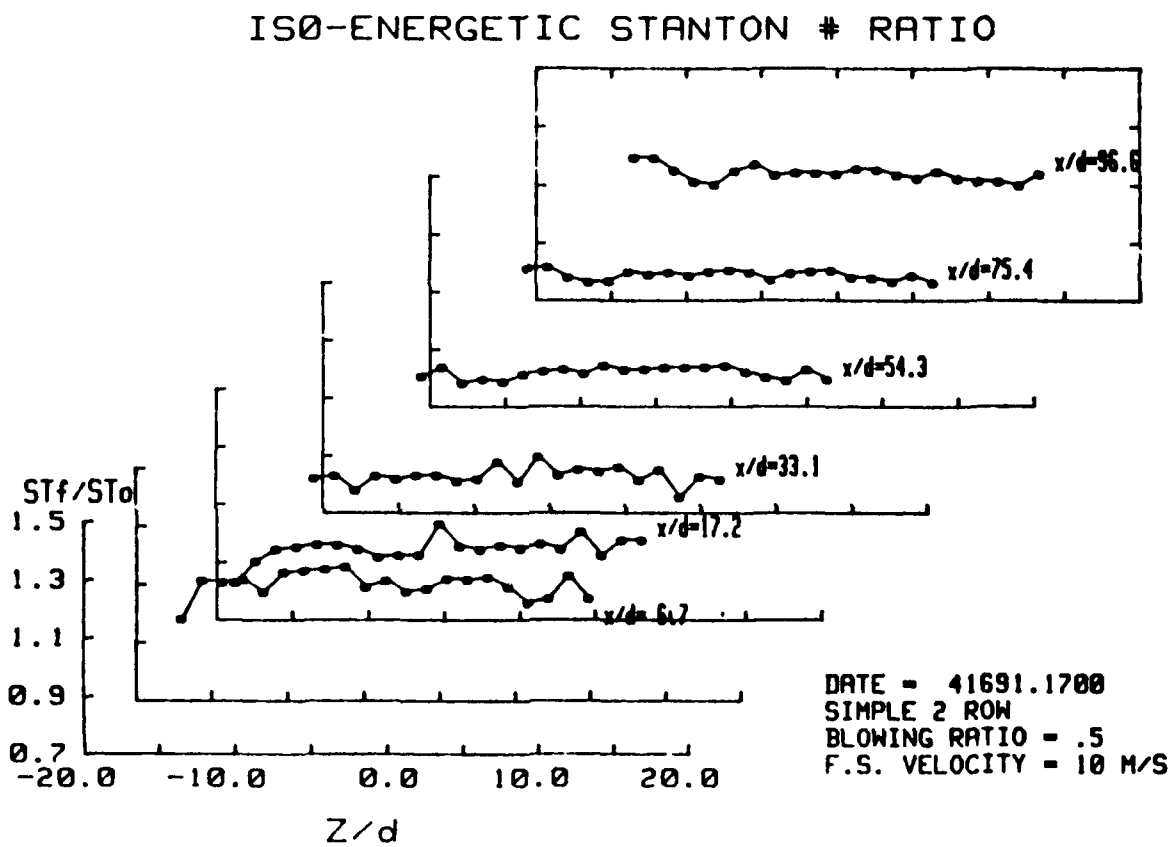


Figure 21. Spanwise Variation of Stf/Sto, Simple Angle, 2 Rows, m=0.5

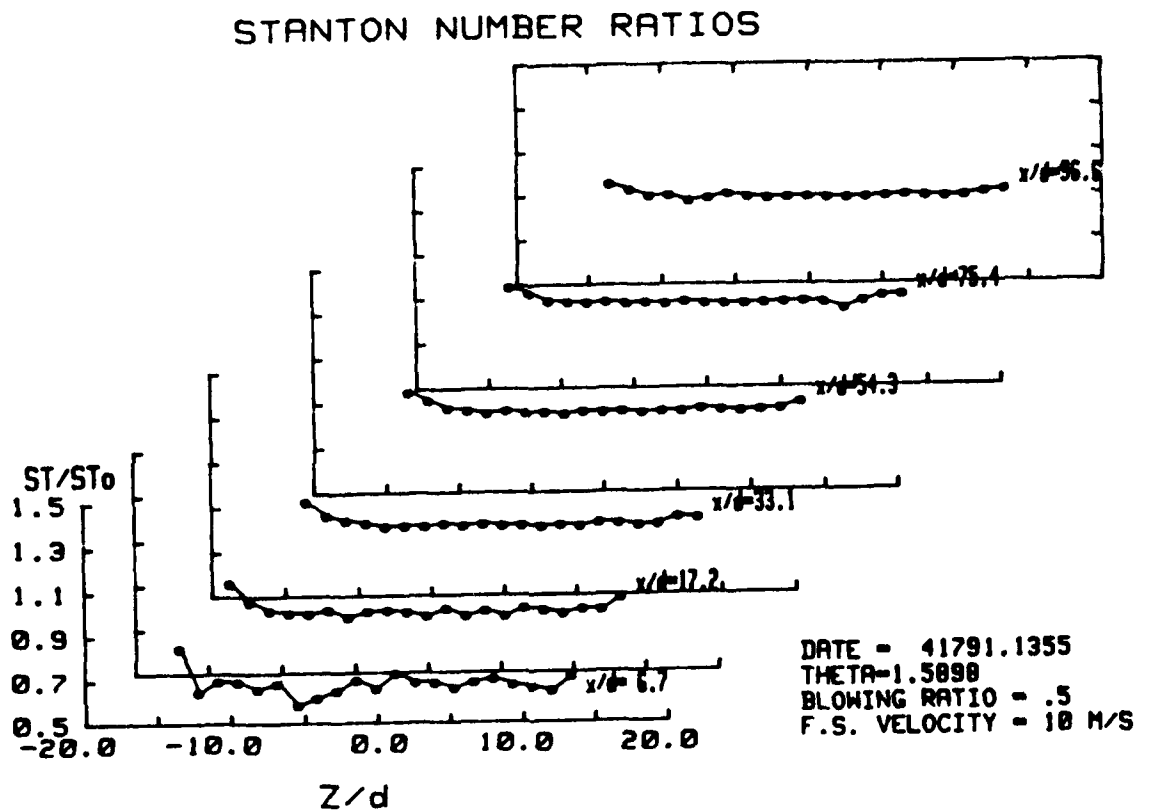


Figure 22. Spanwise Variation of St/Sto, Simple Angle, 2 Rows, m=0.5, θ=1.59

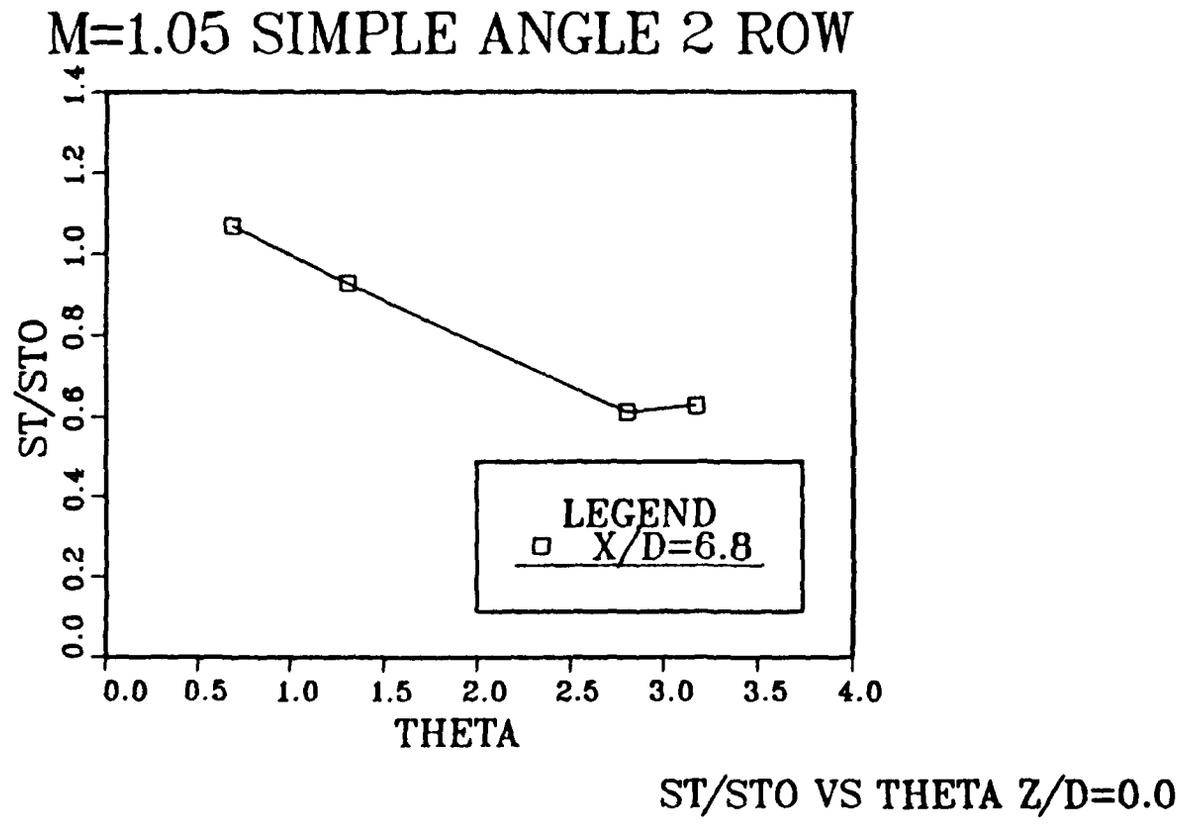


Figure 23. **St/Sto Versus θ, Simple Angle, 2 Rows, m=1.0, x/d=6.8, z/d=0.0**

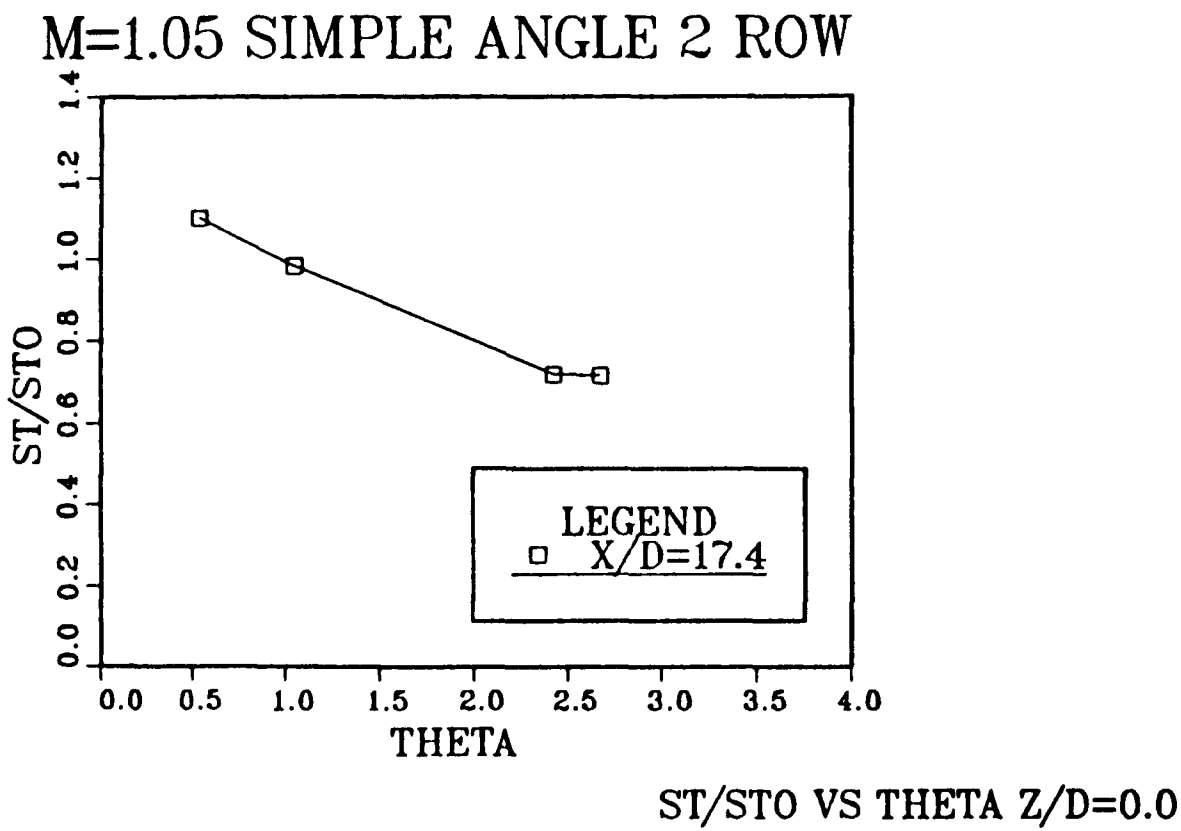


Figure 24. St/Sto Versus θ, Simple Angle, 2 Rows, m=1.0, x/d=17.4, z/d=0.0

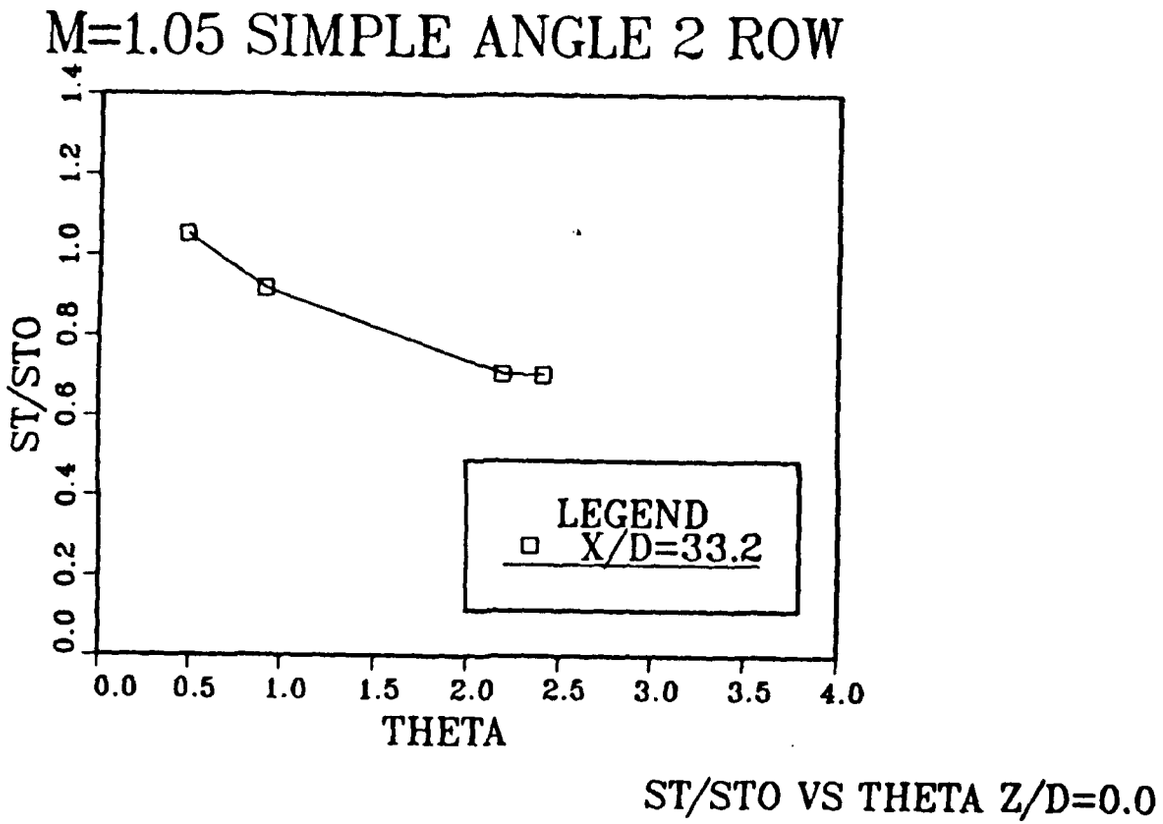


Figure 25. St/Sto Versus θ, Simple Angle, 2 Rows, m=1.0, x/d=33.2, z/d=0.0

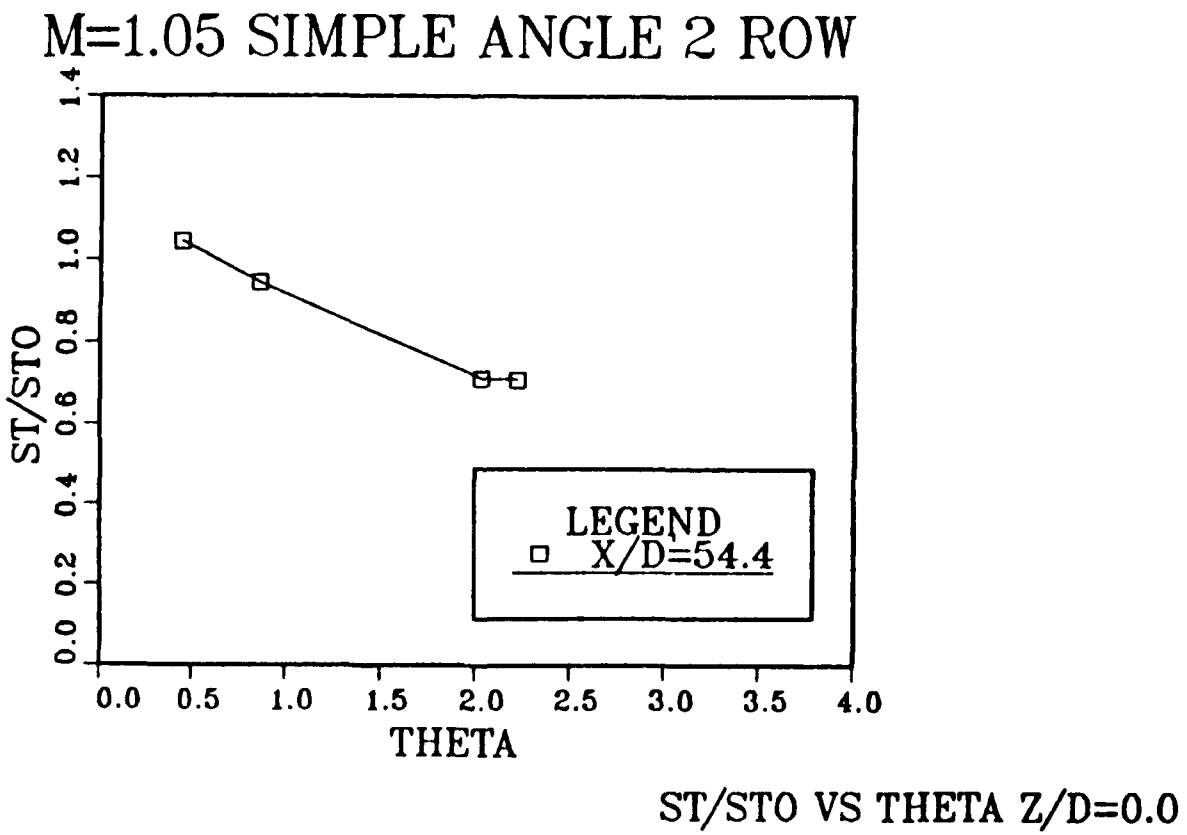


Figure 26. St/Sto Versus θ, Simple Angle, 2 Rows, m=1.0, x/d=54.4, z/d=0.0

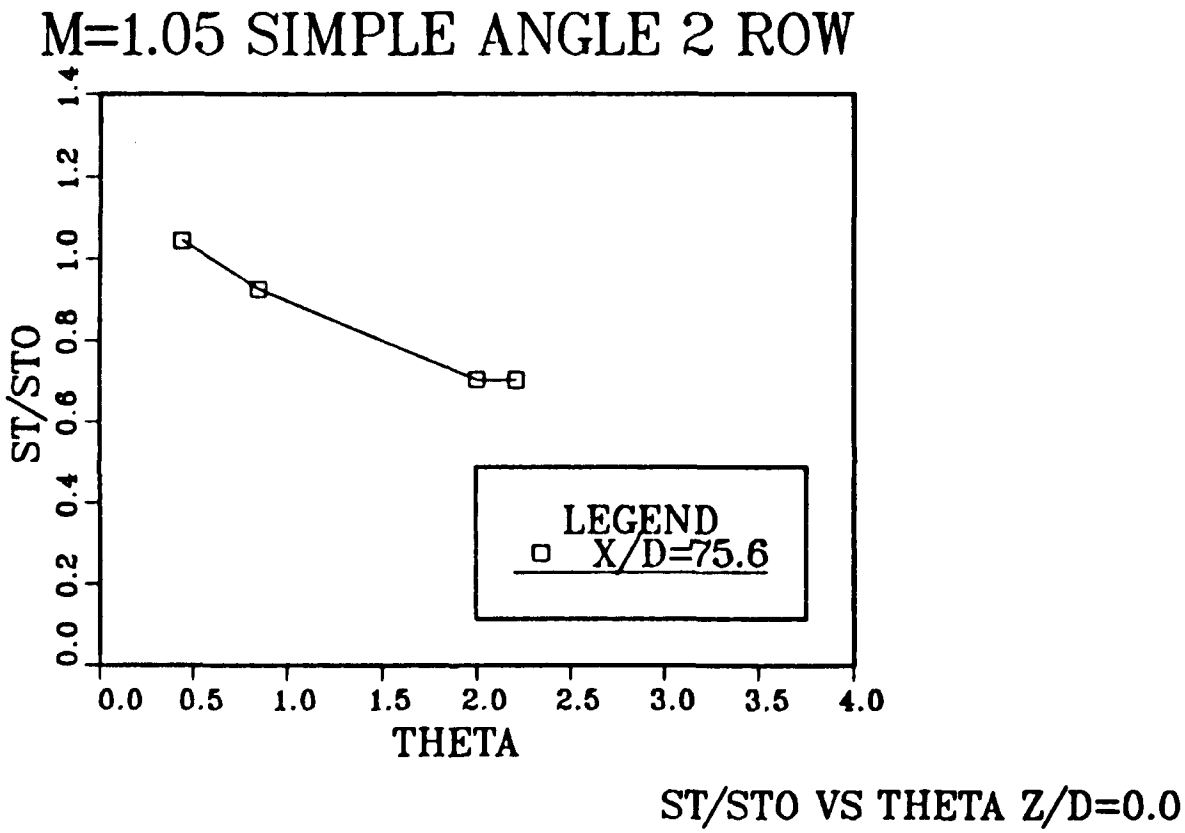


Figure 27. St/Sto Versus θ, Simple Angle, 2 Rows, m=1.0, x/d=75.6, z/d=0.0

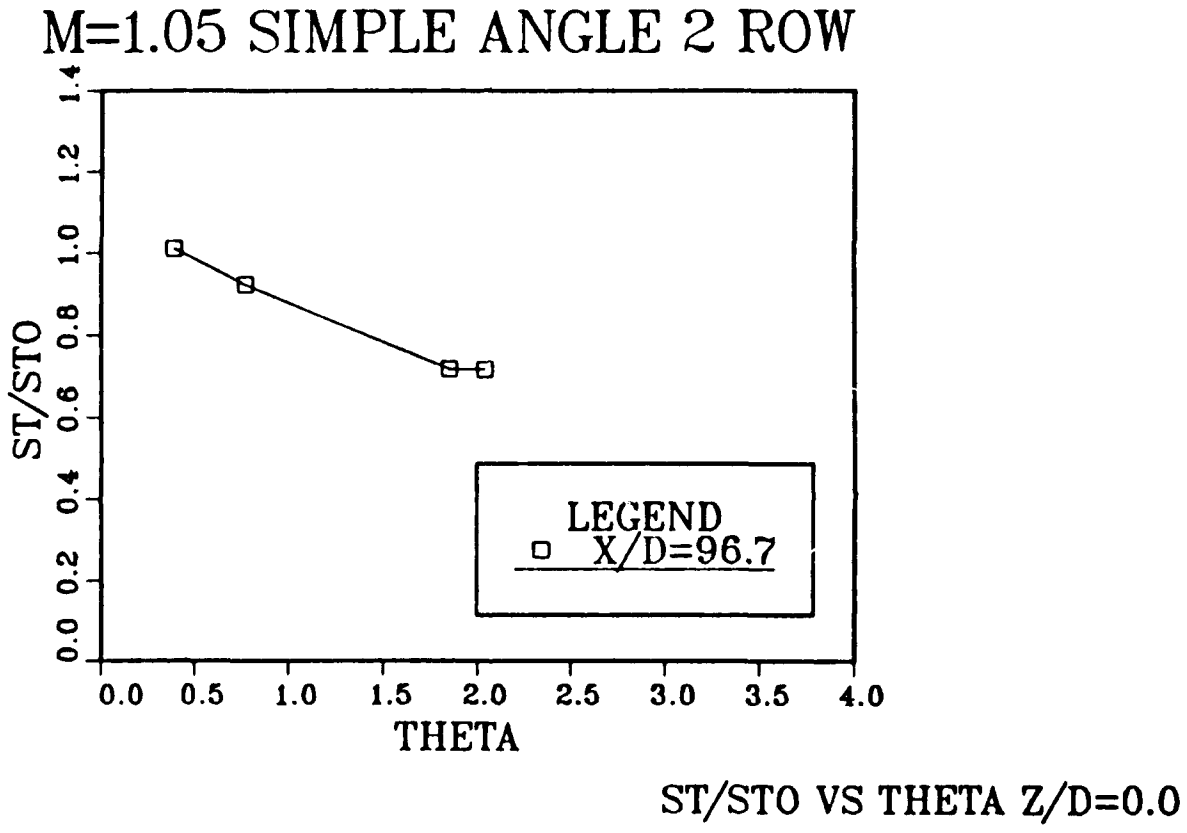


Figure 28. St/Sto Versus θ, Simple Angle, 2 Rows, m=1.0, x/d=96.7, z/d=0.0

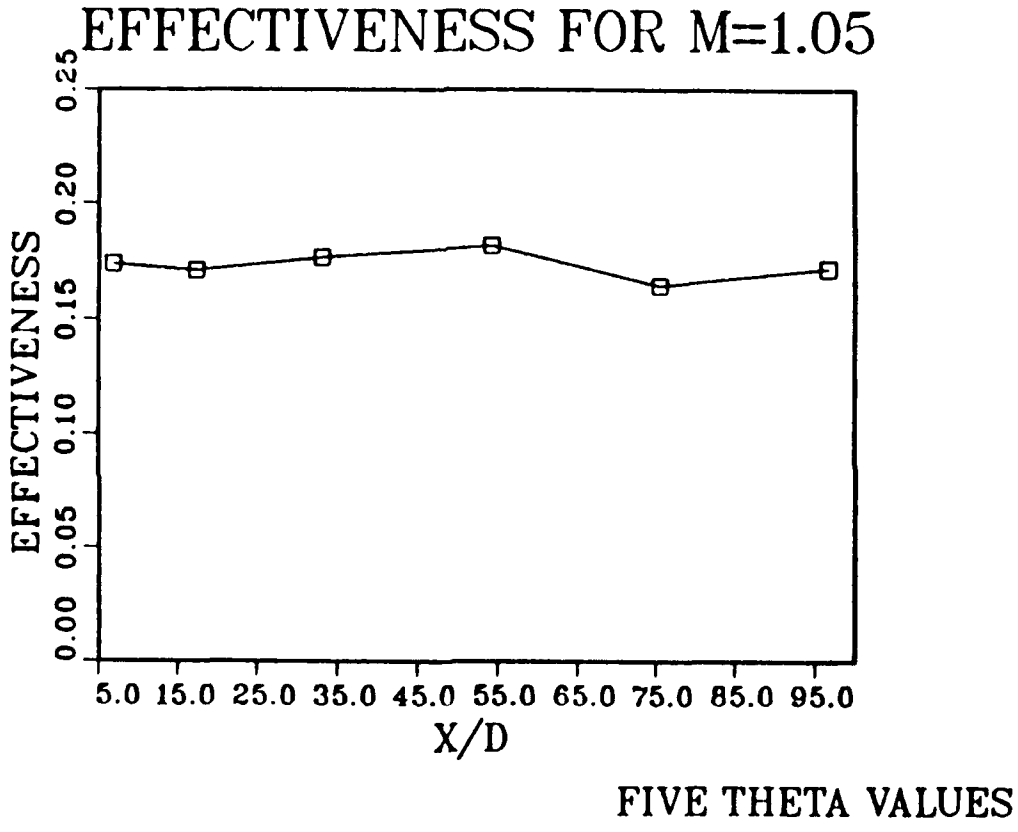


Figure 29. η **Versus x/d, Simple Angle, 2 Rows, m=1.0, Spanwise Average**

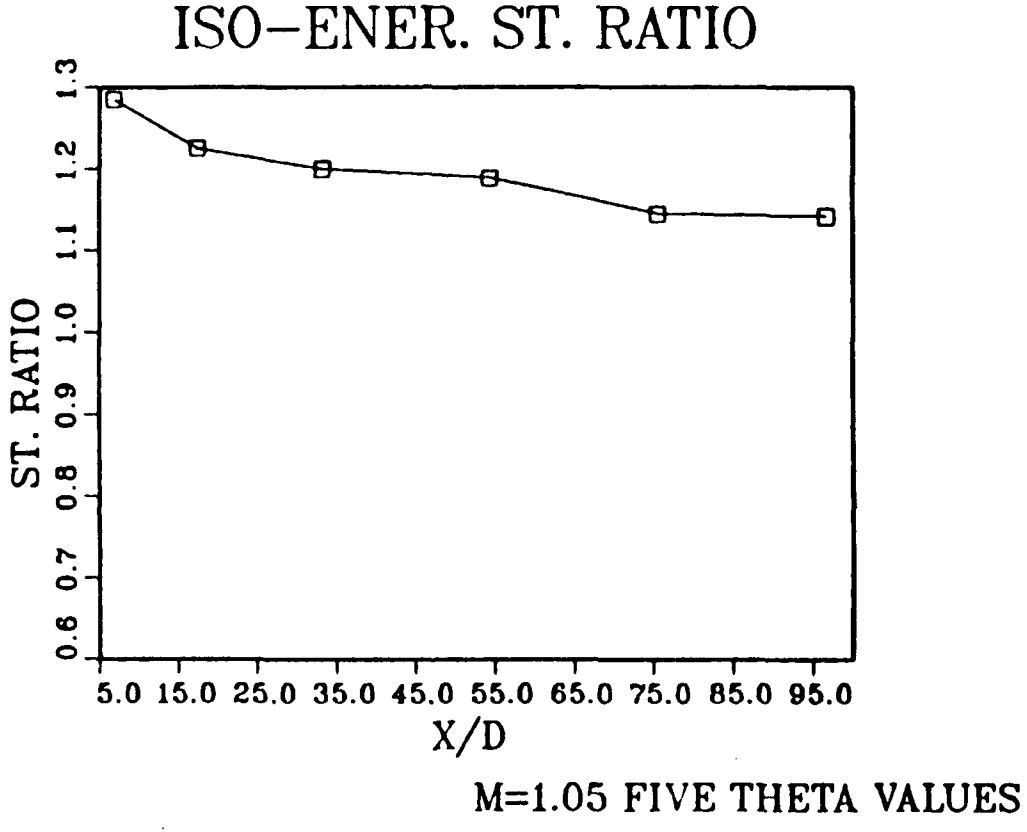


Figure 30. Stf/Sto Versus x/d, Simple Angle, 2 Rows, m=1.0, Spanwise Average

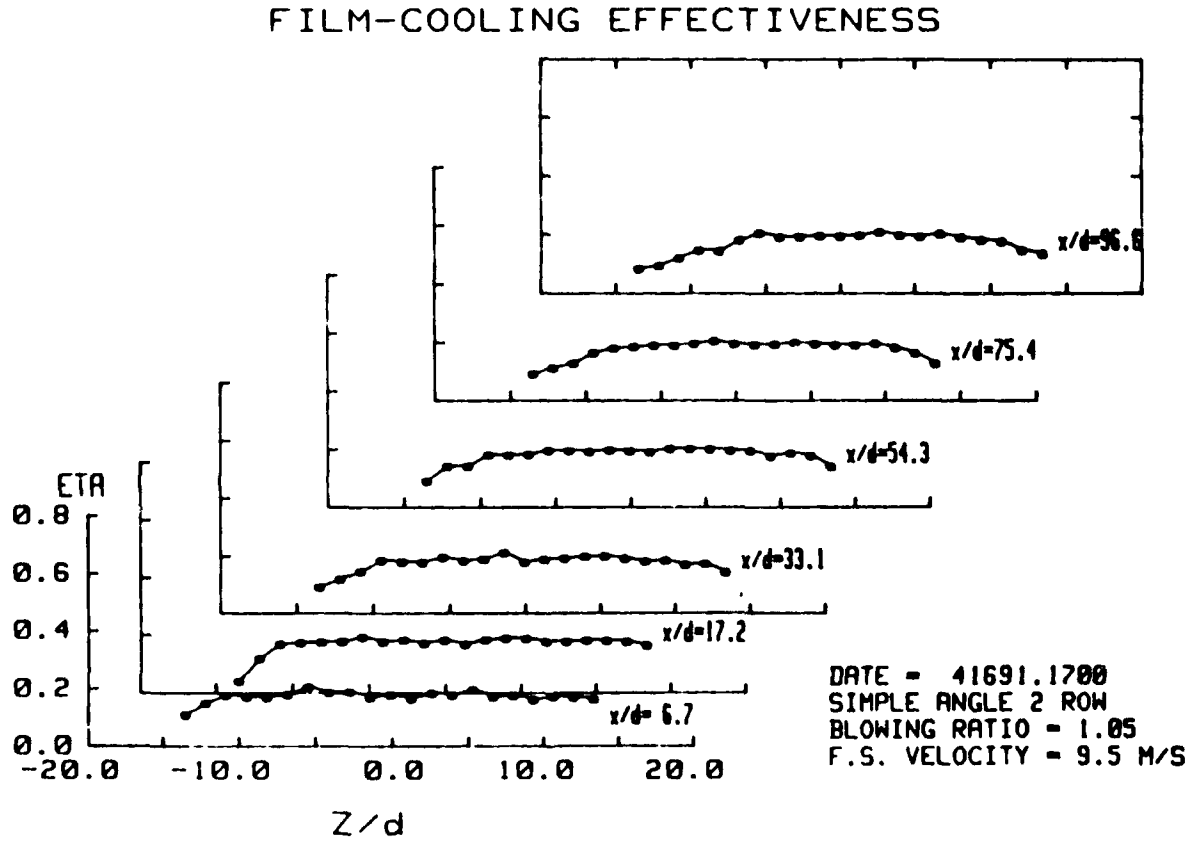


Figure 31. Spanwise Variation of η, Simple Angle, 2 Rows, m=1.0

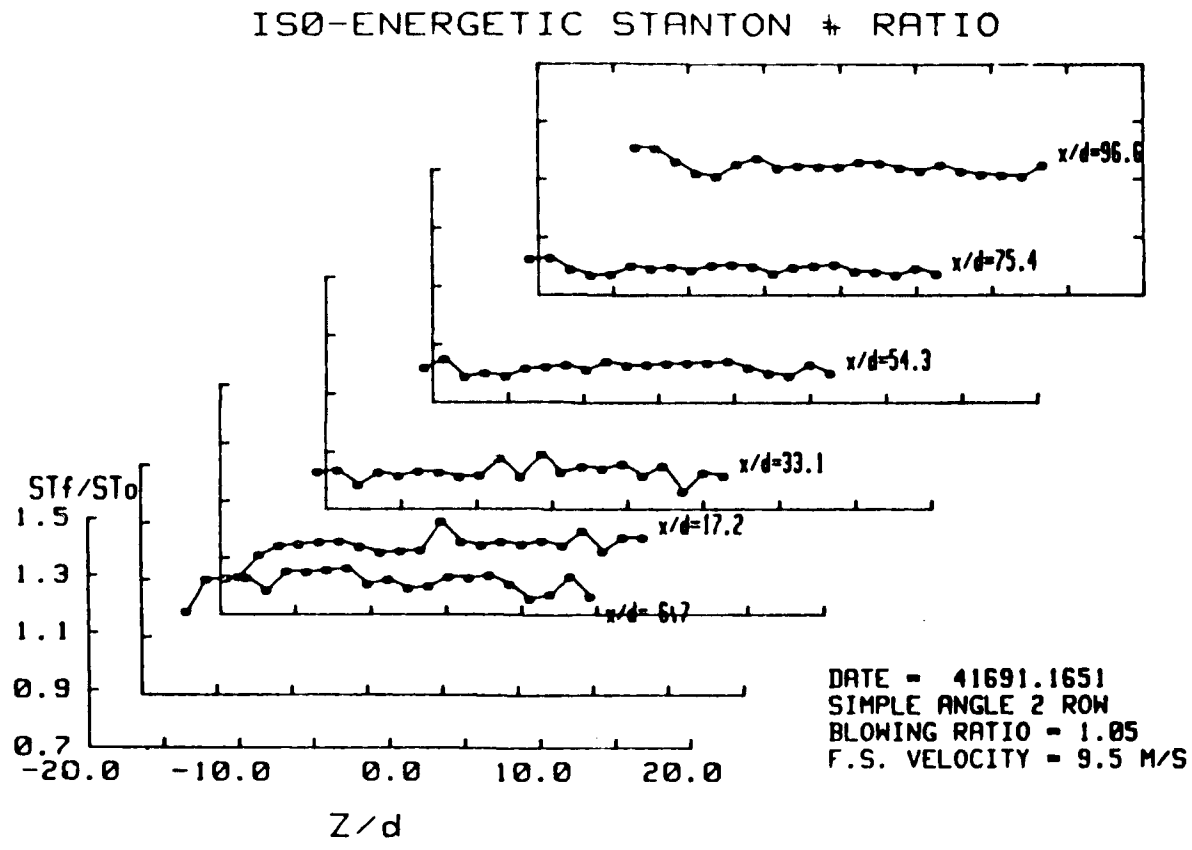


Figure 32. Spanwise Variation of Stf/Sto, Simple Angle, 2 Rows, m=1.0

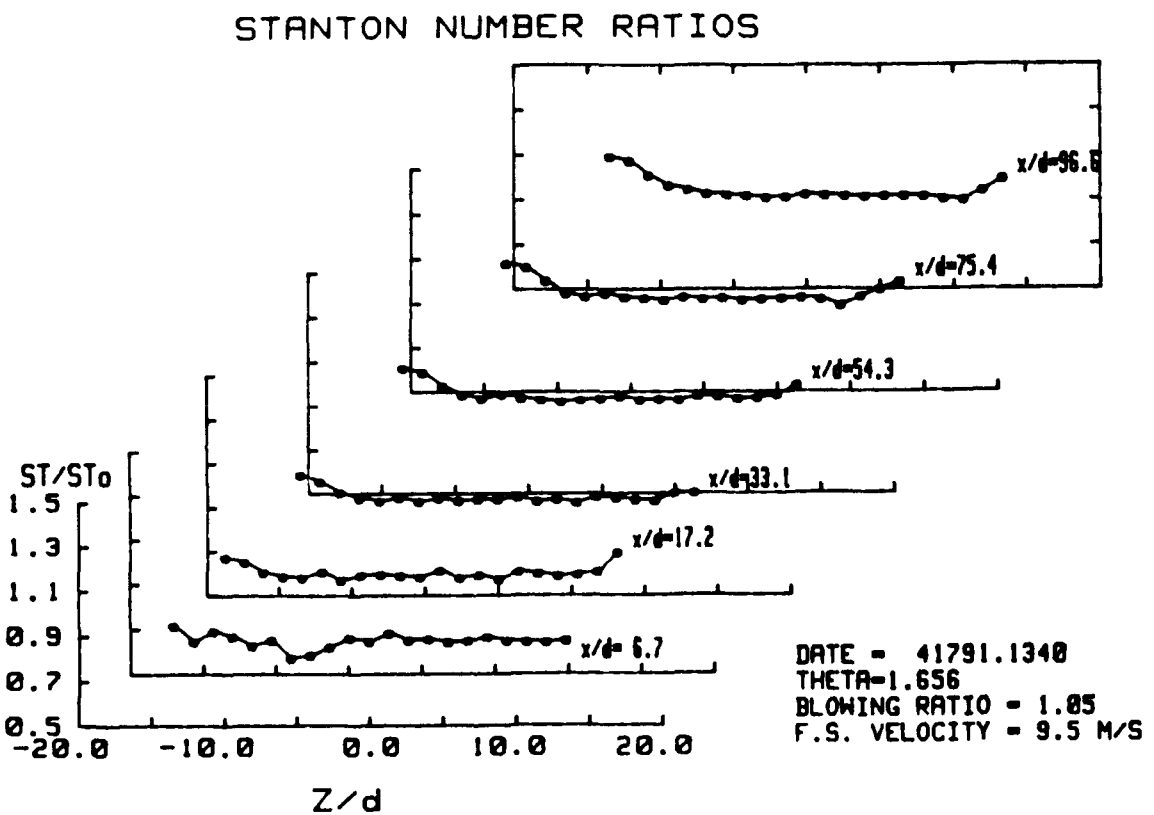


Figure 33. Spanwise Variation of St/Sto, Simple Angle, 2 Rows, m=1.0, θ=1.66

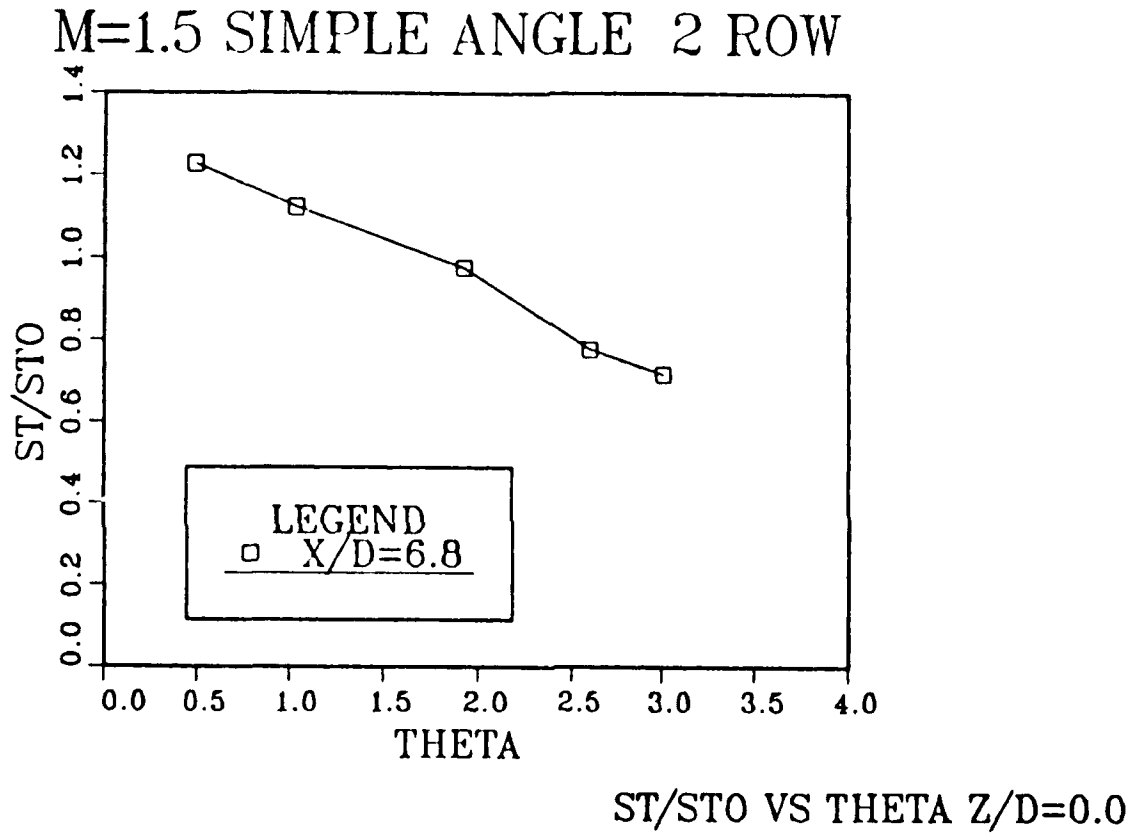


Figure 34. St/Sto Versus θ, Simple Angle, 2 Rows, m=1.5, x/d=6.8, z/d=0.0

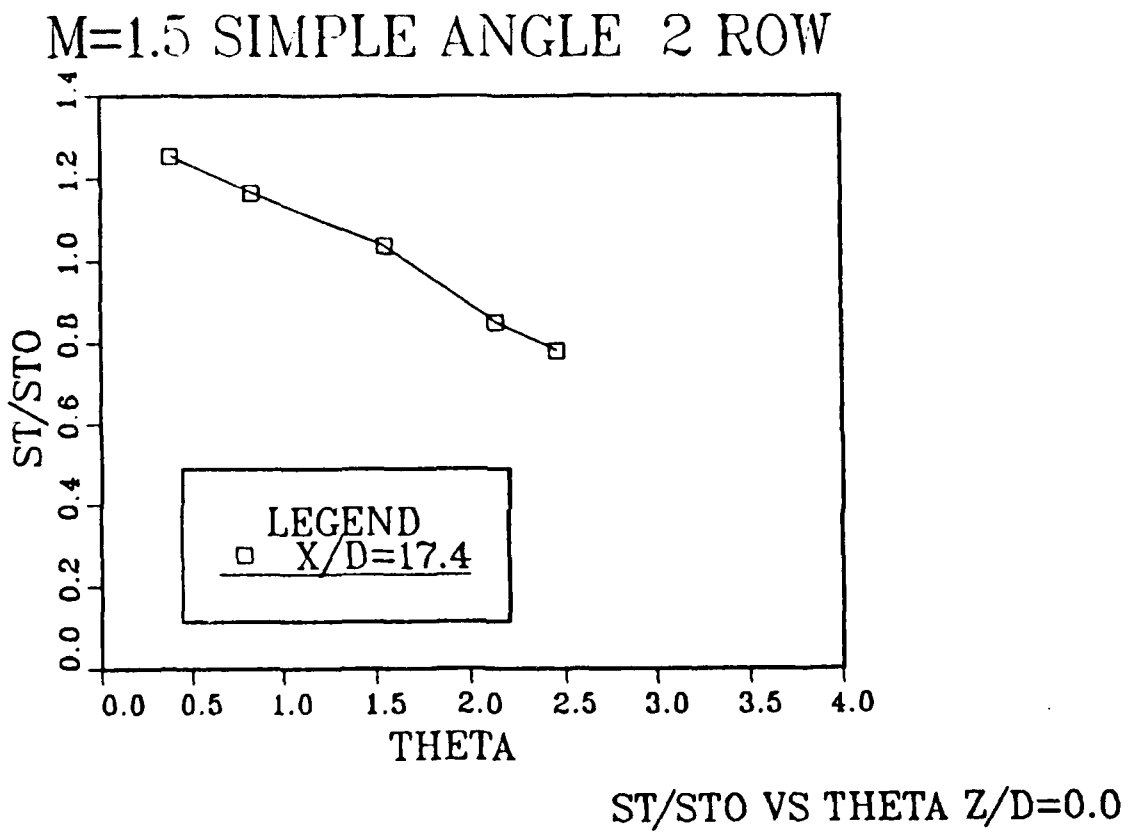


Figure 35. St/Sto Versus θ, Simple Angle, 2 Rows, m=1.5, x/d=17.4, z/d=0.00

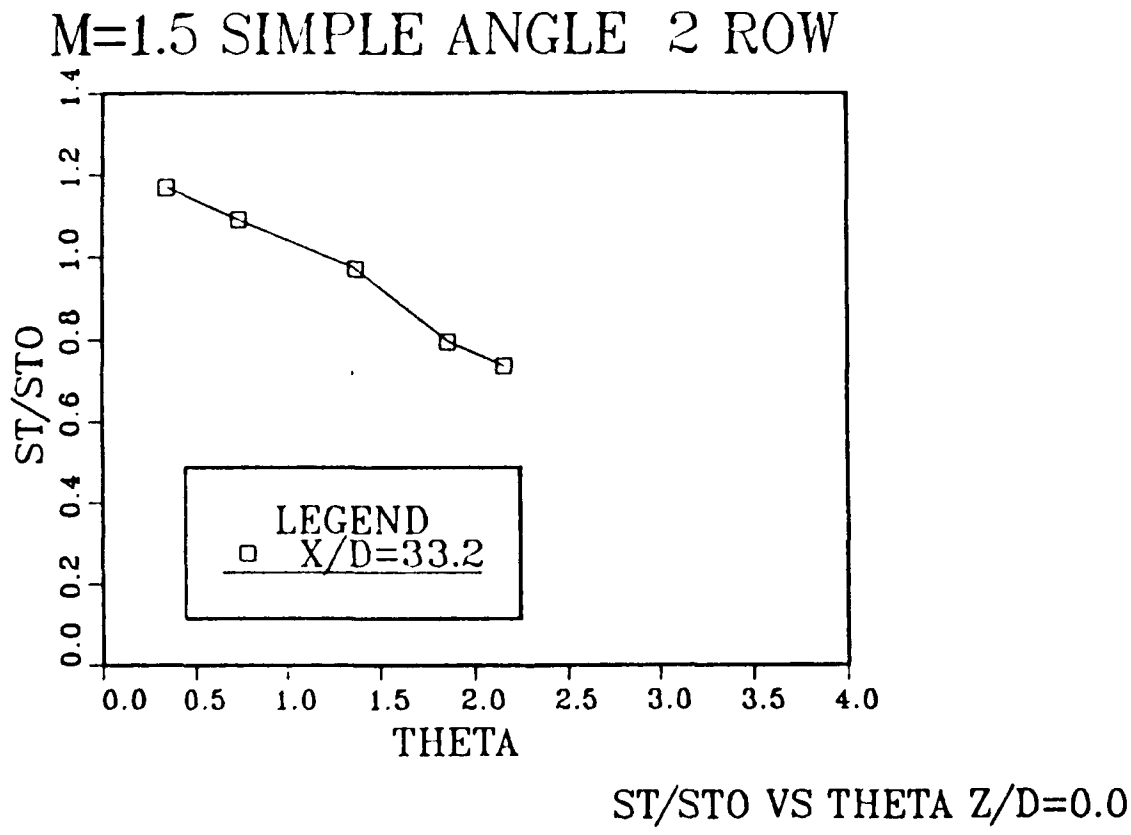


Figure 36. St/Sto Versus θ, Simple Angle, 2 Rows, m=1.5, x/d=33.2, z/d=0.0

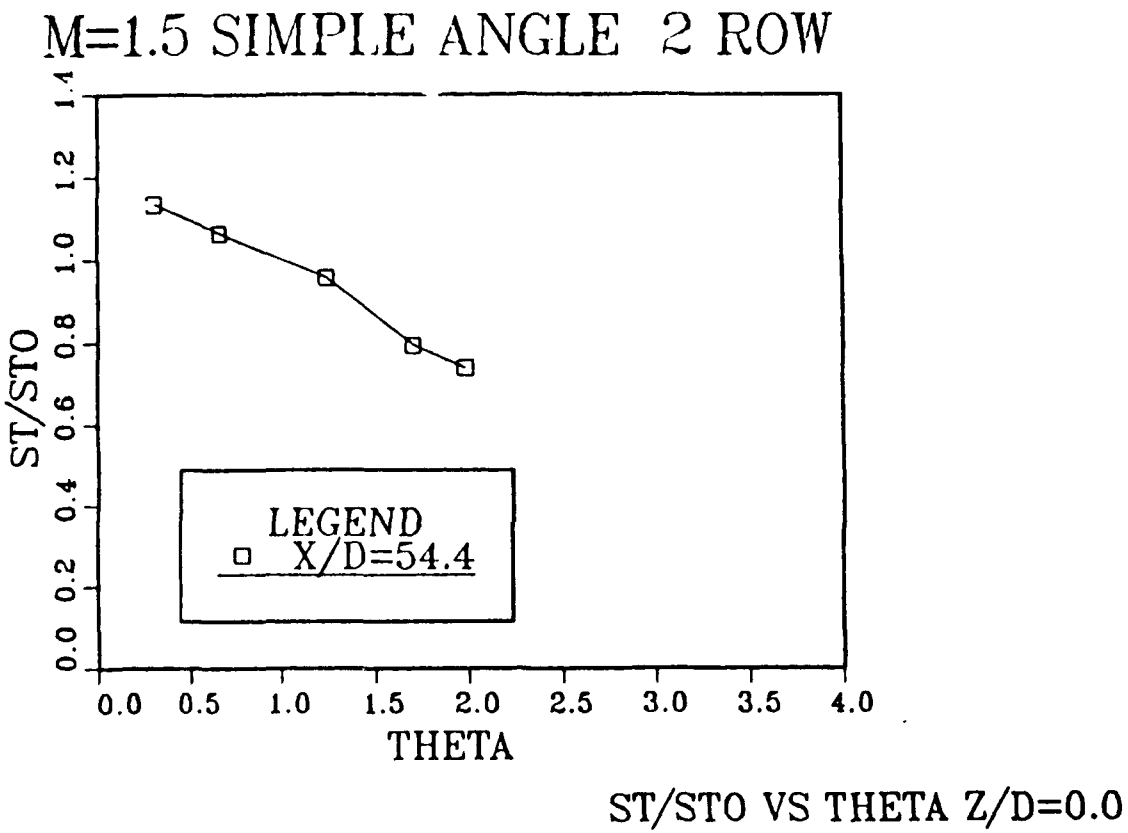


Figure 37. St/Sto Versus θ, Simple Angle, 2 Rows, m=1.5, x/d=54.4, z/d=0.0

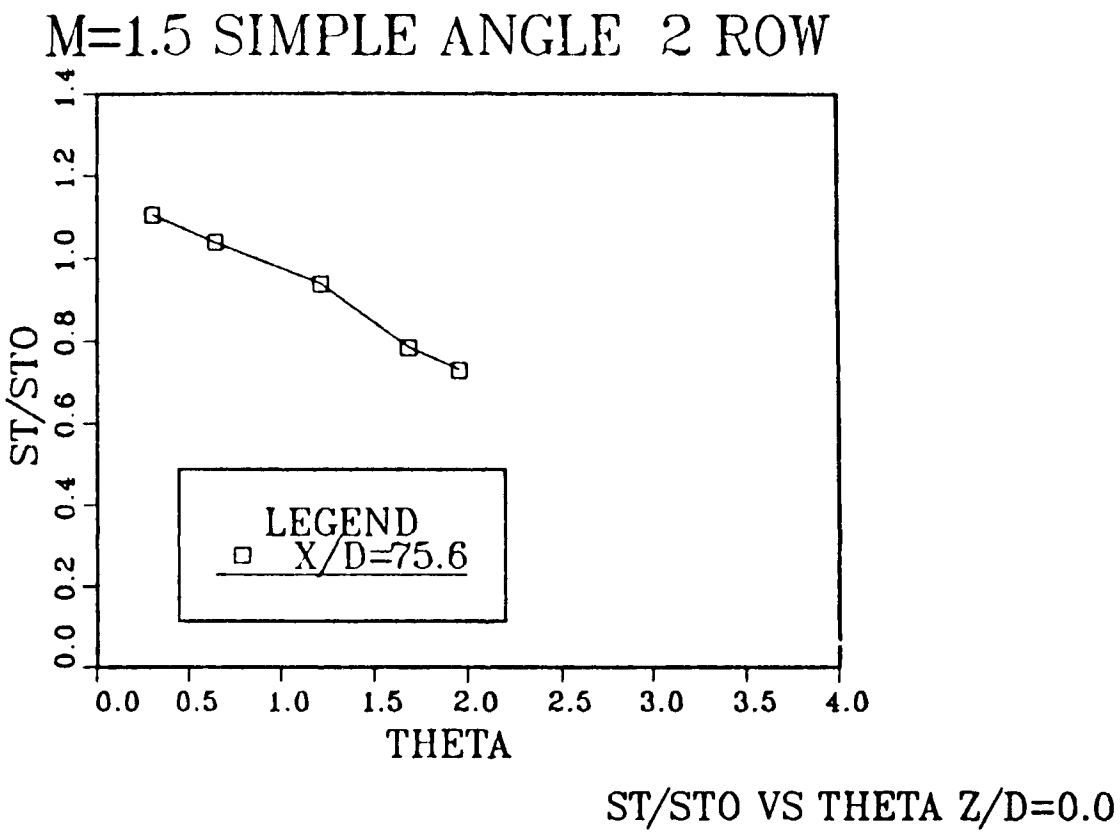


Figure 38. St/Sto Versus θ, Simple Angle, 2 Rows, m=1.5, x/d=75.6, z/d=0.0

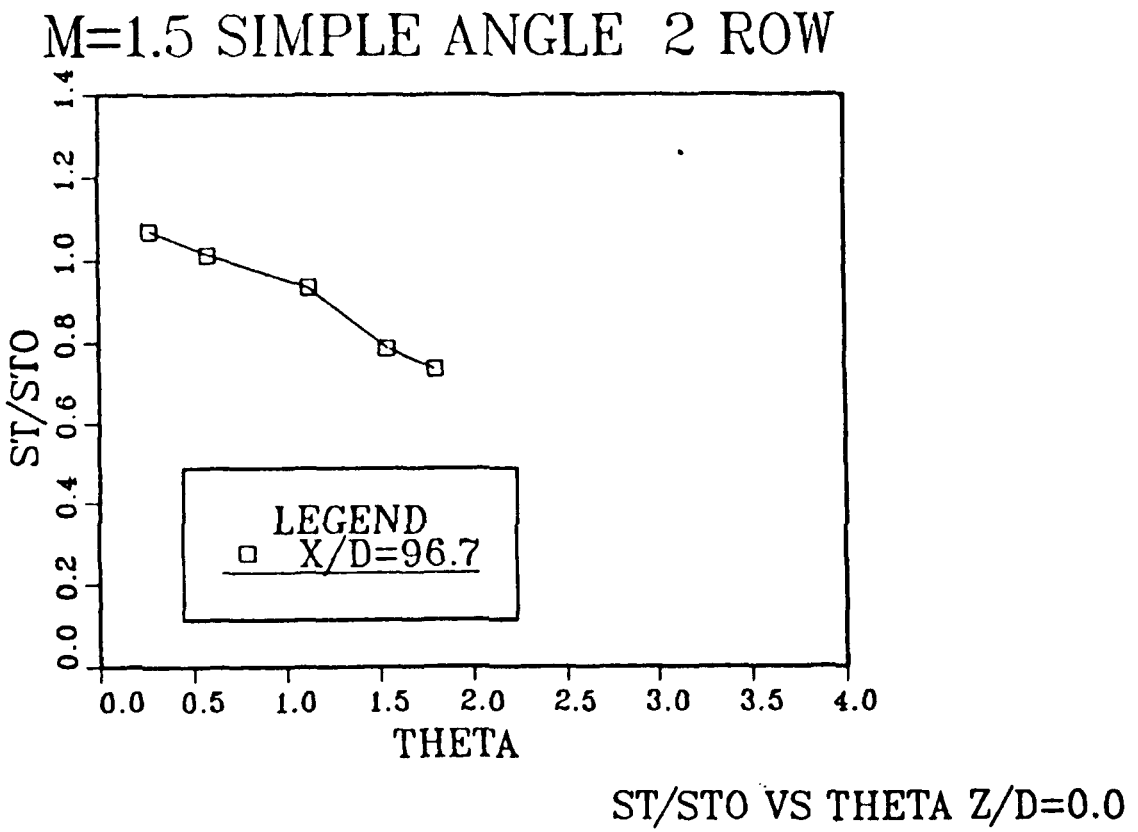


Figure 39. St/Sto Versus θ, Simple Angle, 2 Rows, m=1.5, x/d=96.7, z/d=0.0

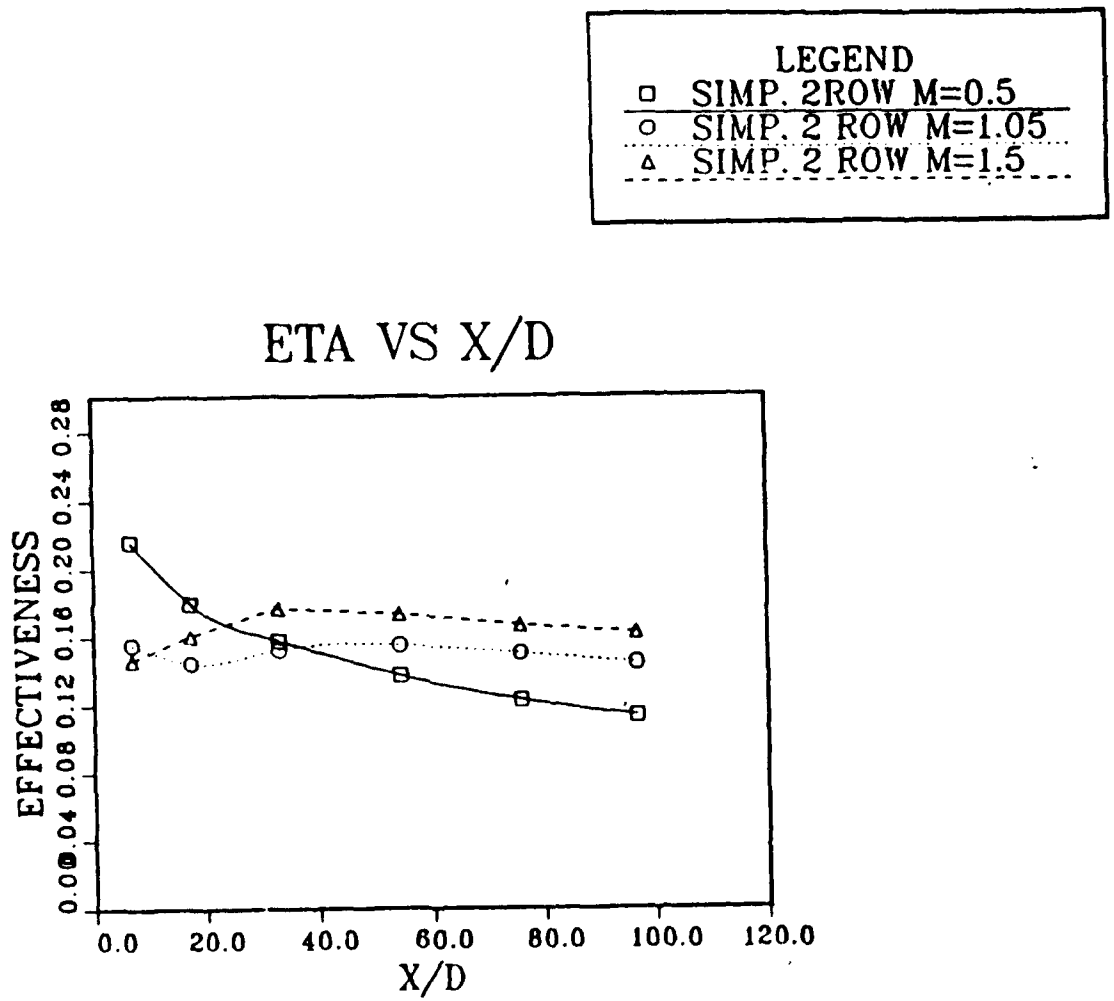


Figure 40. η Versus x/d, Simple Angle, 2 Rows, m=1.5, Spanwise Average

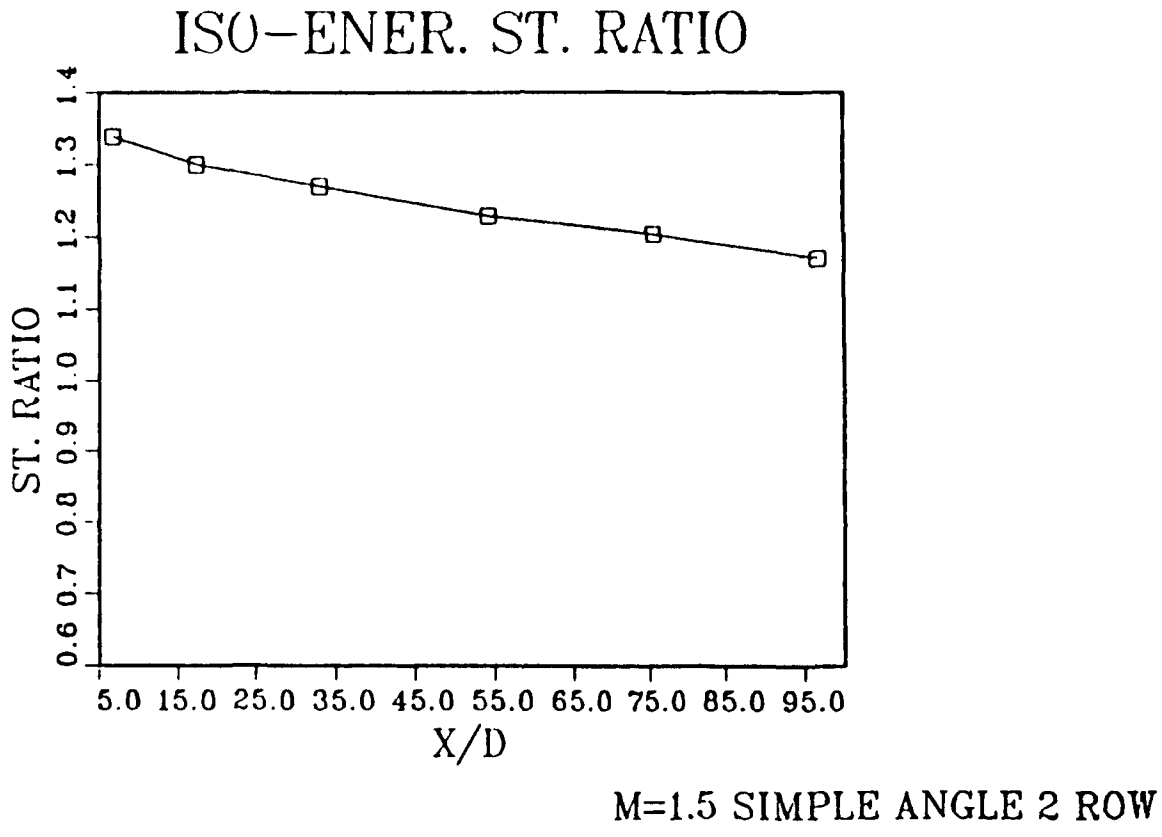


Figure 41. Stf/Sto Versus x/d, Simple Angle, 2 Rows, m=1.5, Spanwise Average

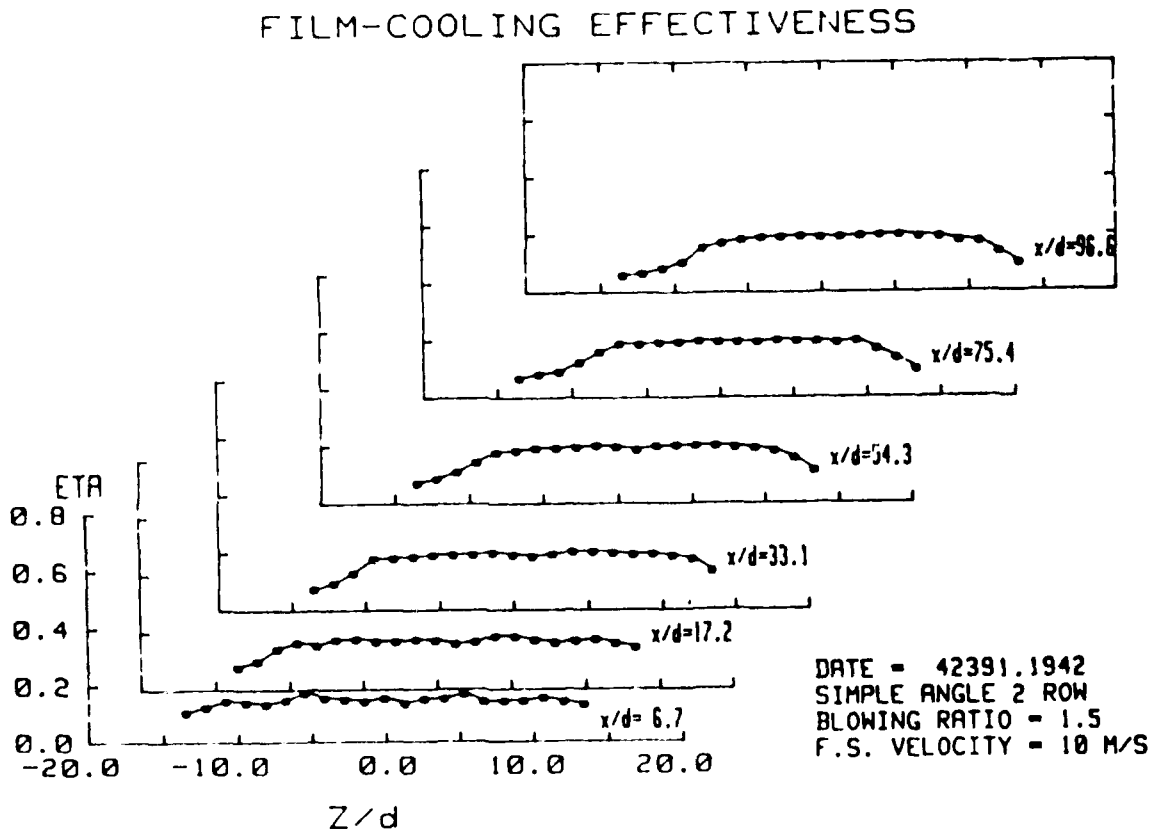


Figure 42 Spanwise Variation of η, Simple Angle, 2 Rows, m=1.5

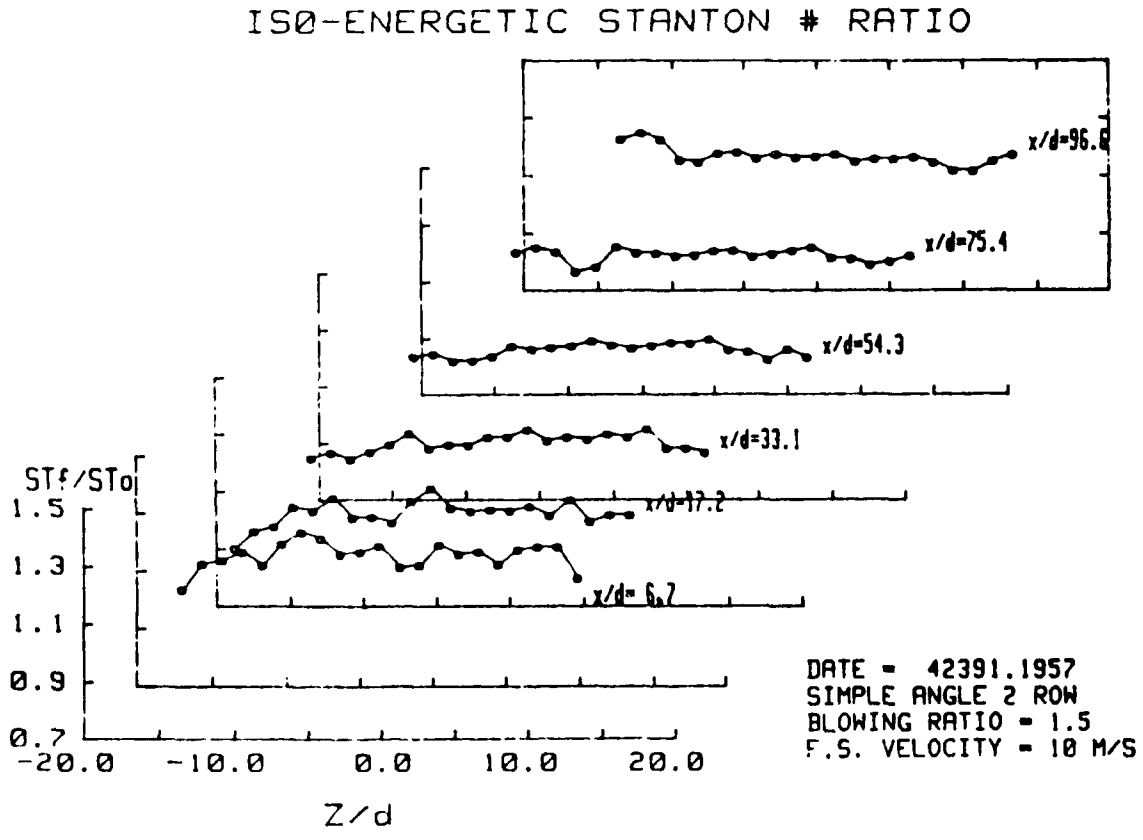


Figure 43. Spanwise Variation of Stf/Sto, Simple Angle, 2 Rows, m=1.5

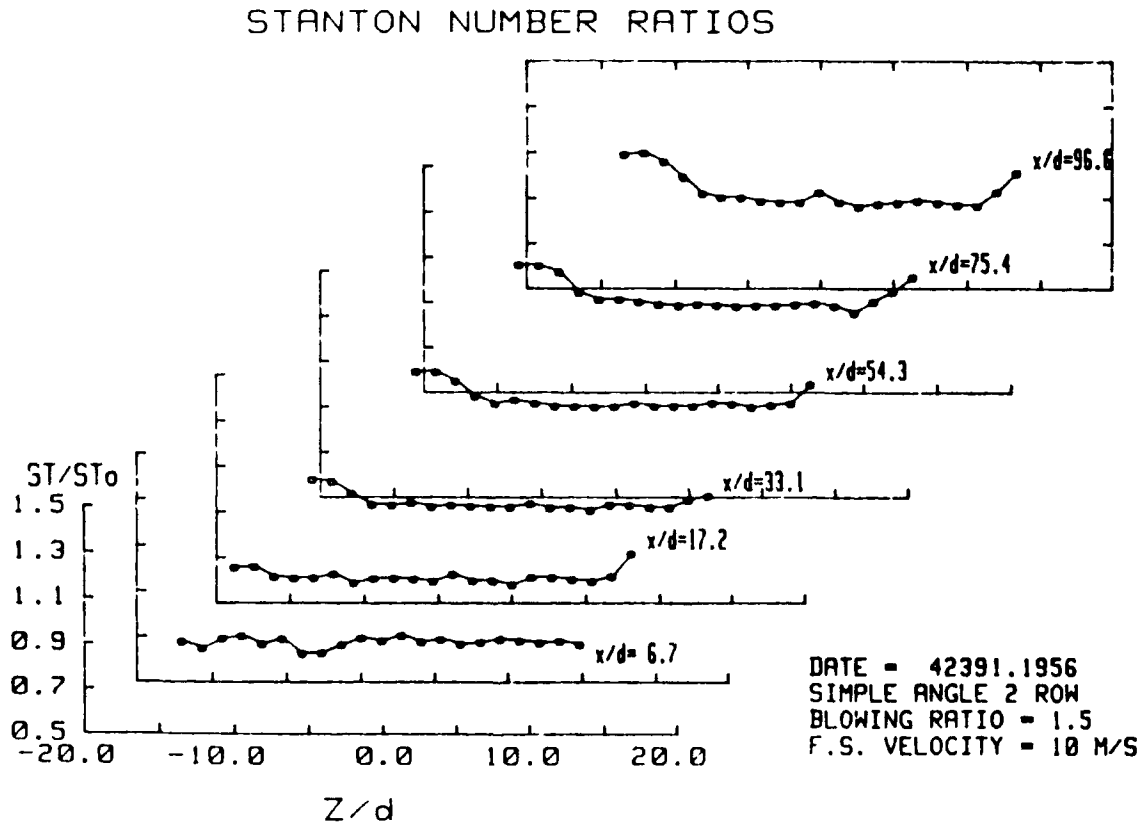


Figure 44. Spanwise Variation of St/Sto, Simple Angle, 2 Rows, m=1.5, θ=1.66

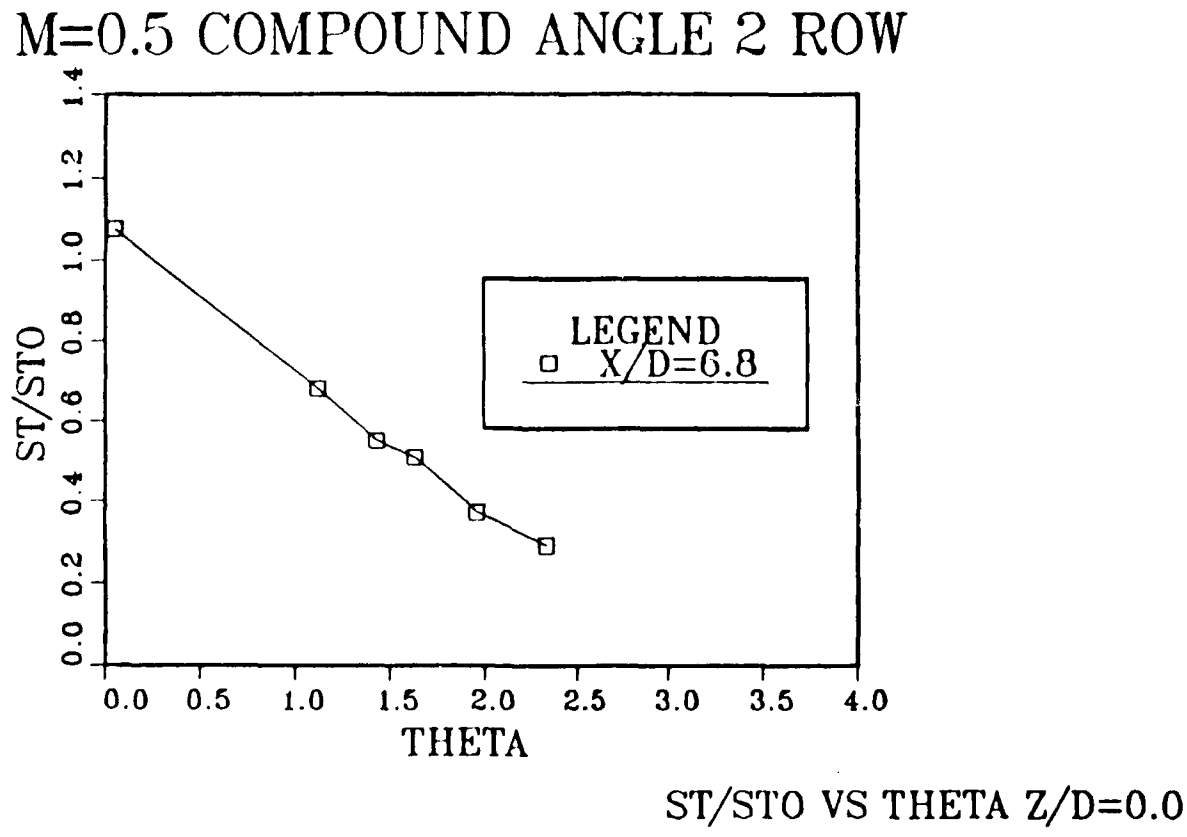


Figure 45. St/Sto Versus θ, Compound Angle, 2 rows, m=0.5, x/d=6.8, z/d=0.0

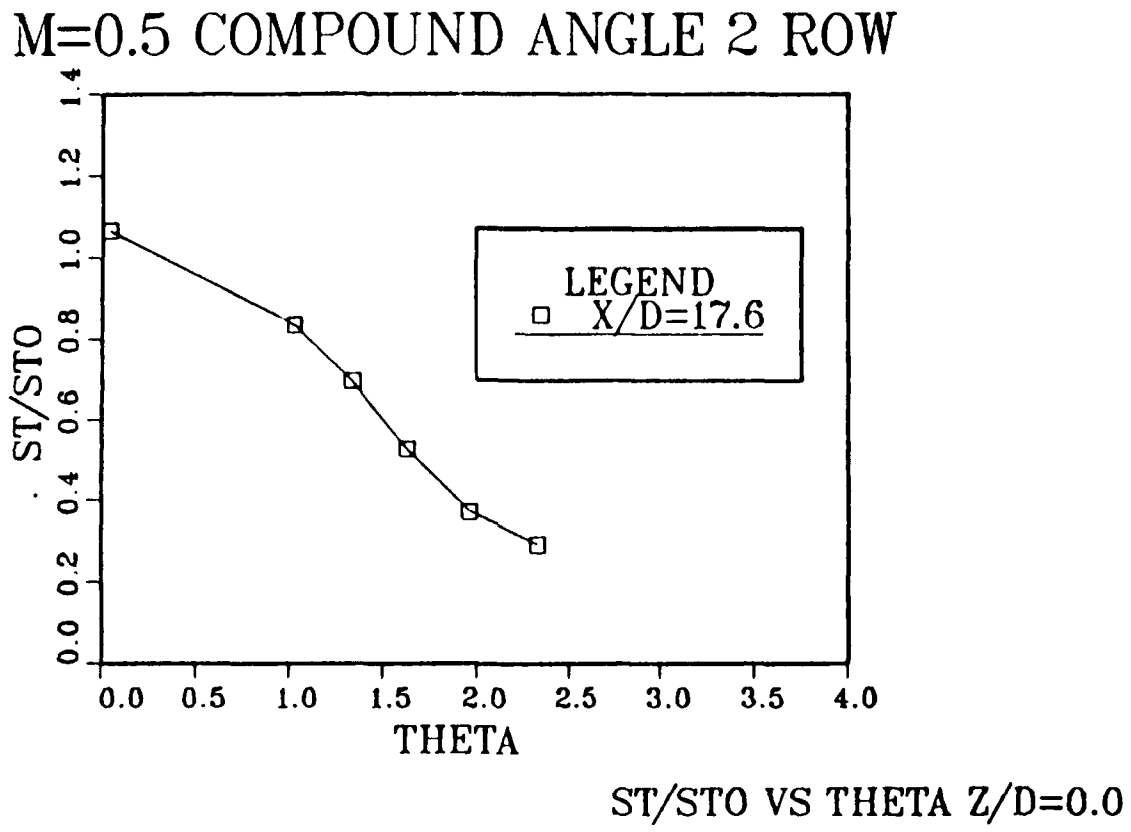


Figure 46. St/Sto Versus θ Compound Angle, 2 Rows, m=0.5, x/d=17.6, z/d=0.0

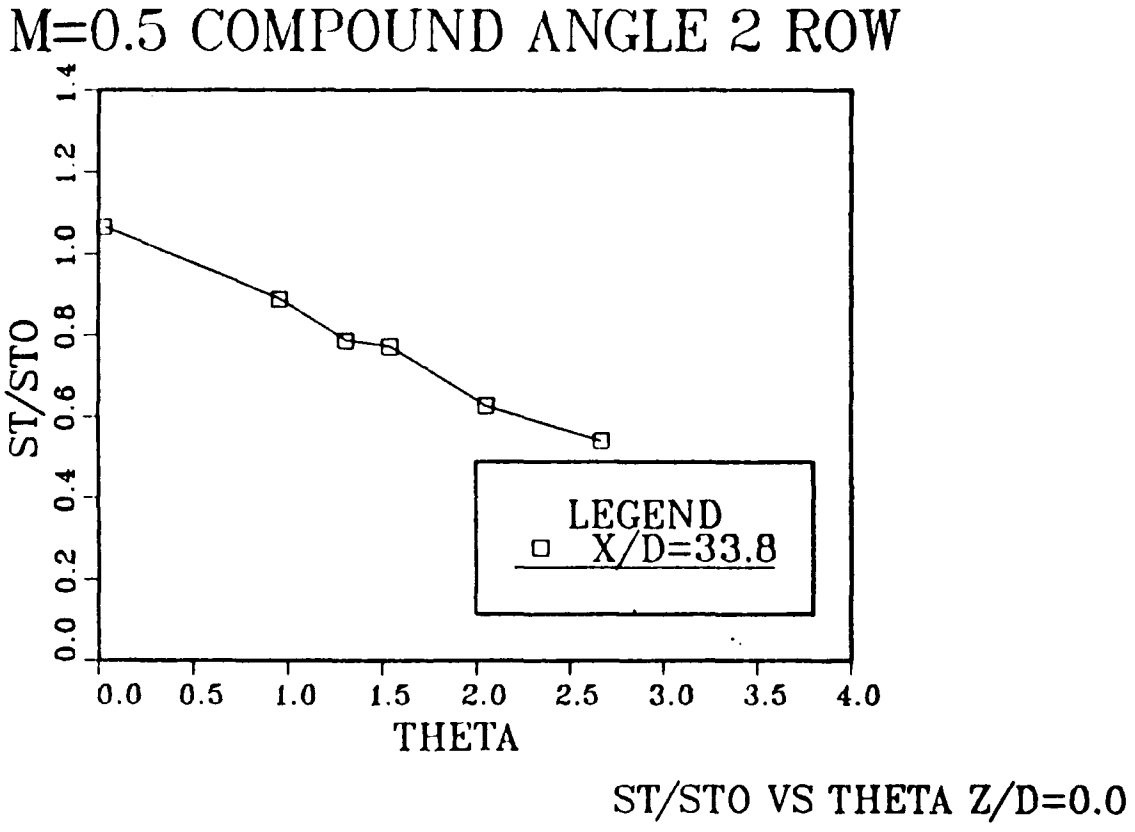


Figure 47. St/Sto Versus θ, compound Angle, 2 Rows, m=0.5, x/d=33.8, z/d=0.0

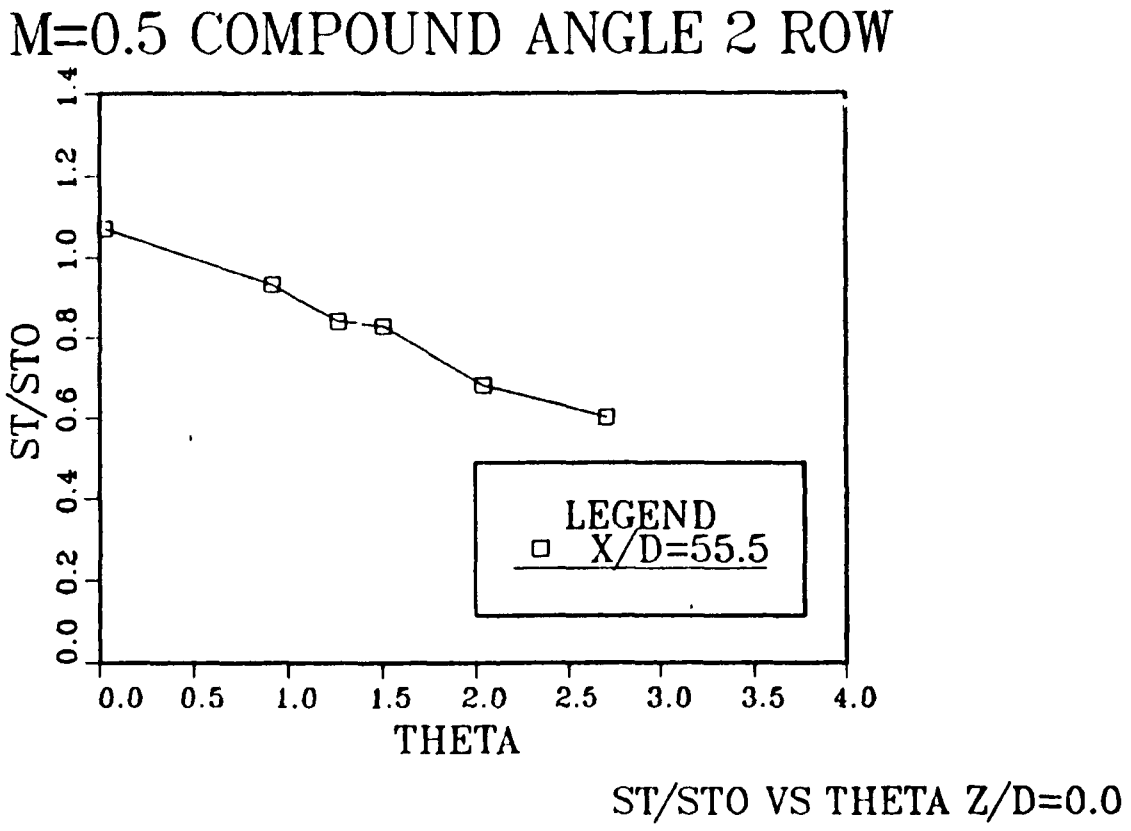


Figure 48. St/Sto Versus θ, Compound Angle, 2 Rows, m=0.5, x/d=55.5, z/d=0.0

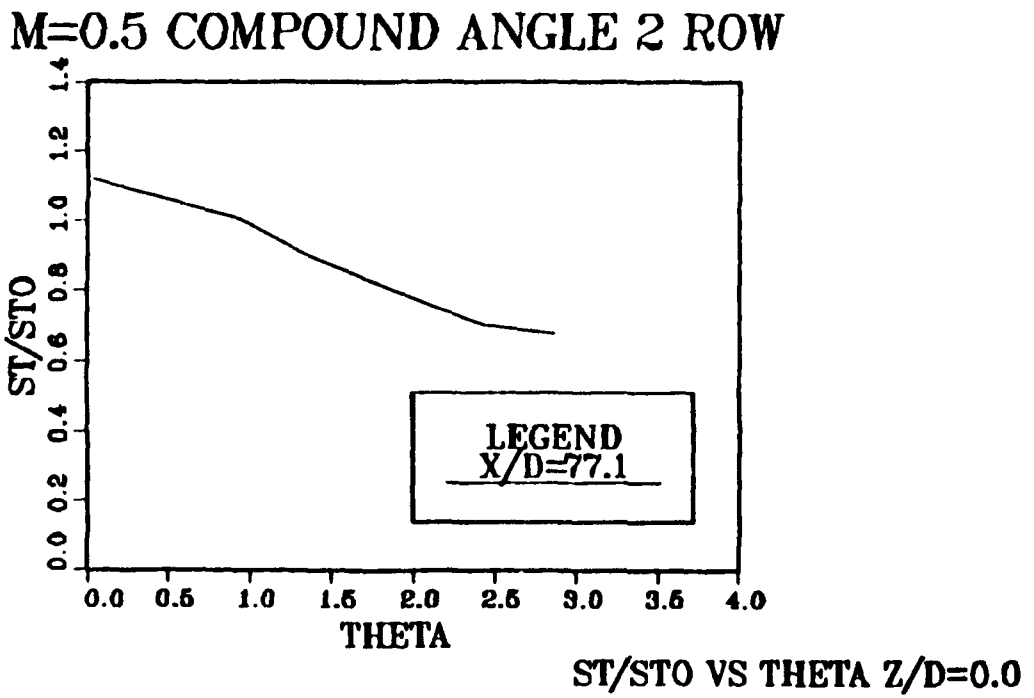


Figure 49. **St/Sto Versus θ, Compound Angle, 2 Rows, m=0.5, x/d=77.1, z/d=0.0**

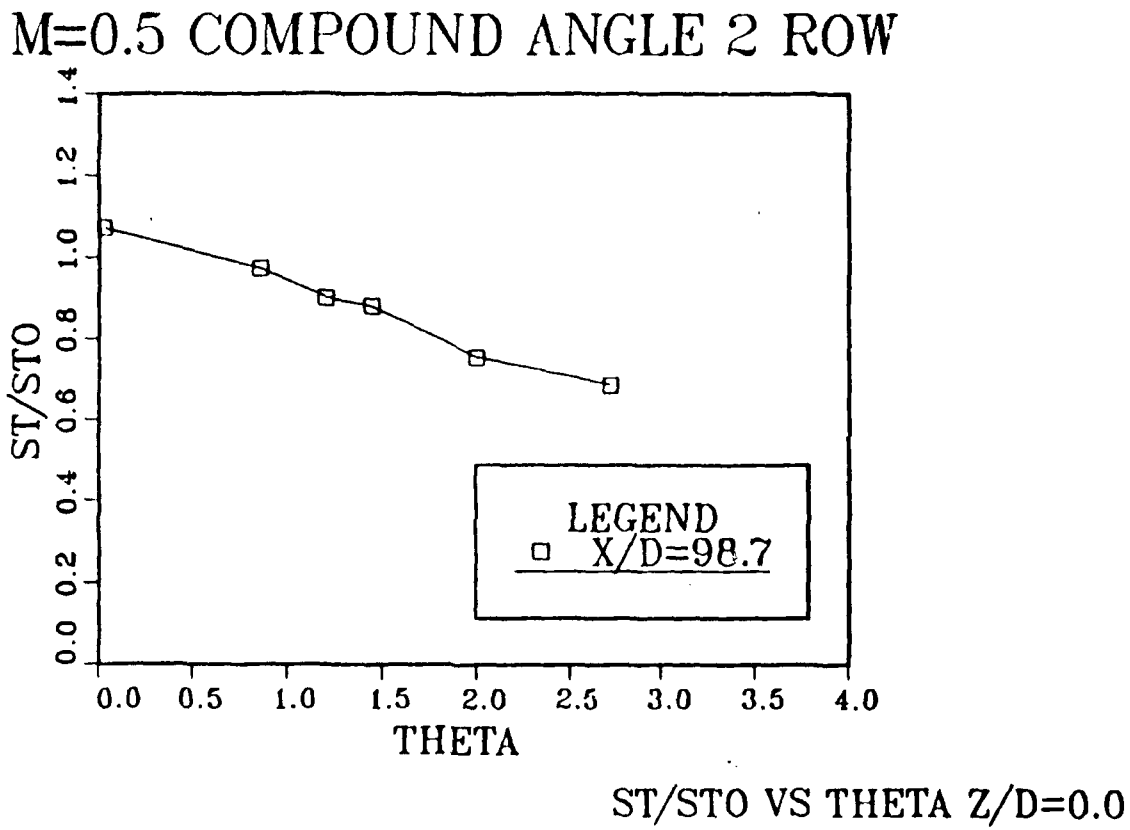


Figure 50. **St/Sto Versus θ, Compound Angle, 2 Rows, m=0.5, x/d=98.7, z/d=0.0**

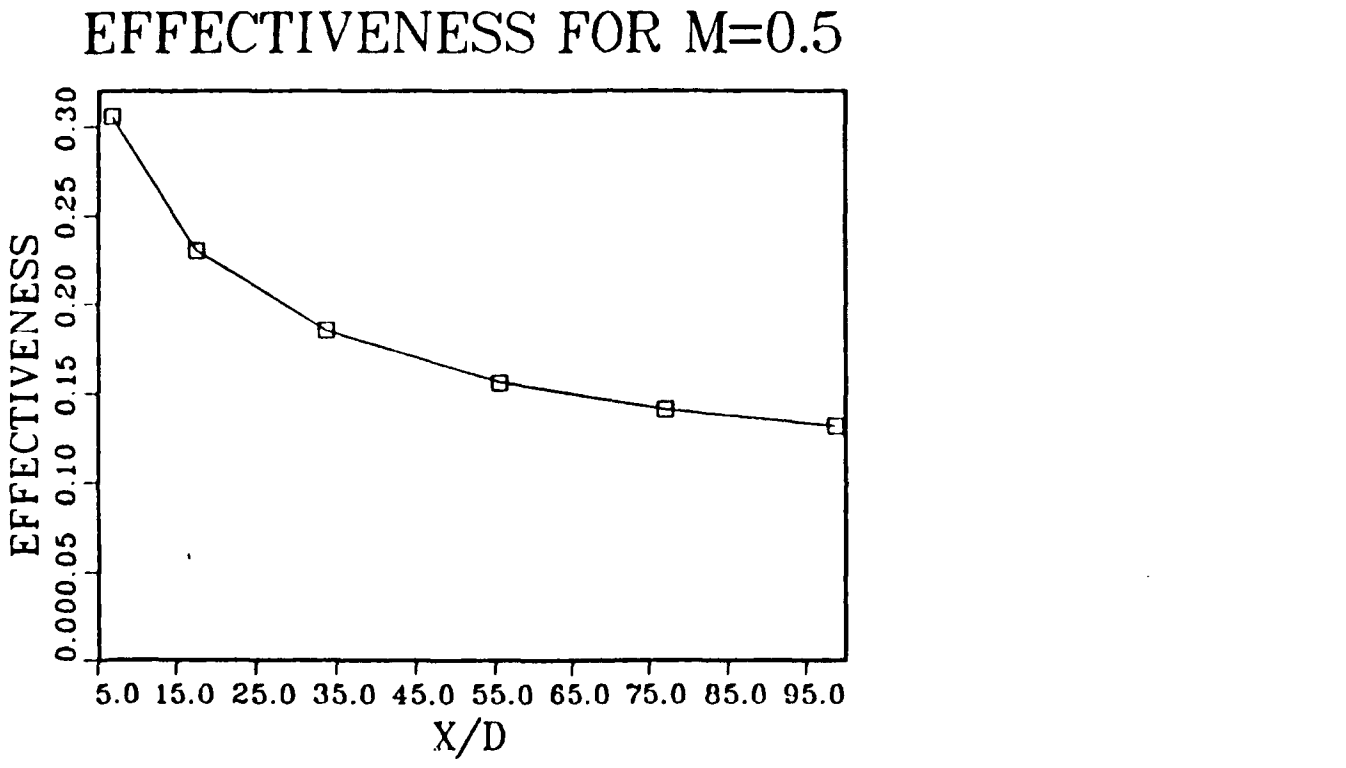


Figure 51. **η Versus x/d, Compound Angle, 2 Rows, m=0.5, Spanwise Average**

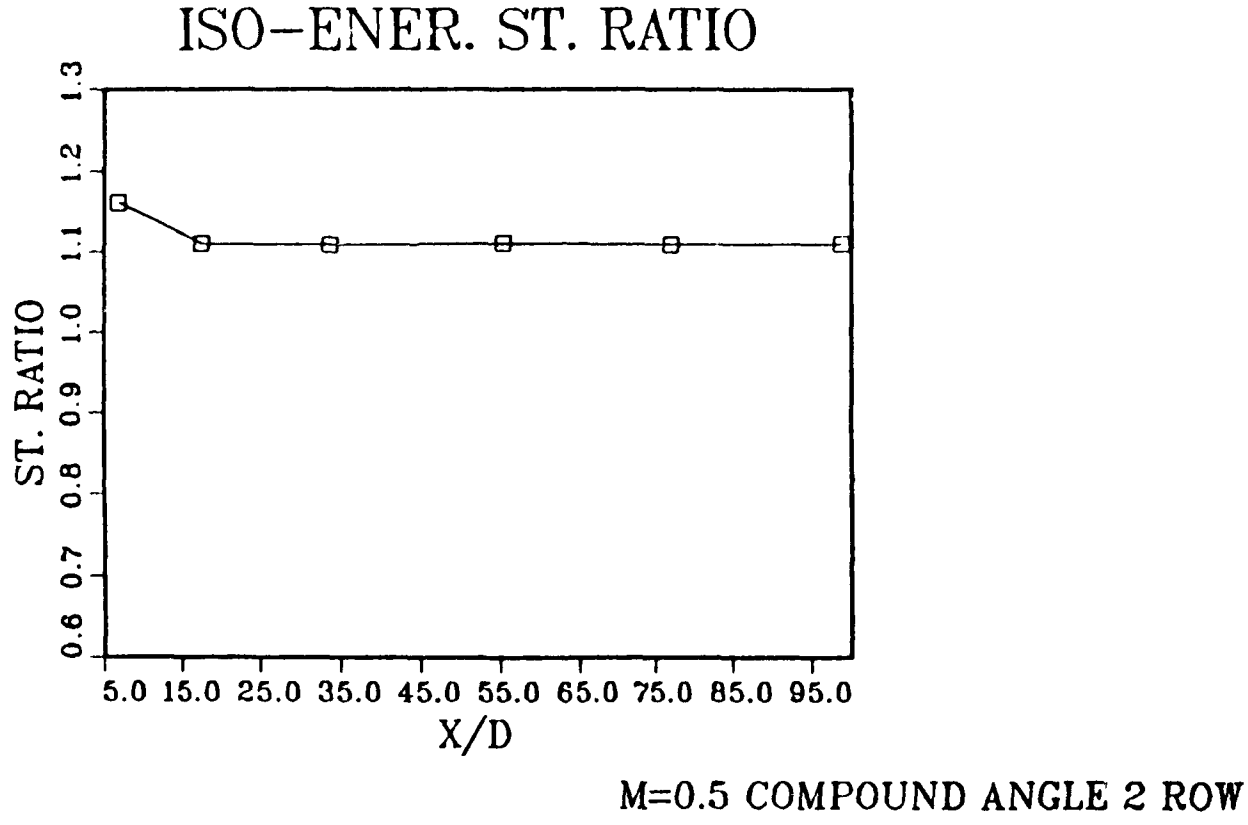


Figure 52. Stf/Sto Versus x/d, Compound Angle, 2 Rows, m=0.5, Spanwise Average

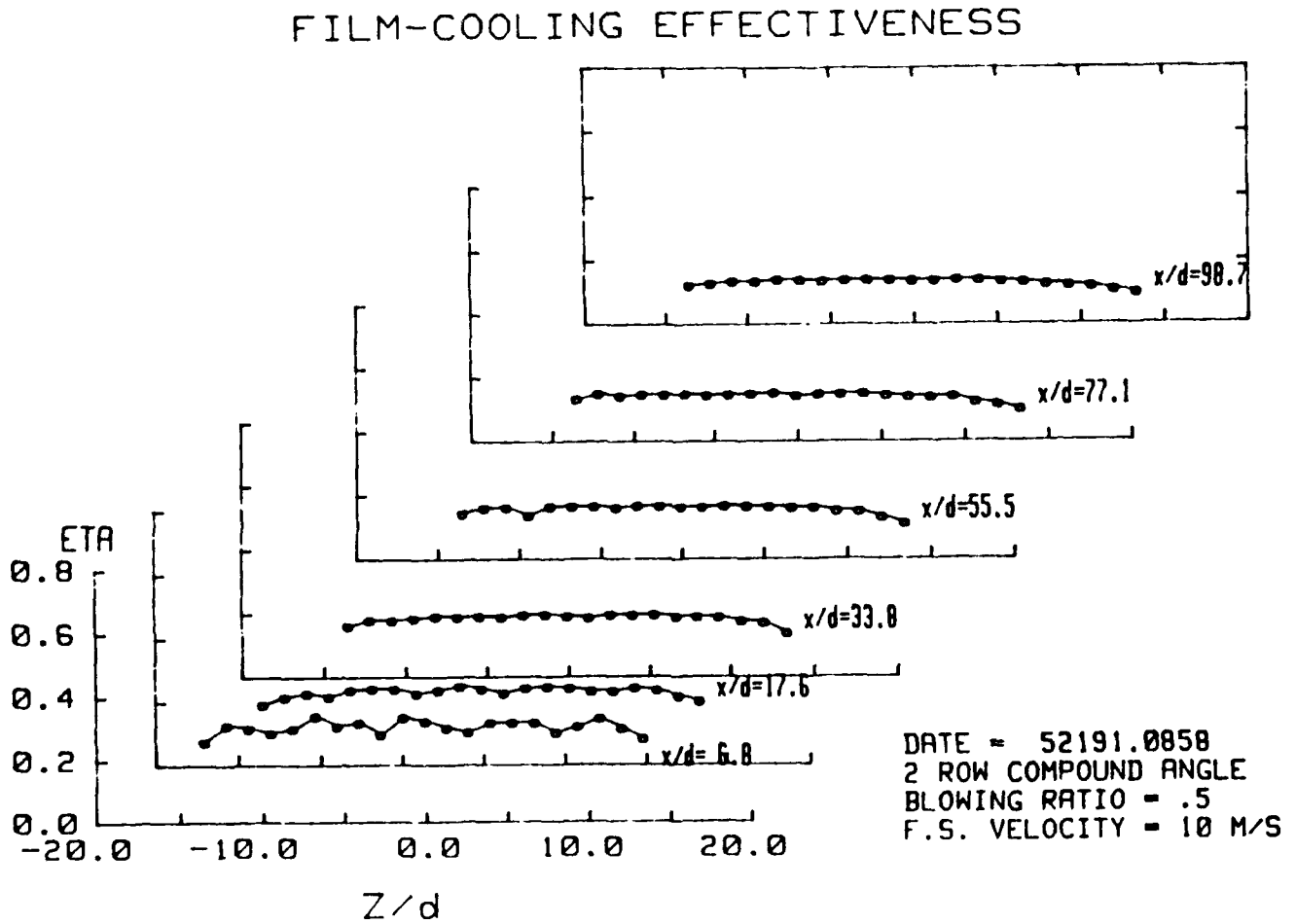


Figure 53. Spanwise Variation of η, Compound Angle, 2 Rows, m=0.5

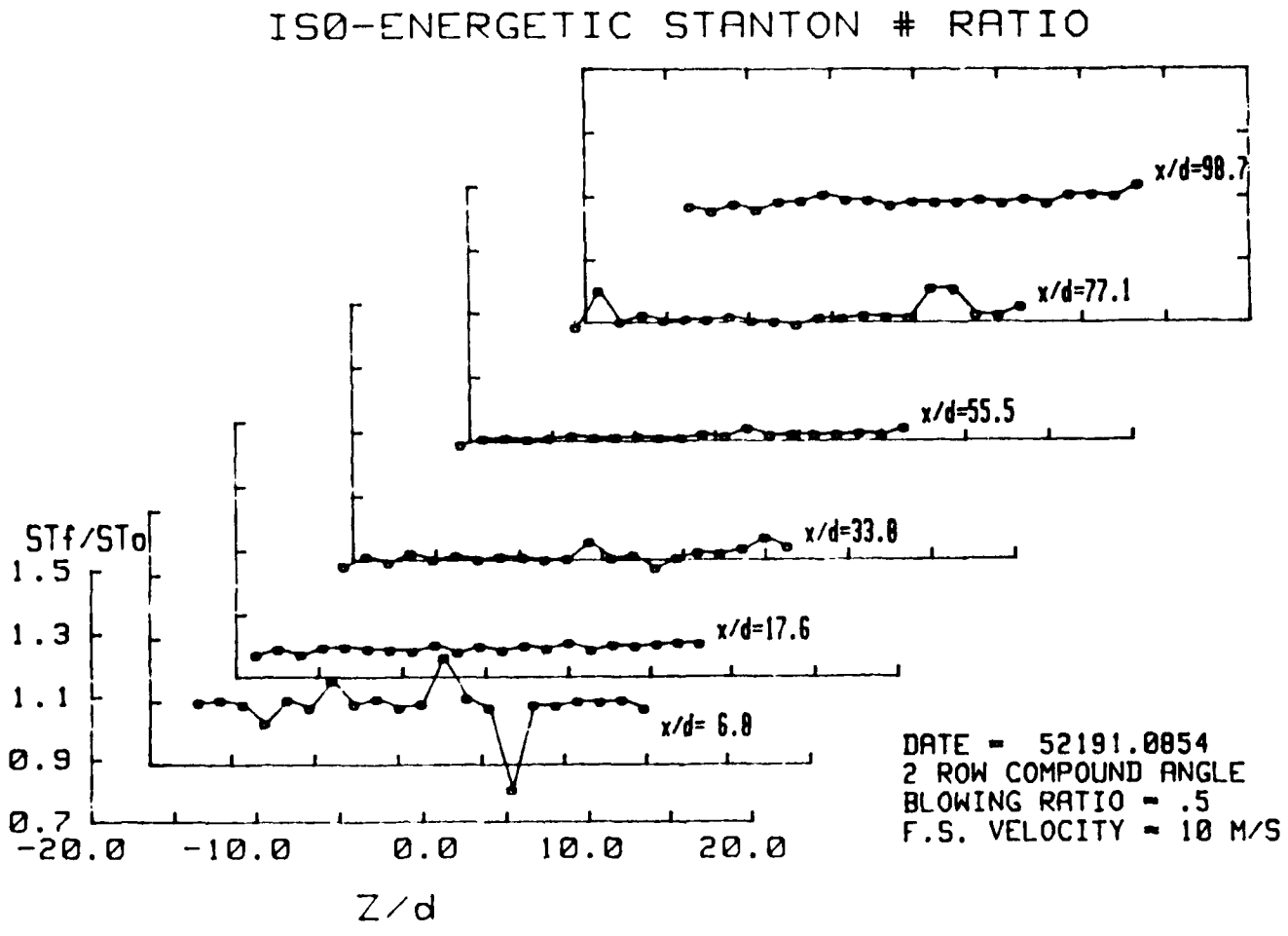


Figure 54. Spanwise Variation of Stf/Sto, Compound Angle, 2 Rows, m=0.5

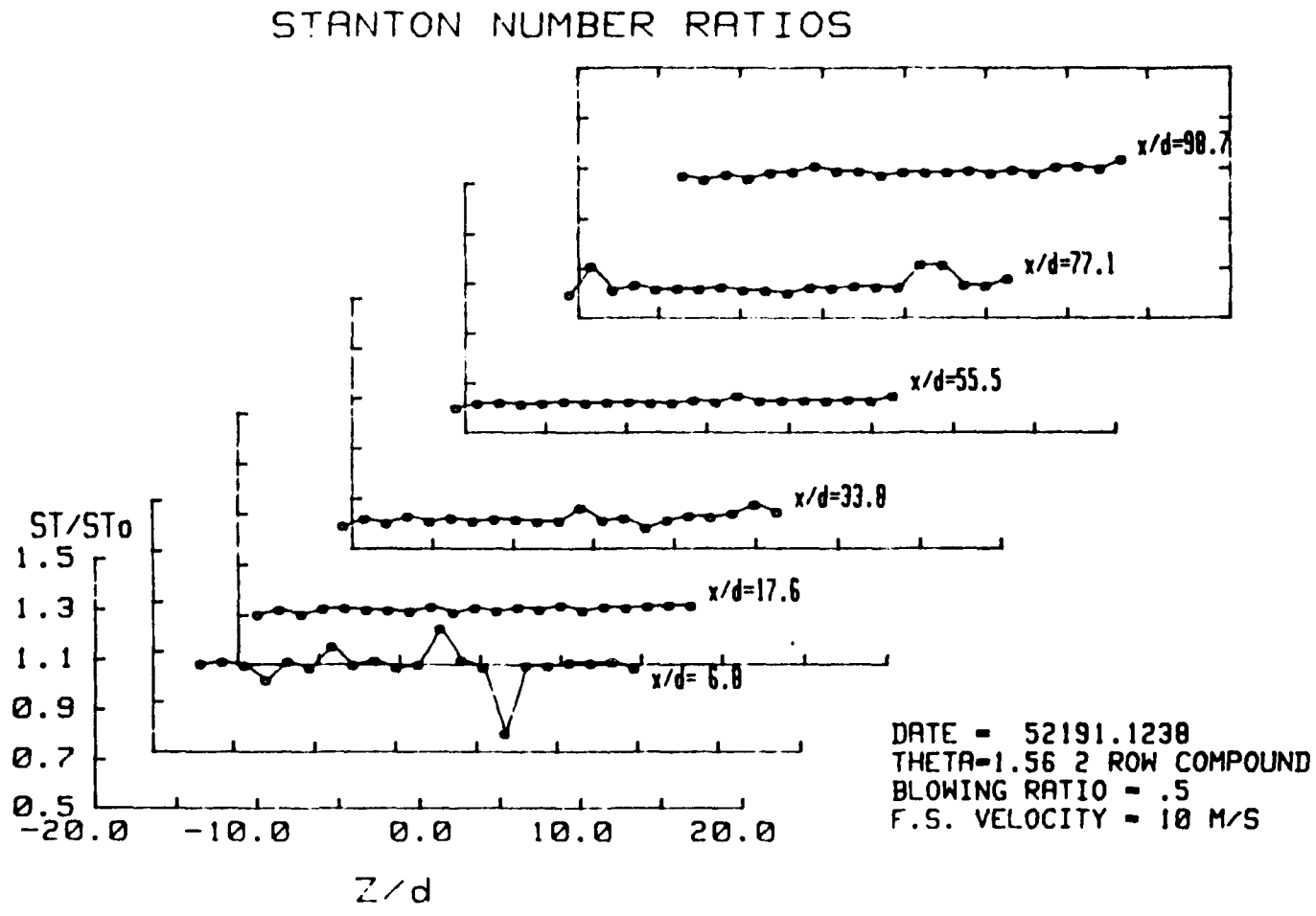


Figure 55. Spanwise Variation of St/Sto, Compound Angle, 2 Rows, m=0.5, θ=1.54

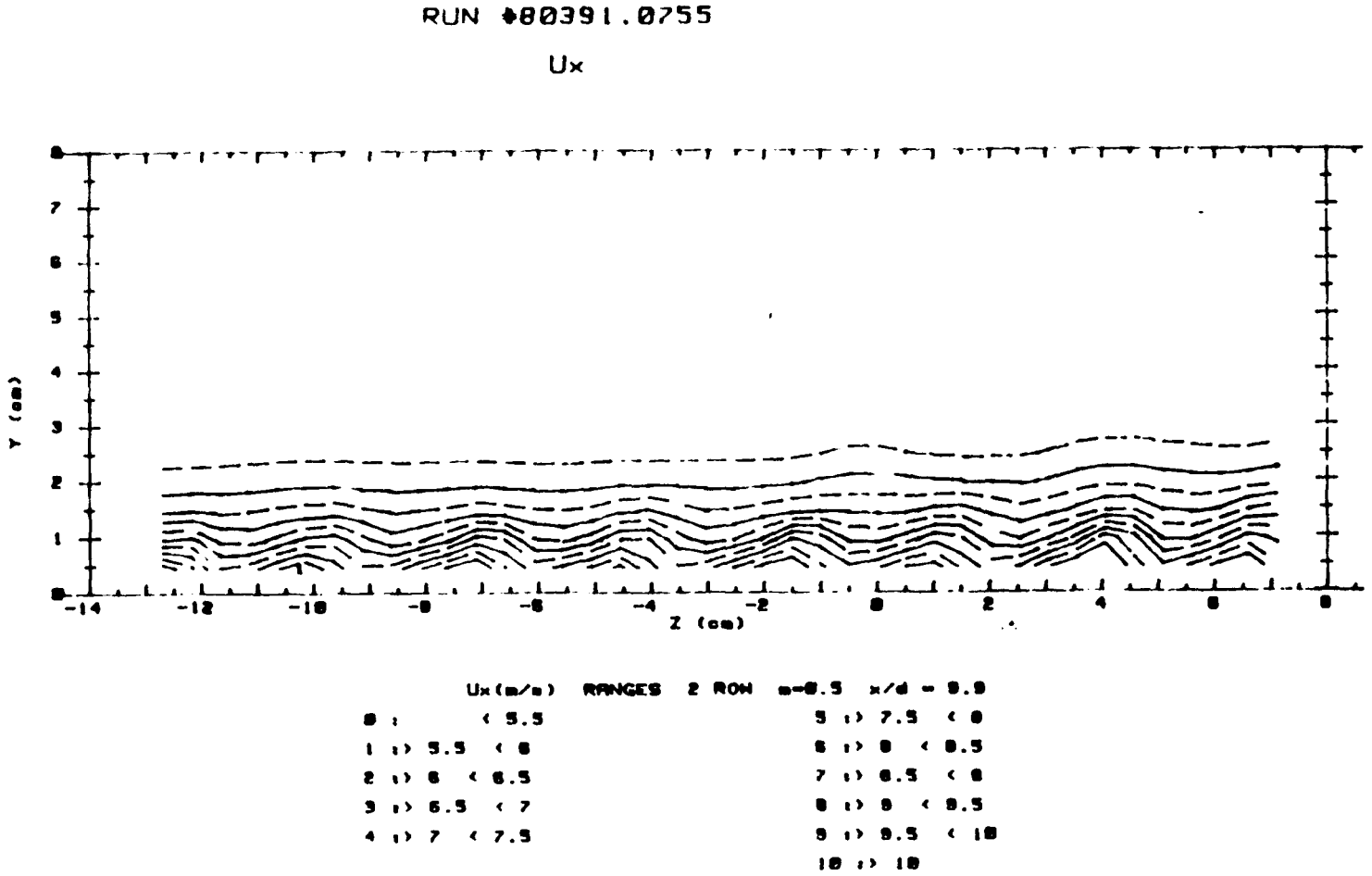


Figure 56. Streamwise Velocity Field, Compound Angle, 2 Rows, m=0.5, x/d=9.9

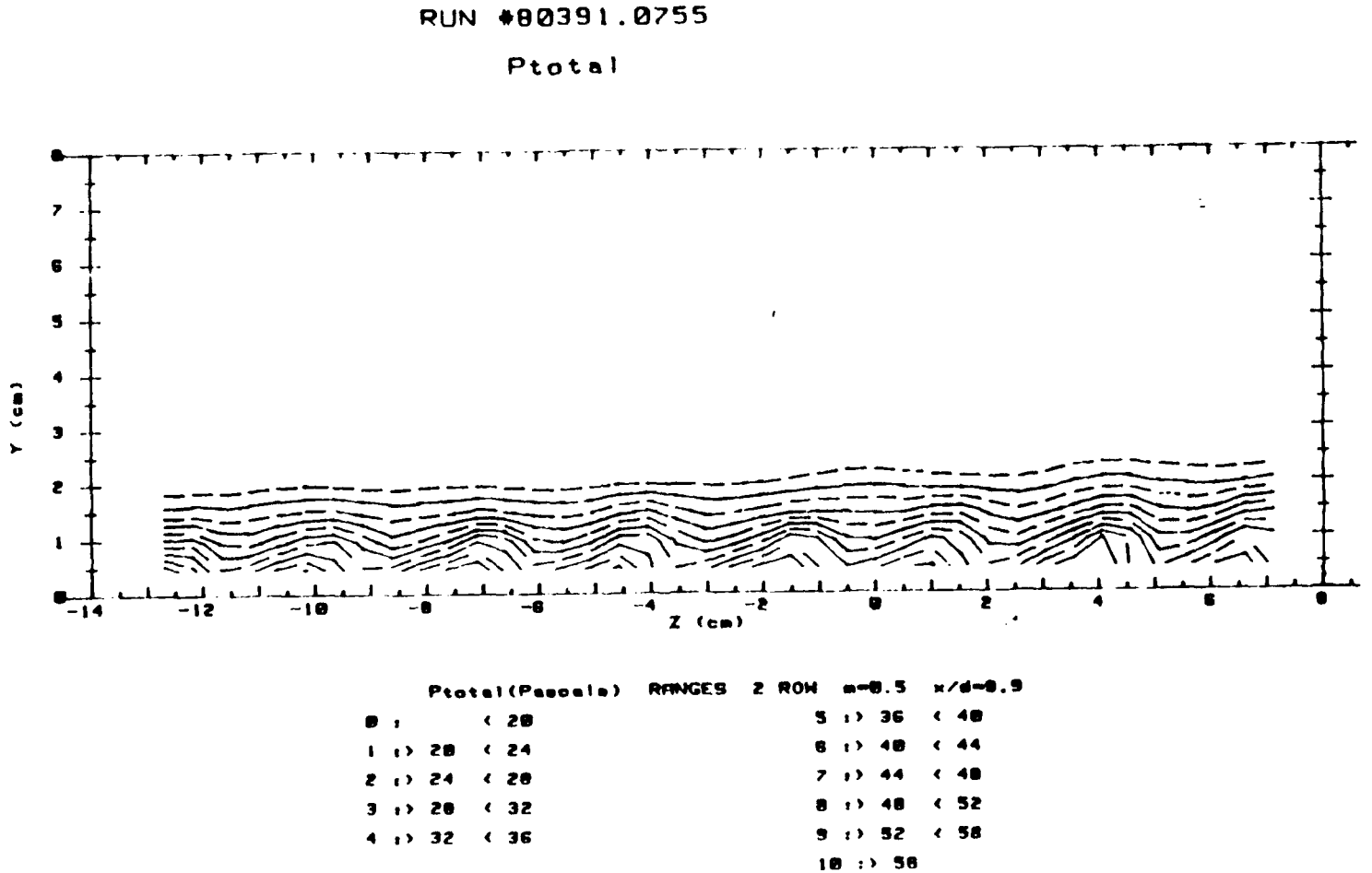


Figure 57. Streamwise Pressure Field, Compound Angle, 2 Rows, m=0.5, x/d=9.9

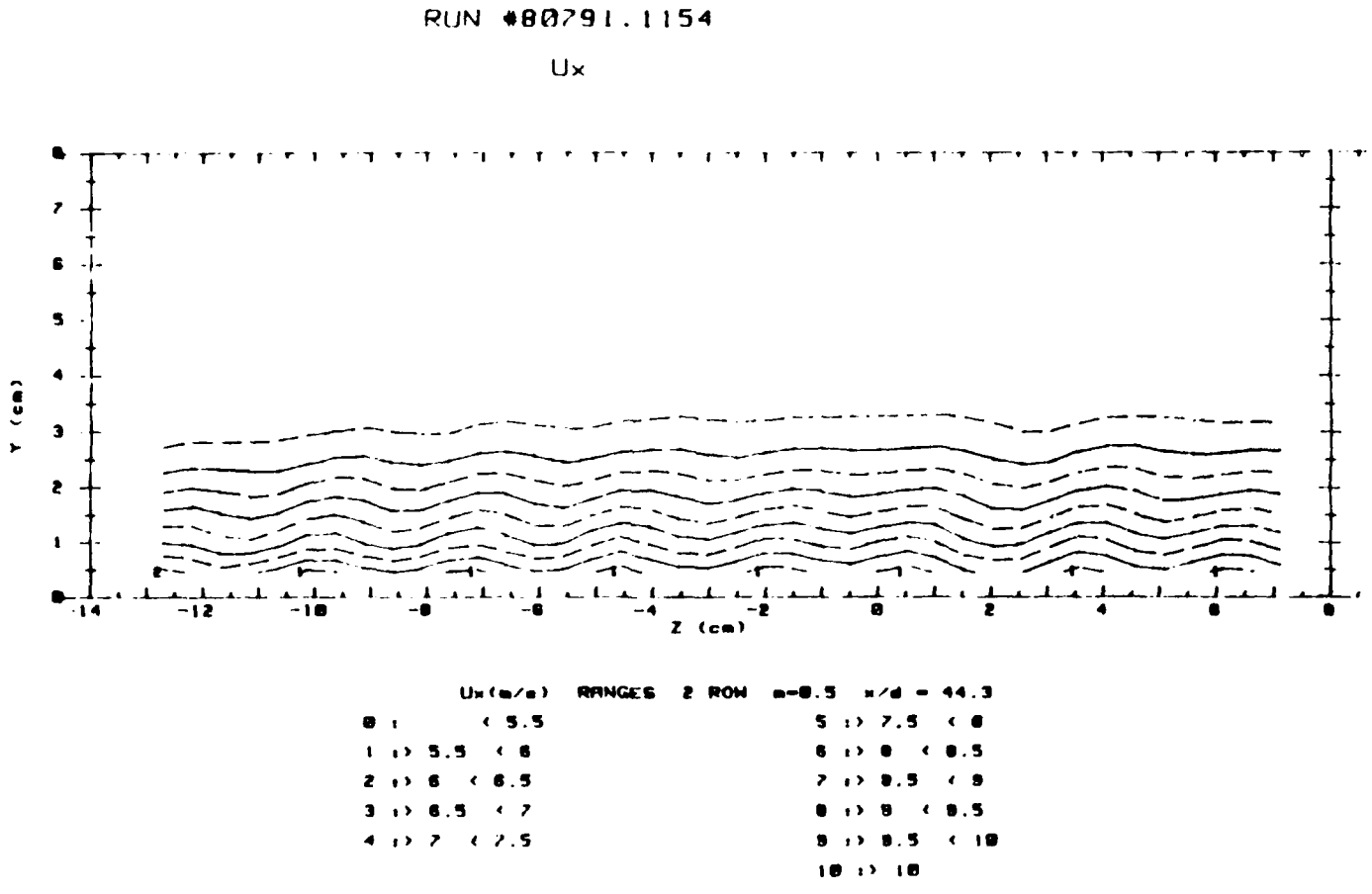


Figure 58. Streamwise Velocity Field, Compound Angle, 2 Rows, m=0.5, x/d=44.3

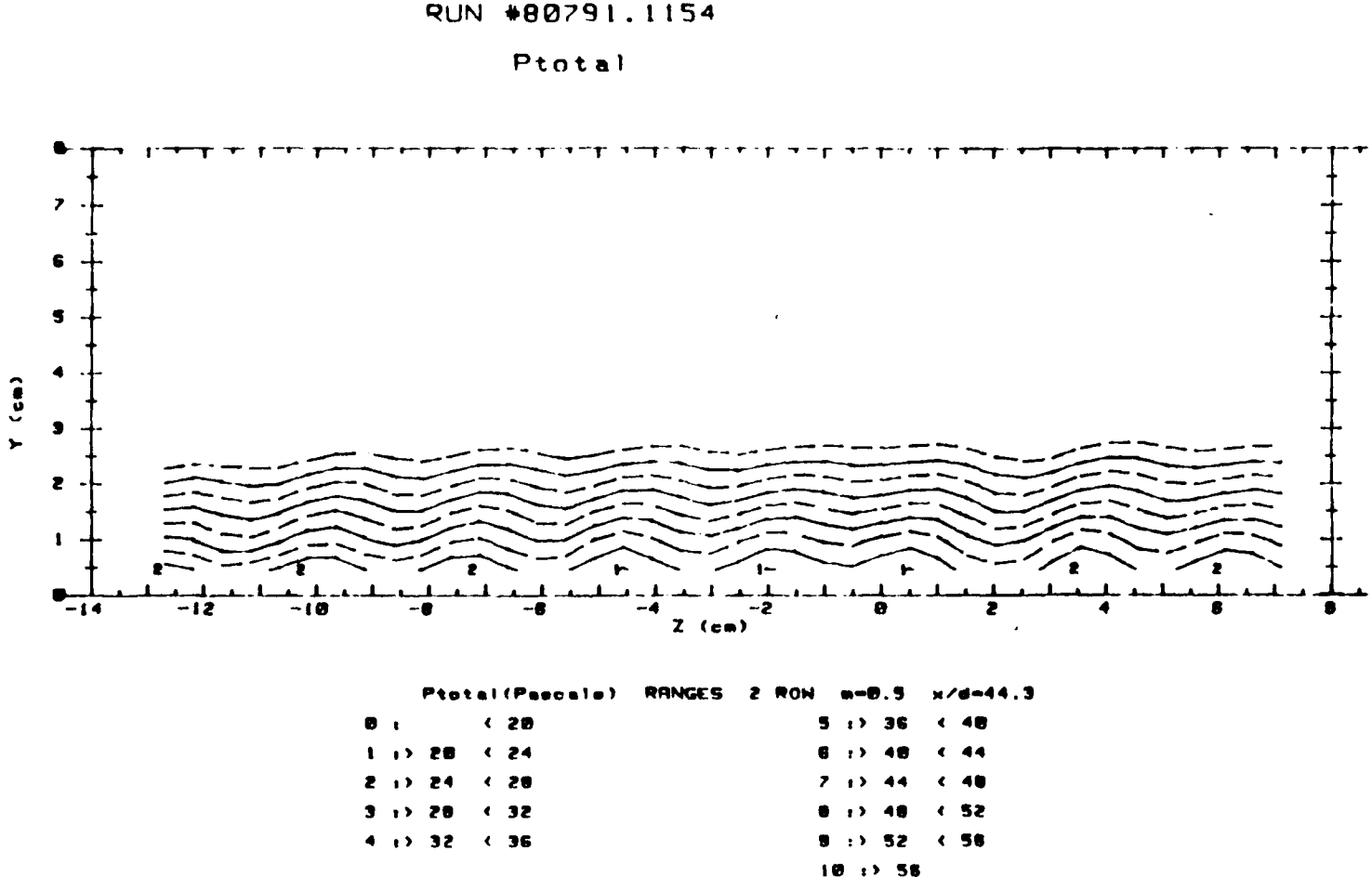


Figure 59. Streamwise Pressure Field, Compound Angle, 2 Rows, m=0.5, x/d=44.3

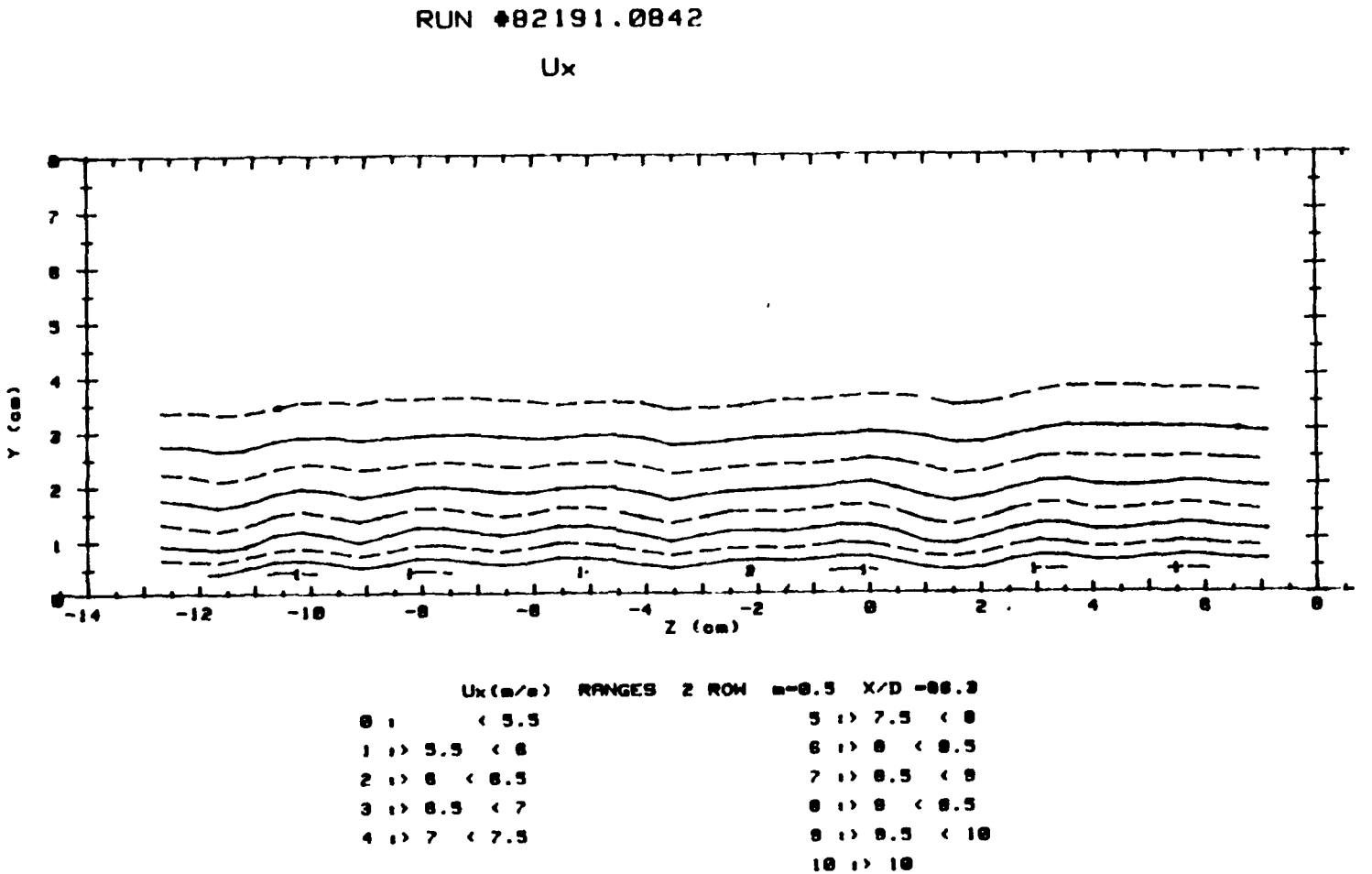


Figure 60. Streamwise Velocity Field, Compound Angle, 2 Rows, m=0.5, x/d=86.3

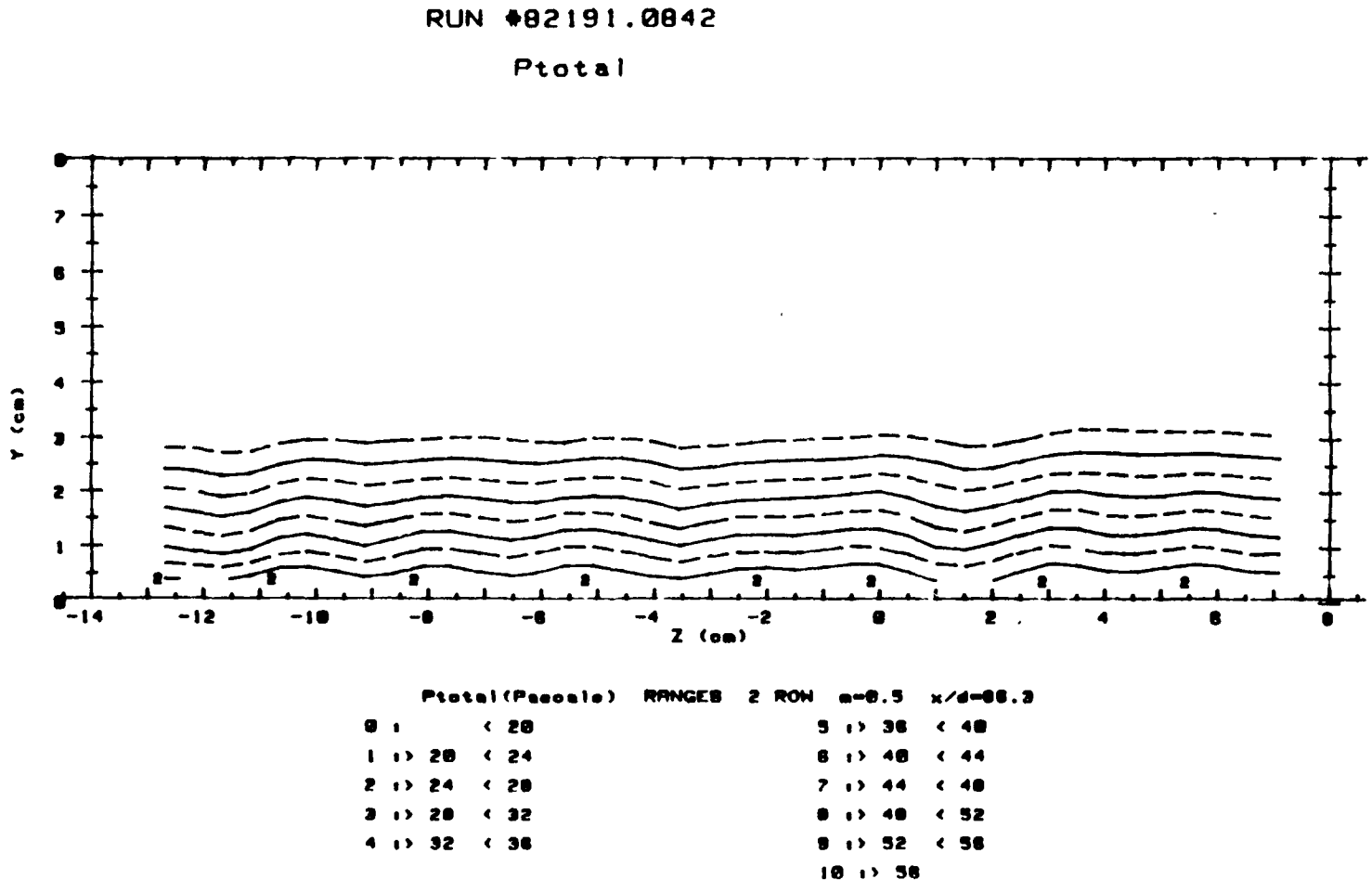


Figure 61. Streamwise Pressure Field, Compound Angle, 2 Rows, m=0.5, x/d=86.3

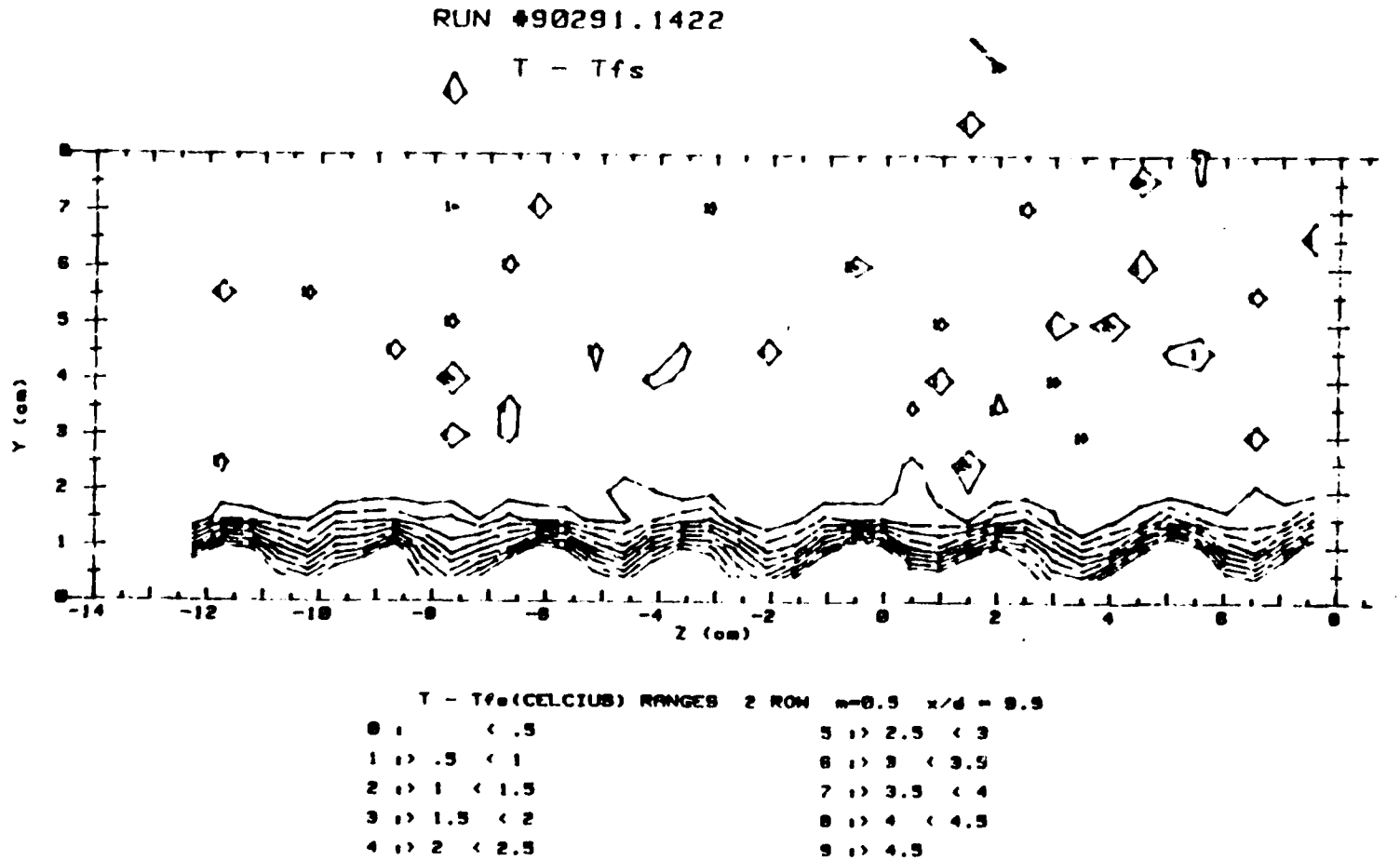


Figure 62. Streamwise Injectant Distribution, Compound Angle, 2 Row, m=0.5, x/d=9.9

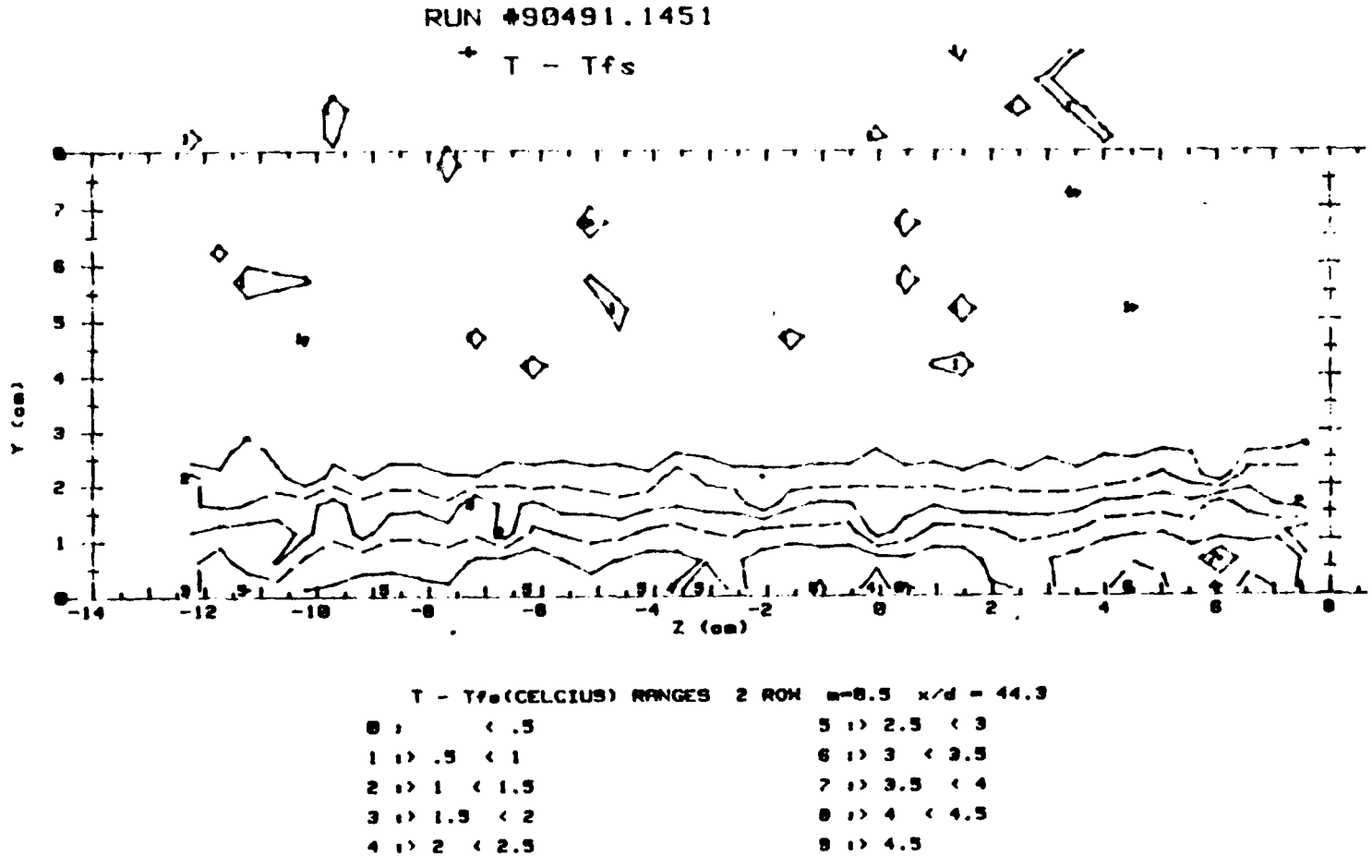


Figure 63. Streamwise Injectant Distribution, Compound Angle, 2 Rows, m=0.5, x/d=44.3

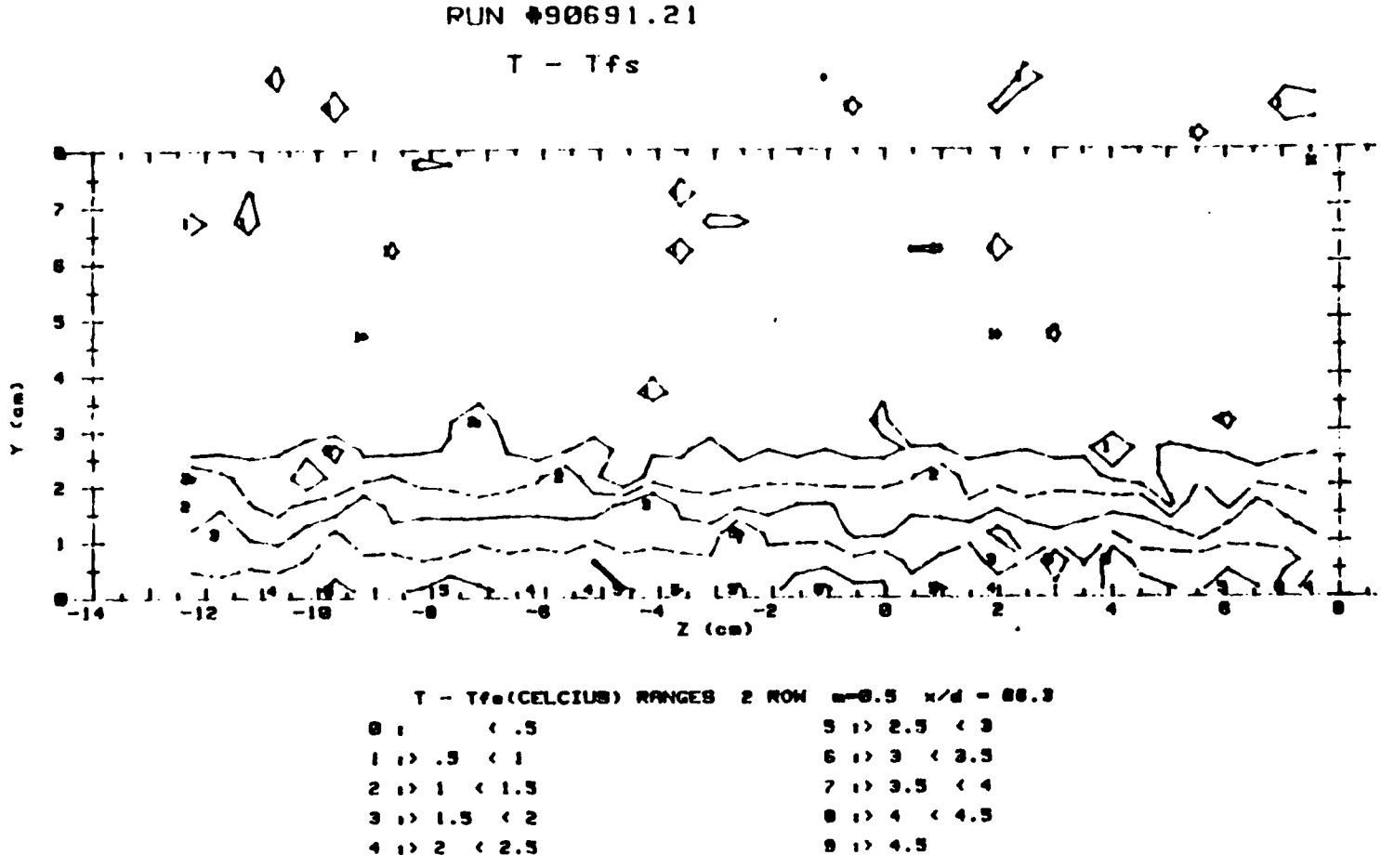


Figure 64. Streamwise Injectant Distribution, Compound Angle, 2 Rows, m=0.5, x/d=86.3

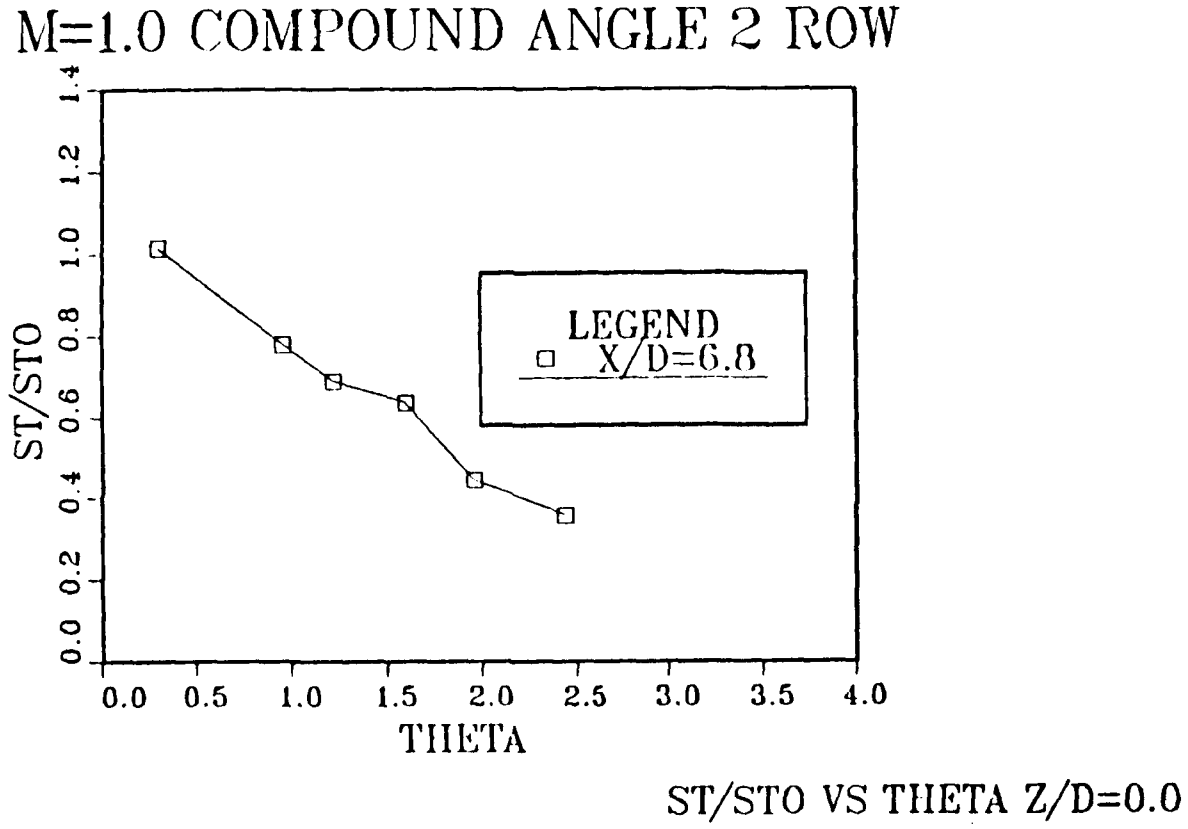


Figure 65. St/Sto Versus θ, Compound Angle, 2 Rows, m=1.0, x/d=6.8, z/d=0.0

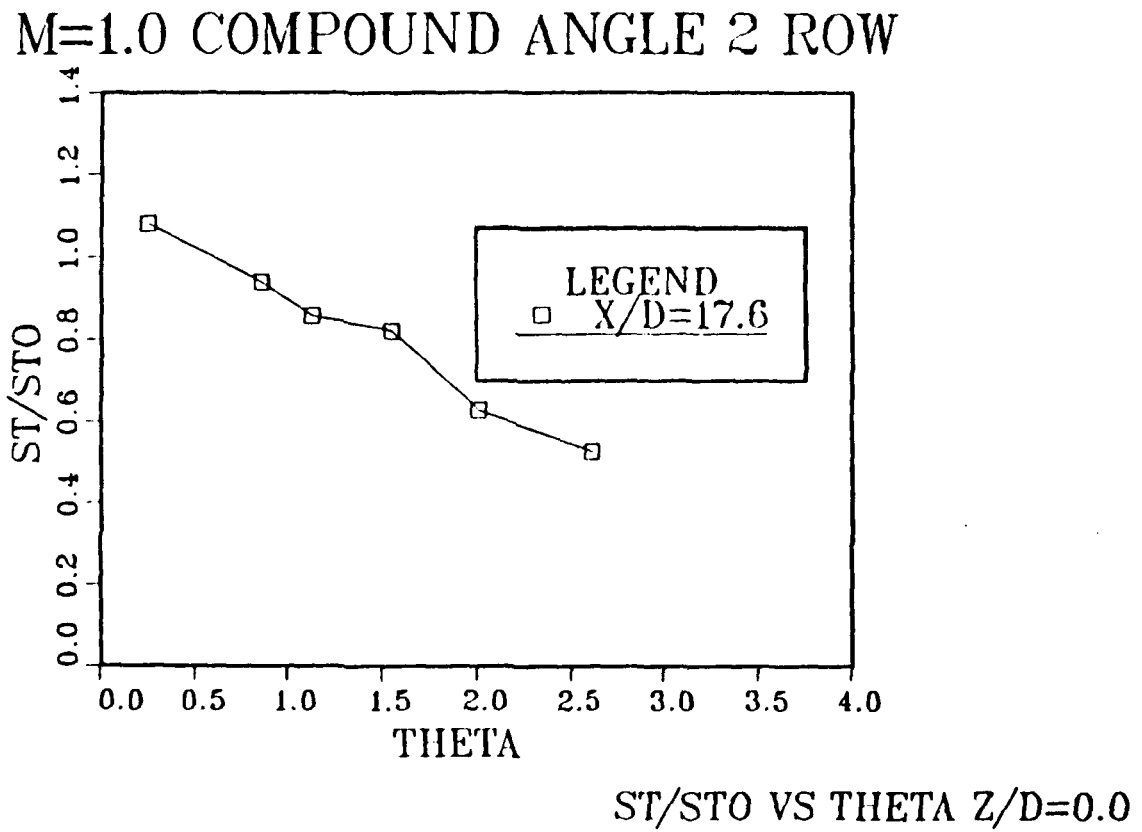


Figure 66. St/Sto Versus θ Compound Angle, 2 Rows, m=1.0, x/d=17.6, z/d=0.0

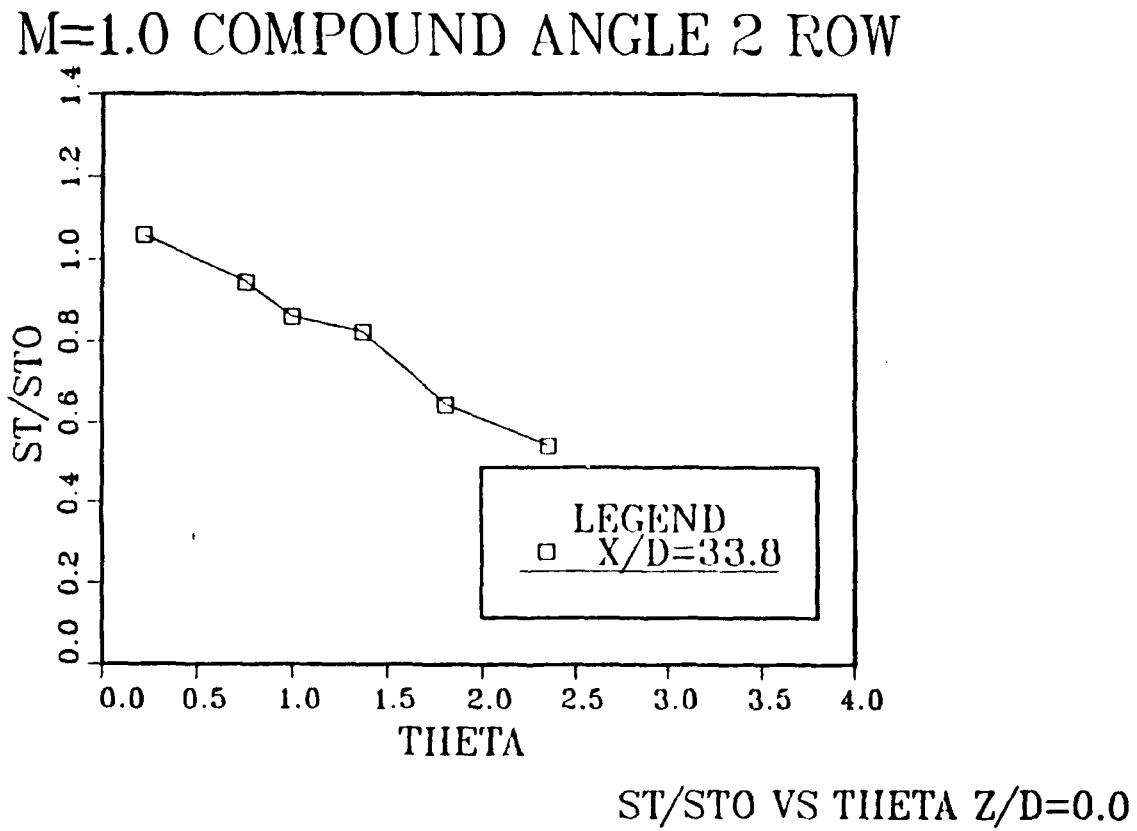


Figure 67. St/Sto Versus θ, Compound Angle, 2 rows, m=1.0, x/d=33.8, z/d=0.0

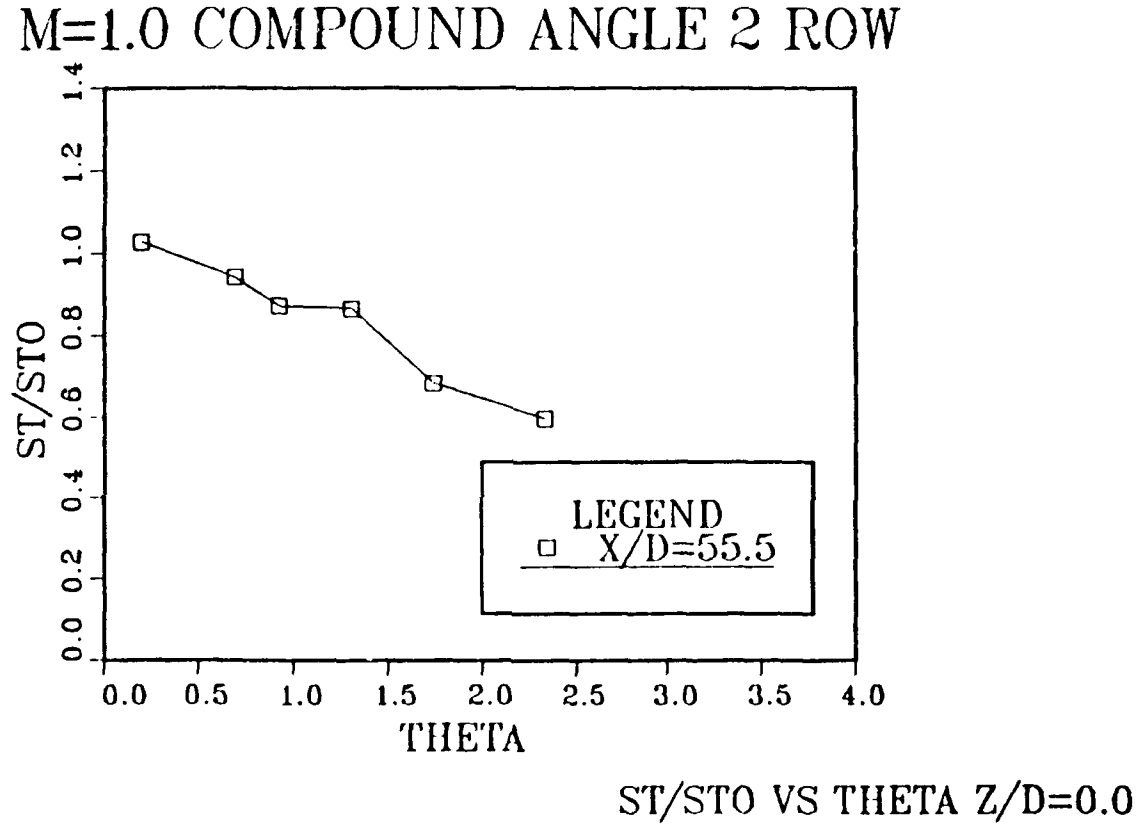


Figure 68. St/Sto Versus θ, Compound Angle, 2 Rows, m=1.0, x/d=55.5, z/d=0.0

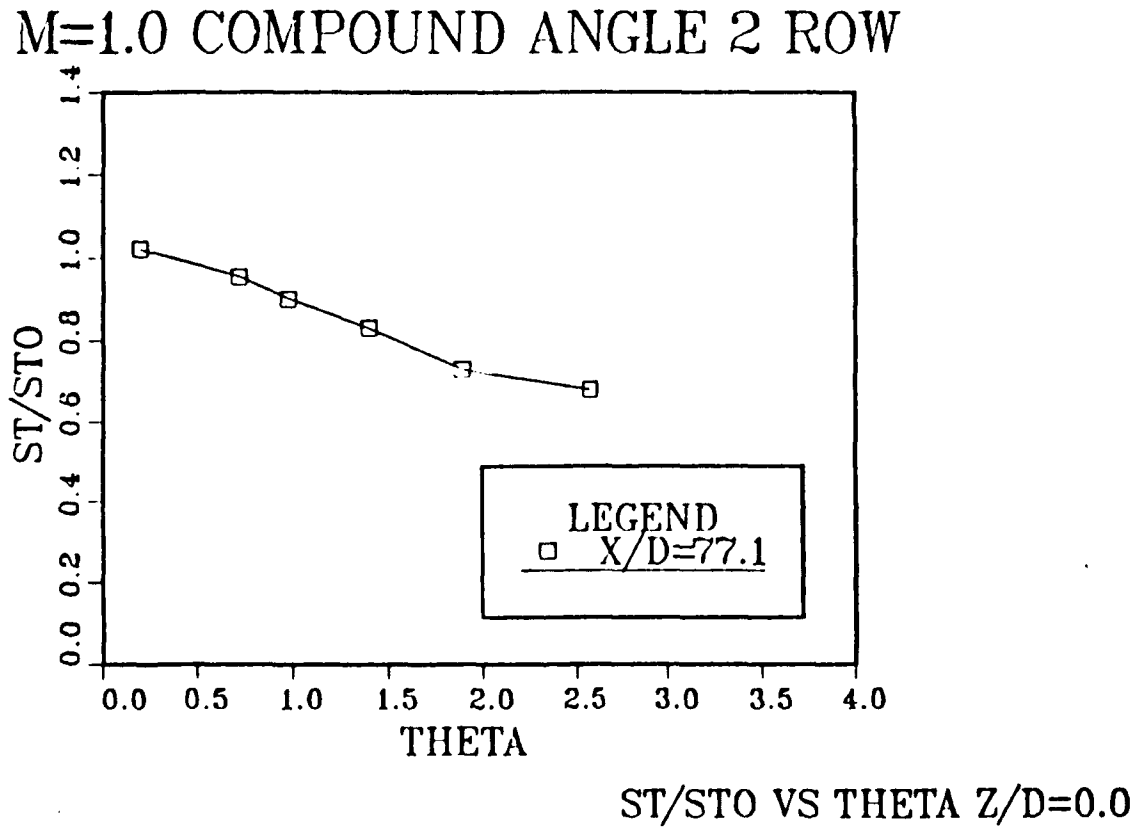


Figure 69. St/Sto Versus θ, Compound Angle, 2 Rows, m=1.0, x/d=77.1, z/d=0.0

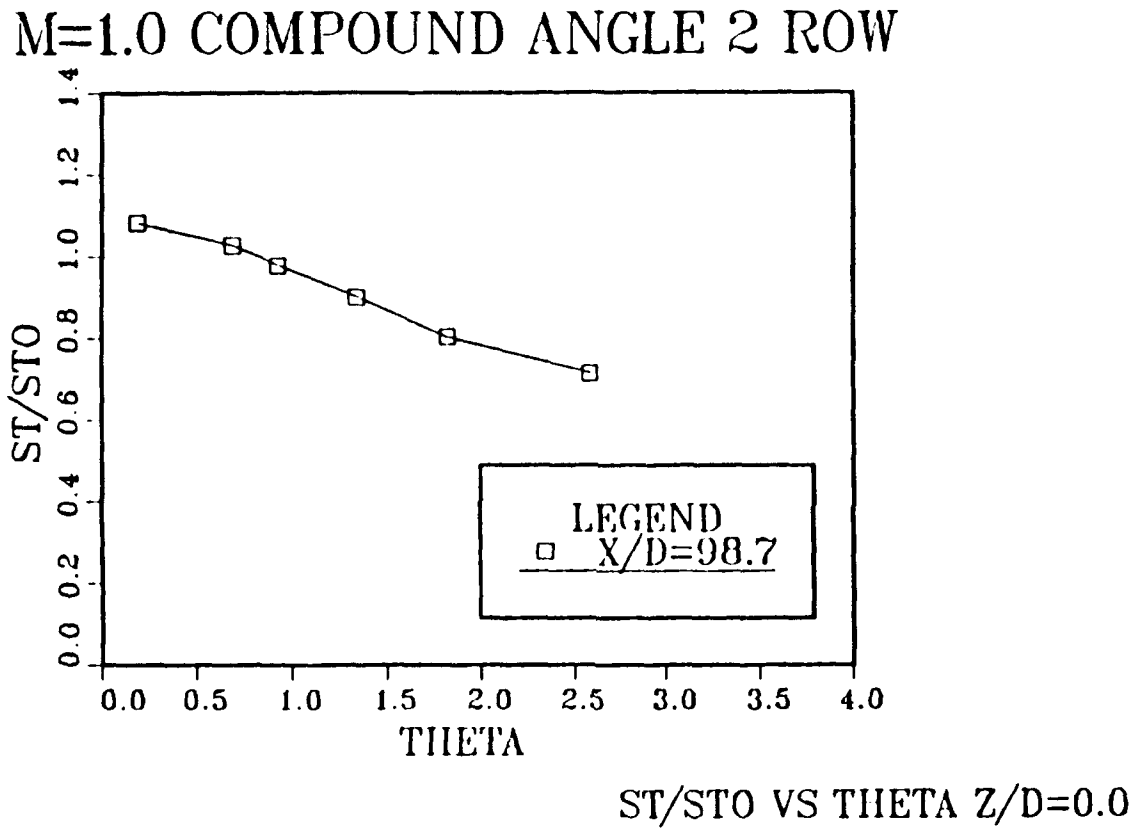


Figure 70. St/Sto Versus θ Compound Angle, 2 Rows, m=1.0, x/d=98.7, z/d=0.0

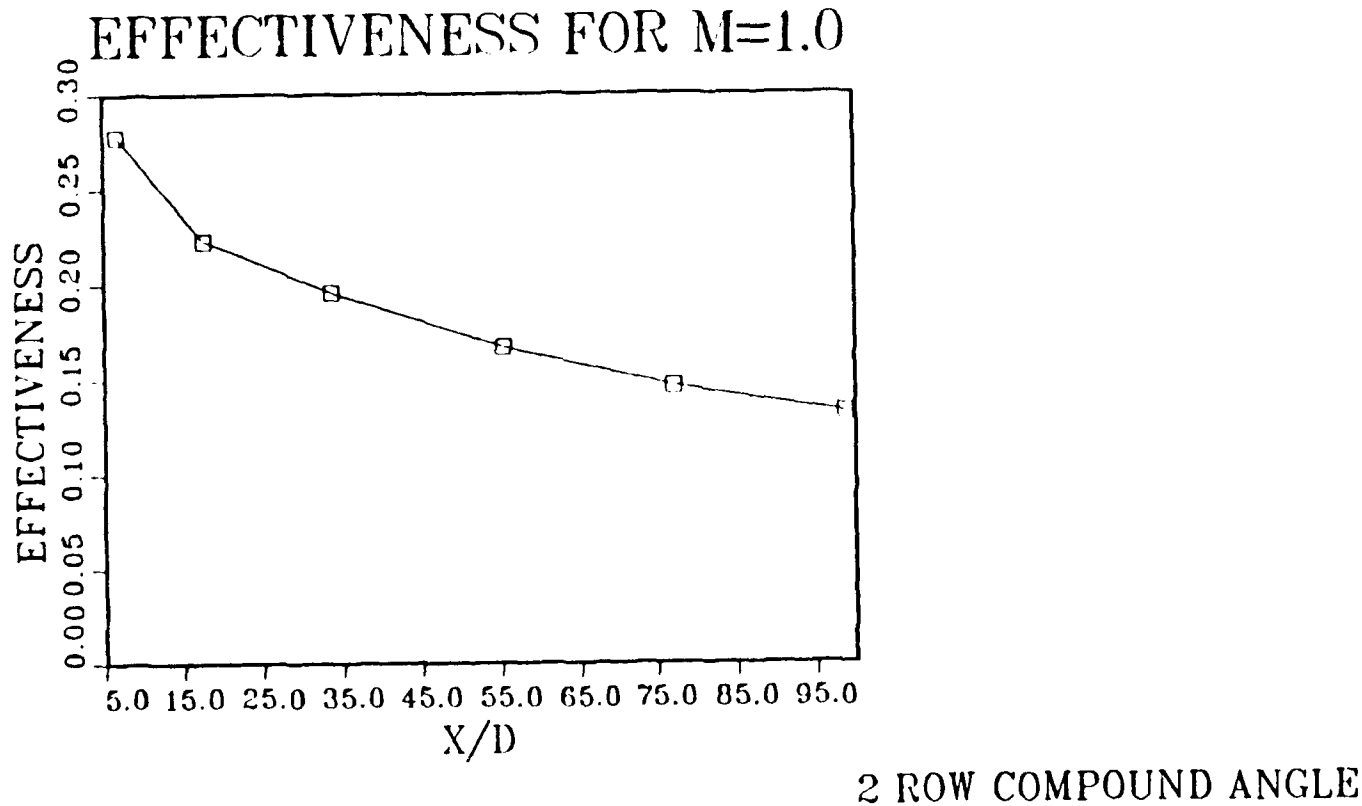


Figure 71. η Versus x/d, Compound Angle, 2 Rows, m=1.0, Spanwise Average

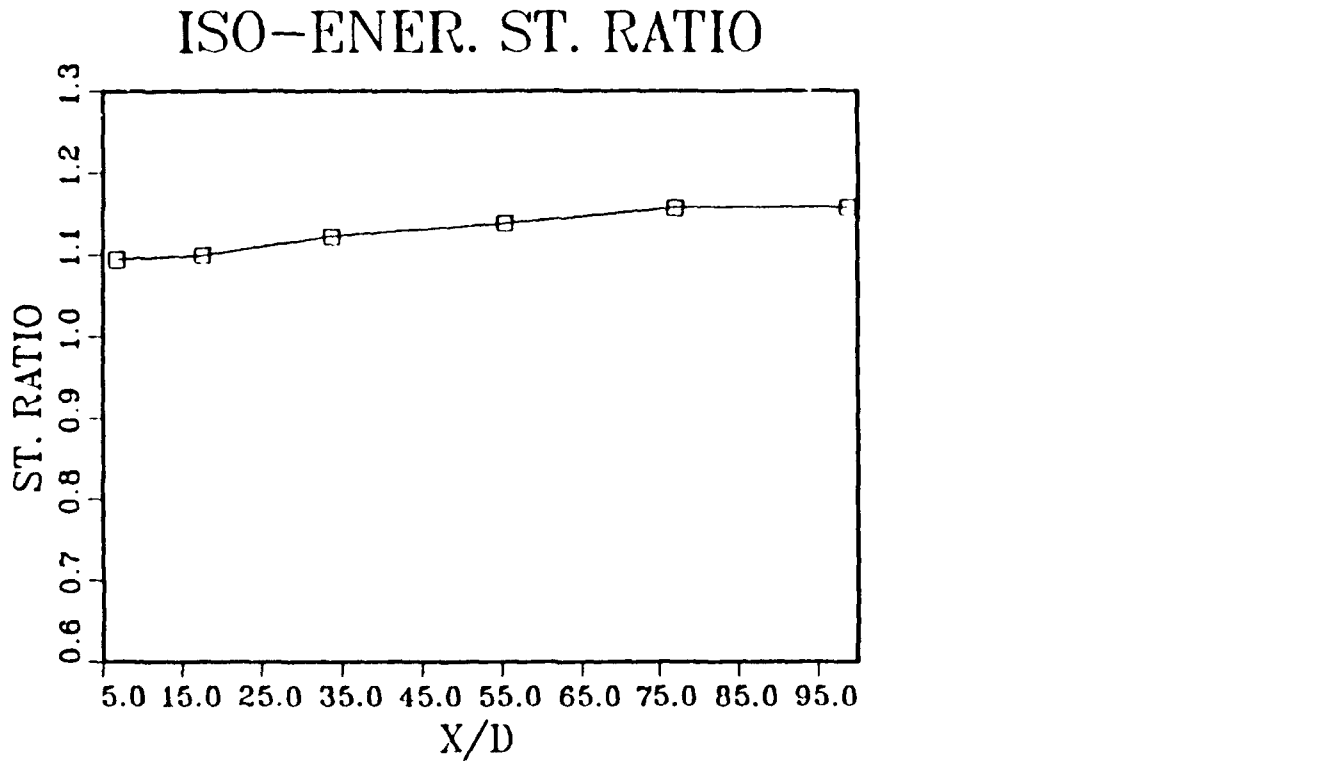


Figure 72. Stf/Sto Versus x/d, Compound Angle, 2 Rows, m=1.0, Spanwise Average

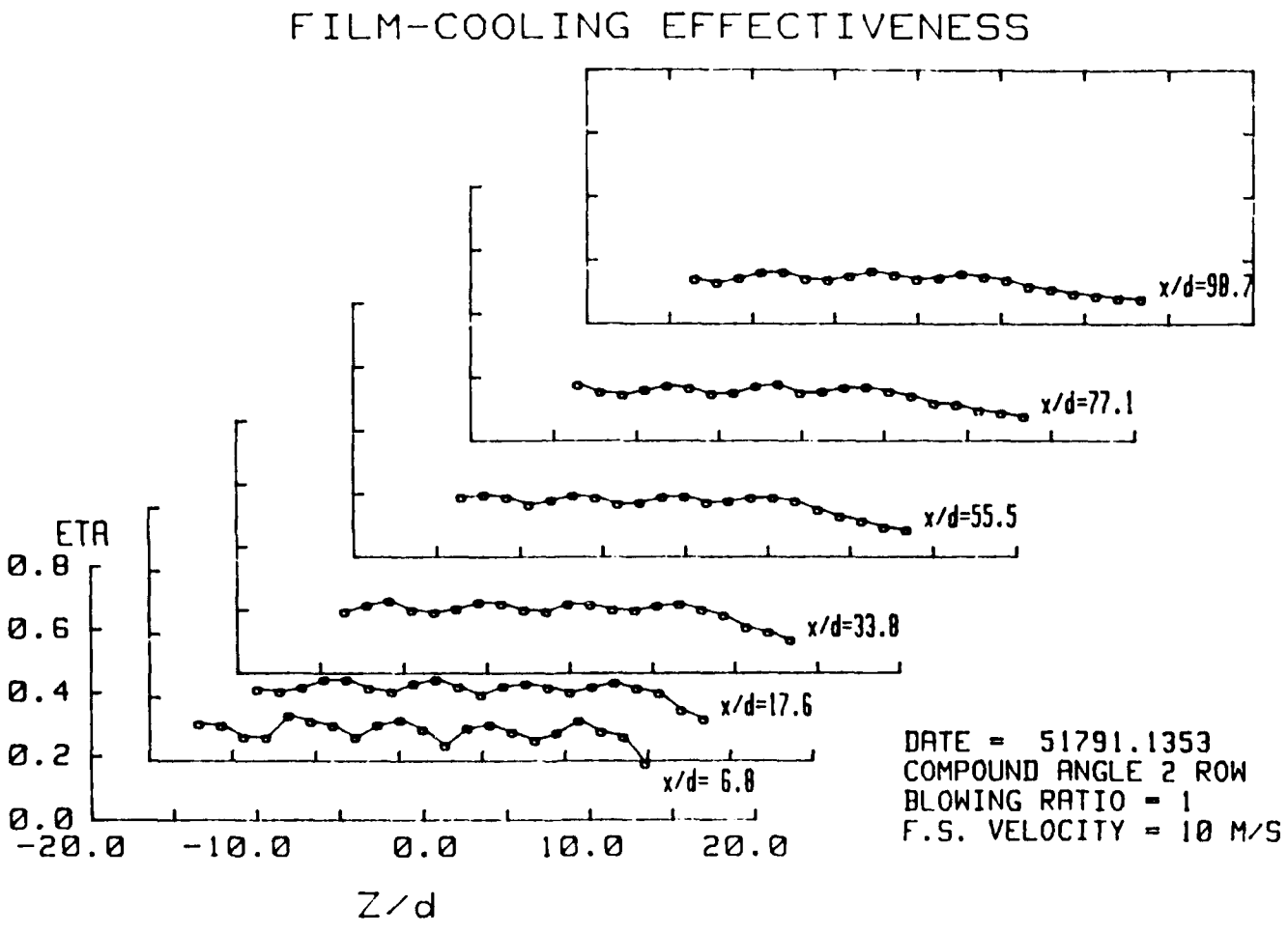


Figure 73. Spanwise Variation of η, Compound Angle, 2 Rows, m=1.0

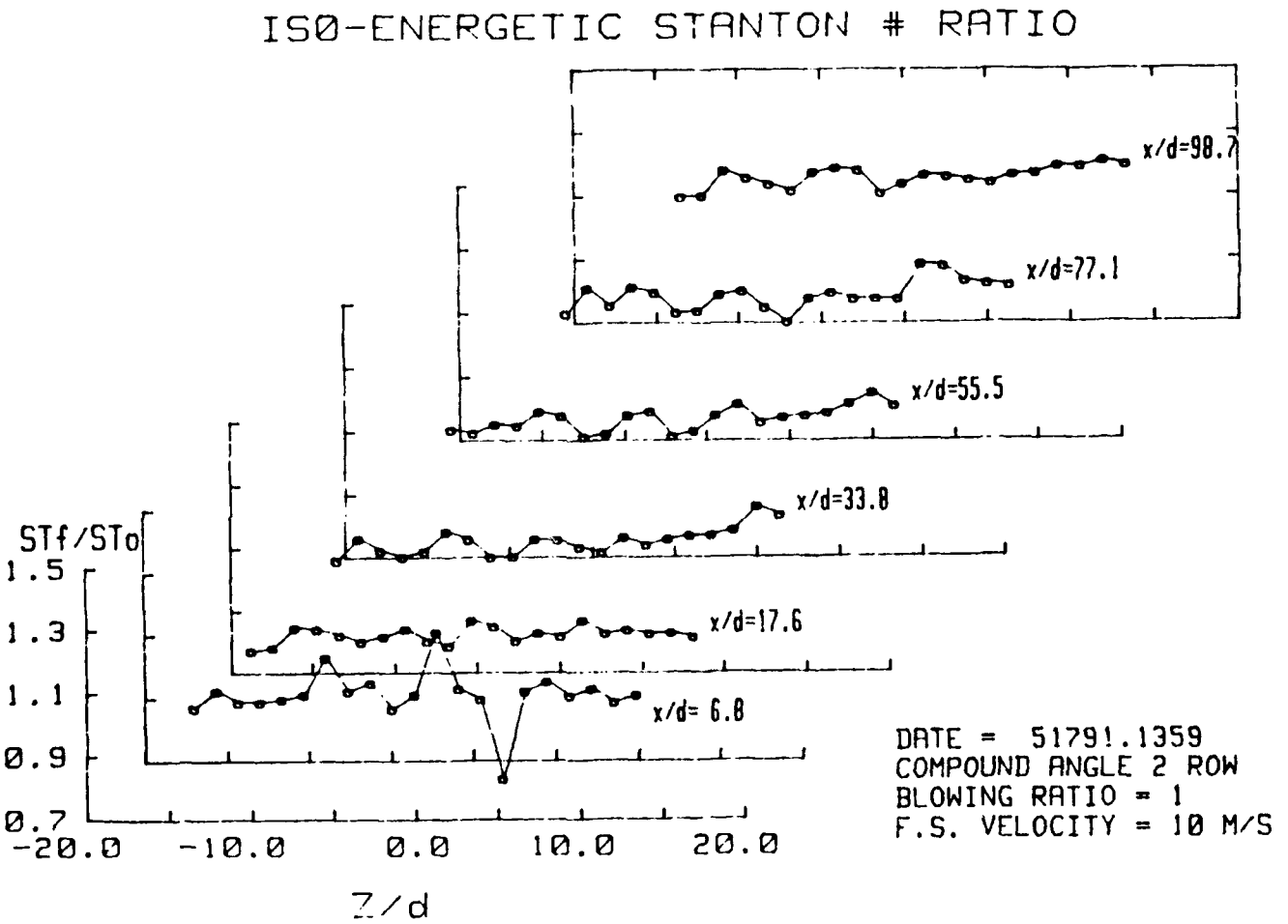


Figure 74. Spanwise Variation of Stf/Sto, Compound Angle, 2 Rows, m=1.0

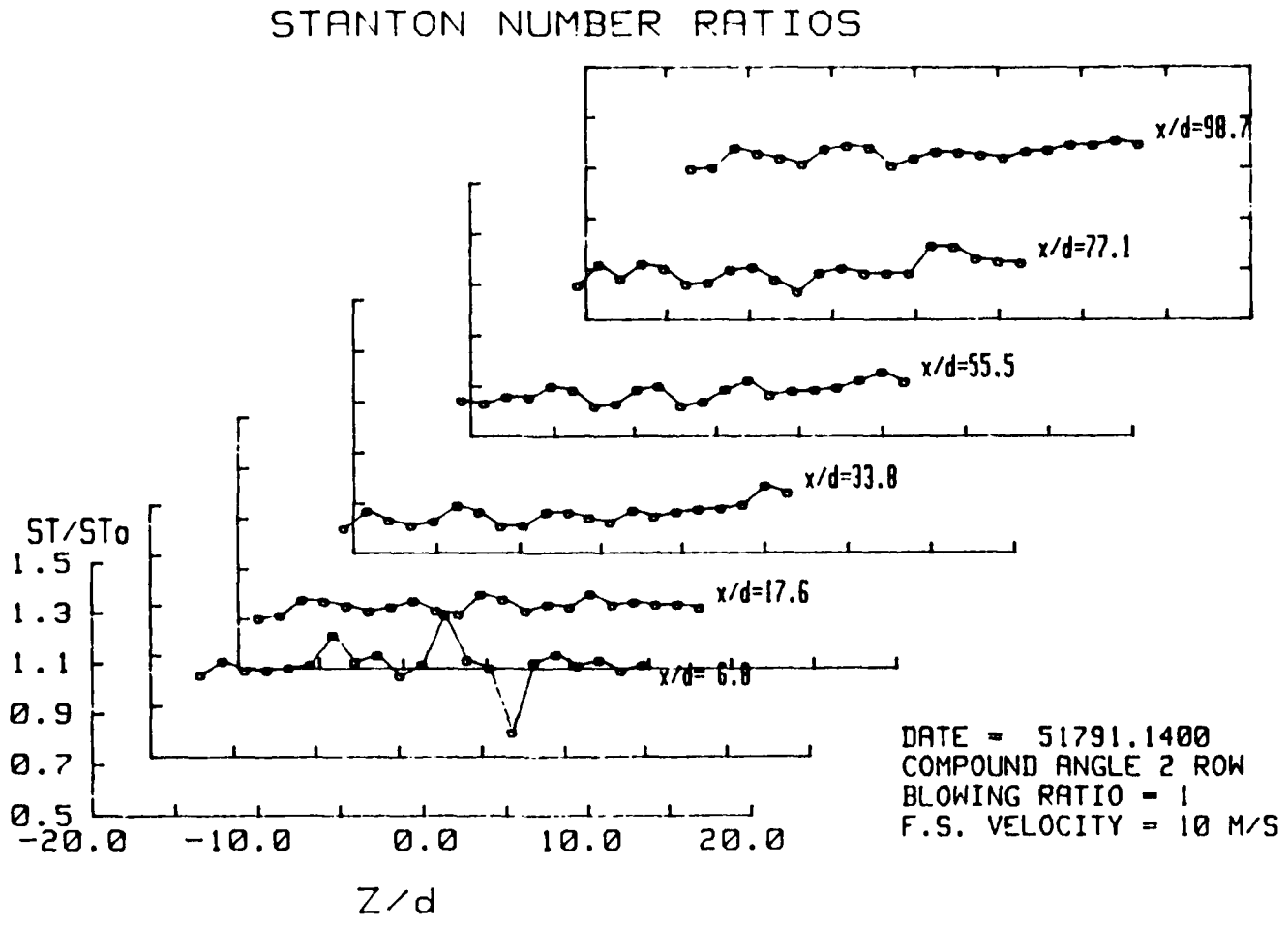


Figure 75. Spanwise Variation of St/Sto, Compound Angle, 2 Rows, m=1.00, θ=1.72

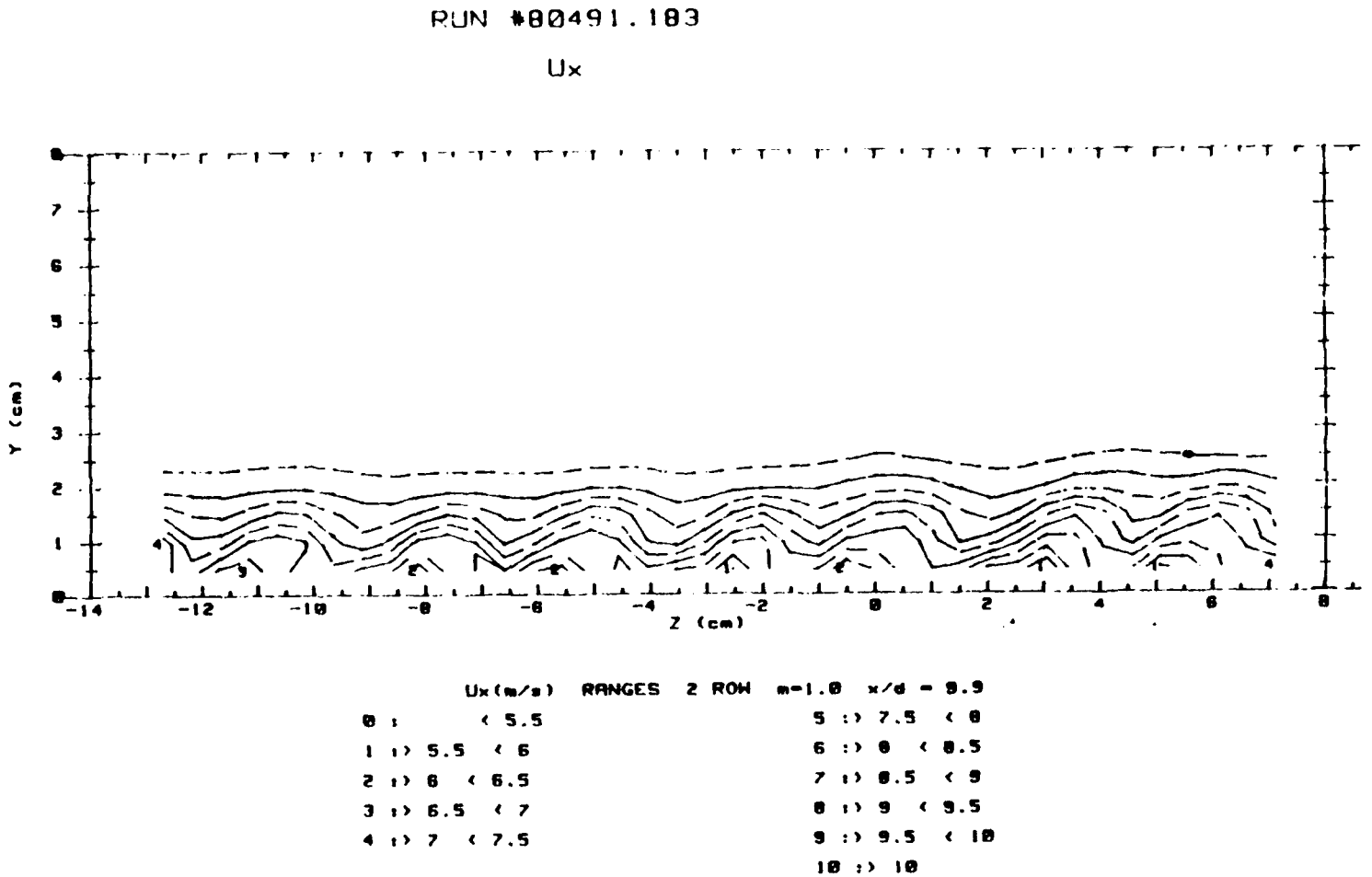


Figure 76. Streamwise Velocity Field, Compound Angle, 2 Rows, m=1.0, x/d=9.9

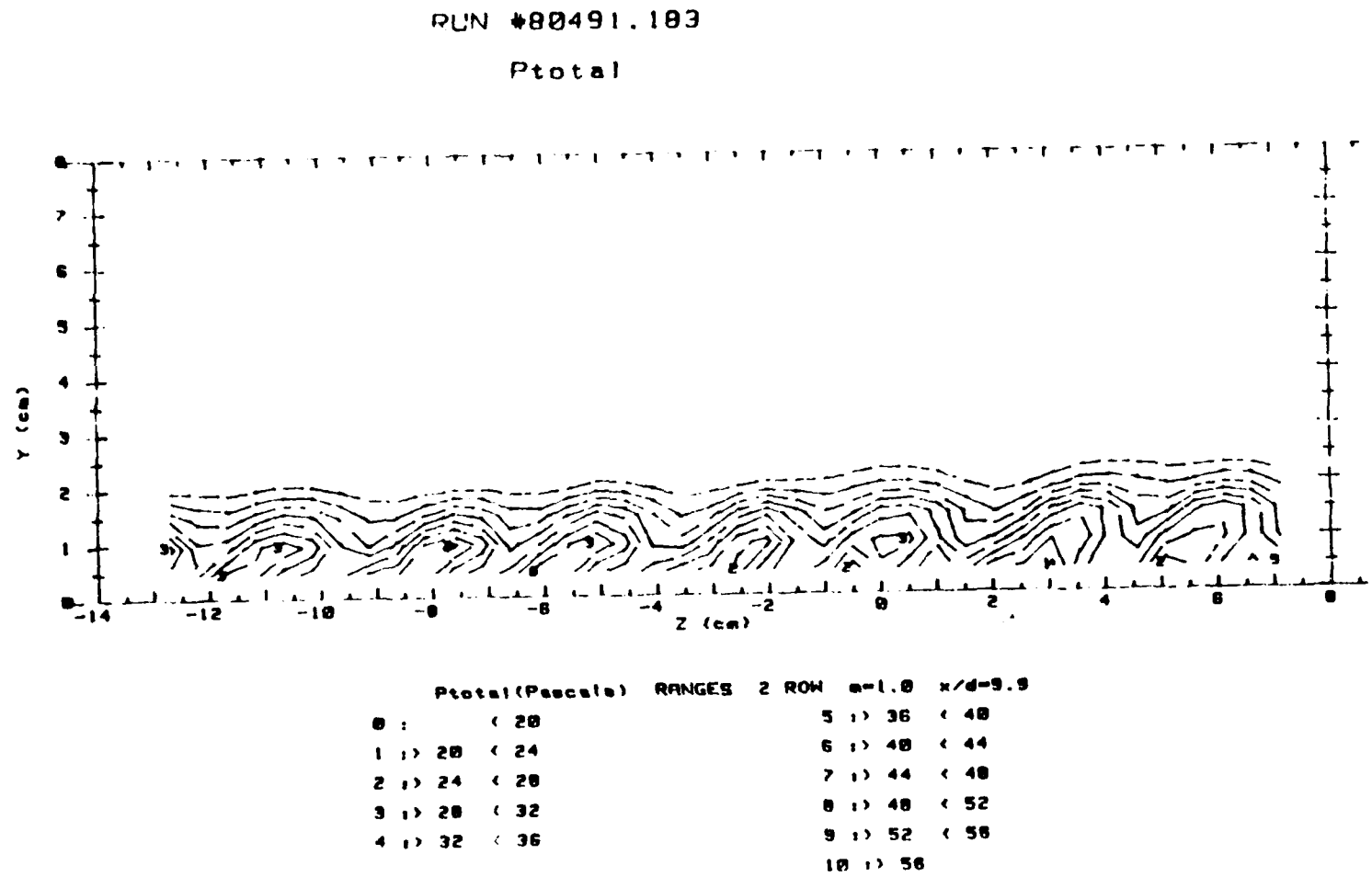


Figure 77. Streamwise Pressure Field, Compound Angle, 2 Rows, m=1.0, x/d=9.9

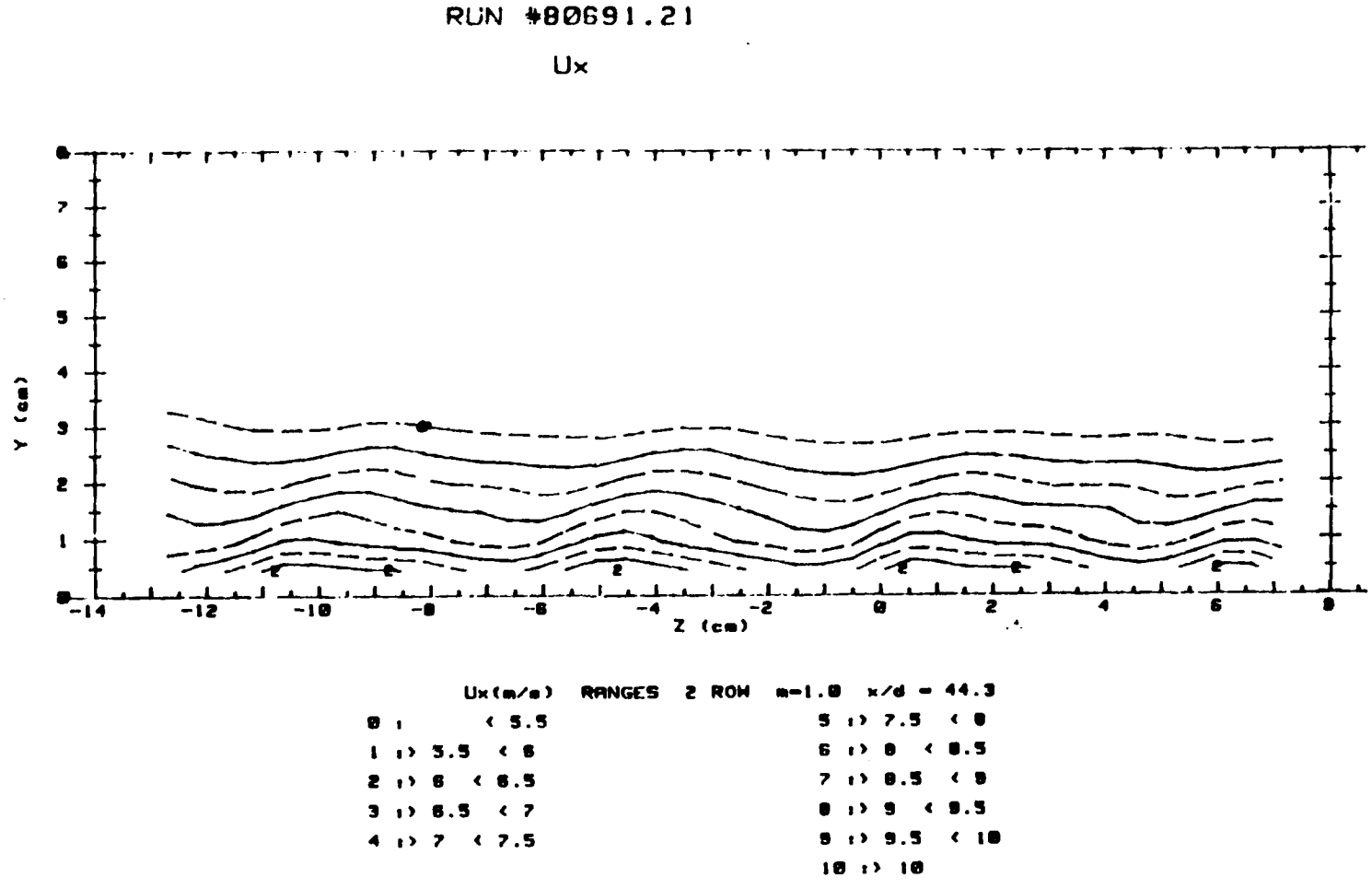


Figure 78. Streamwise Velocity Field, Compound Angle, 2 Rows, m=1.0, x/d=44.3

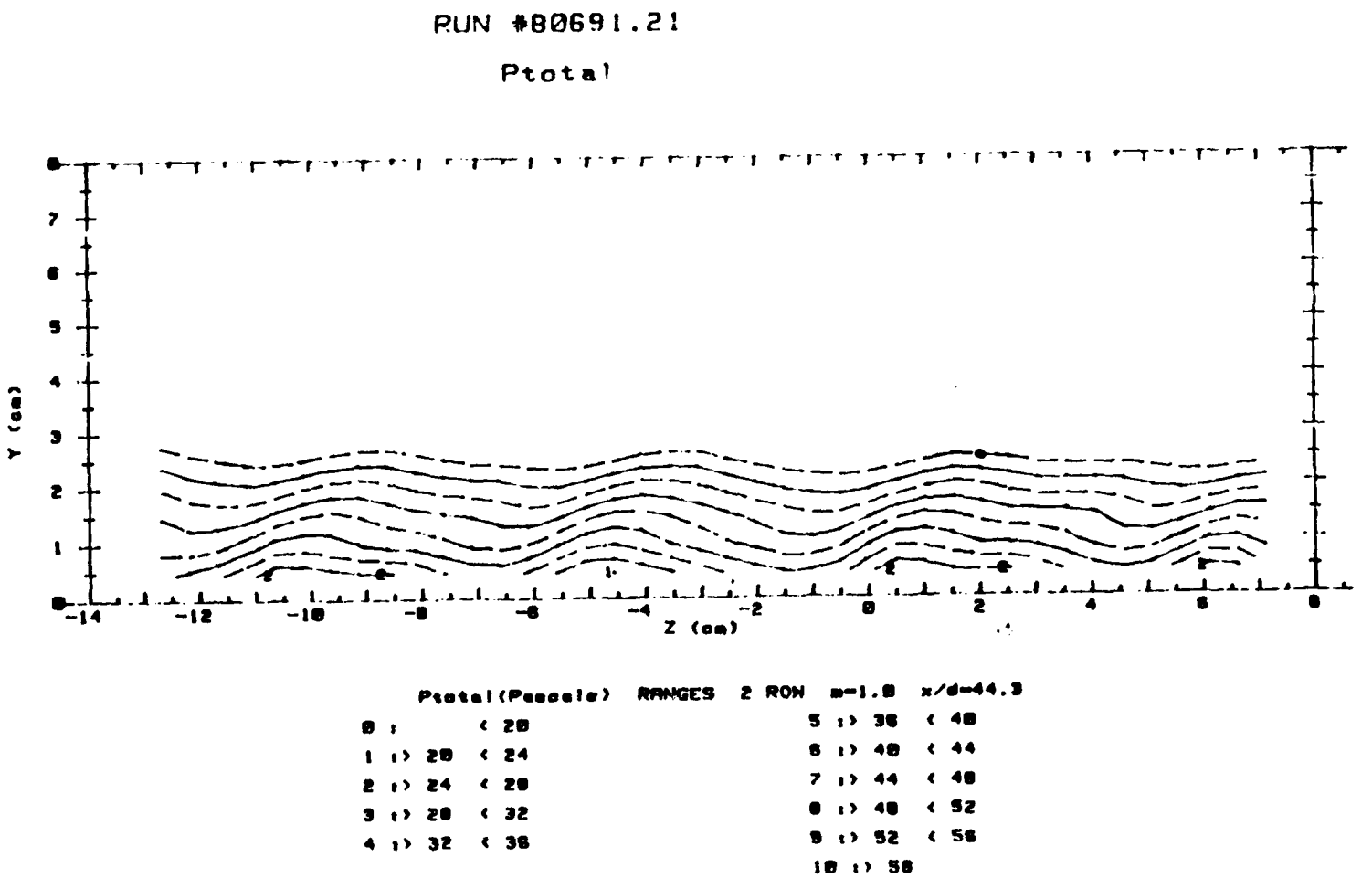


Figure 79. Streamwise Pressure Field, Compound Angle, 2 Rows, m=1.0, x/d=44.3

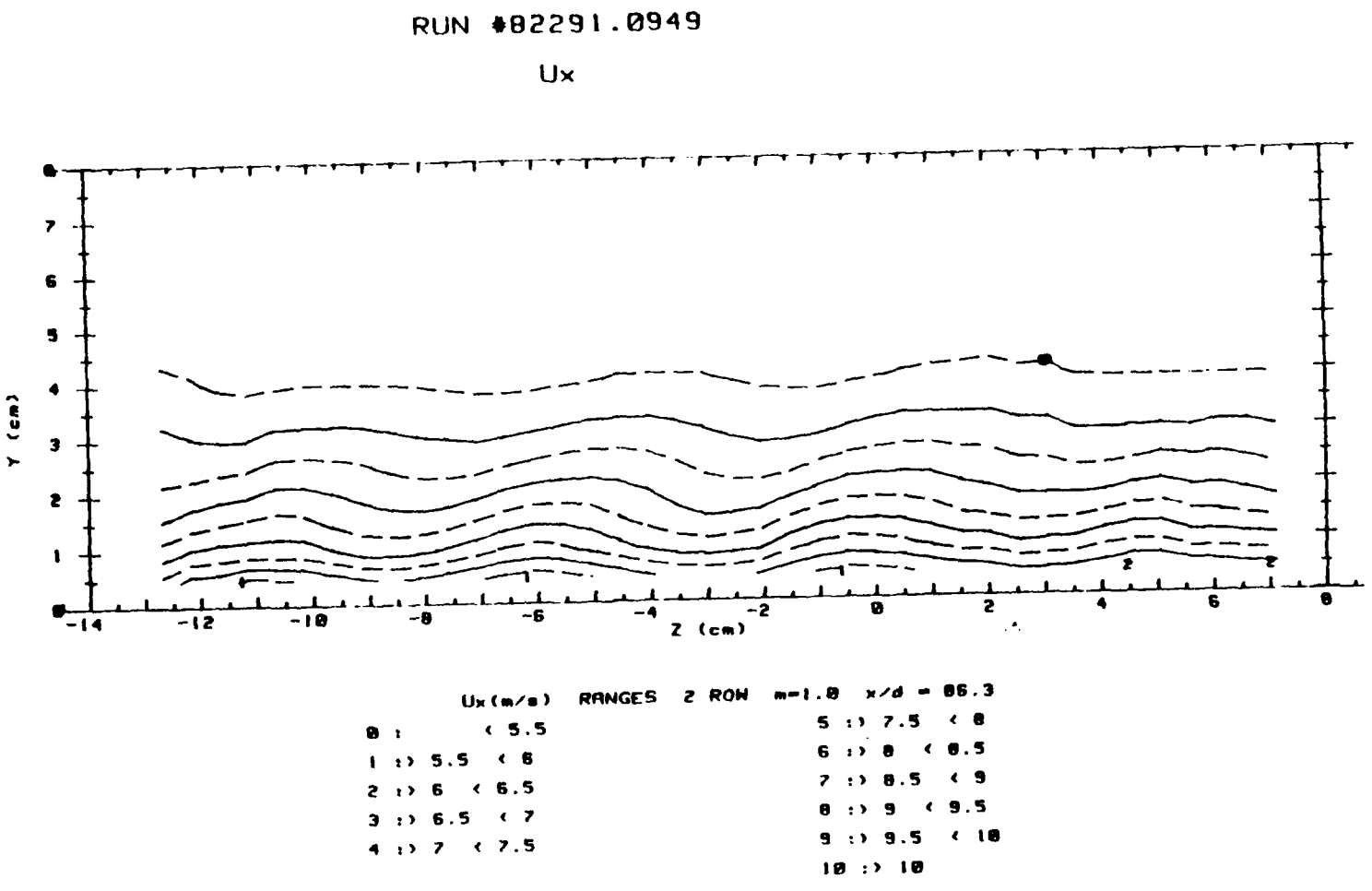


Figure 80. Streamwise Velocity Field, Compound Angle, 2 Rows, m=1.0, x/d=86.3

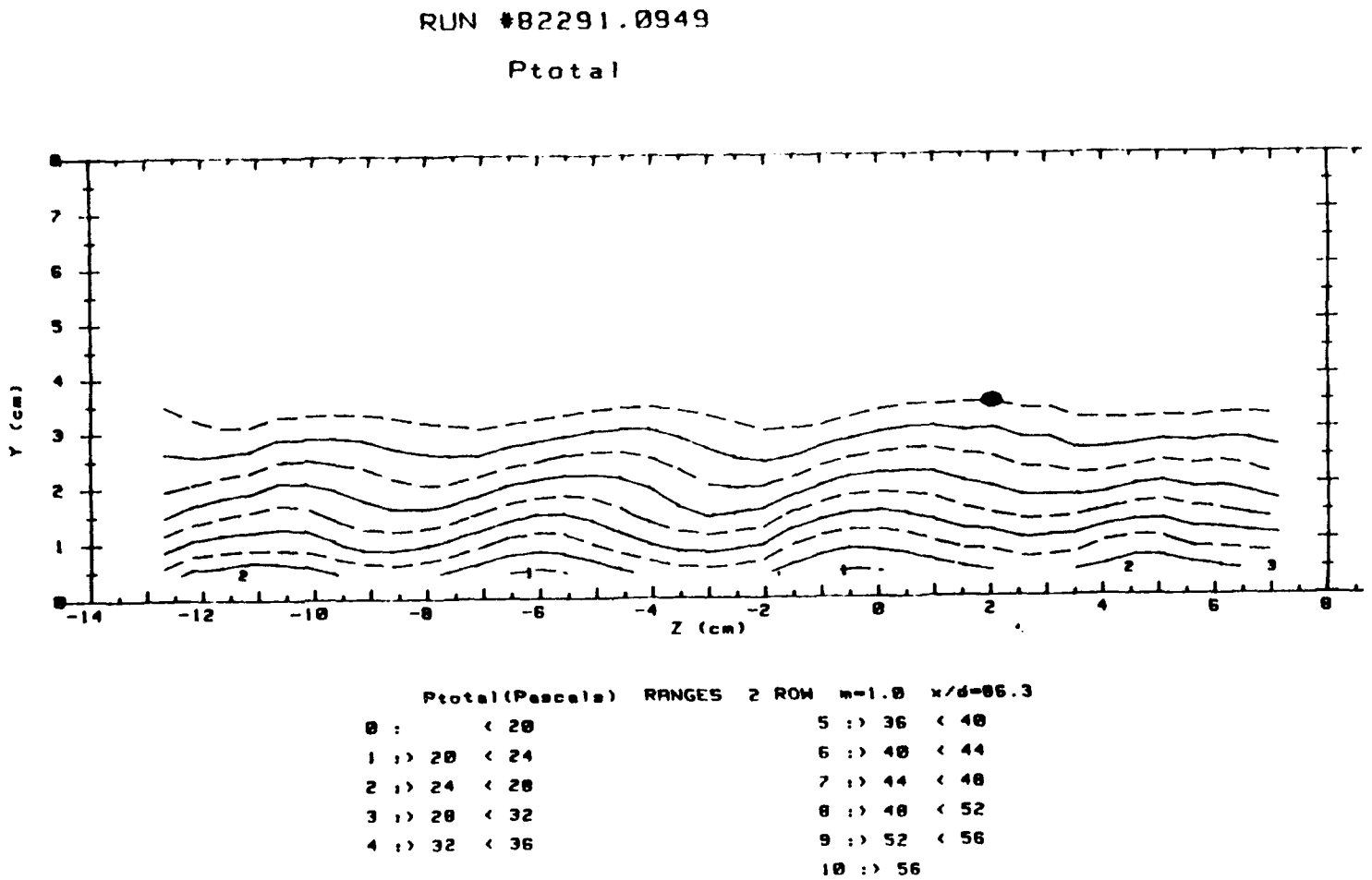


Figure 81. Streamwise Pressure Field, Compound Angle, 2 Rows, m=1.0, x/d=86.3

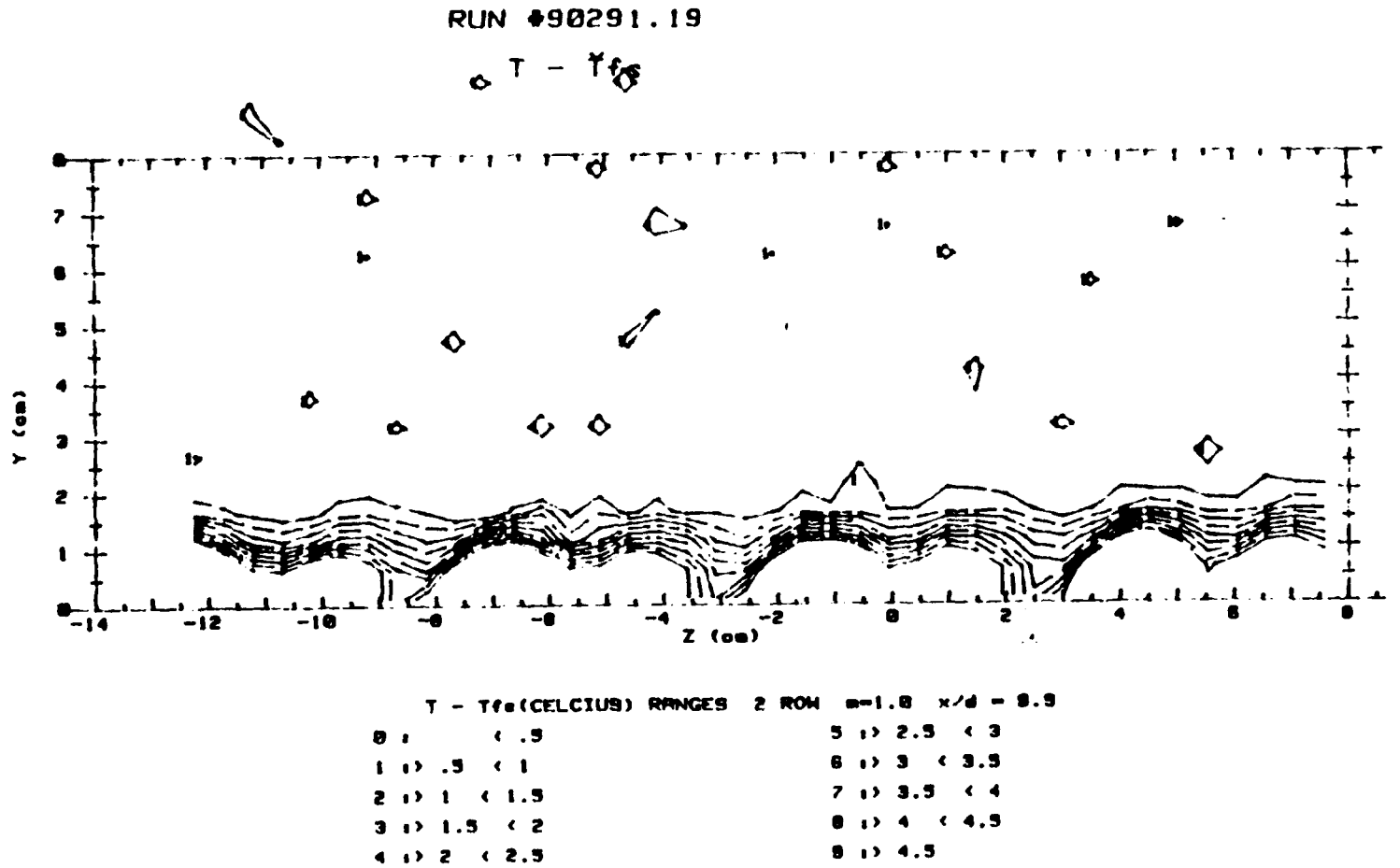


Figure 82. Streamwise Injectant Distribution, Compound Angle, 2 Rows, m=1.0, x/d=9.9

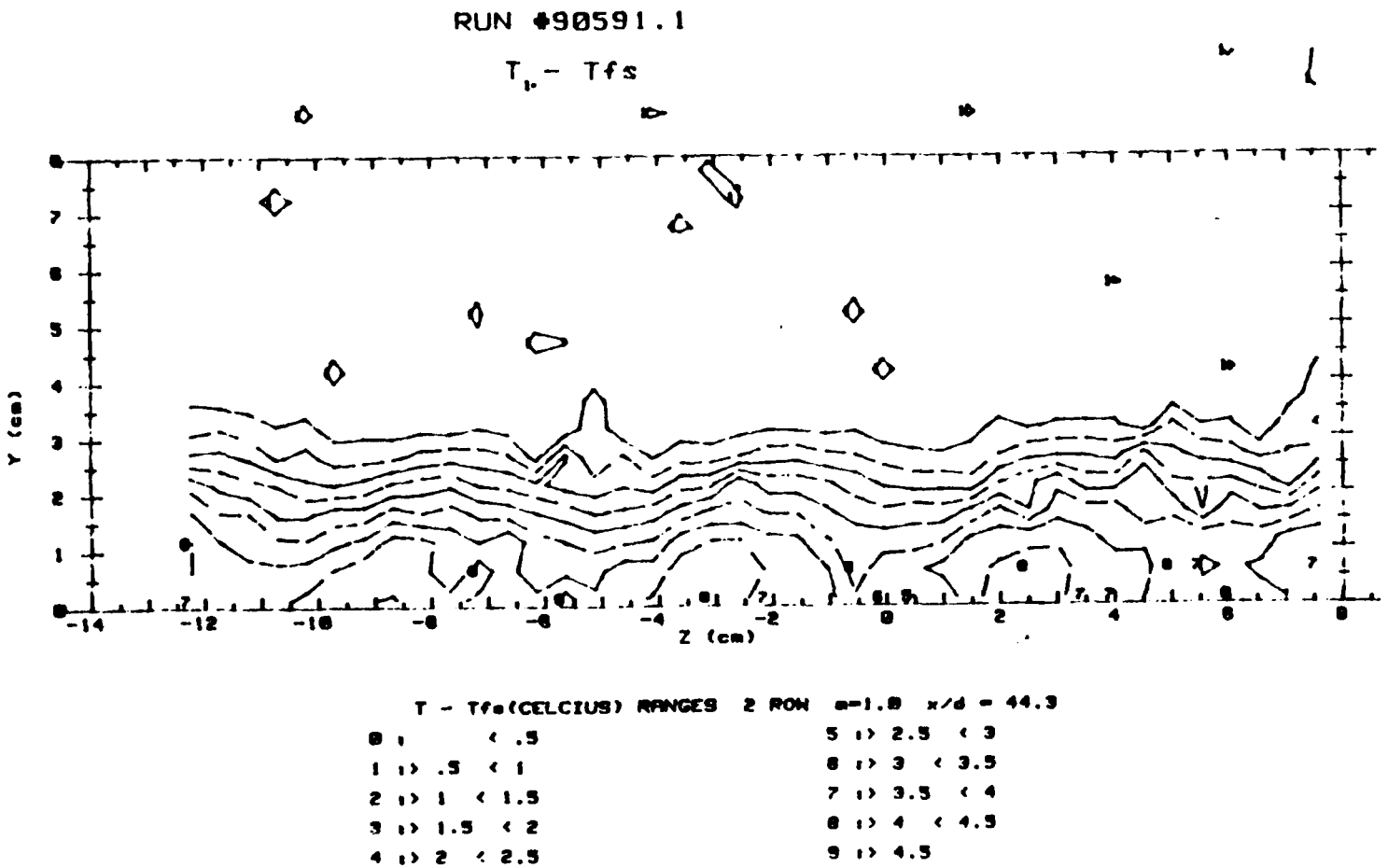


Figure 83. Streamwise Injectant Distribution, Compound Angle, 2 Rows, m=1.0, x/d=44.3

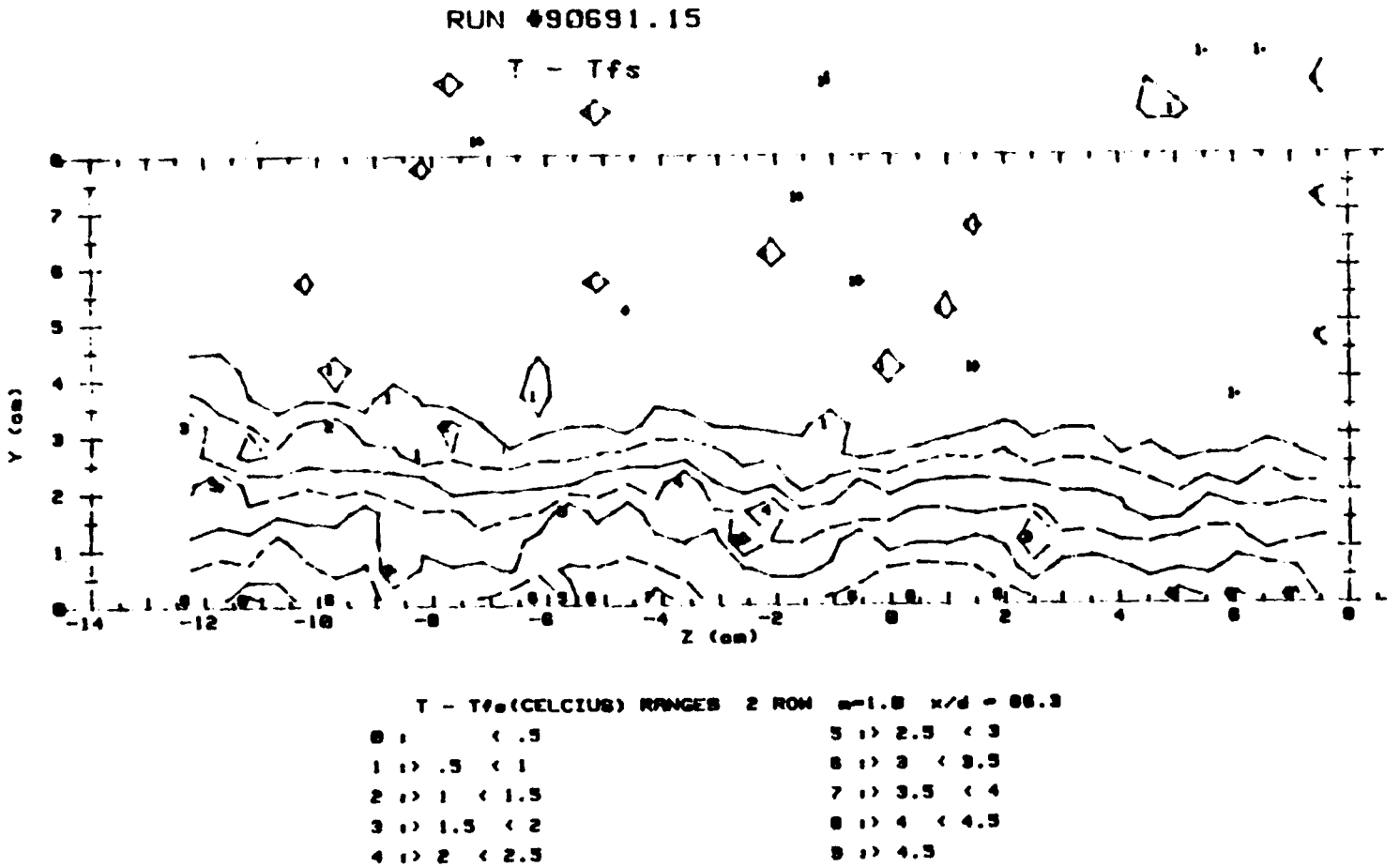


Figure 84. Streamwise Injectant Distribution, Compound Angle, 2 Rows, m=1.0, x/d=86.3

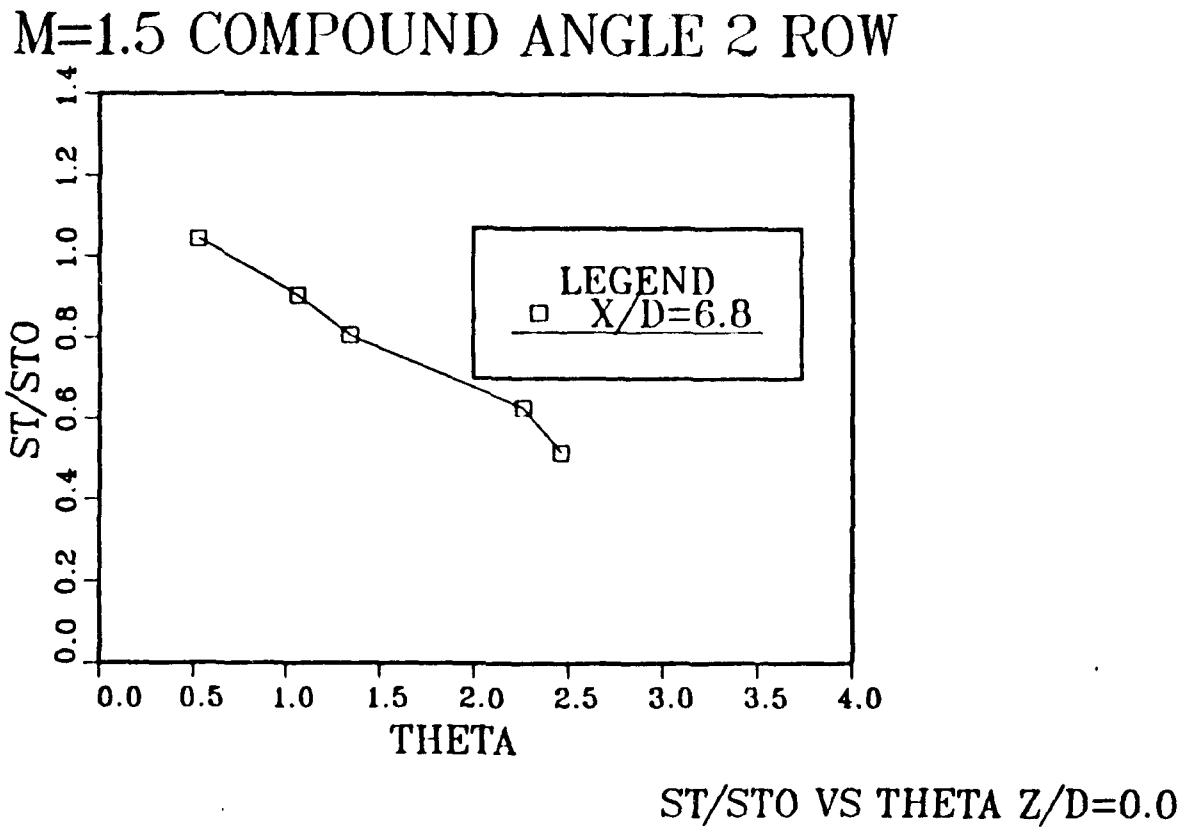


Figure 85. St/Sto Versus θ, Compound Angle, 2 Rows, m=1.5, x/d=6.8, z/d=0.0

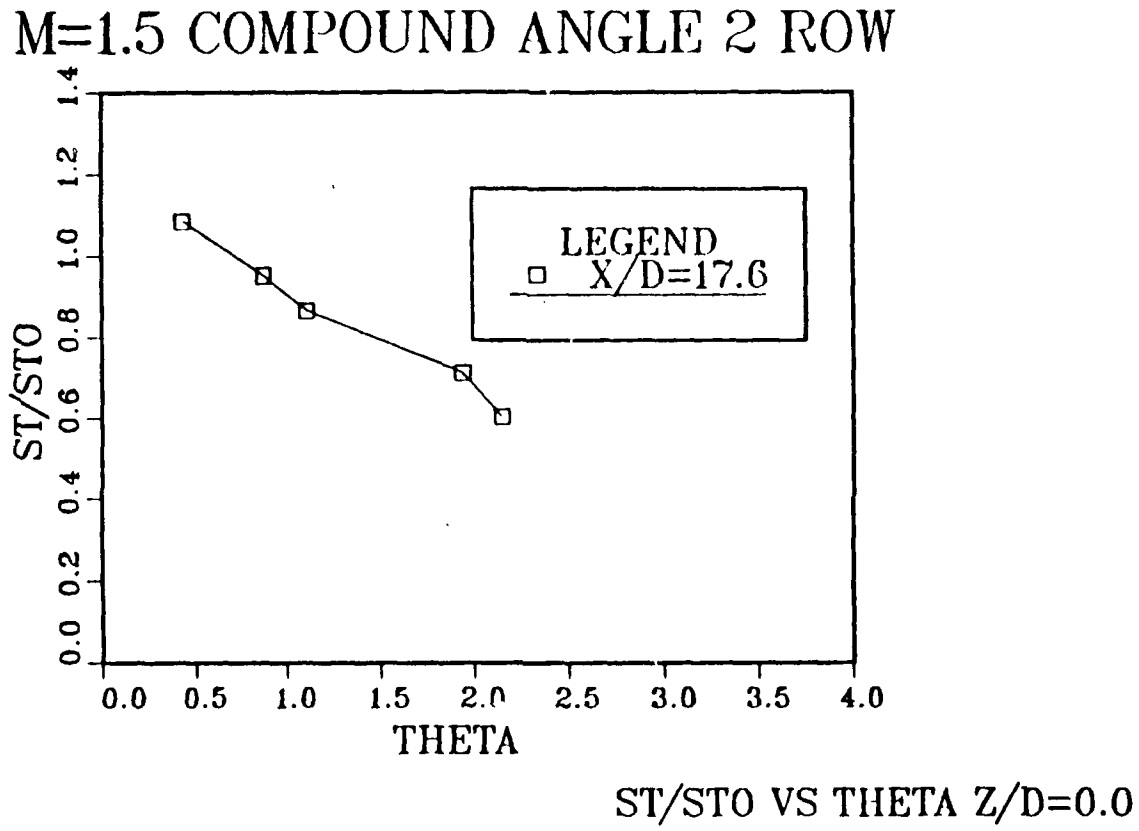


Figure 86. St/Sto Versus θ Compound Angle, 2 Rows, m=1.5, x/d=17.6, z/d=0/0

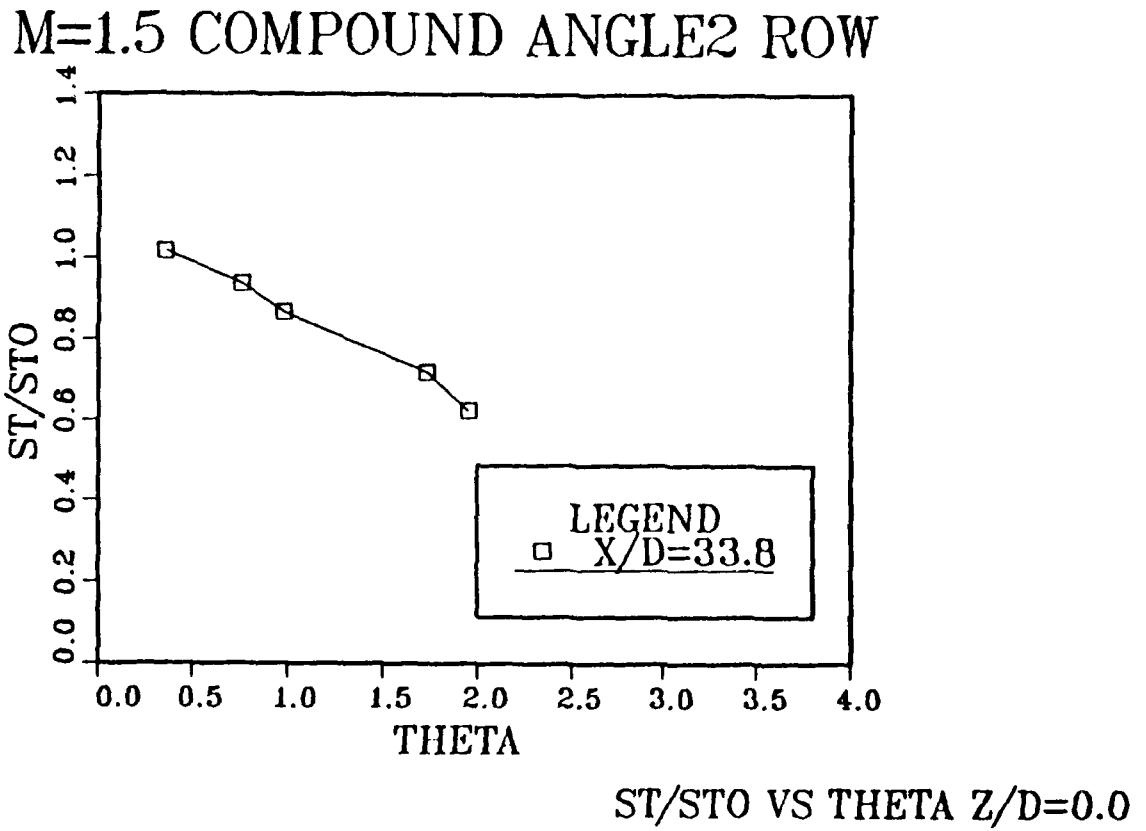


Figure 87. St/Sto Versus θ, Compound Angle, 2 Rows, m=1.5, x/d=33.8, z/d=0.0

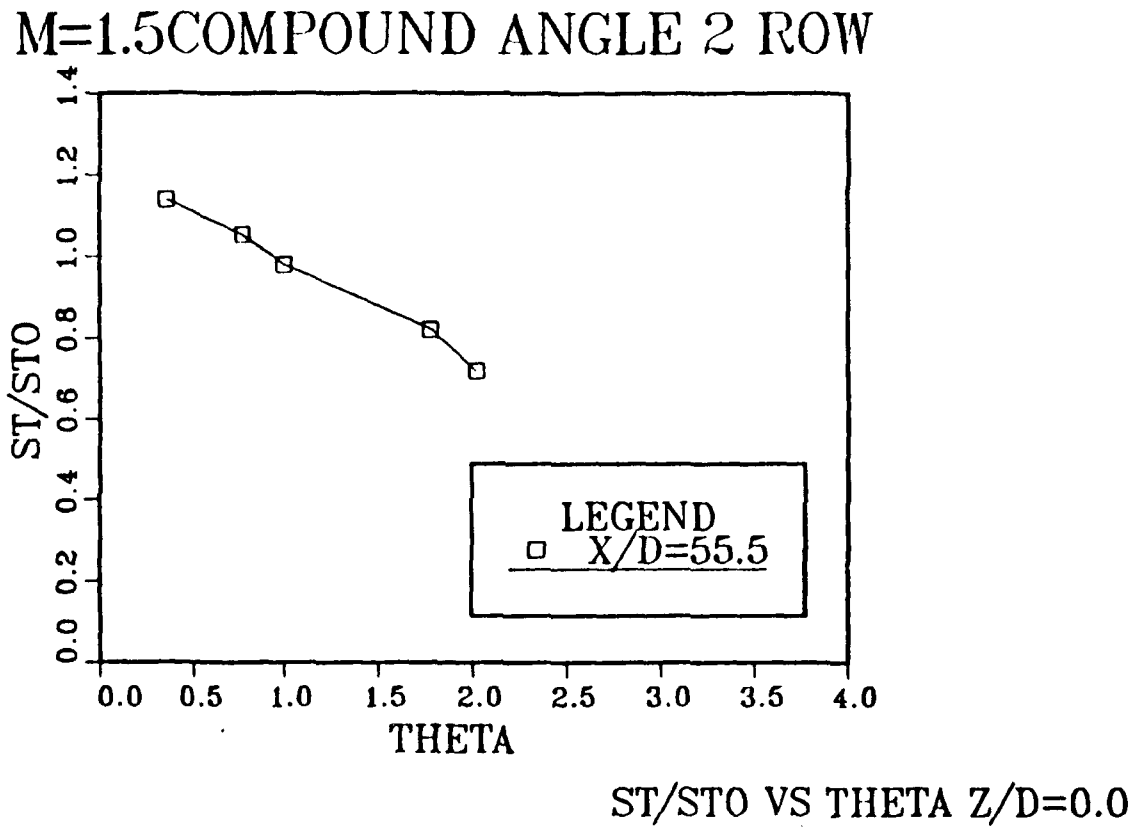


Figure 88. St/Sto Versus θ, Compound Angle, 2 Rows, m=1.5, x/d=55.5, z/d=0.0

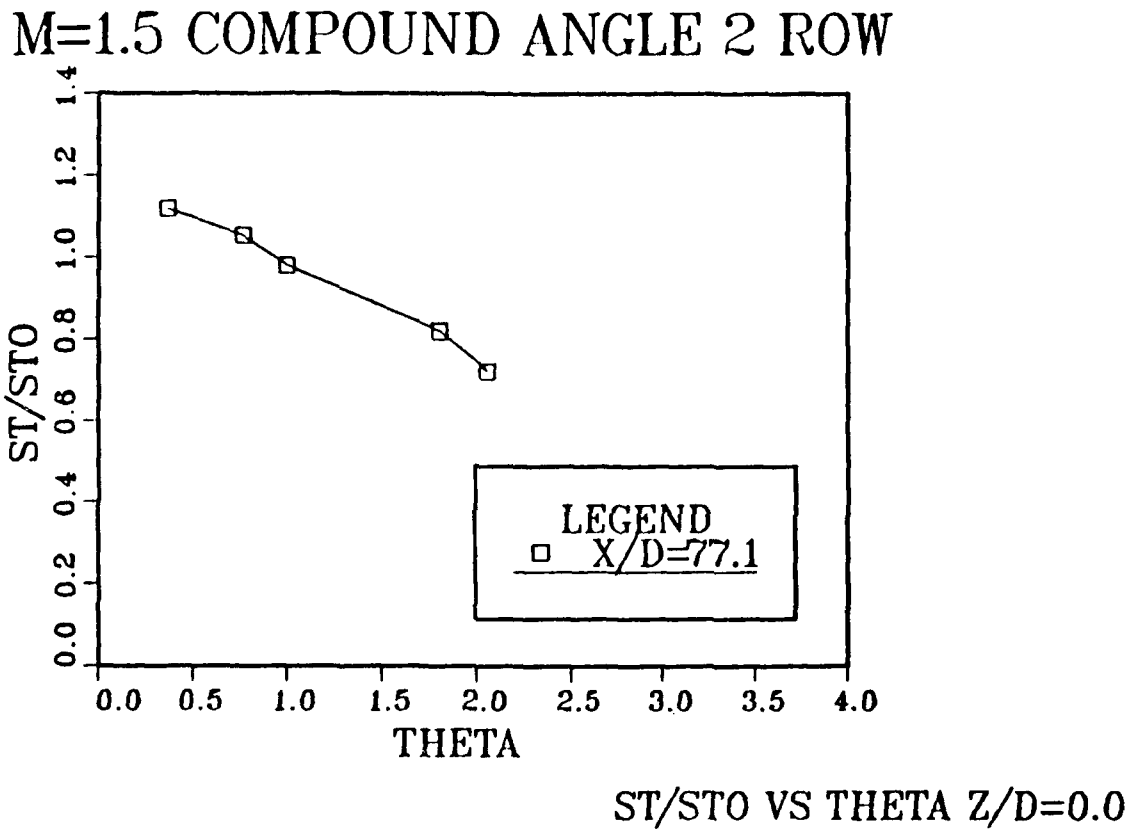


Figure 89. St/Sto Versus θ, Compound Angle, 2 Rows, m=1.5, x/d=77.1, z/d=0.0

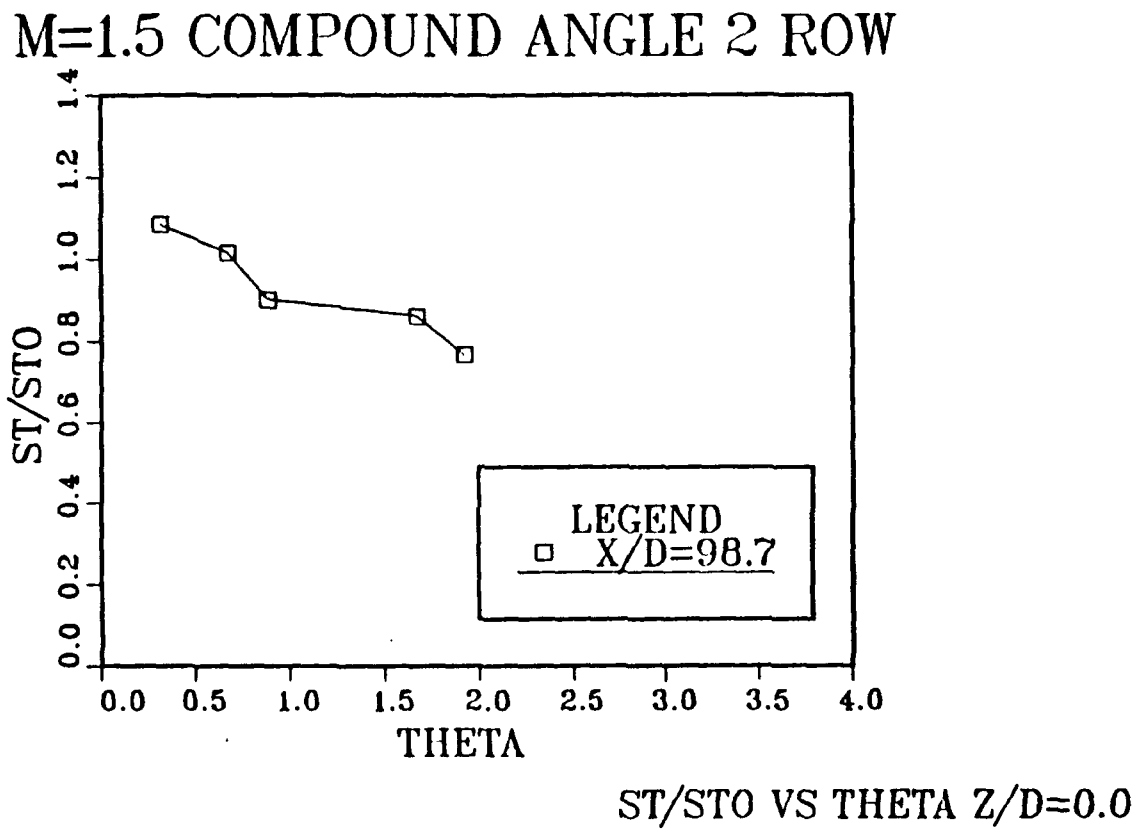


Figure 90. St/Sto Versus θ, Compound Angle, 2 Rows, m=1.5, x/d=98.7, z/d=0.0

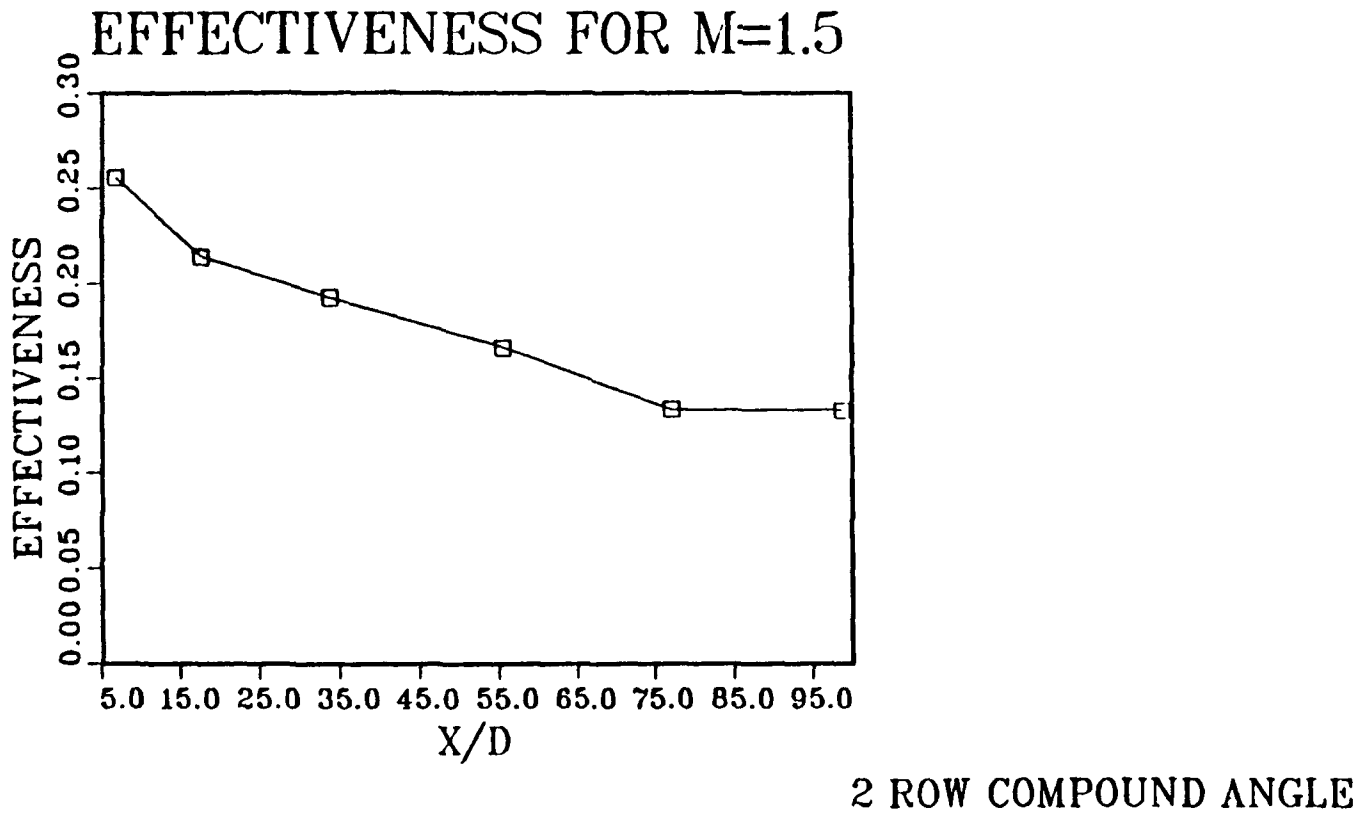


Figure 91. η **Versus x/d, Compound Angle, 2 Rows, m=1.5, Spanwise Average**

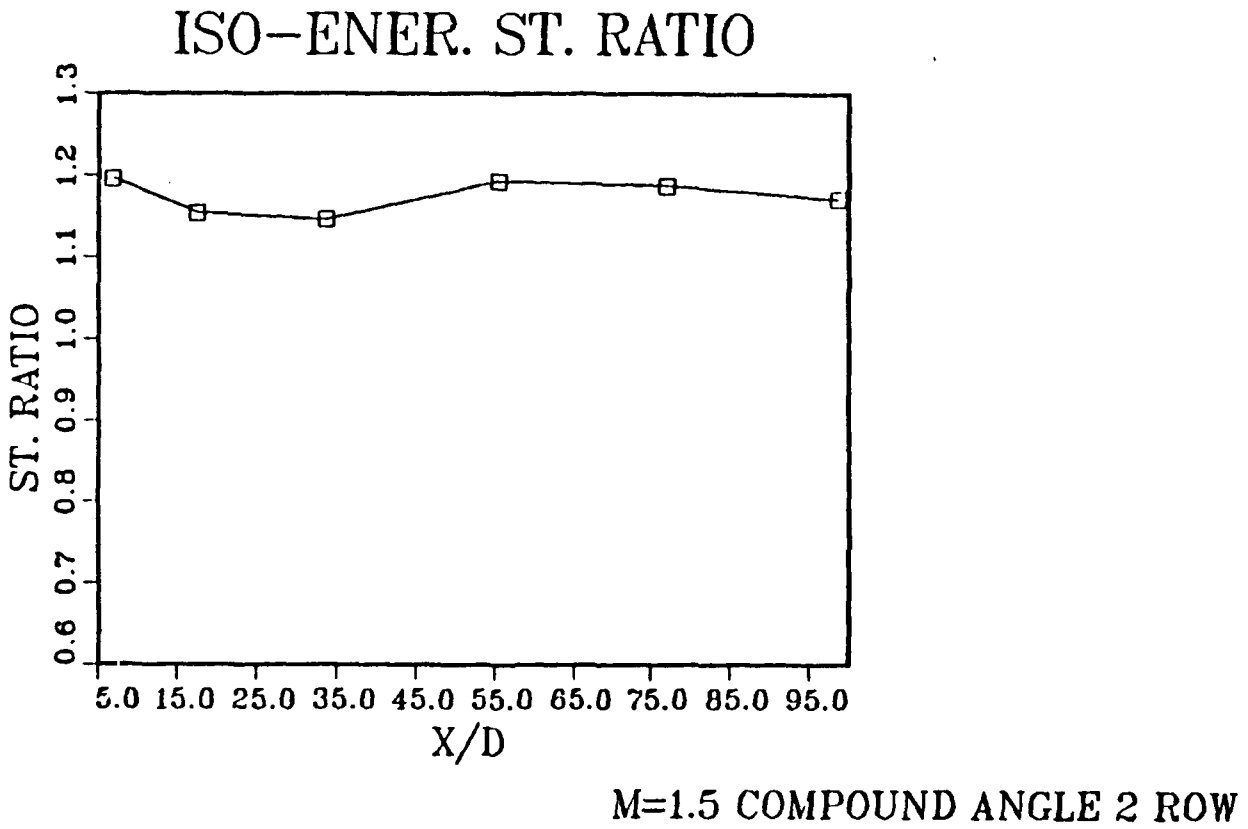


Figure 92. Stf/Sto Versus x/d, Compound Angle, 2 Rows, m=1.5, Spanwise Average

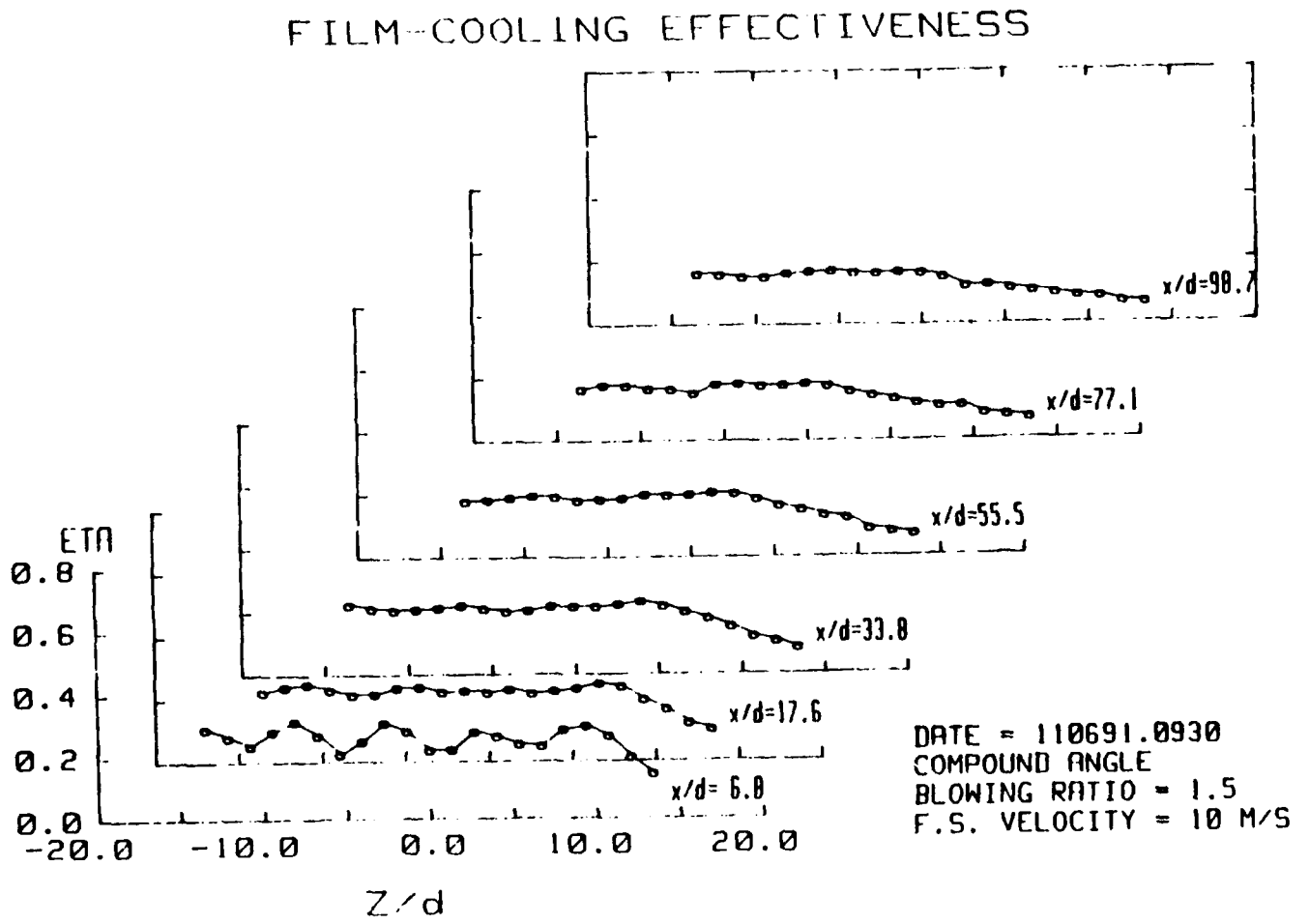


Figure 93. Spanwise Variation of η, Compound Angle, 2 Rows, m=1.5

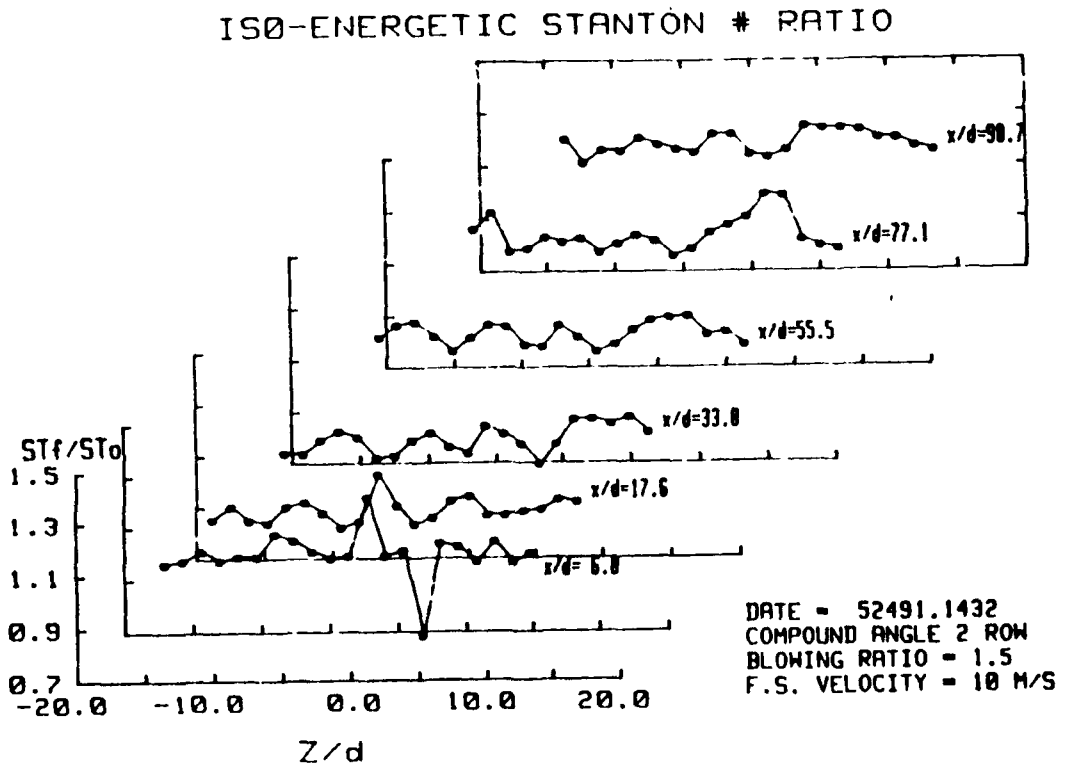


Figure 94. Spanwise Variation of Stf/Sto, Compound Angle, 2 Rows, m=1.5

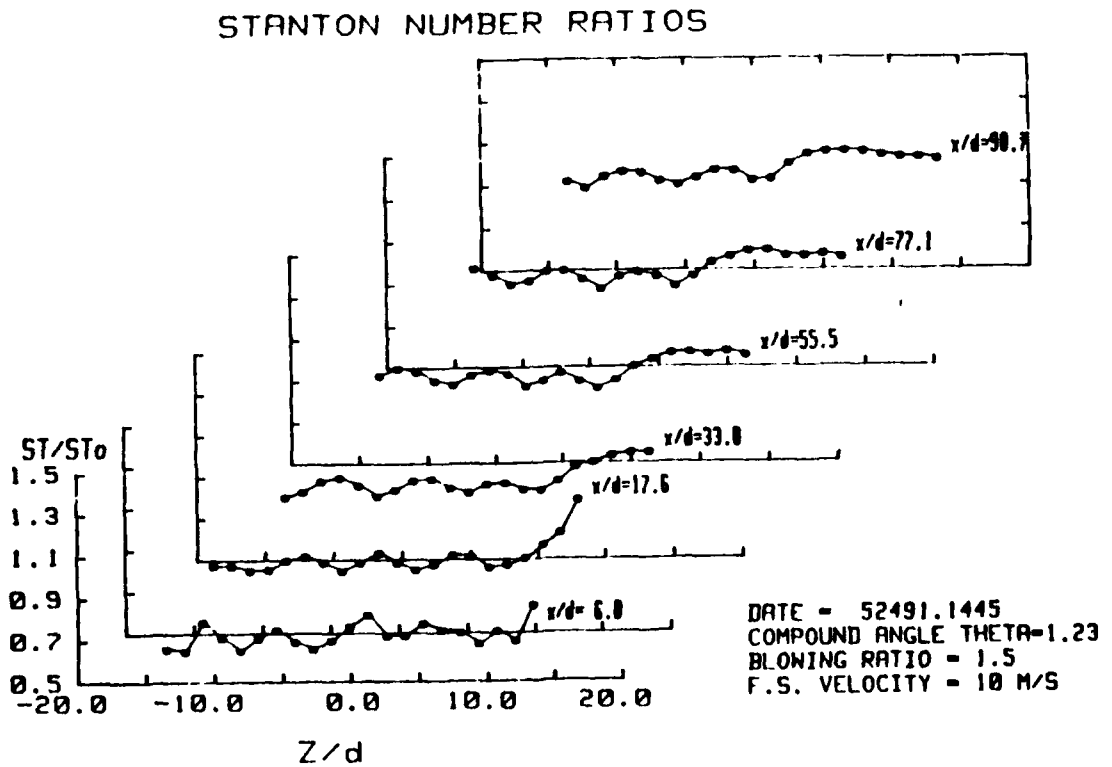


Figure 95. Spanwise Variation of St/Sto, Compound Angle, 2 Rows, m=1.5, θ=1.24

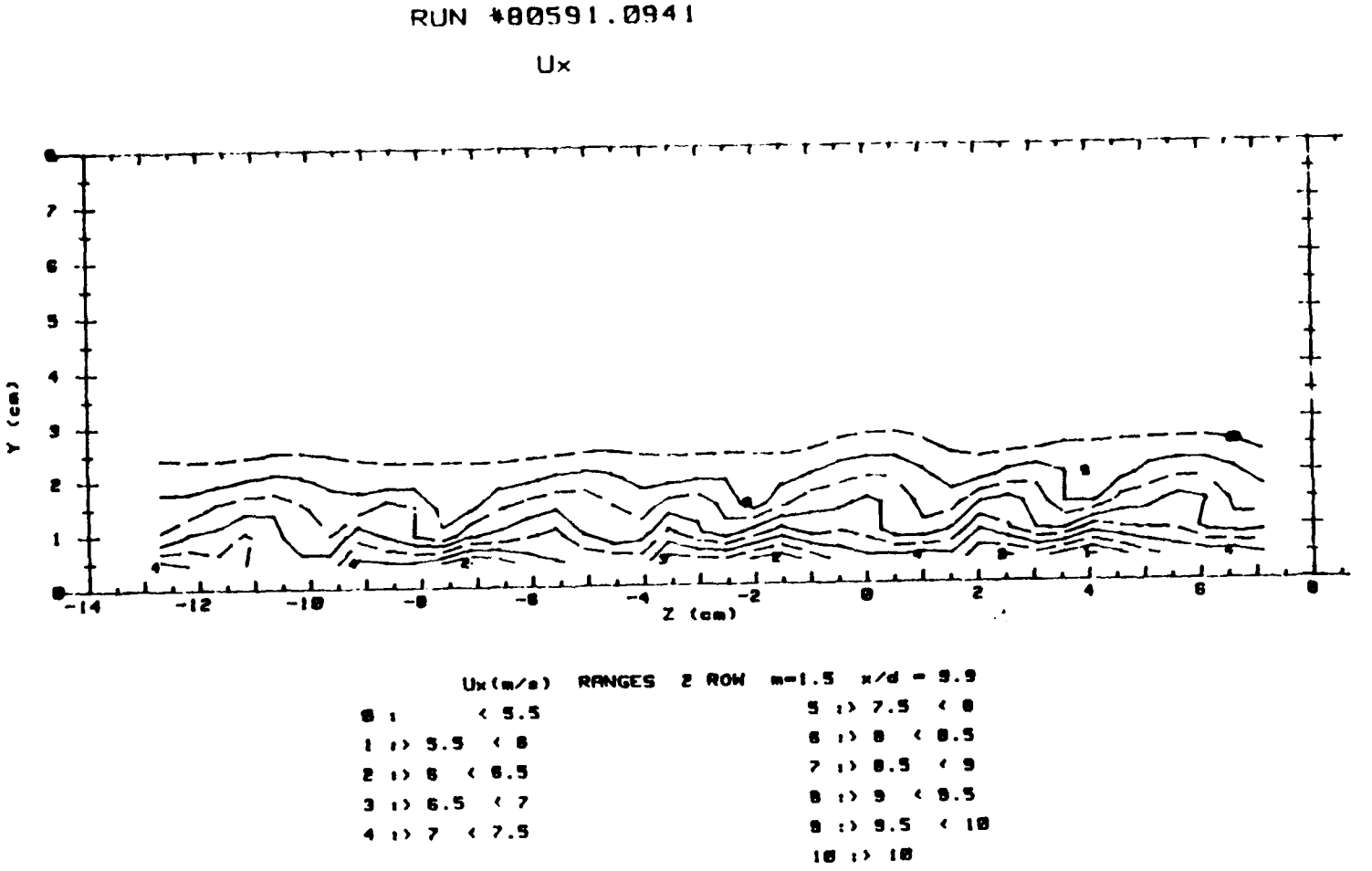


Figure 96. Streamwise Velocity Field, Compound Angle, 2 Rows, m=1.5, x/d=9.9

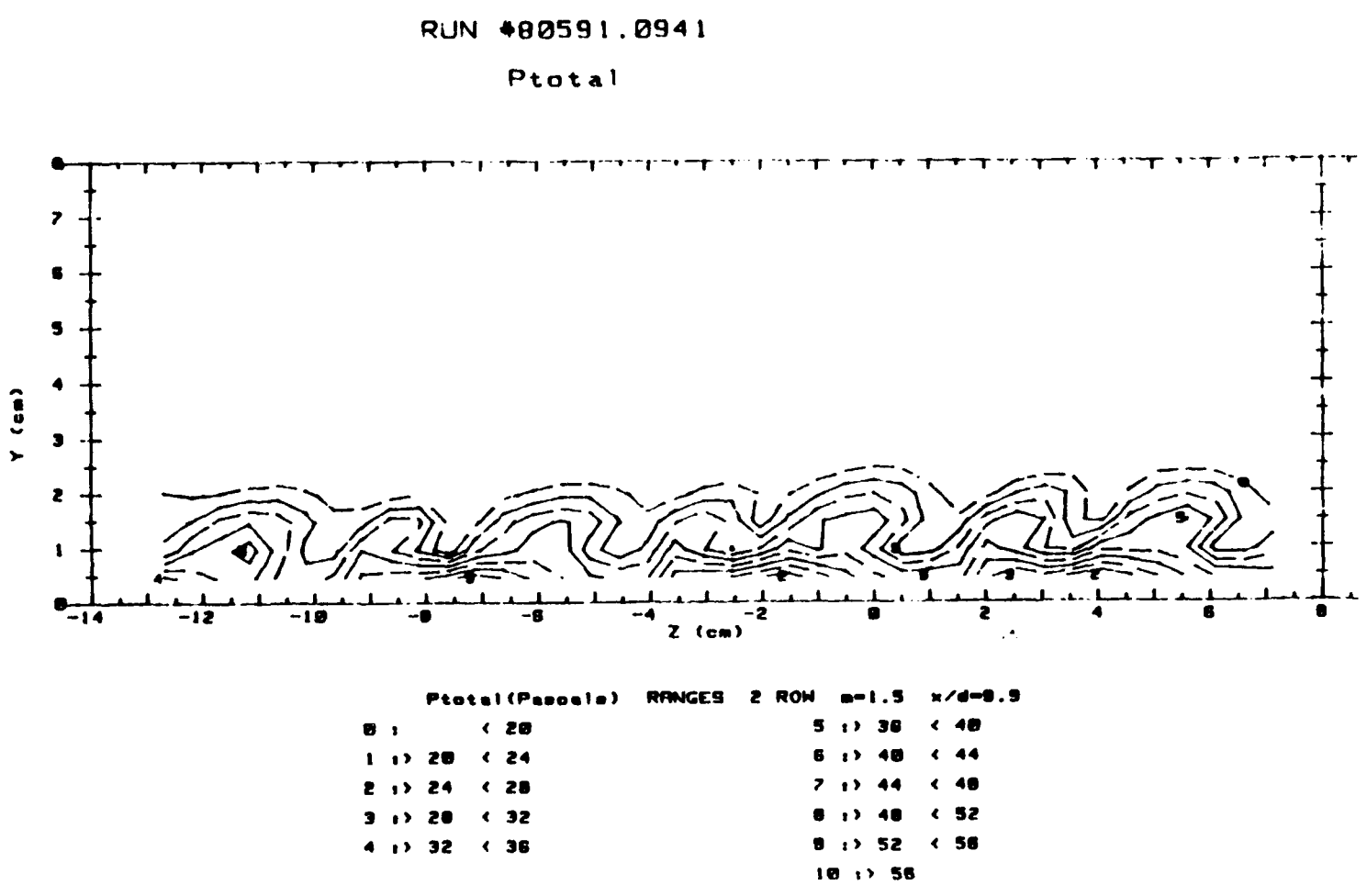


Figure 97. Streamwise Pressure Field, Compound Angle, 2 Rows, m=1.5, x/d=9.9

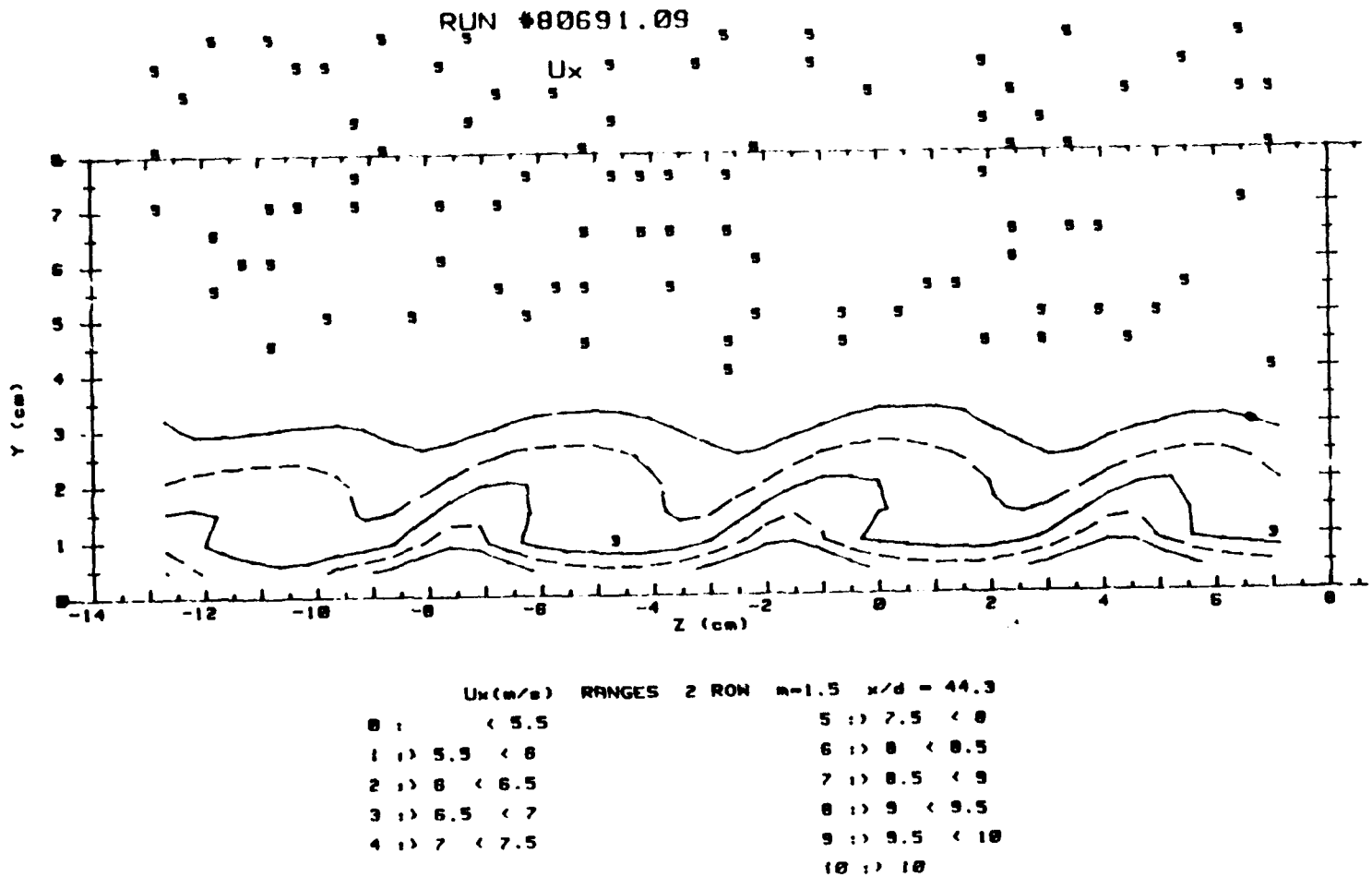


Figure 98. Streamwise Velocity Field, Compound Angle, 2 Rows, m=1.5, x/d=44.3

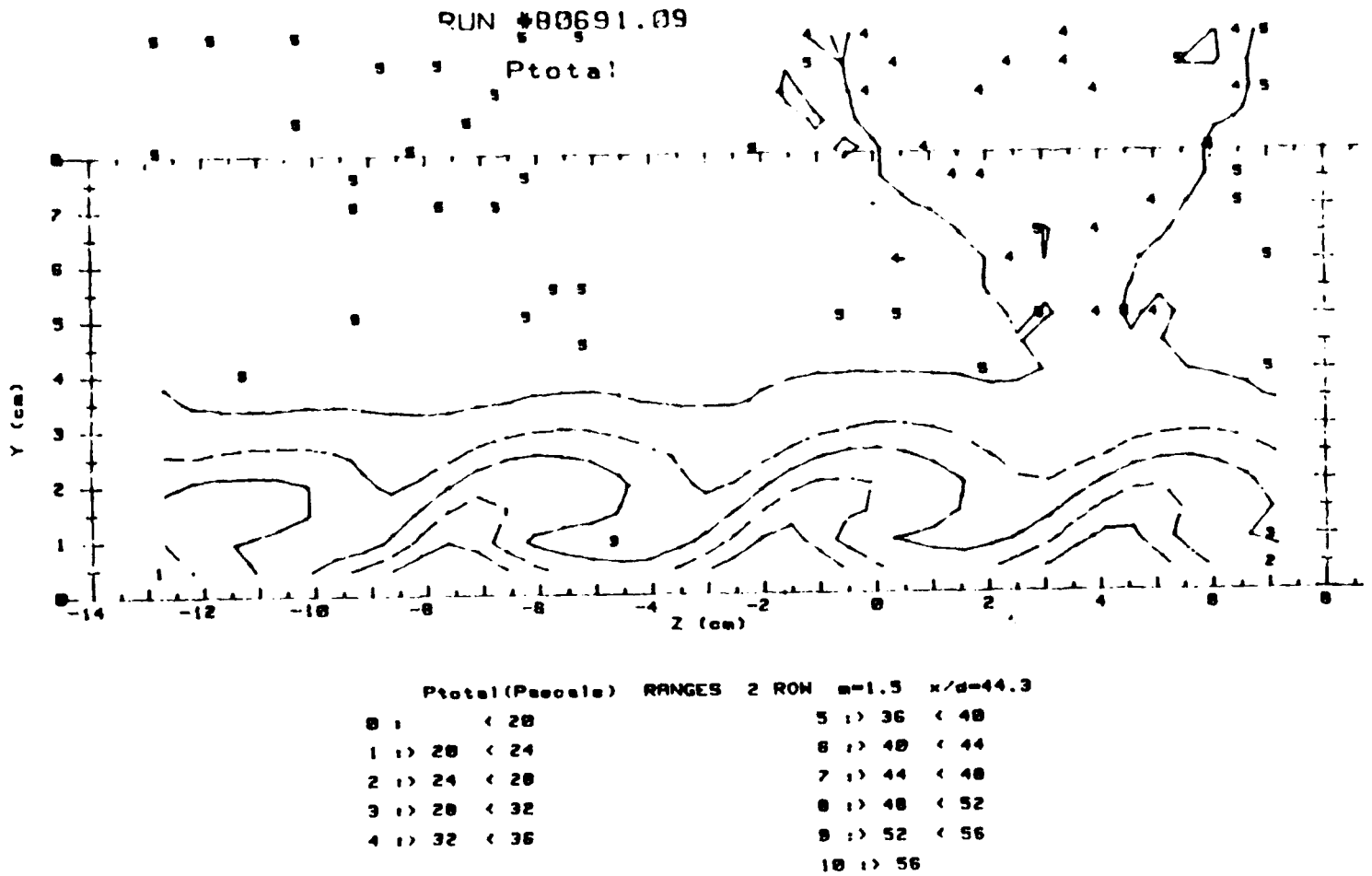


Figure 99. Streamwise Pressure Field, Compound Angle, 2 Rows, m=1.5, x/d=44.3

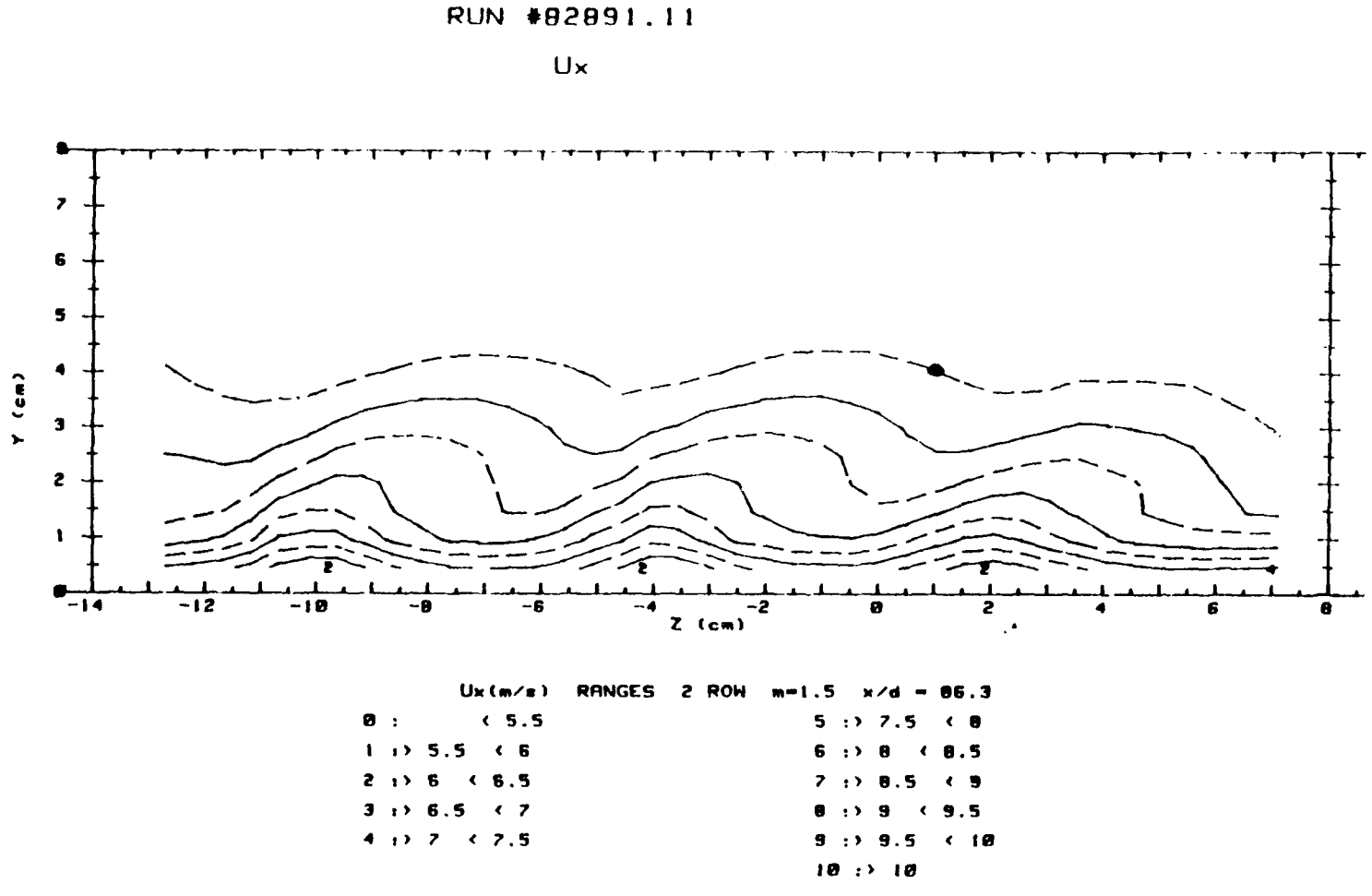


Figure 100. Streamwise Velocity Field, Compound Angle, 2 Rows, m=1.5, x/d=86.3

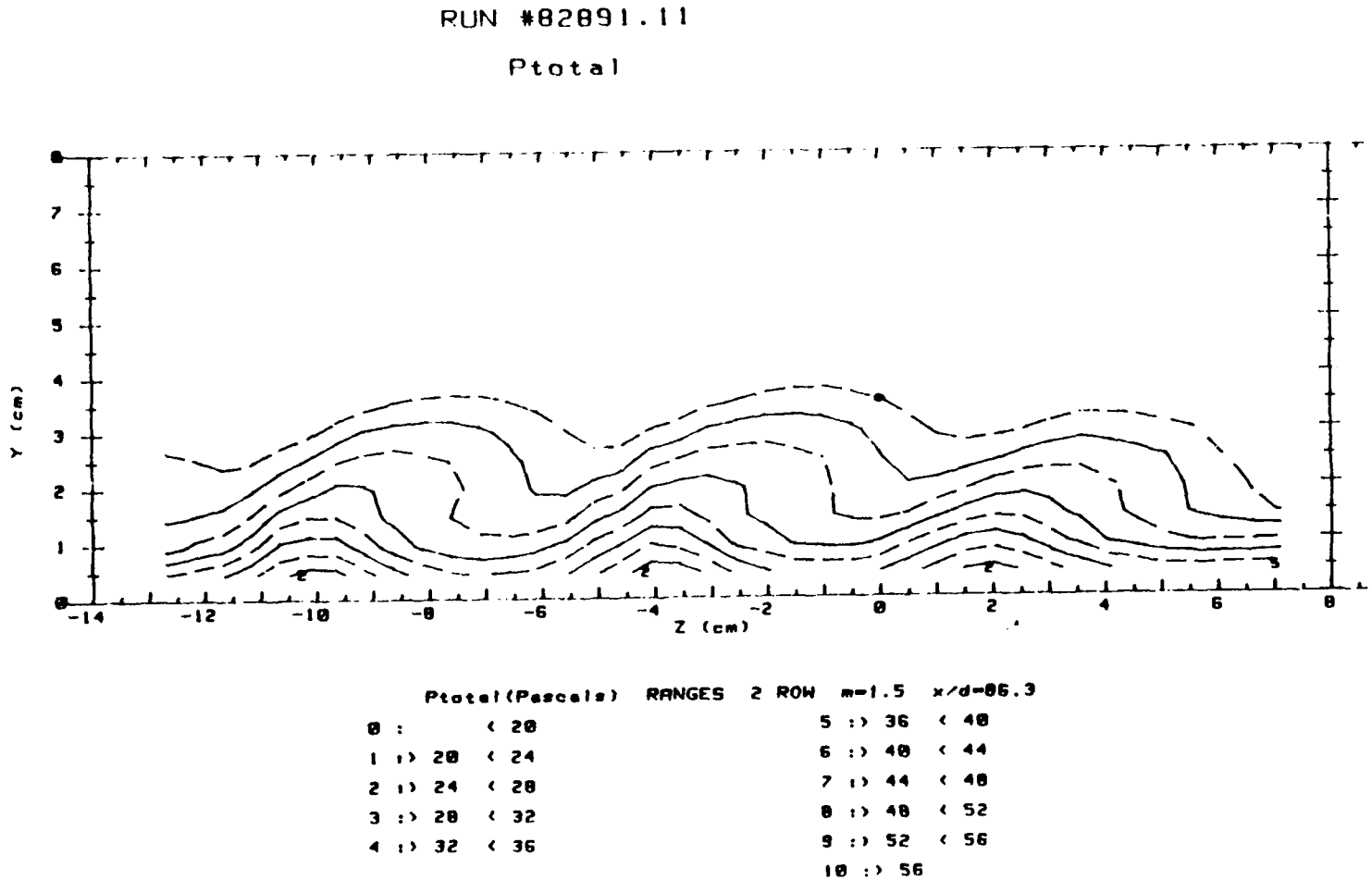


Figure 101. Streamwise Pressure Field, Compound Angle, 2 Rows, m=1.5, x/d=86.3

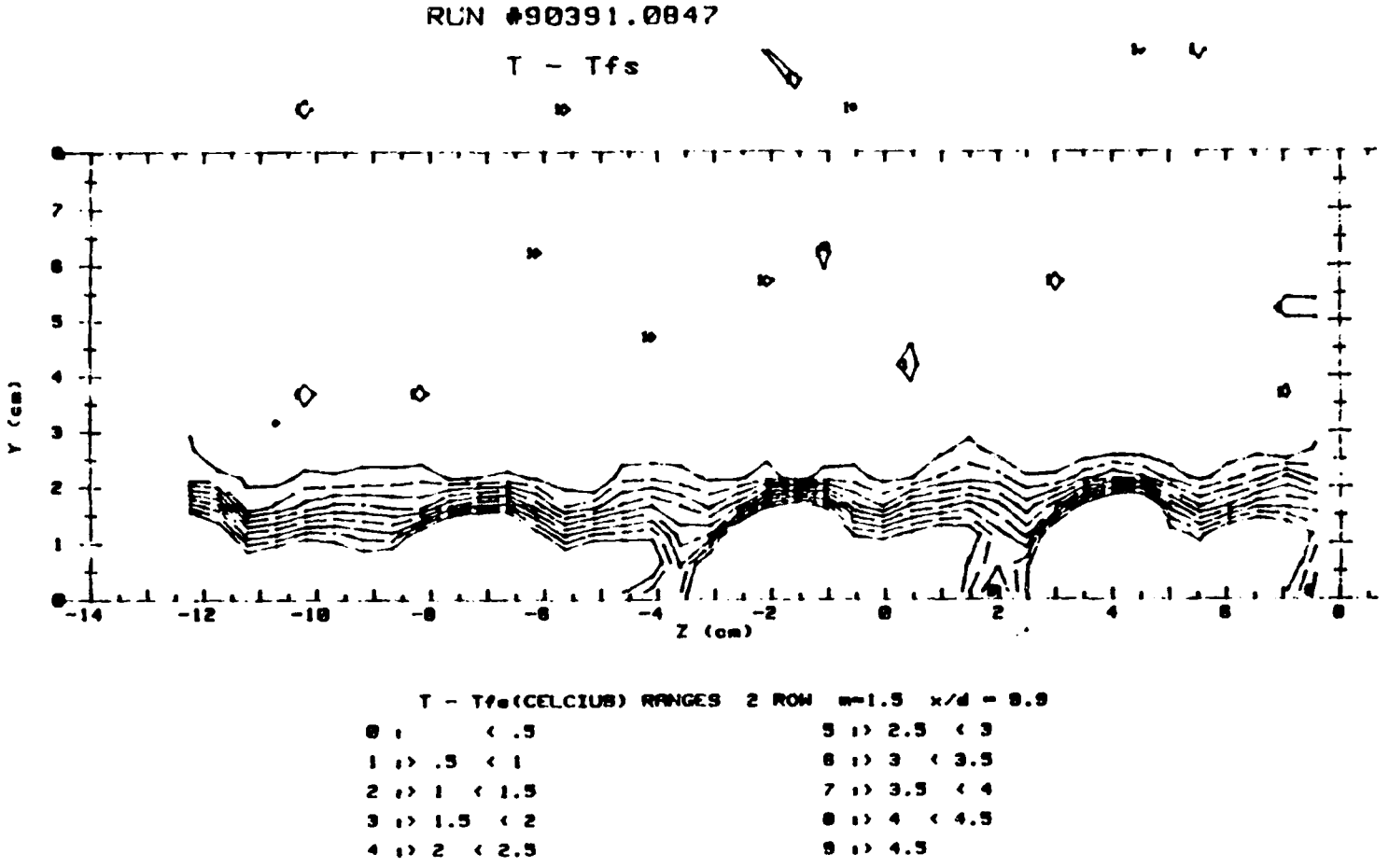


Figure 102. Streamwise Injectant Distribution, Compound Angle, 2 Rows, m=1.5, x/d=9.9

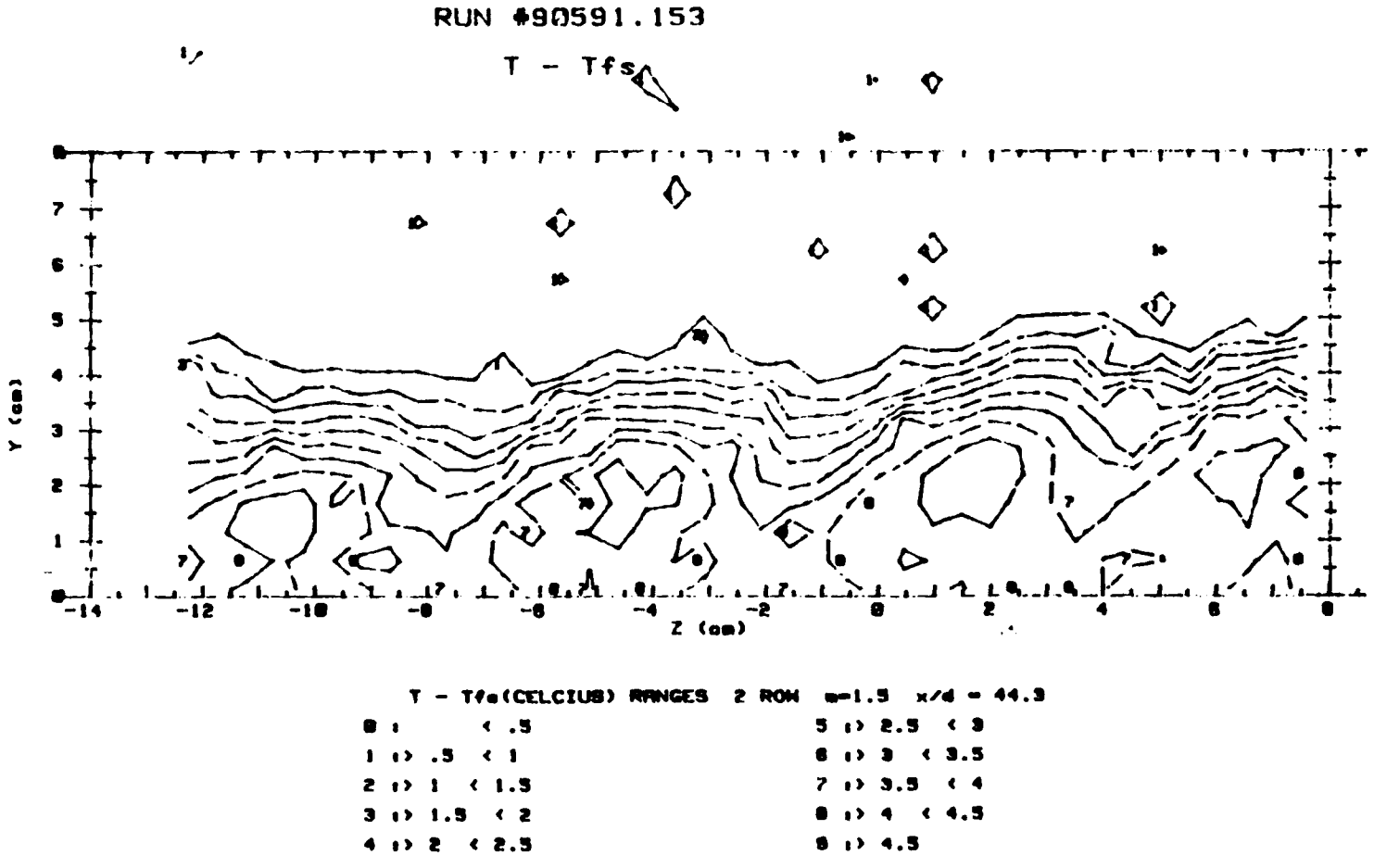


Figure 103. Streamwise Injectant Distribution, Compound Angle, 2 rows, m=0.5, x/d=44.3

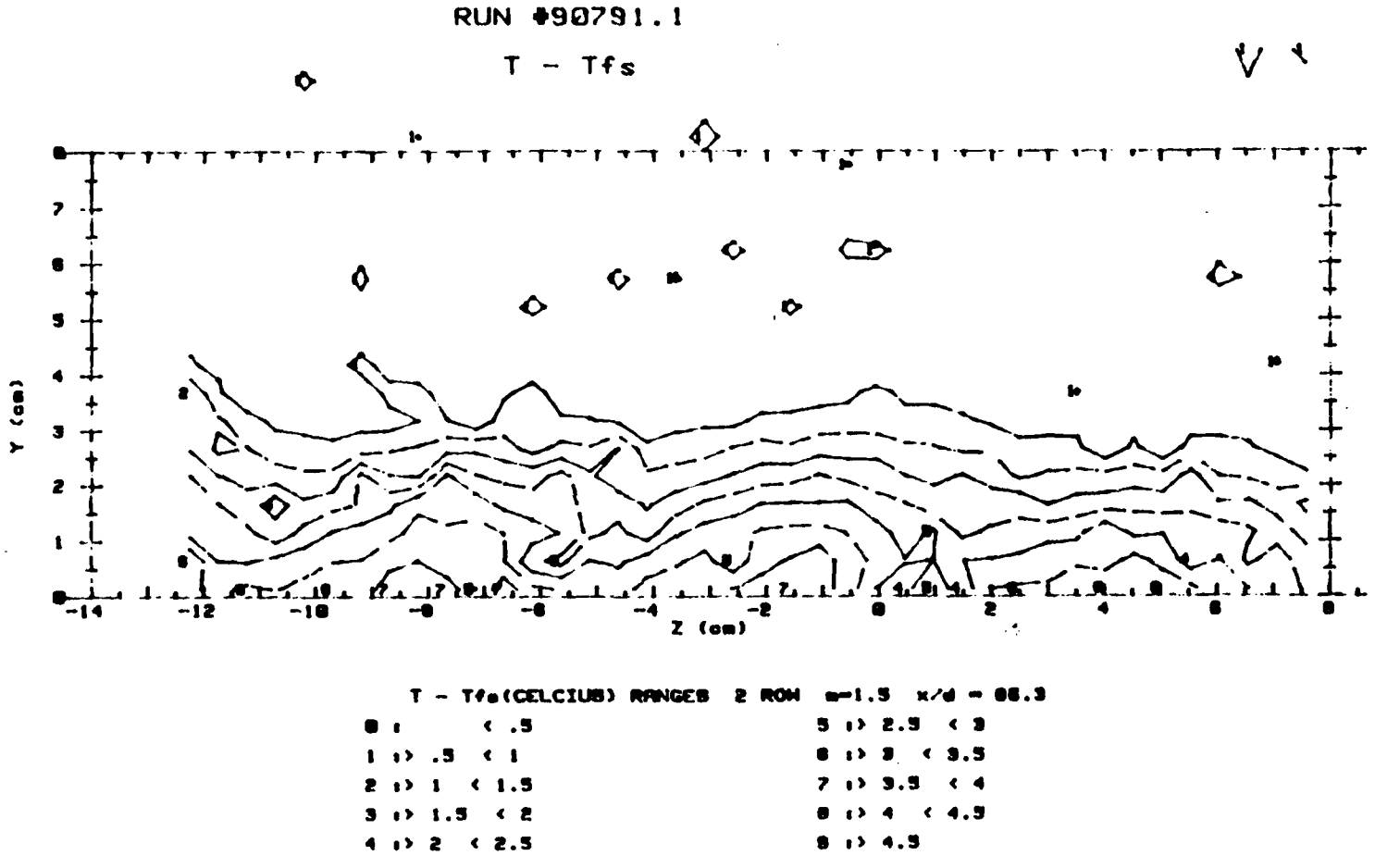


Figure 104. Streamwise Injectant Distribution, Compound Angle, 2 Rows, m=0.5, x/d=44.3

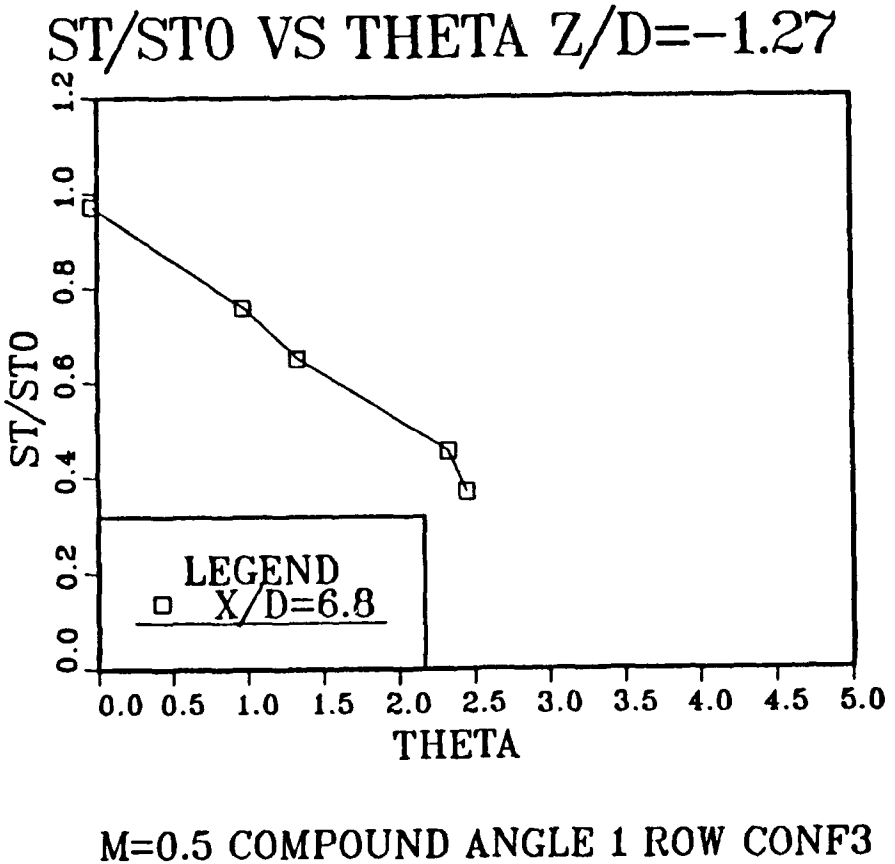


Figure 105. St/Sto Versus θ, Compound Angle, 1 Row, m=0.5, x/d=6.8

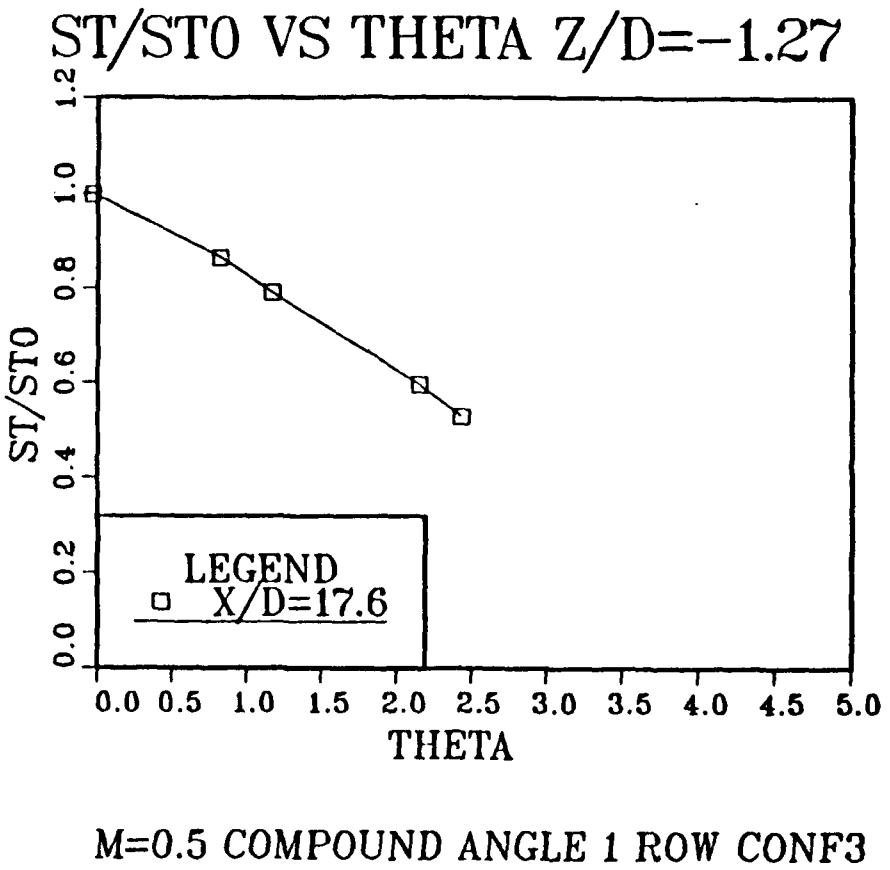


Figure 106. St/Sto Versus θ, Compound Angle, 1 Row, m=0.5, x/d=17.6

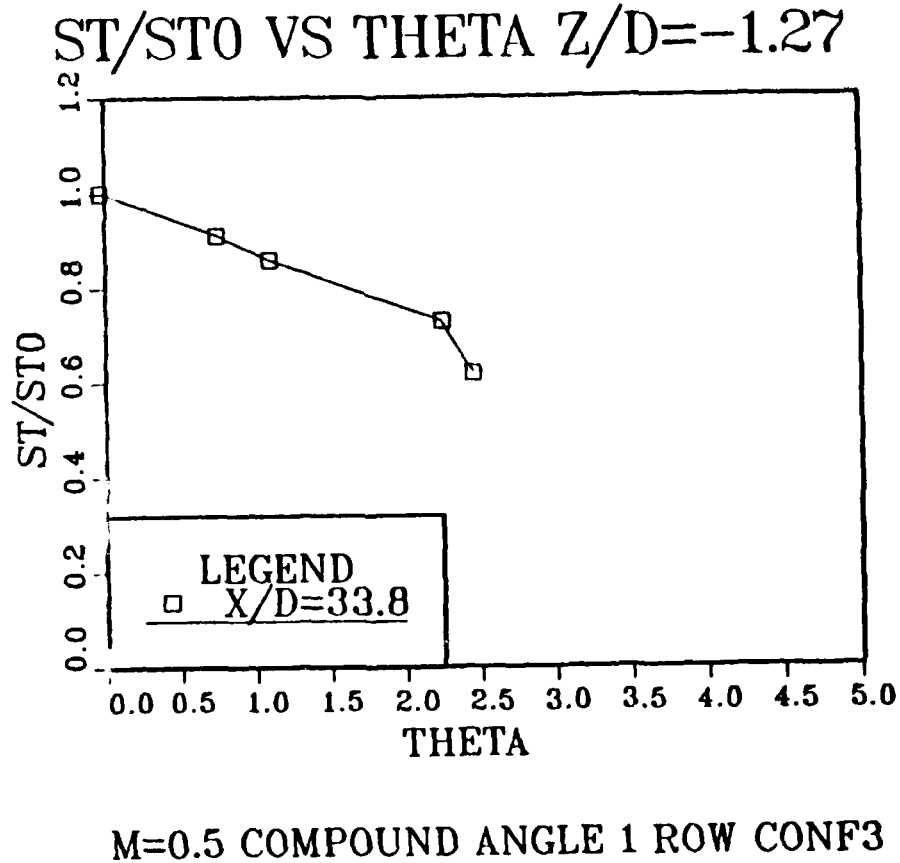


Figure 107. St/Sto Versus θ, Compound Angle, 1 row, m=0.5, x/d=33.8, z/d=-1.27

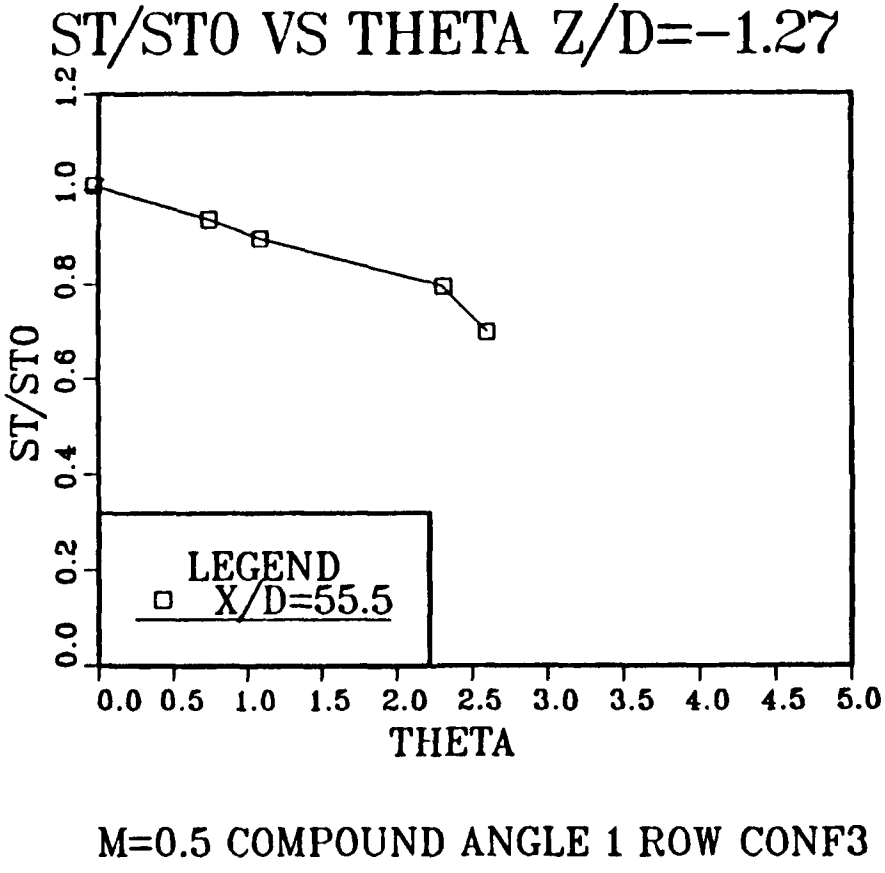


Figure 108. St/Sto Versus θ, Compound Angle, 1 Row, m=0.5, x/d=55.5, z/d=-1..27

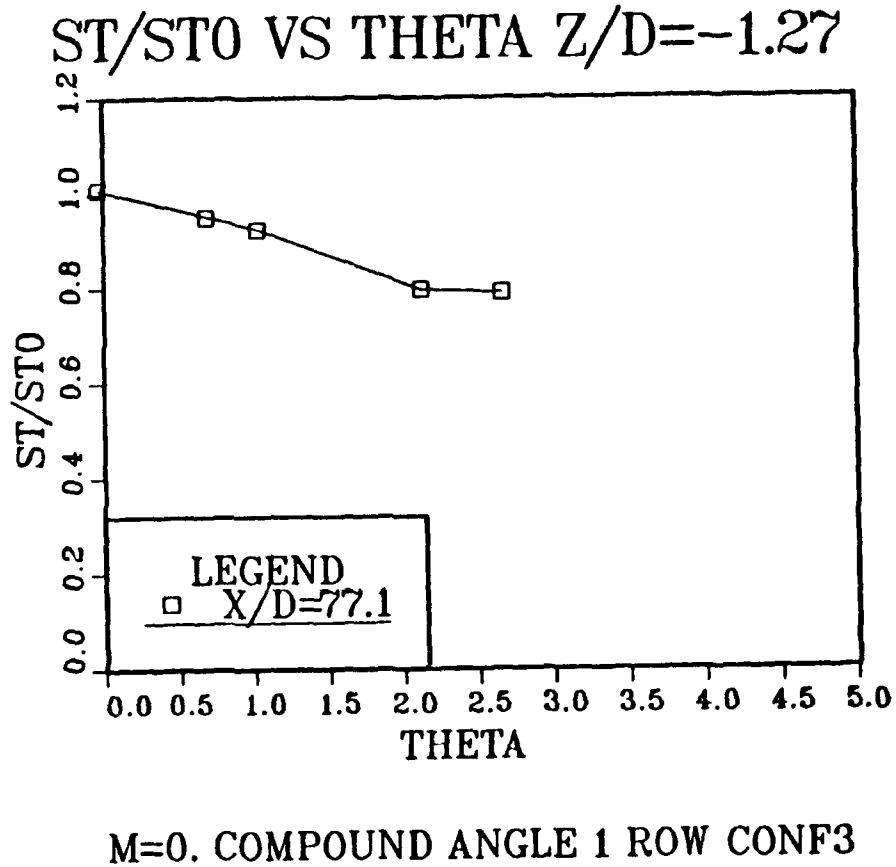


Figure 109. St/Sto Versus θ, Compound Angle, 1 Row, m=0.5, x/d=77.1, z/d=-1.27

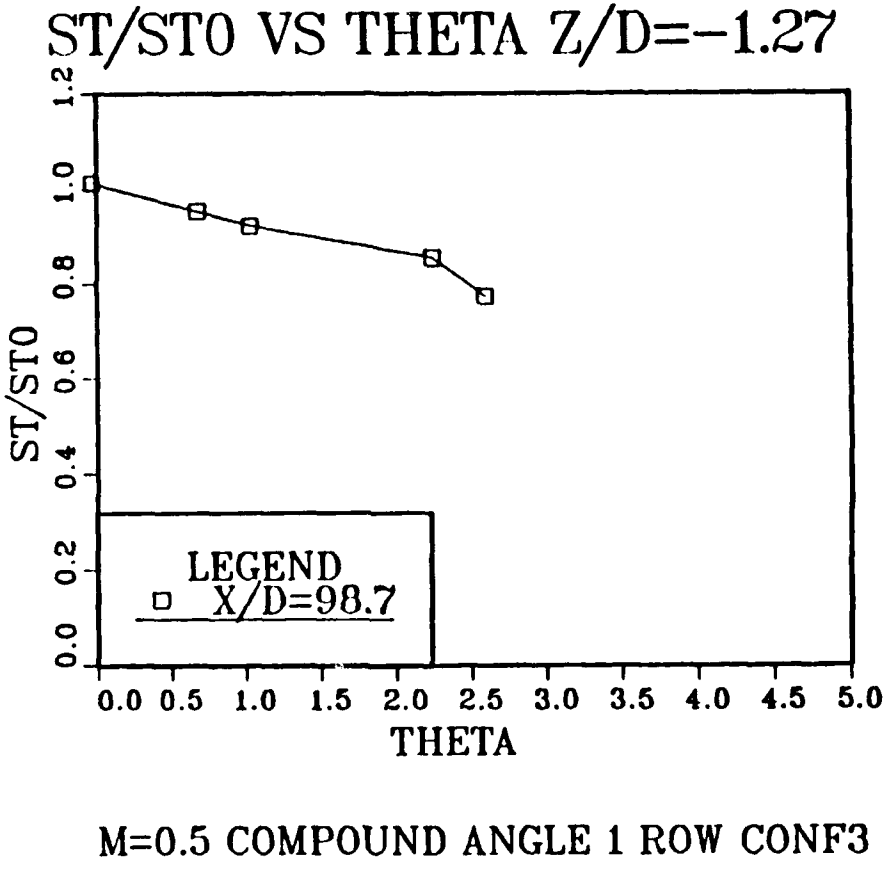


Figure 110. St/Sto Versus θ, Compound Angle, 1 Row, m=0.5, x/d=98..7, z/d=-1.27

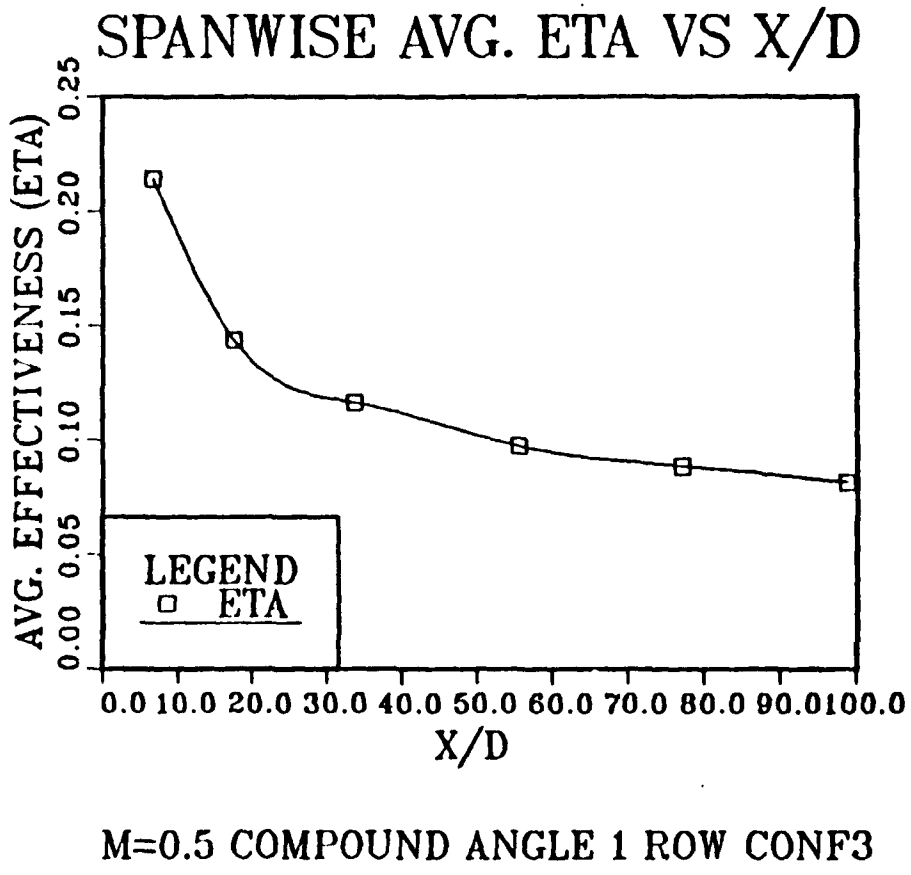


Figure 111. η Versus x/d, Compound Angle, 1 Row, m=0.5, Spanwise Average

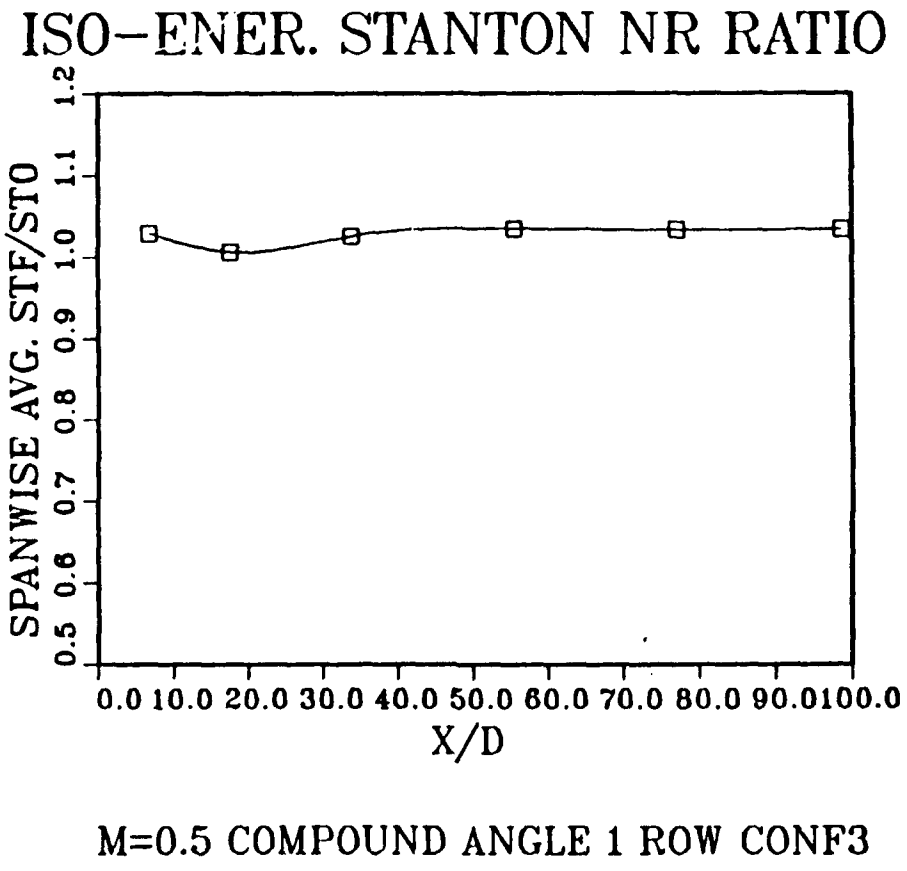


Figure 112. Stf/Sto Versus x/d, Compound Angle, 1 Row, m=0.5, Spanwise Average

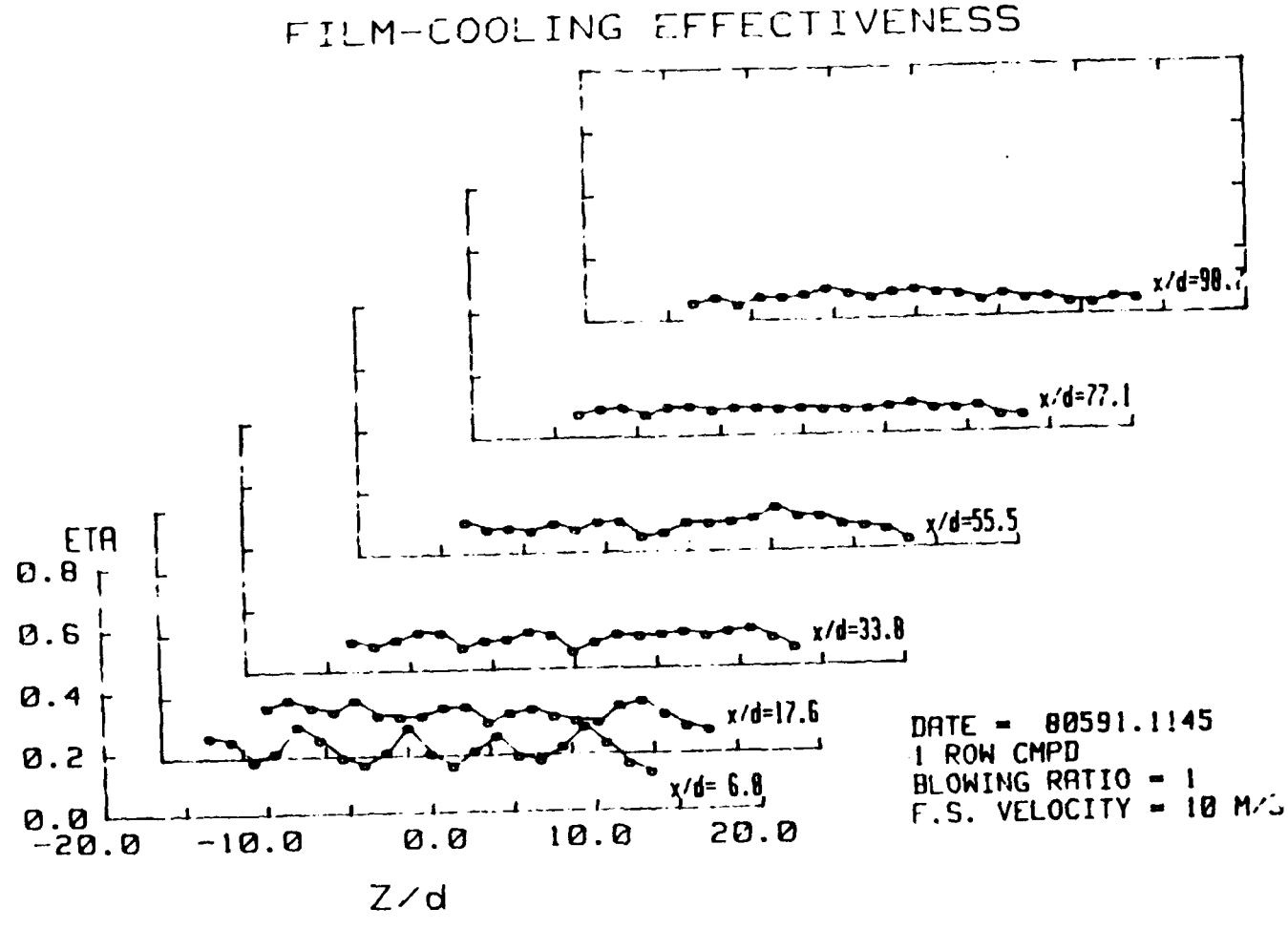


Figure 113. Spanwise Variation of η, Compound Angle, 1 Row, m=0.5

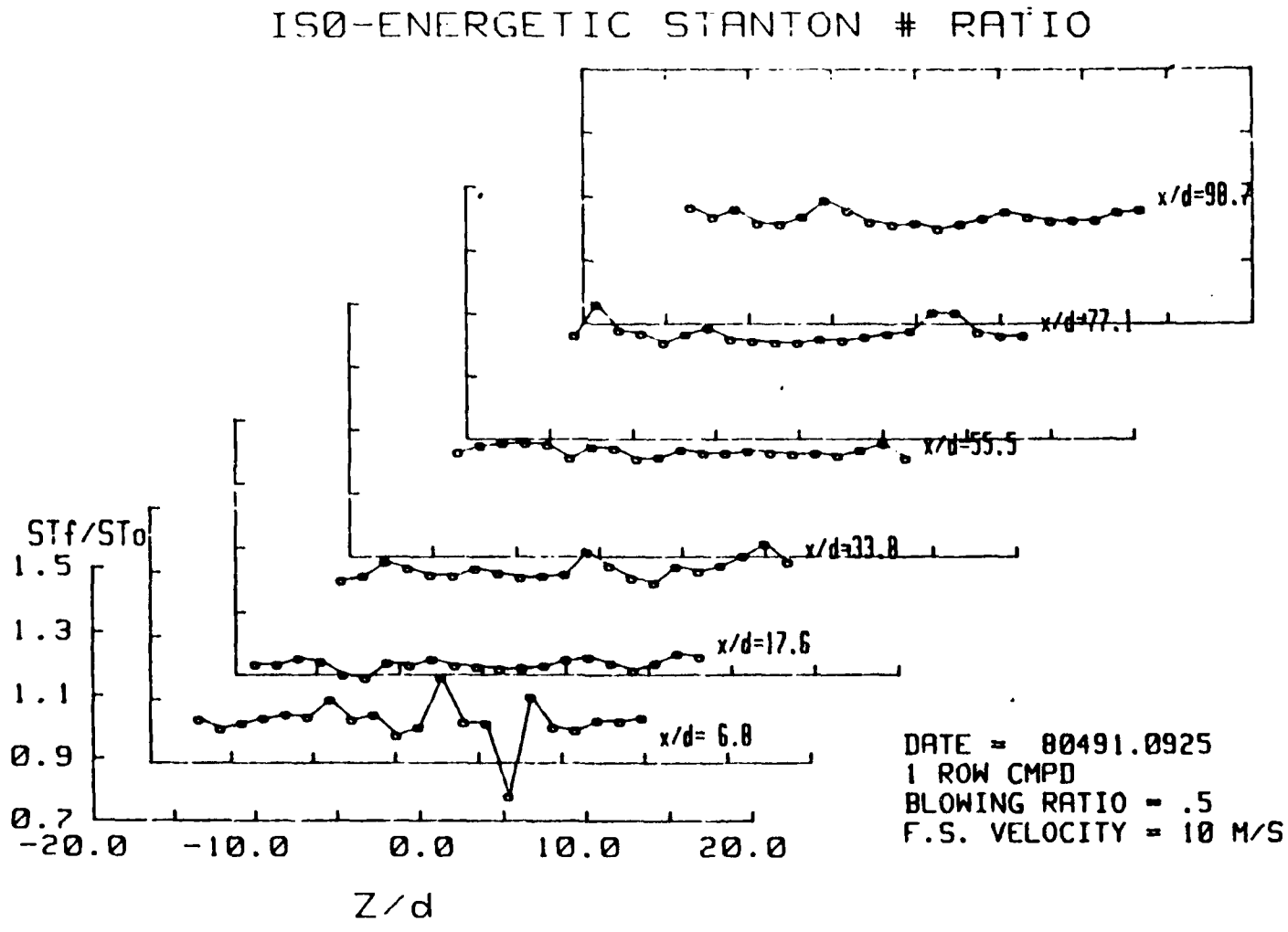


Figure 114. Spanwise Variation of Stf/Sto, Compound Angle, 1 Row, m=0.5

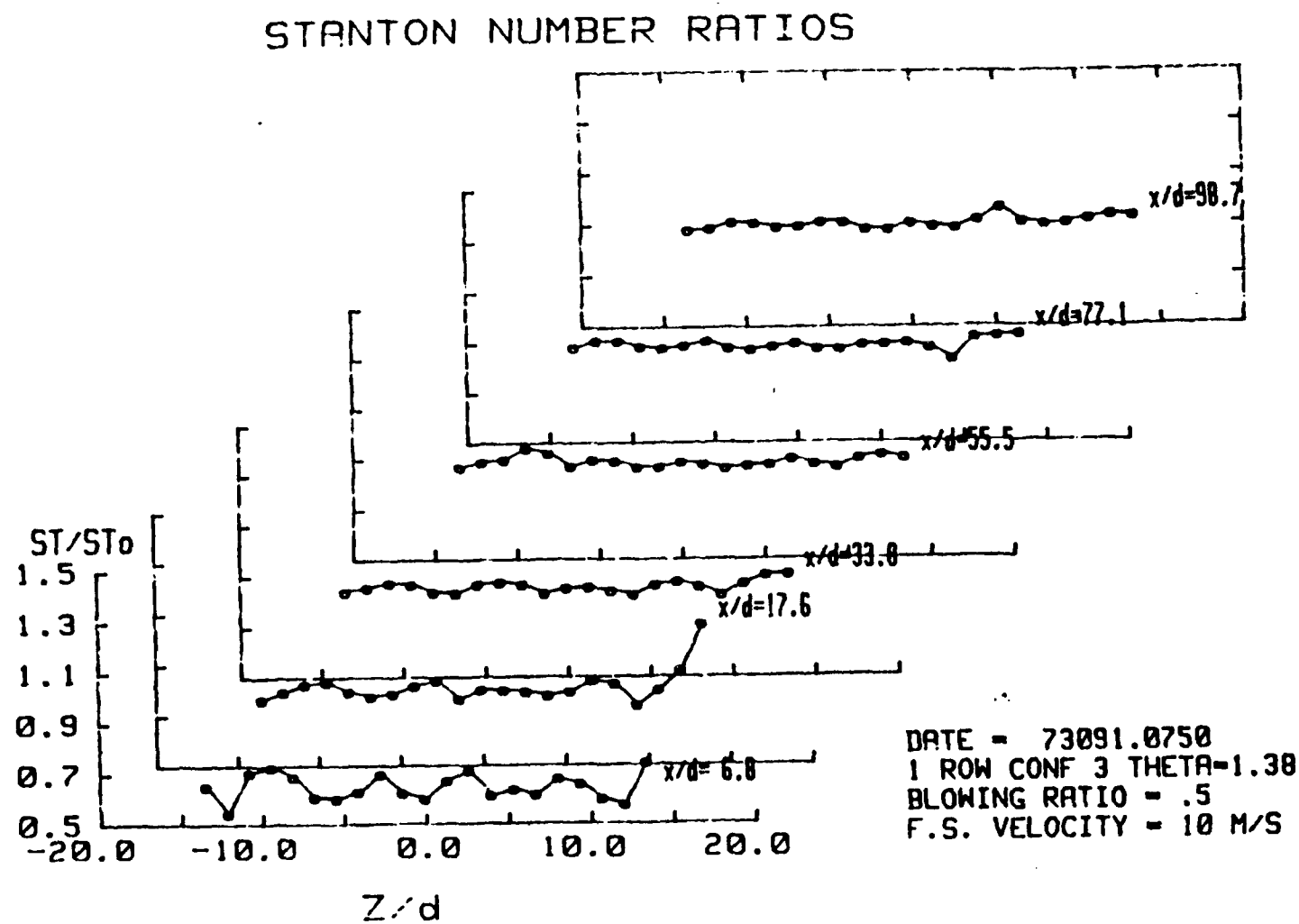


Figure 115. Spanwise Variation of St/Sto, Compound Angle, 1 Row, m=0.5, θ=1.37

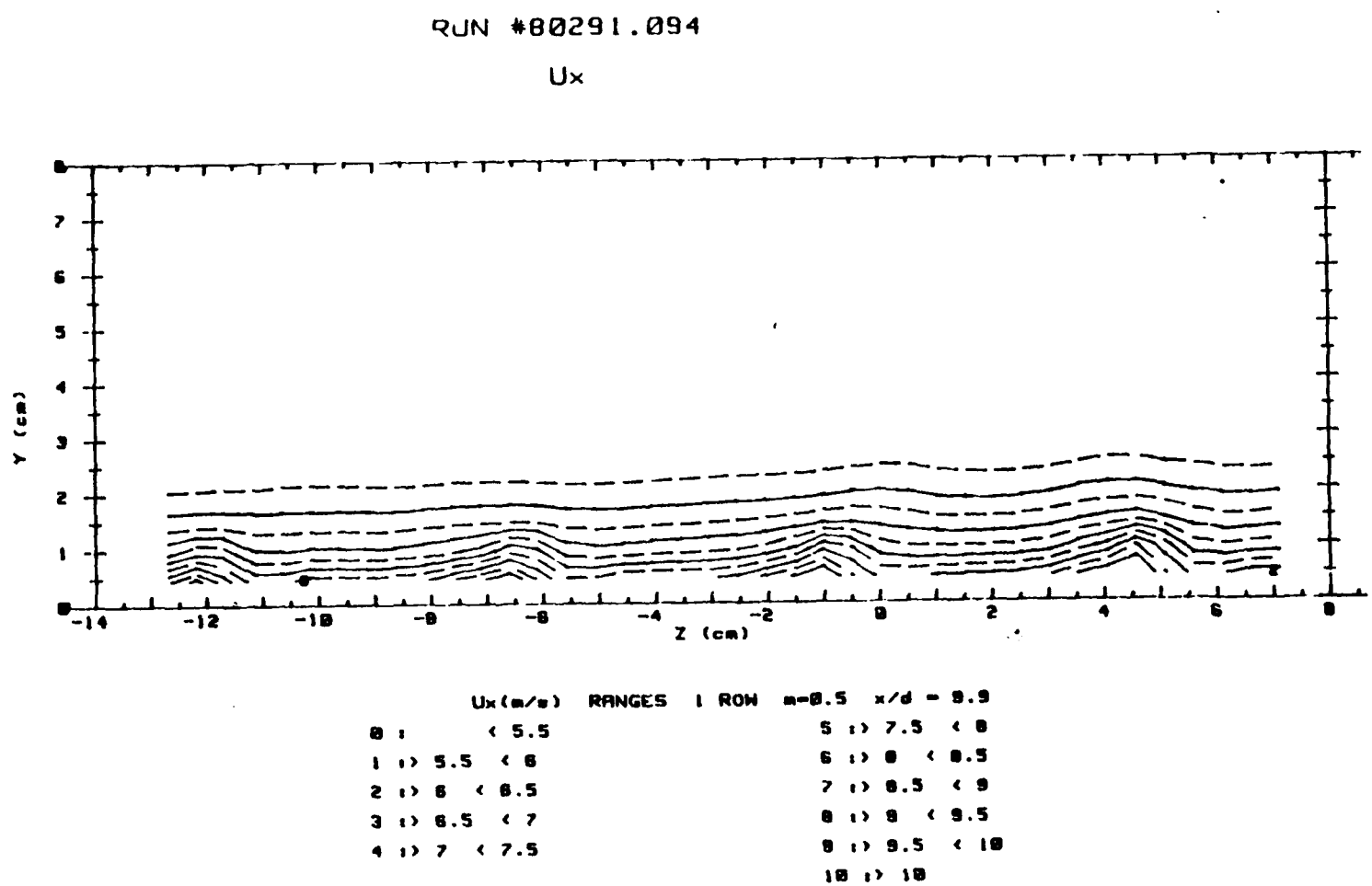


Figure 116. Streamwise Velocity Field, Compound Angle, 1 Row, m=0.5, x/d=9.9

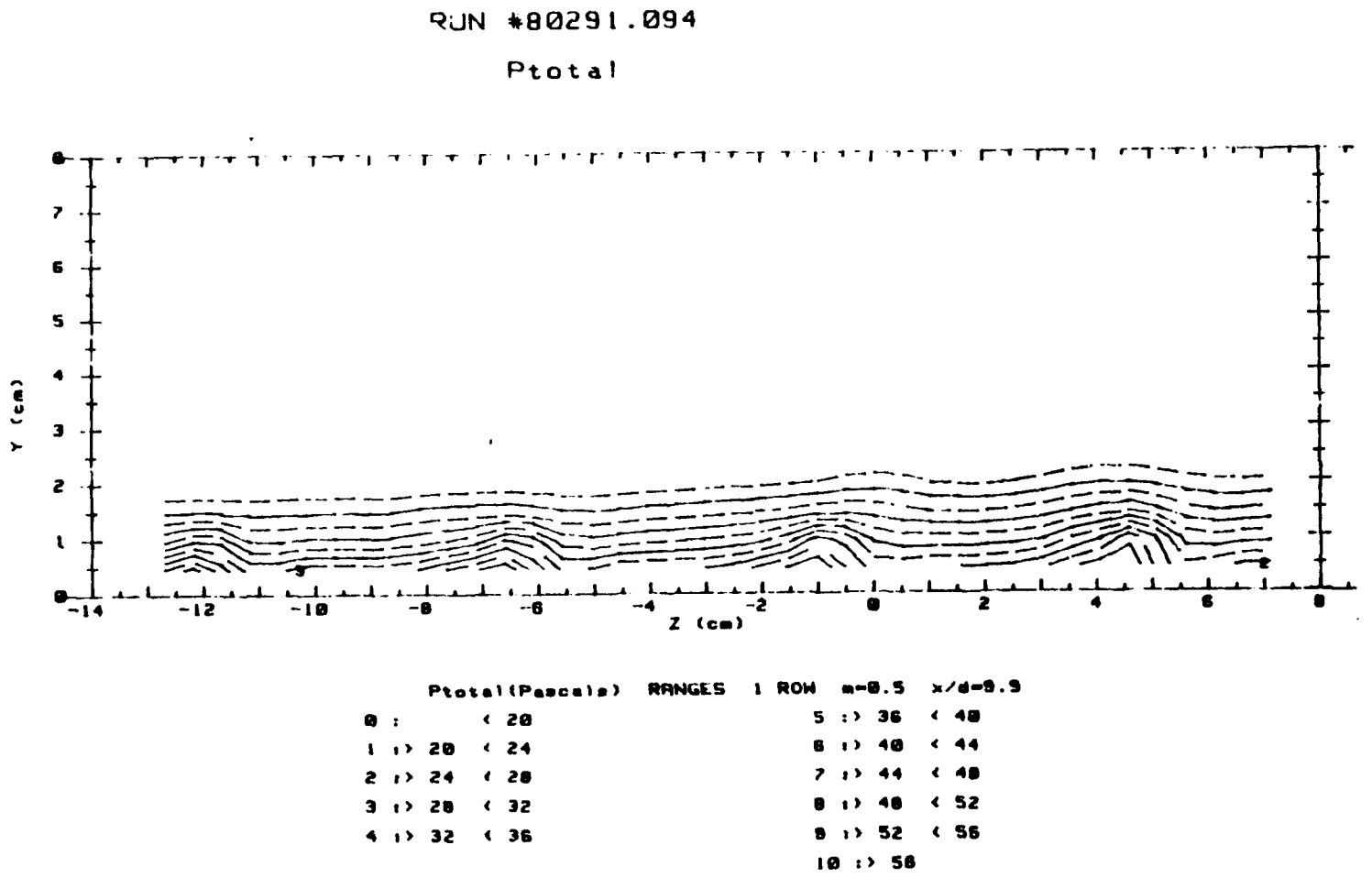


Figure 117. Streamwise Pressure Field, Compound Angle, 1 Row, m=0.5, x/d=9.9

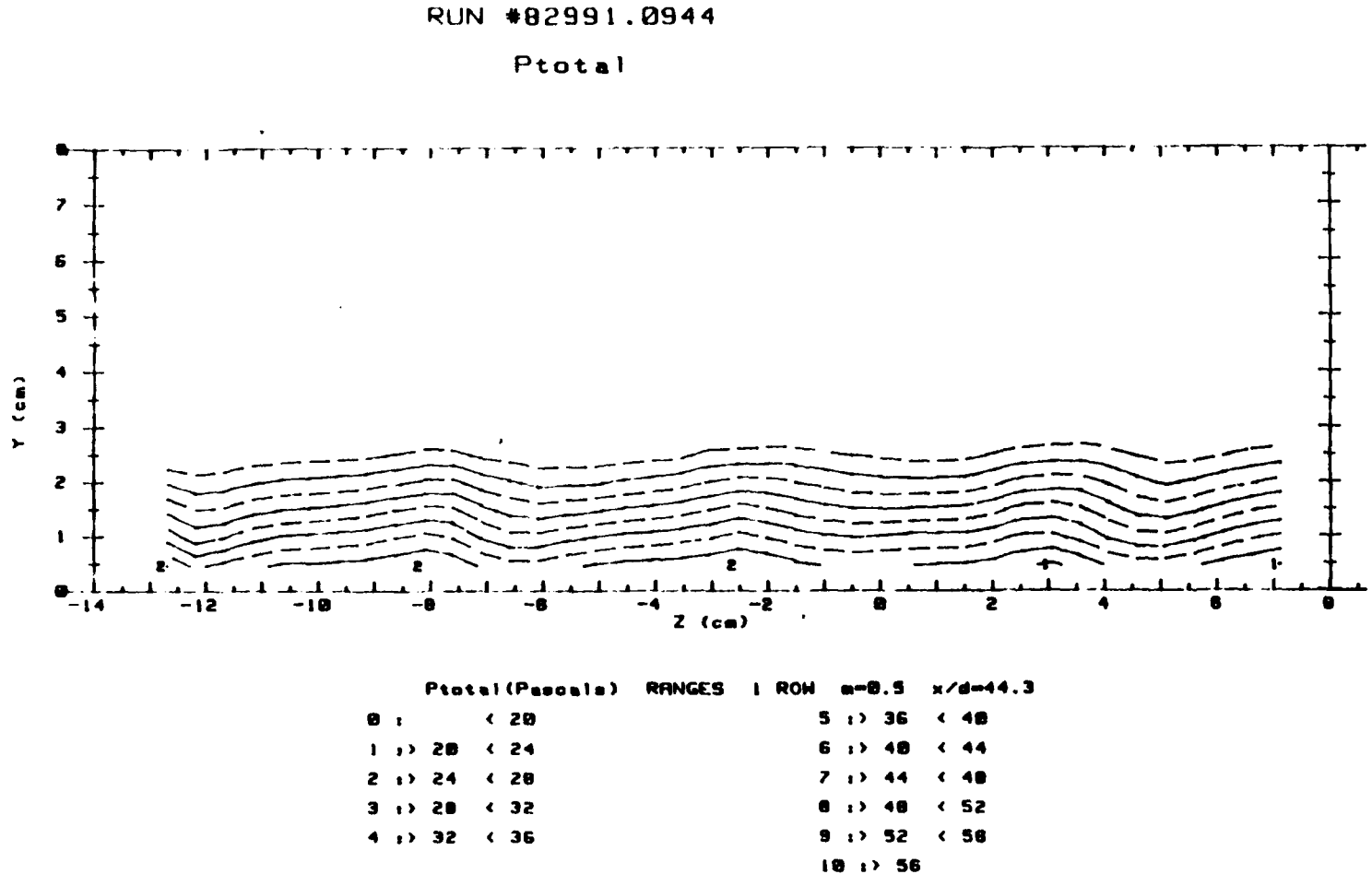


Figure 118. Streamwise Velocity Field, Compound Angle, 1 Row, m=0.5, x/d=44.3

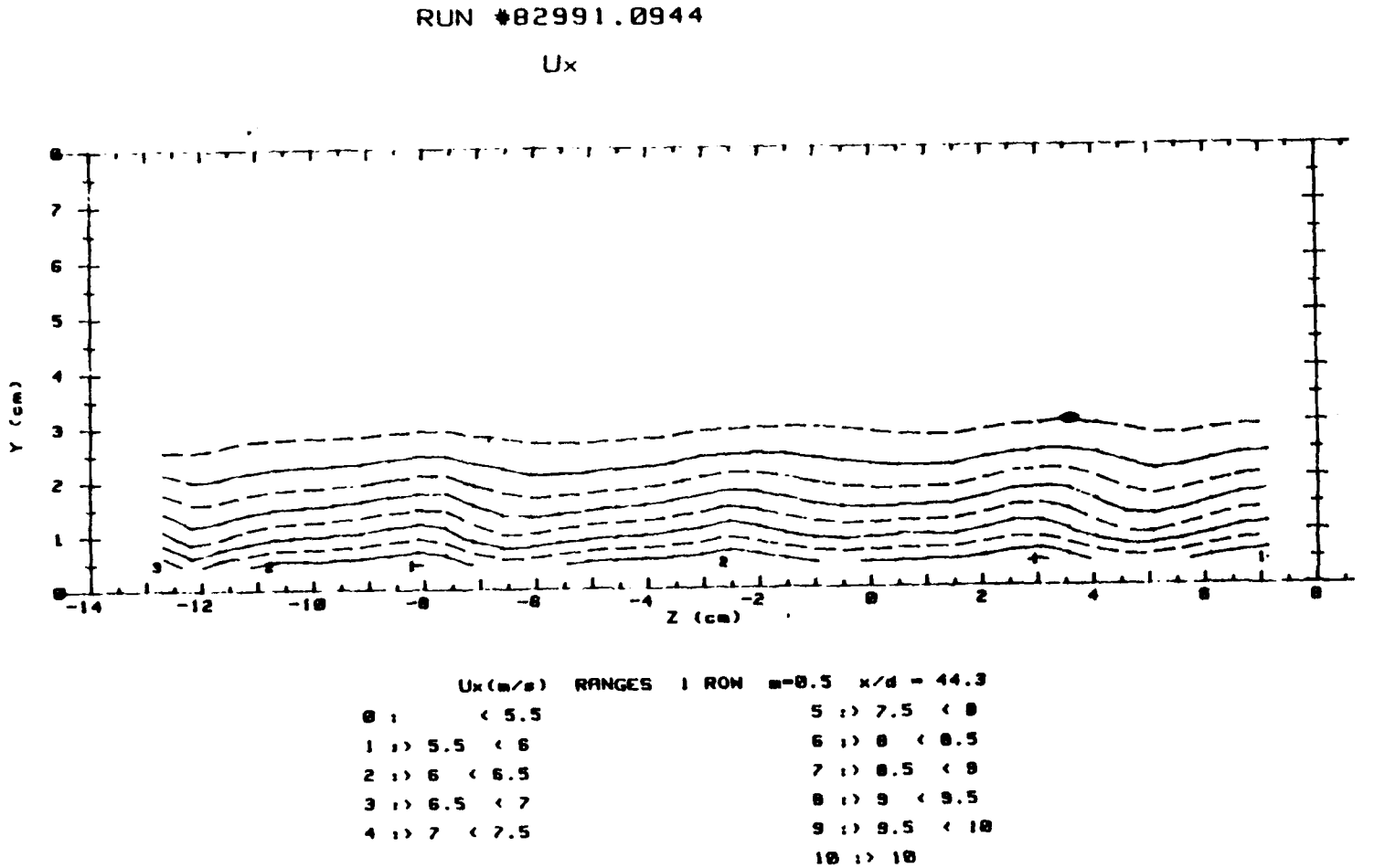


Figure 119. Streamwise Pressure Field, Compound Angle, 1 Row, m=0.5, x/d=44.3

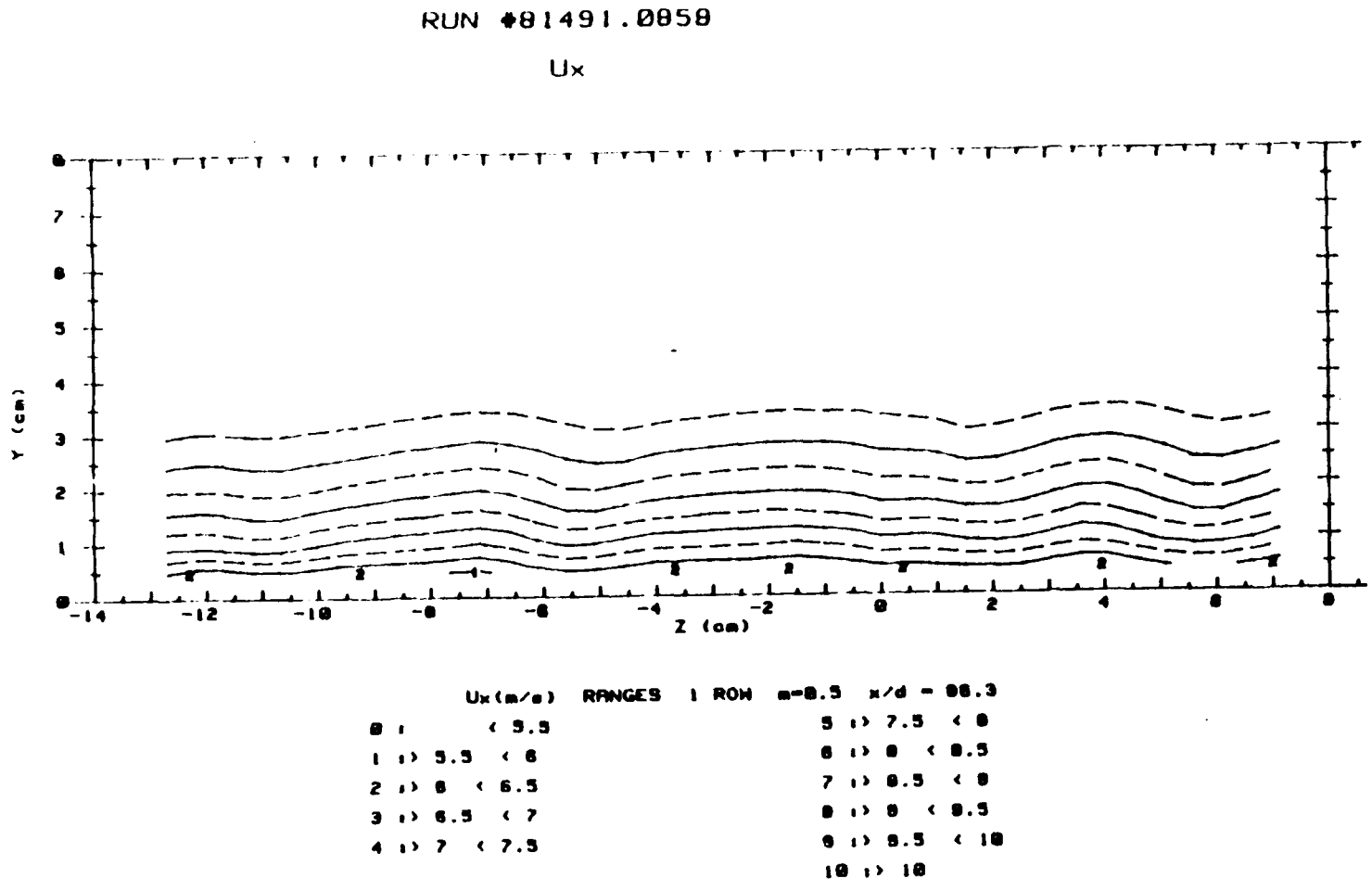


Figure 120. Streamwise Velocity Field, Compound Angle, 1 Row, m=0.5, x/d=86.3

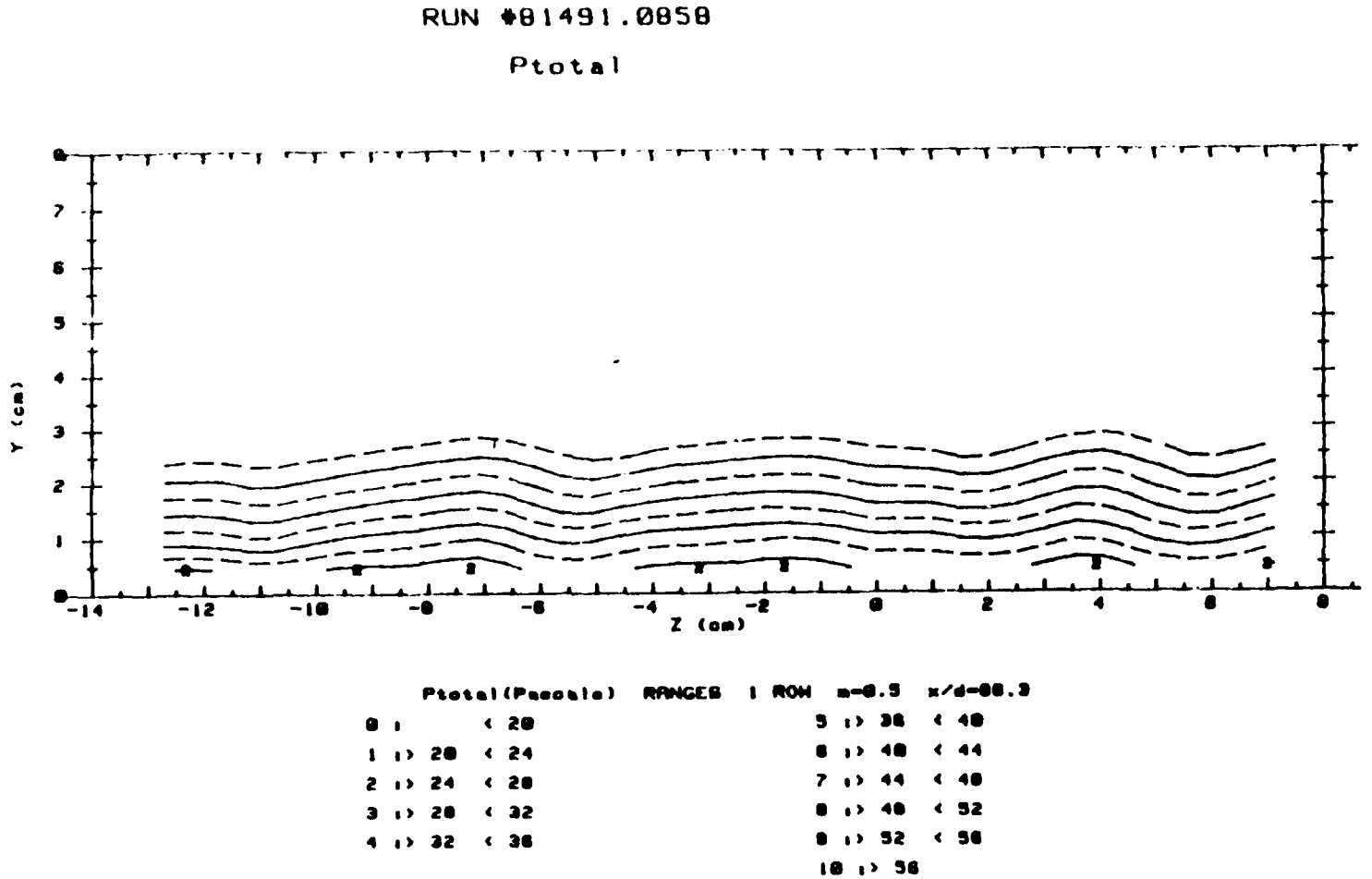


Figure 121. Streamwise Pressure Field, Compound Angle, 1 Row, m=0.5, x/d=86.3

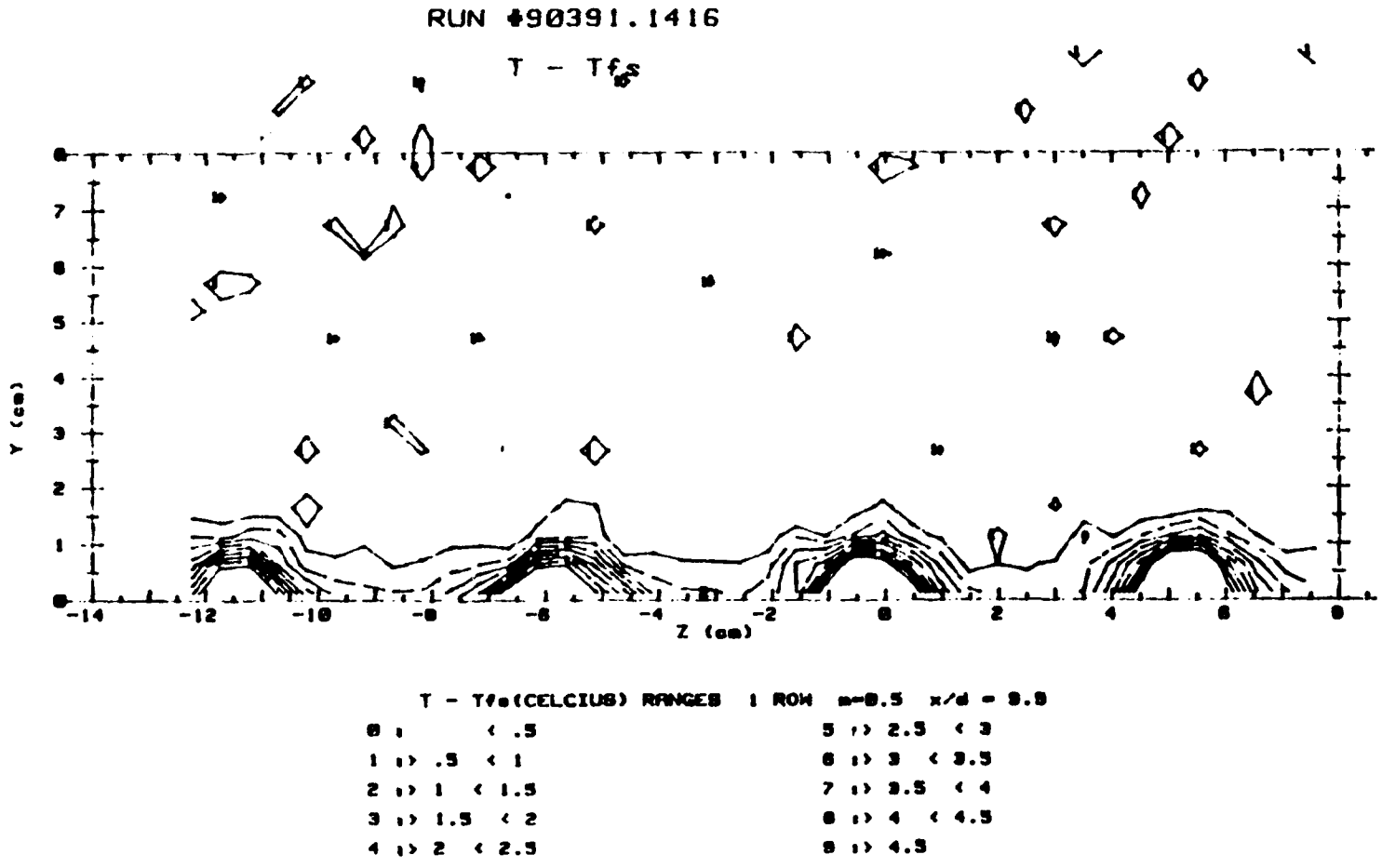


Figure 122. Streamwise Injectant Distribution, Compound Angle, 1 Row, m=0.5, x/d=9.9

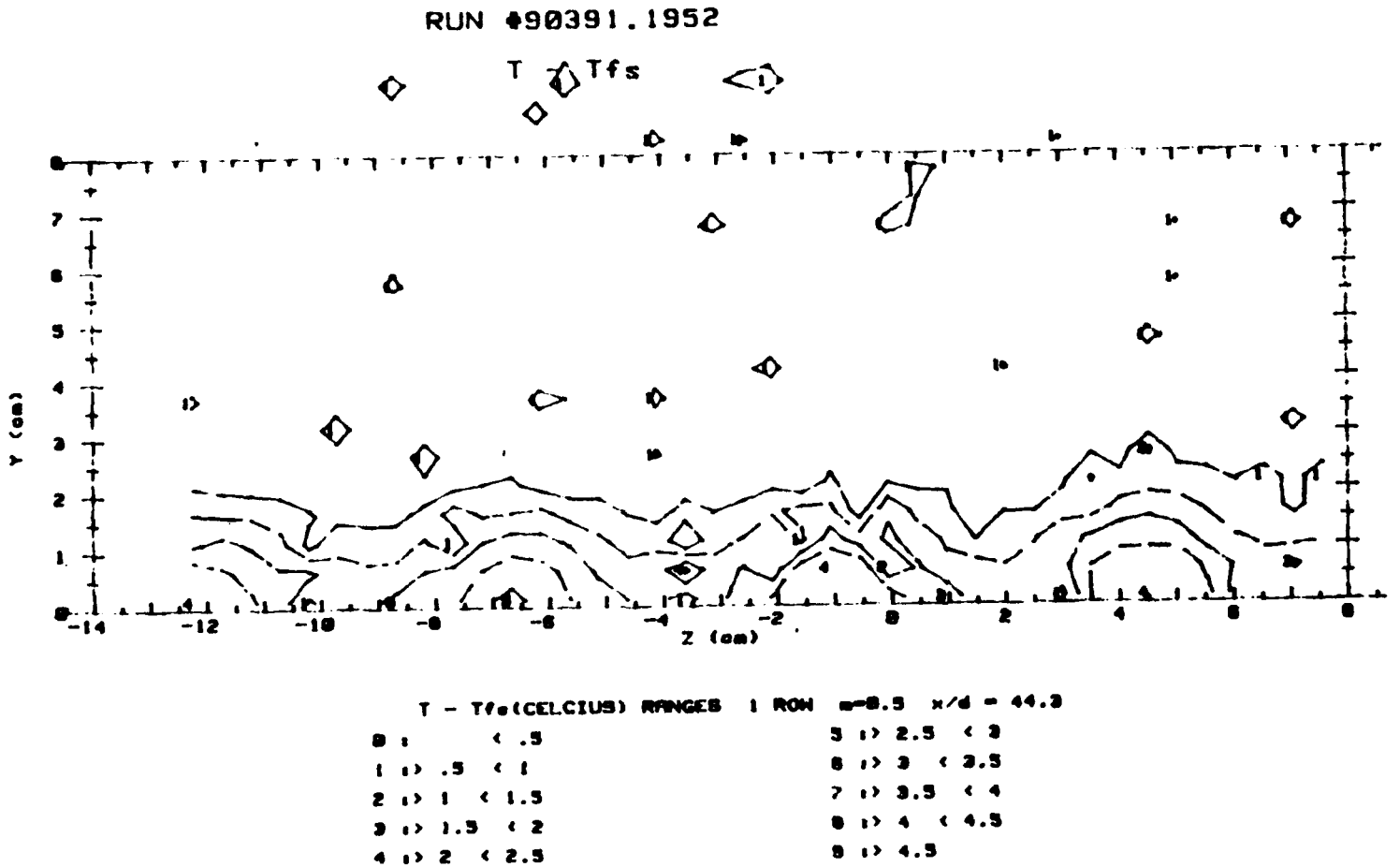


Figure 123. Streamwise Injectant Distribution, Compound Angle, 1 Row, m=0.5, x/d=44.3

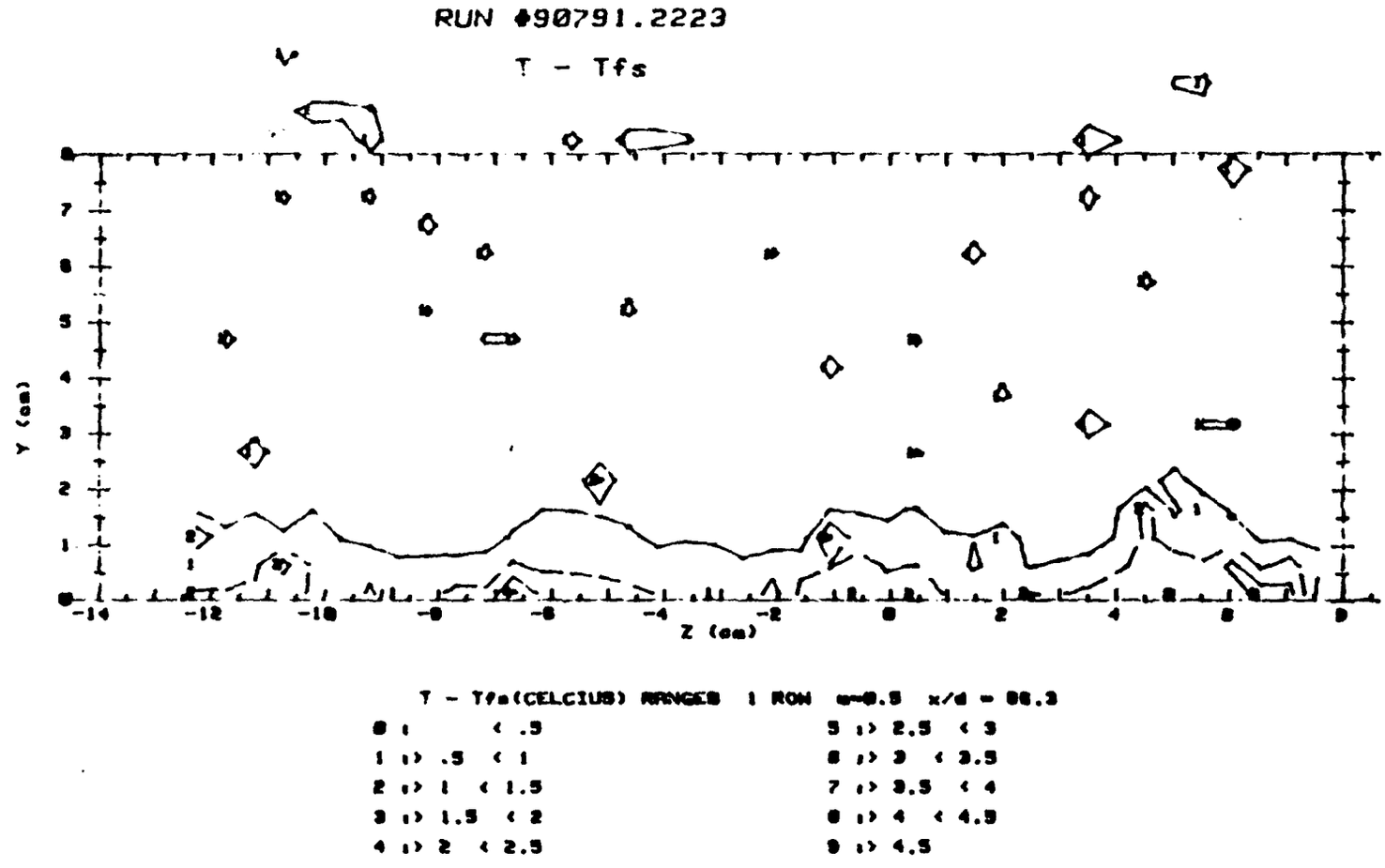


Figure 124. Streamwise Injectant Distribution, Compound Angle, 1 Row, x=0.5, x/d=86.3

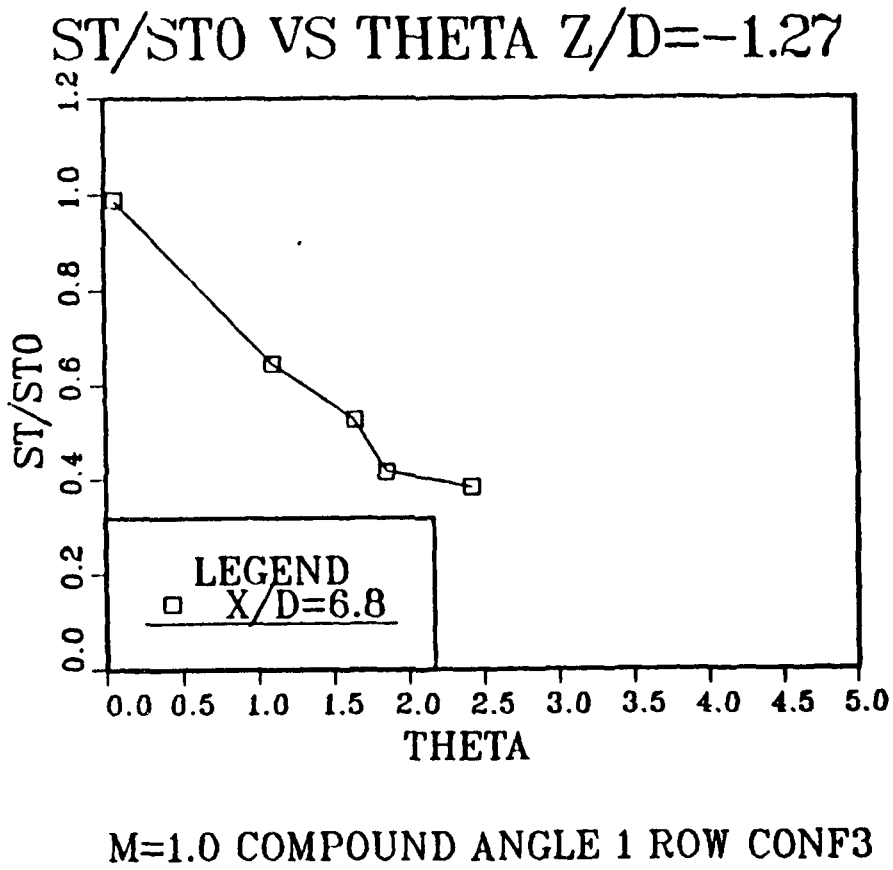


Figure 125. St/Sto Versus θ, Compound Angle, 1 Row, m=1.0, x/d=6.8, z/d=-1.27

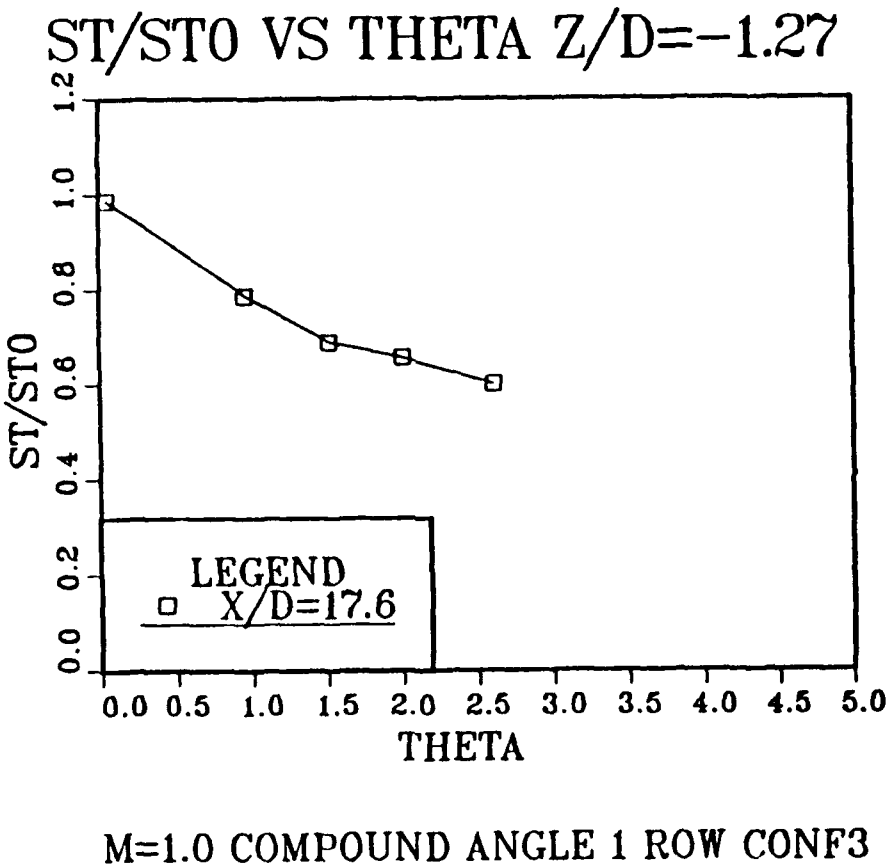


Figure 126. St/Sto Versus θ, Compound Angle, 1 Row, m=1.0, x/d=17.6, z/d=-1.27

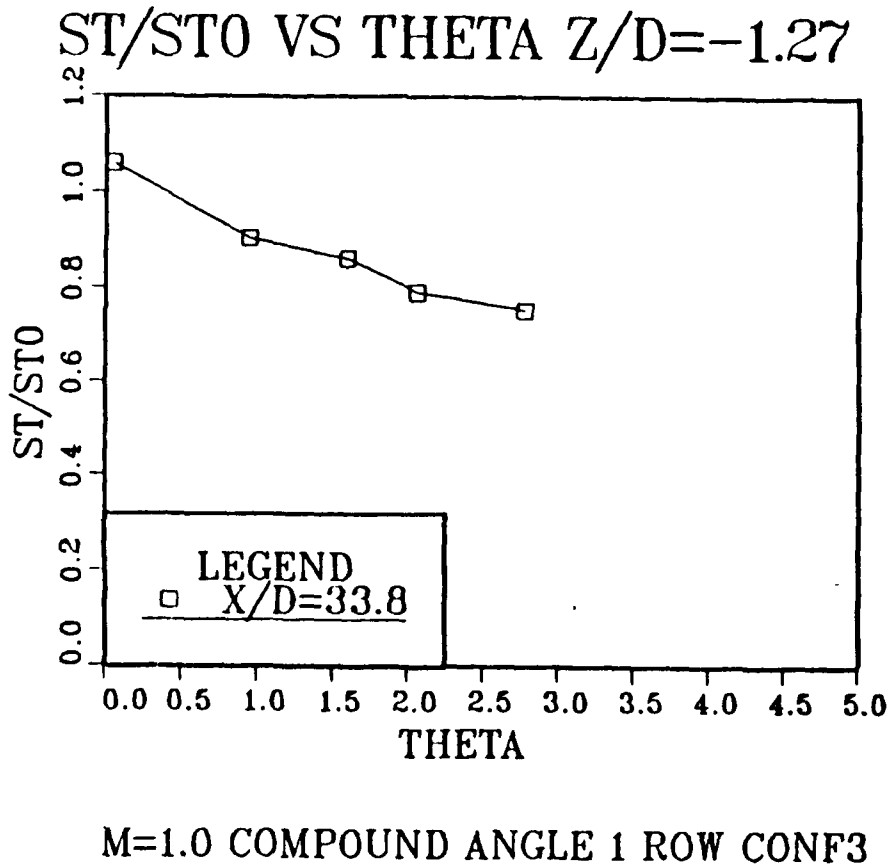


Figure 127. St/Sto Versus θ, Compound Angle, 1 Row, m=1.0, x/d=33.8, z/d=-1.27

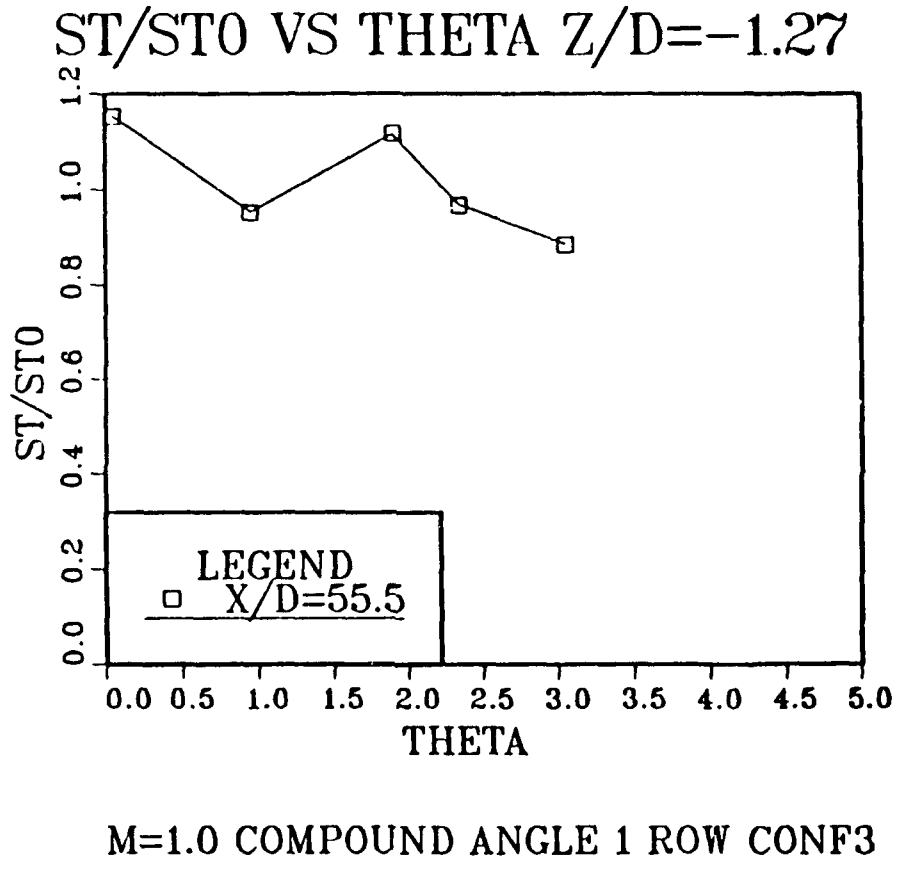


Figure 128. St/Sto Versus θ, Compound Angle, 1 Row, m=1.0, x/d=55.5, z/d=-1.27

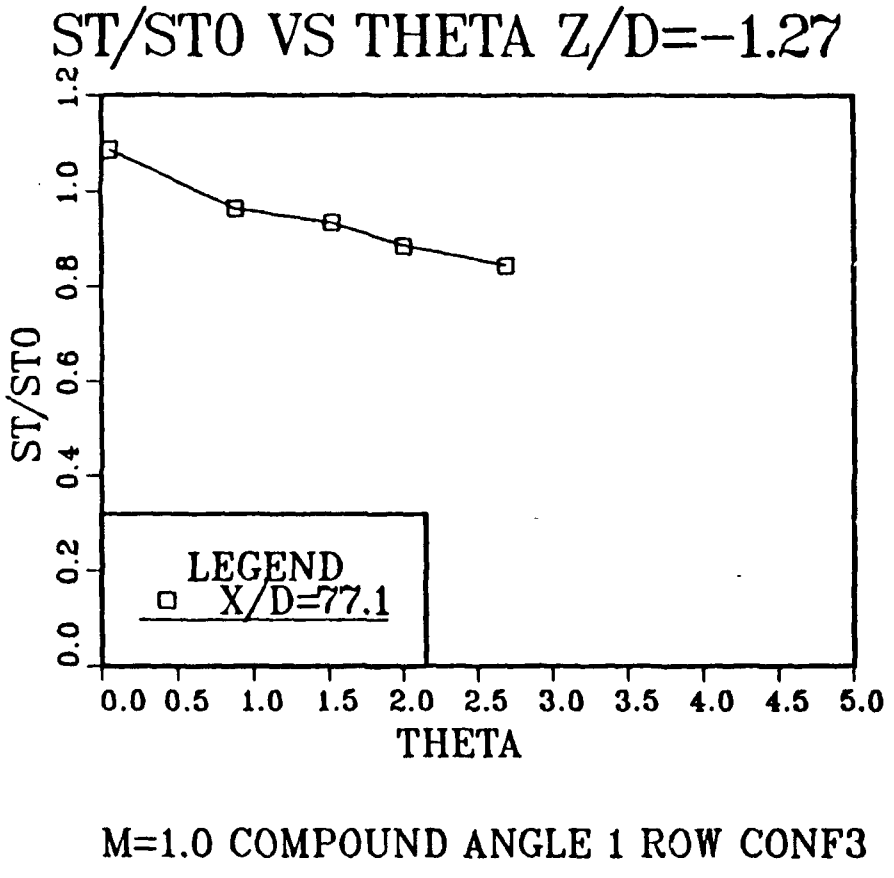


Figure 129. St/Sto Versus θ, Compound Angle, 1 Row, m=1.0, x/d=77.1, z/d=-1.27

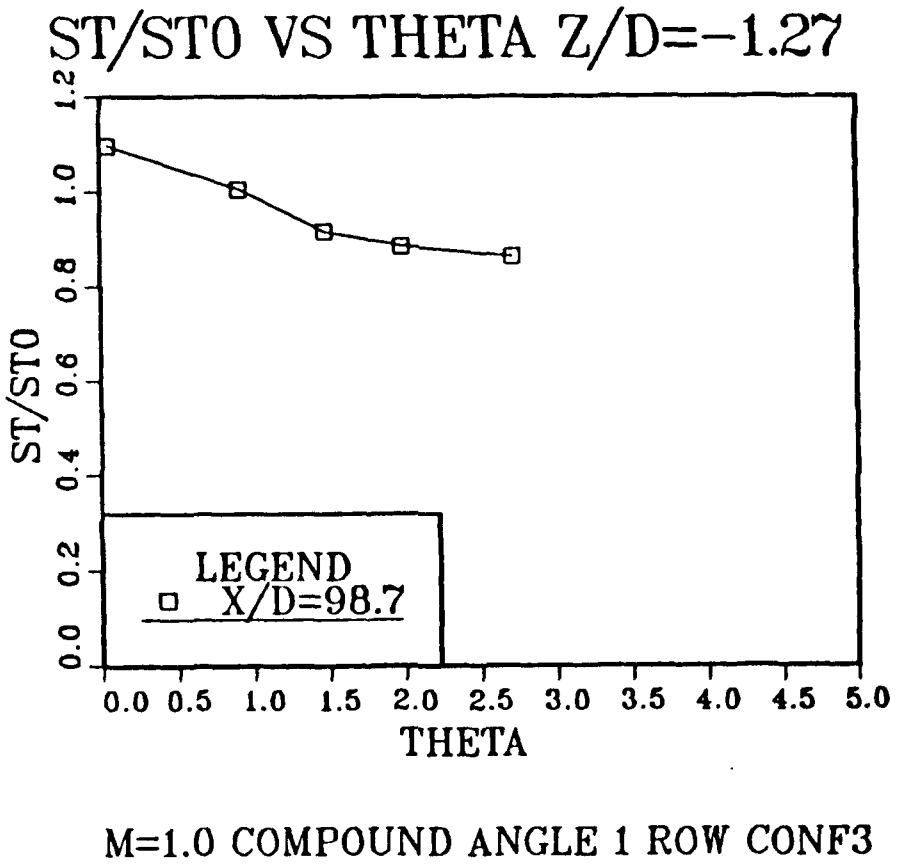


Figure 130. St/Sto Versus θ, Compound Angle, 1 Row, m=1.0, x/d=98.7, z/d=-1.27

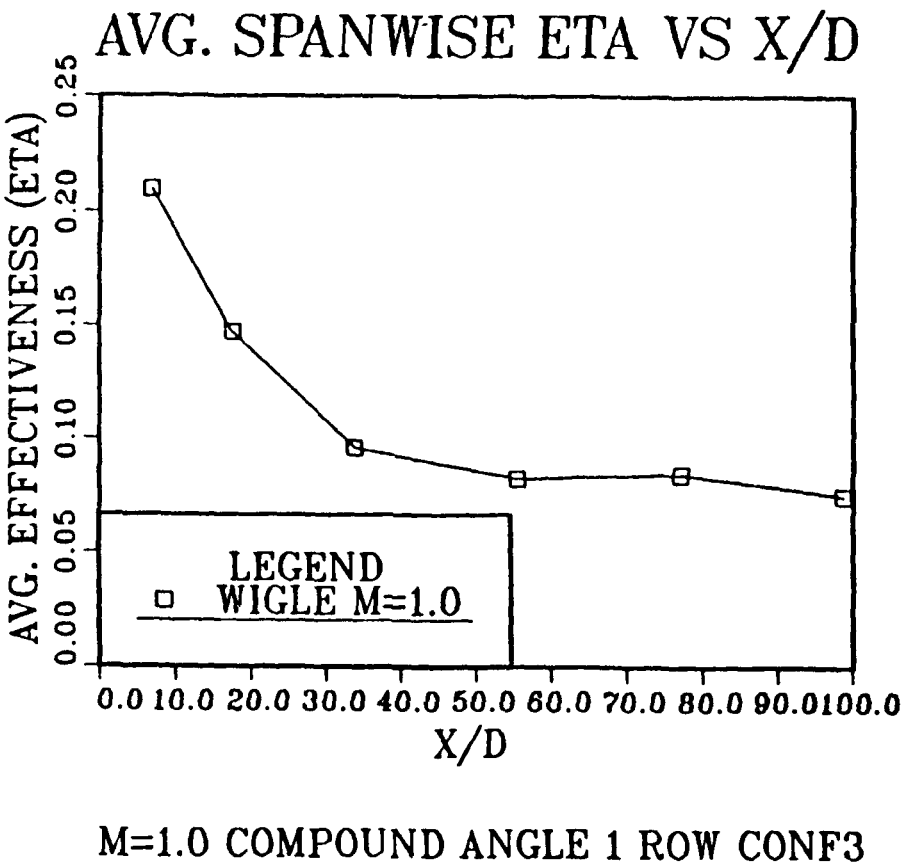


Figure 131. η Versus x/d, Compound Angle, 1 Row, m=1.0, Spanwise Average

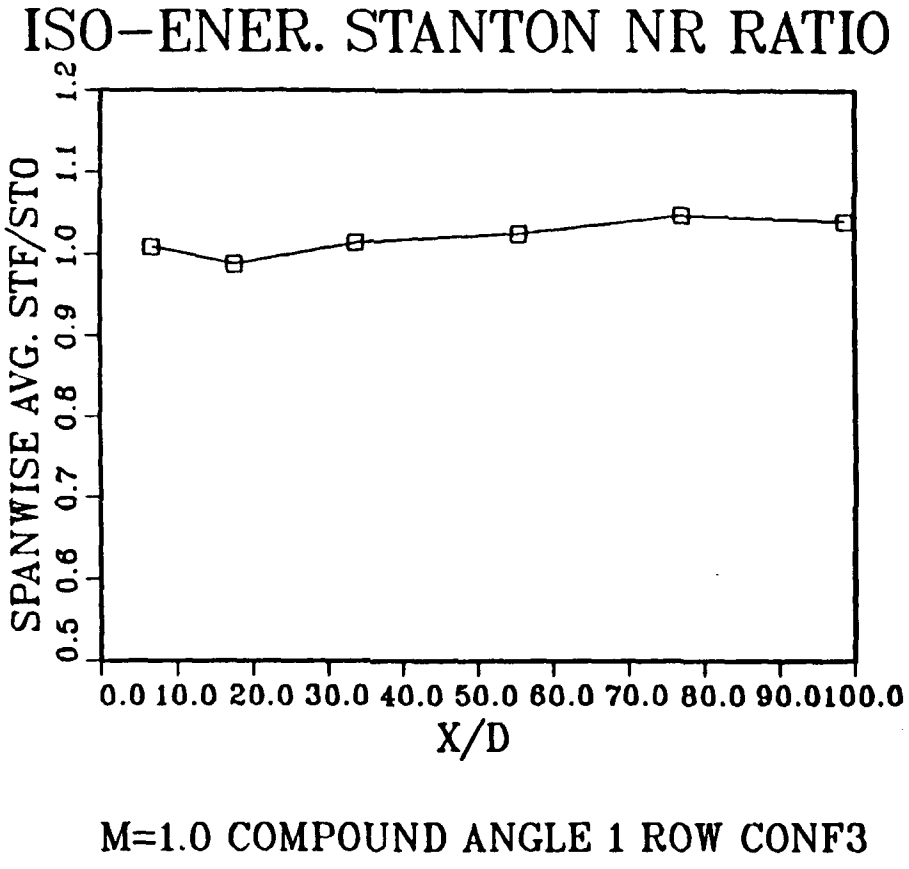


Figure 132. Stf/Sto Versus x/d, Compound Angle, 1 Row, m=1.0, Spanwise Average

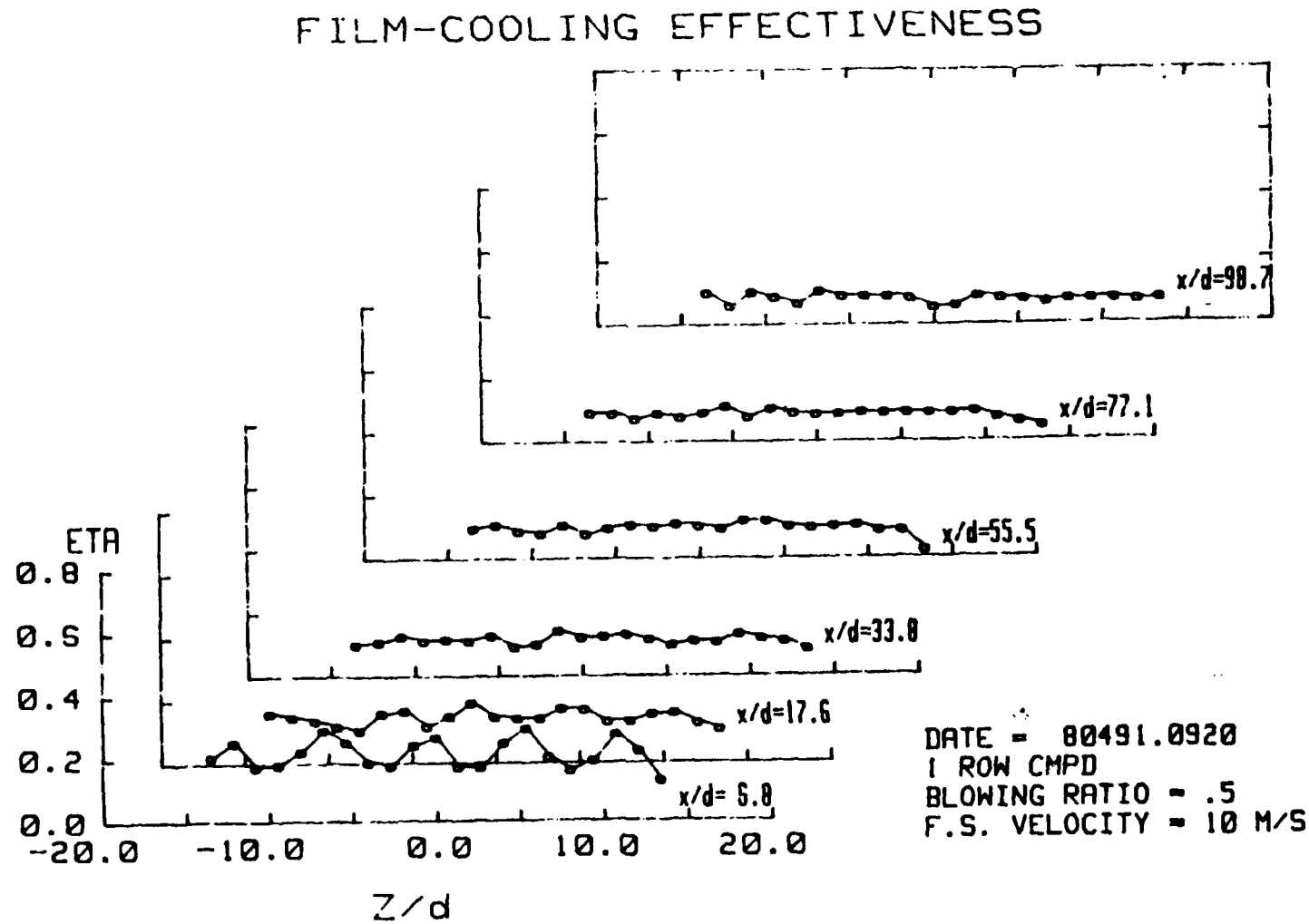


Figure 133. Spanwise Variation of η, Compound Angle, 1 Row, m=1.0

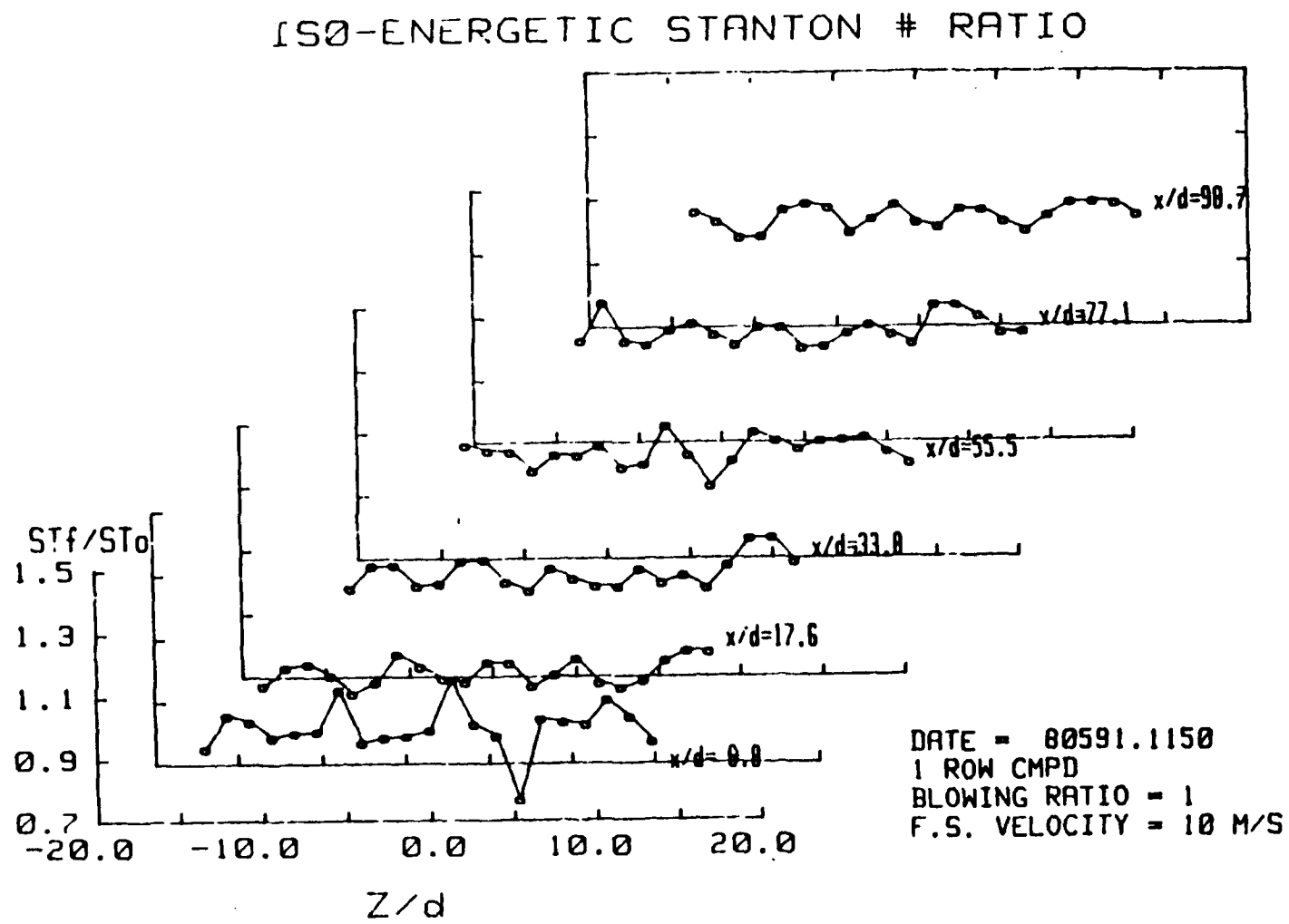


Figure 134. Spanwise Variation of Stf/Sto, Compound Angle, 1 Row, m=1.0

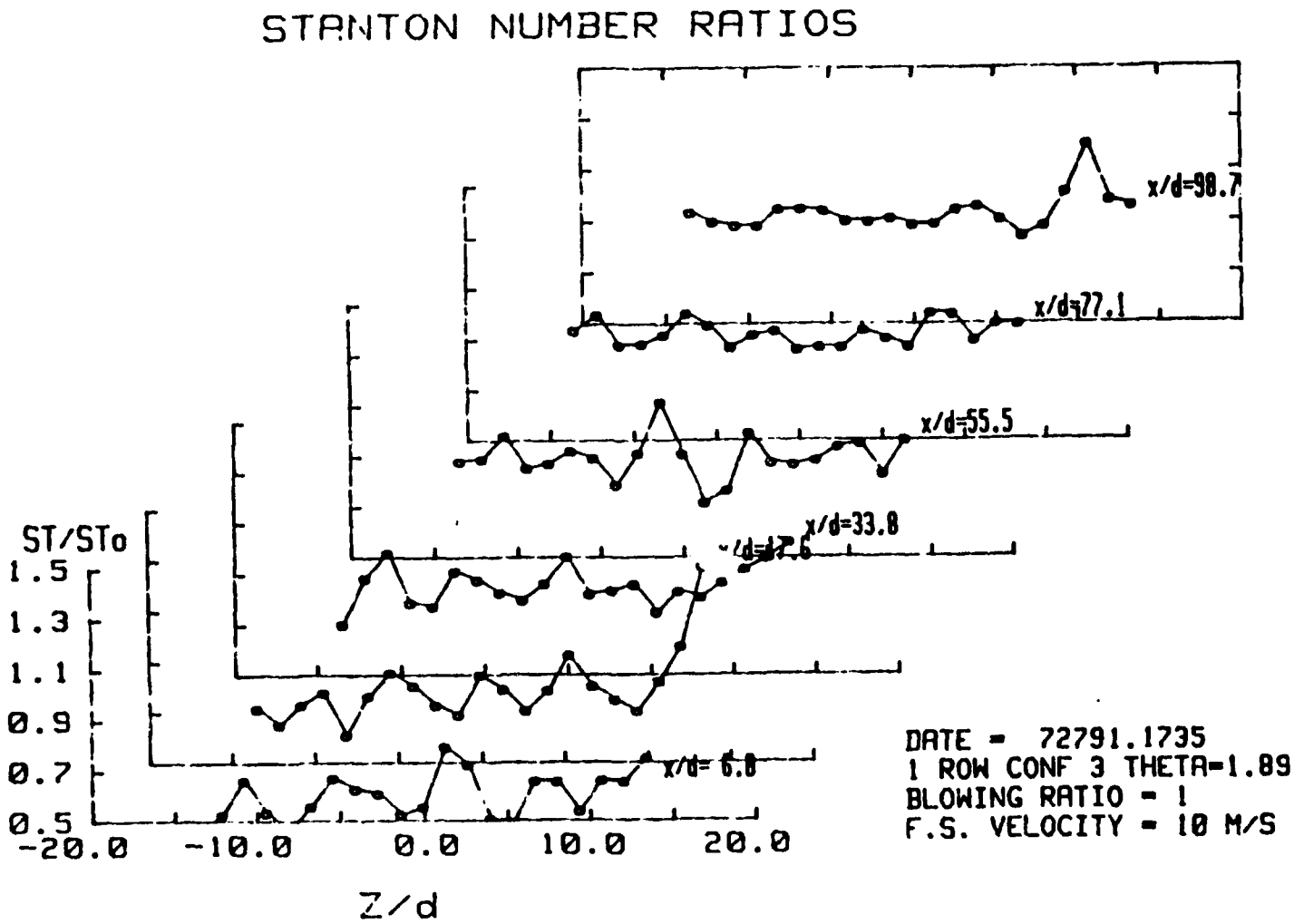


Figure 135. Spanwise Variation of St/Sto, Compound Angle, 1 Row, m=1.0, θ=1.89

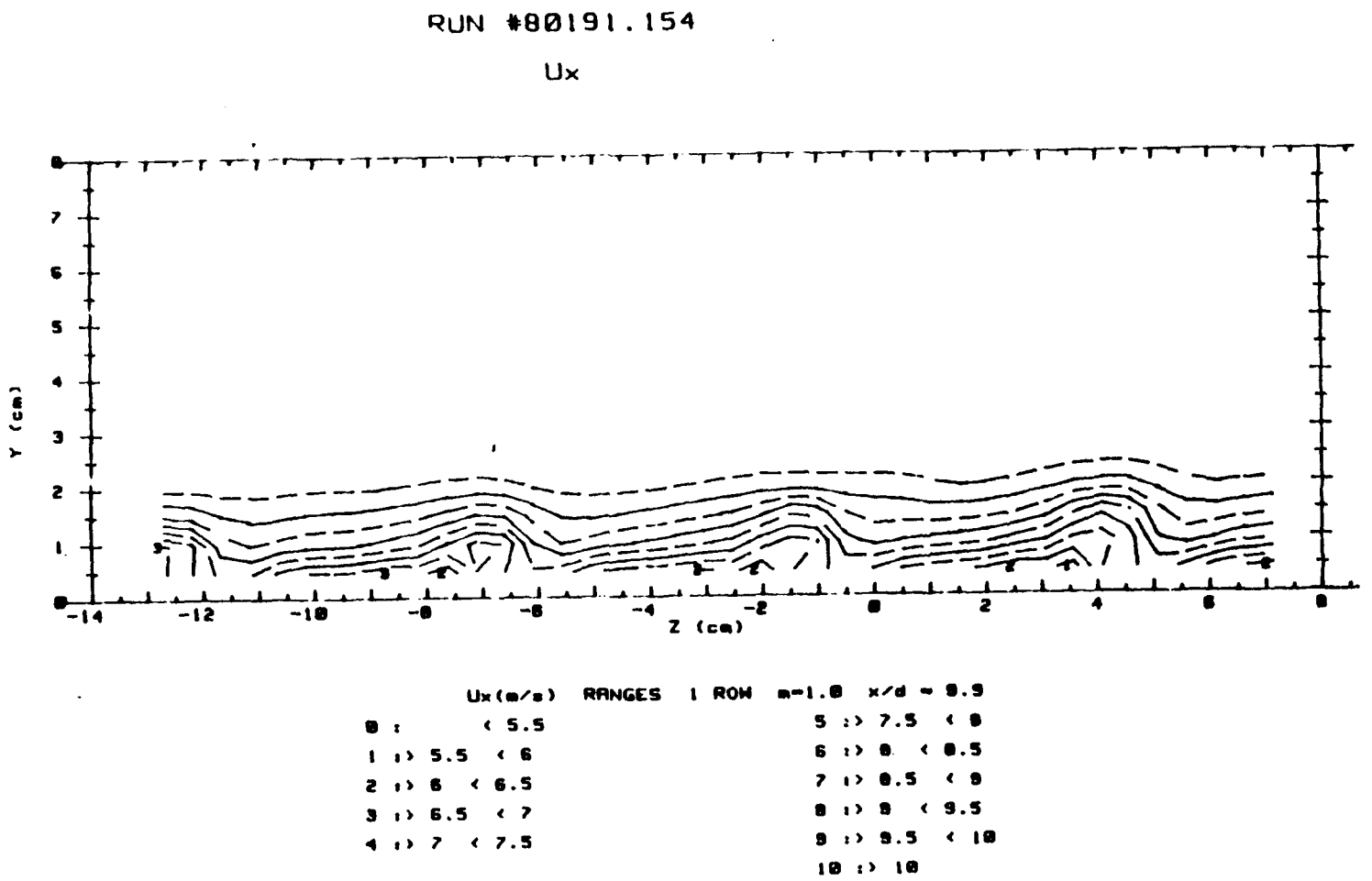


Figure 136. Streamwise Velocity Field, Compound Angle, 1 Row, m=1.0, x/d=9.9

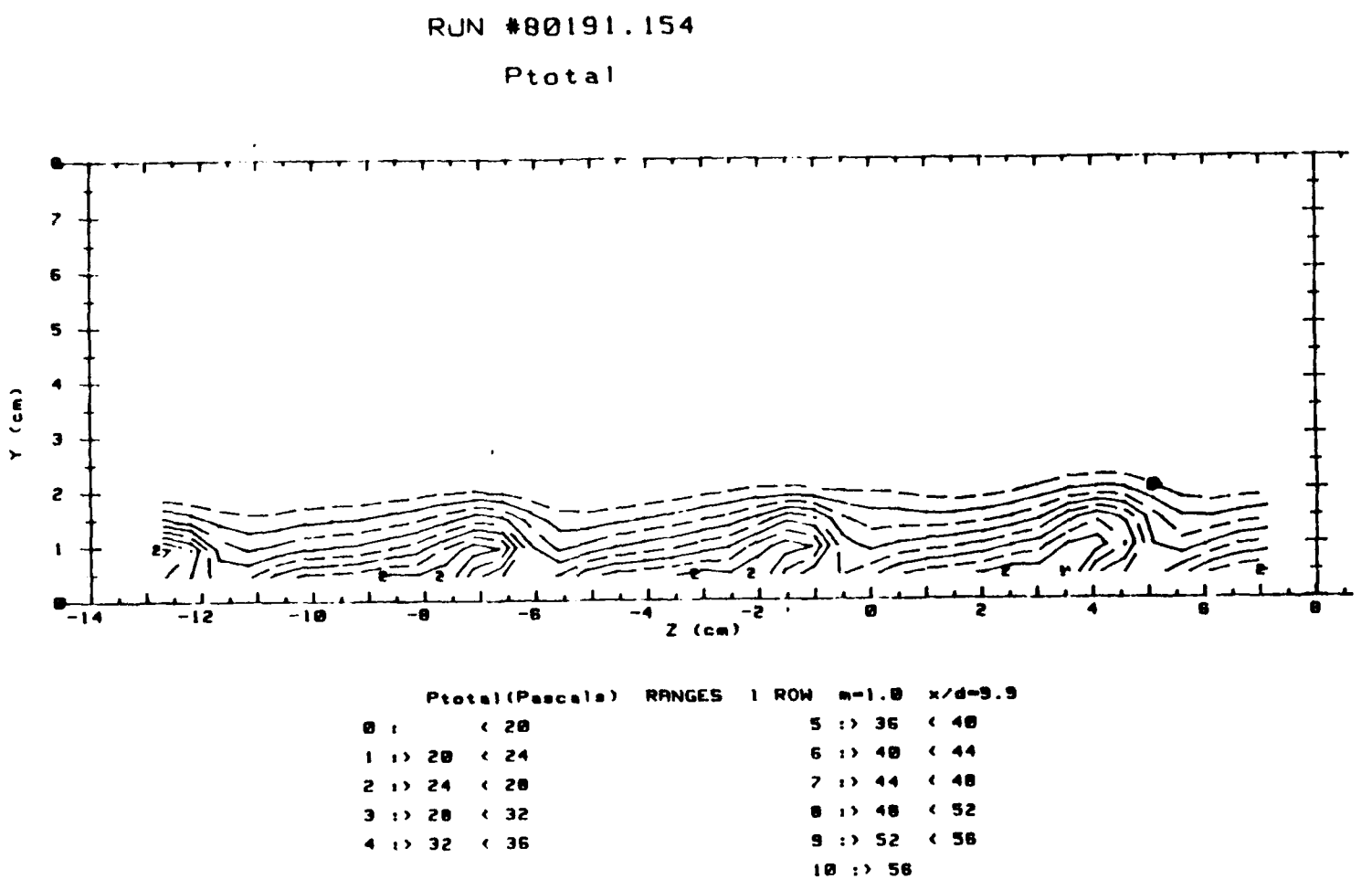


Figure 137. Streamwise Pressure Field, Compound Angle, 1 Row, m=1.0, x/d=9.9

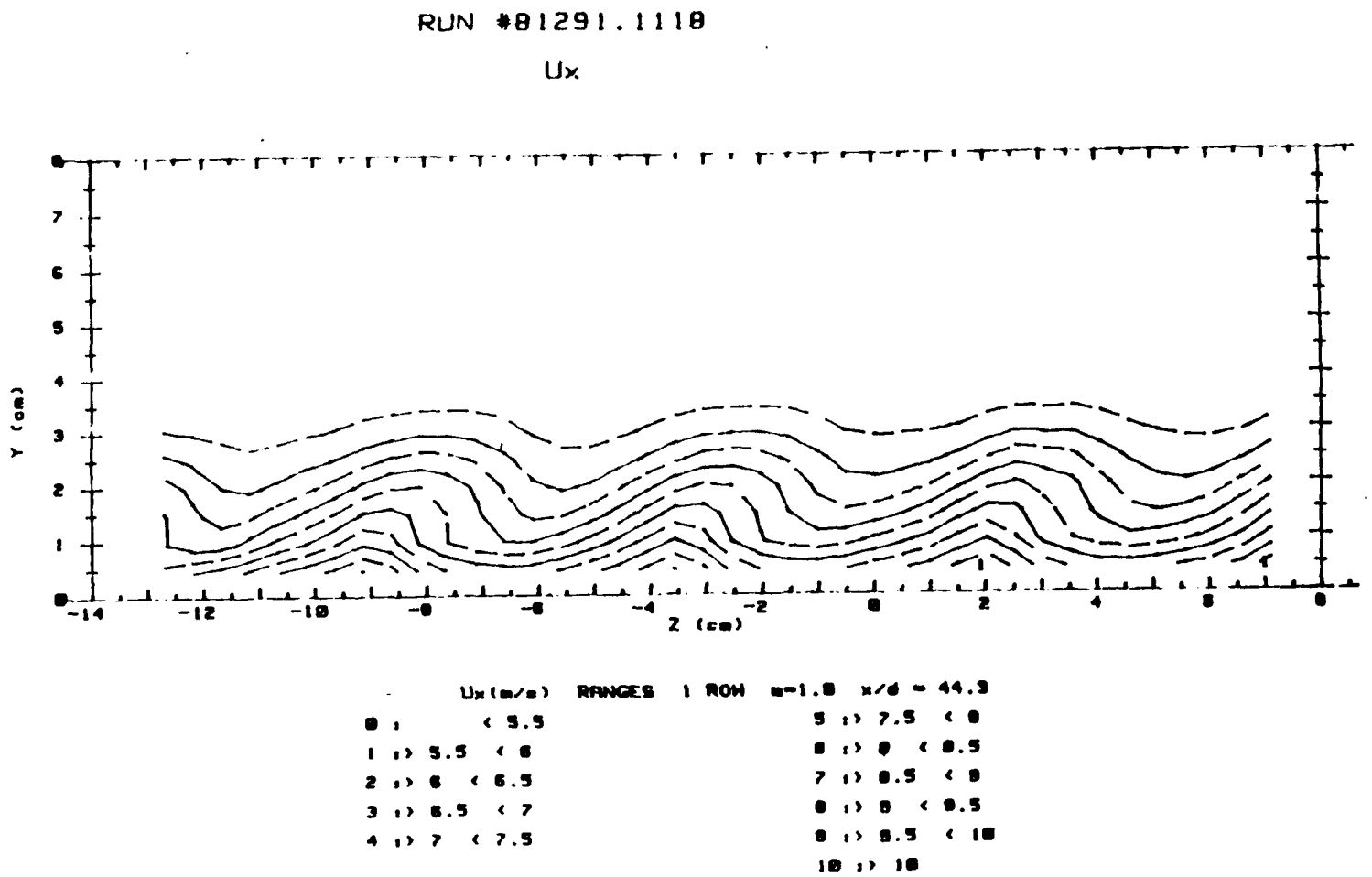


Figure 138. Streamwise Velocity Field, Compound Angle, 1 Row, m=1.0, xx/d=44.3

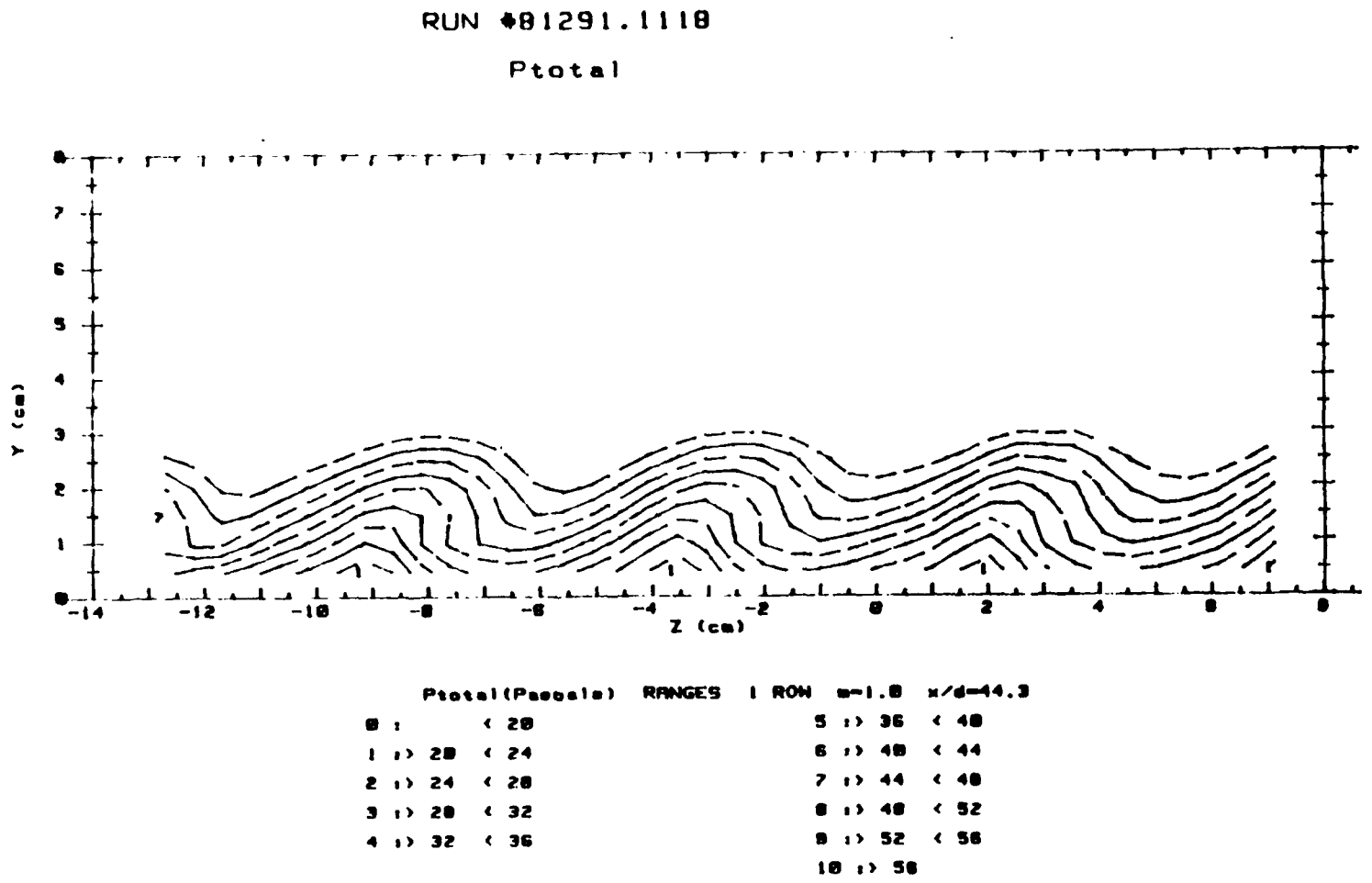


Figure 139. Streamwise Pressure Field, Compound Angle, 1 Row, m=1.0, x/d=44.3

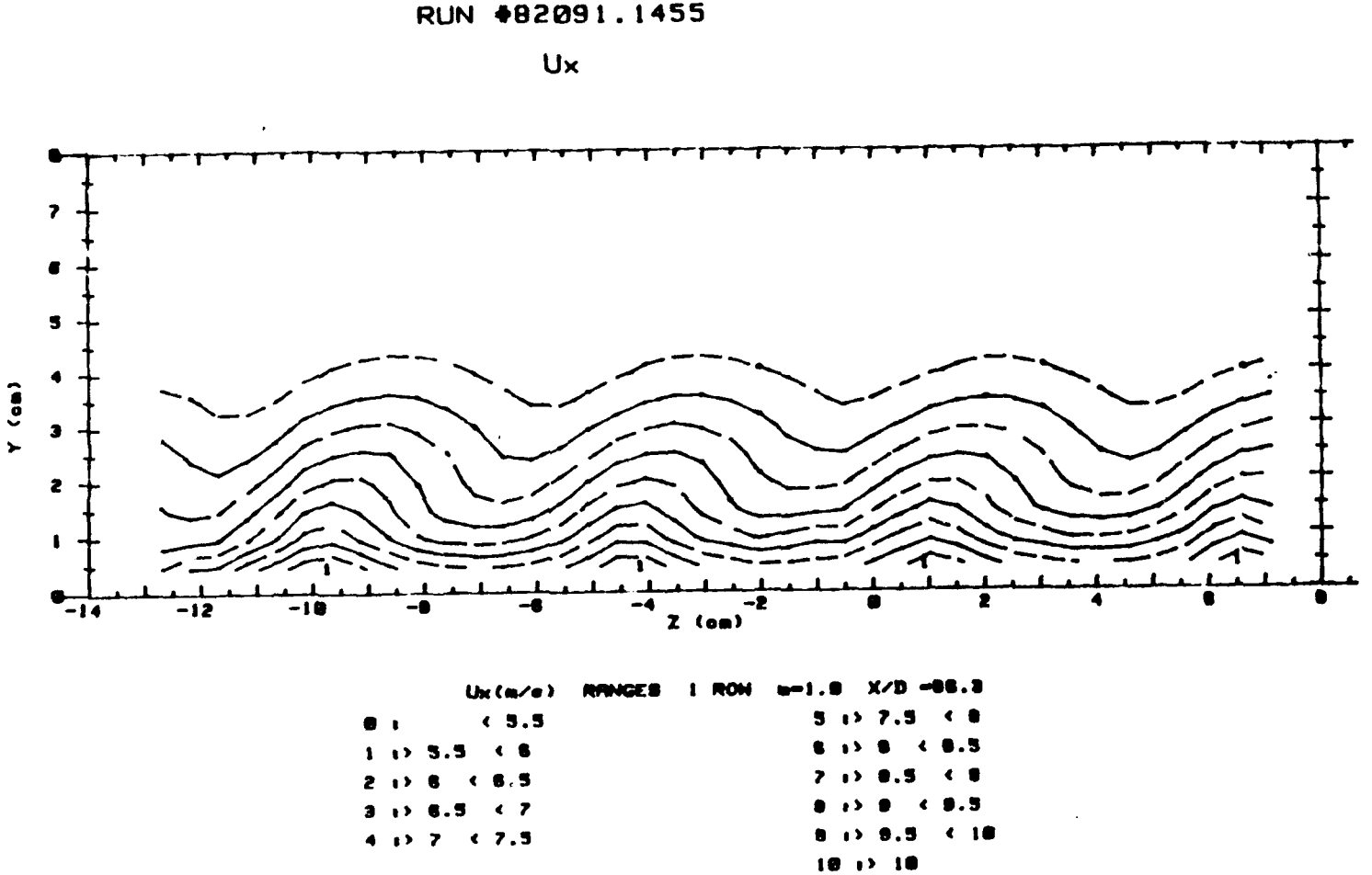


Figure 140. Streamwise Velocity Field, Compound Angle, 1 Row, m=1.0, x/d=86.3

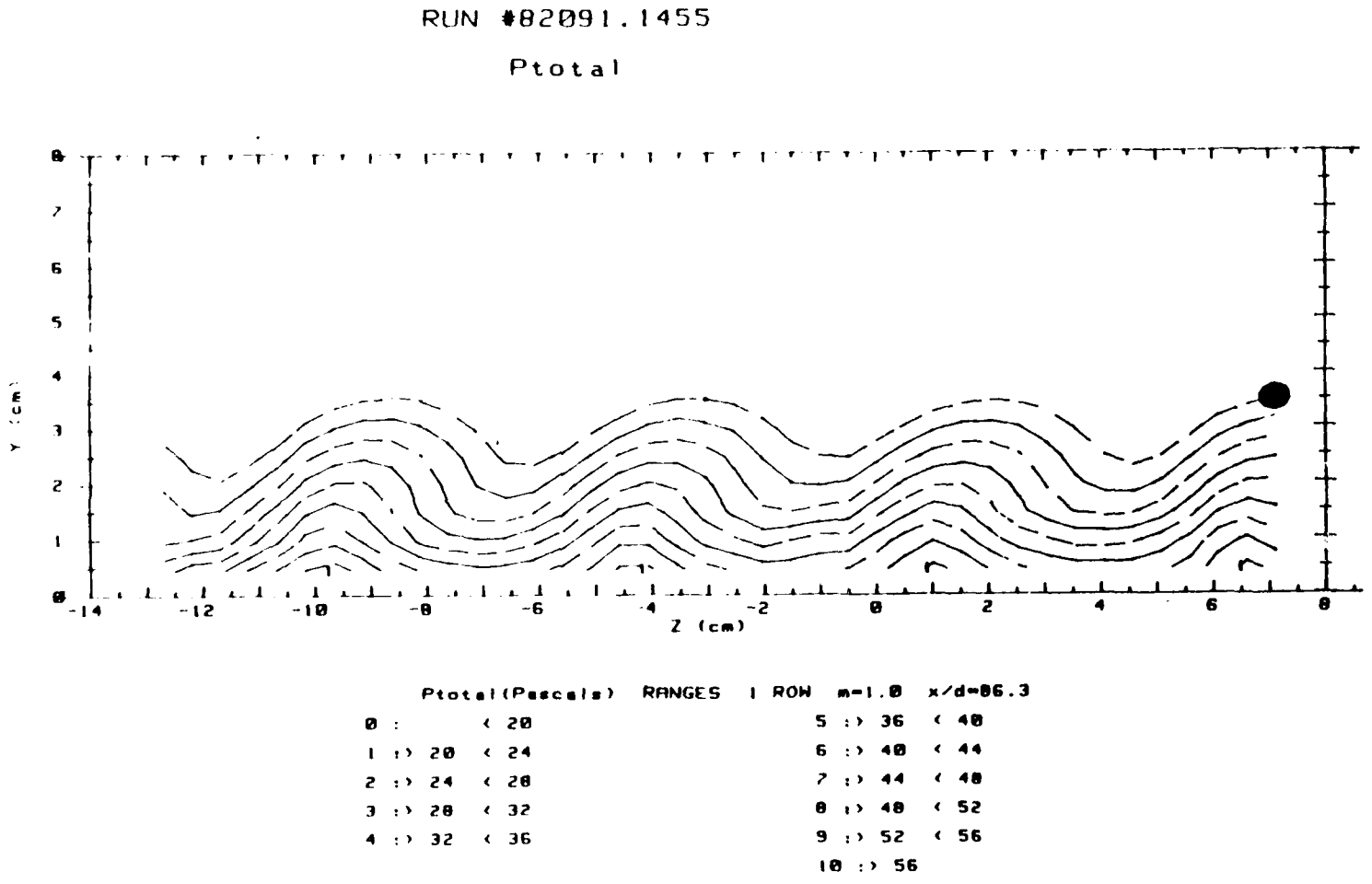


Figure 141. Streamwise Pressure Field, Compound Angle, 1 Row, m=1.0, x/d=86.3

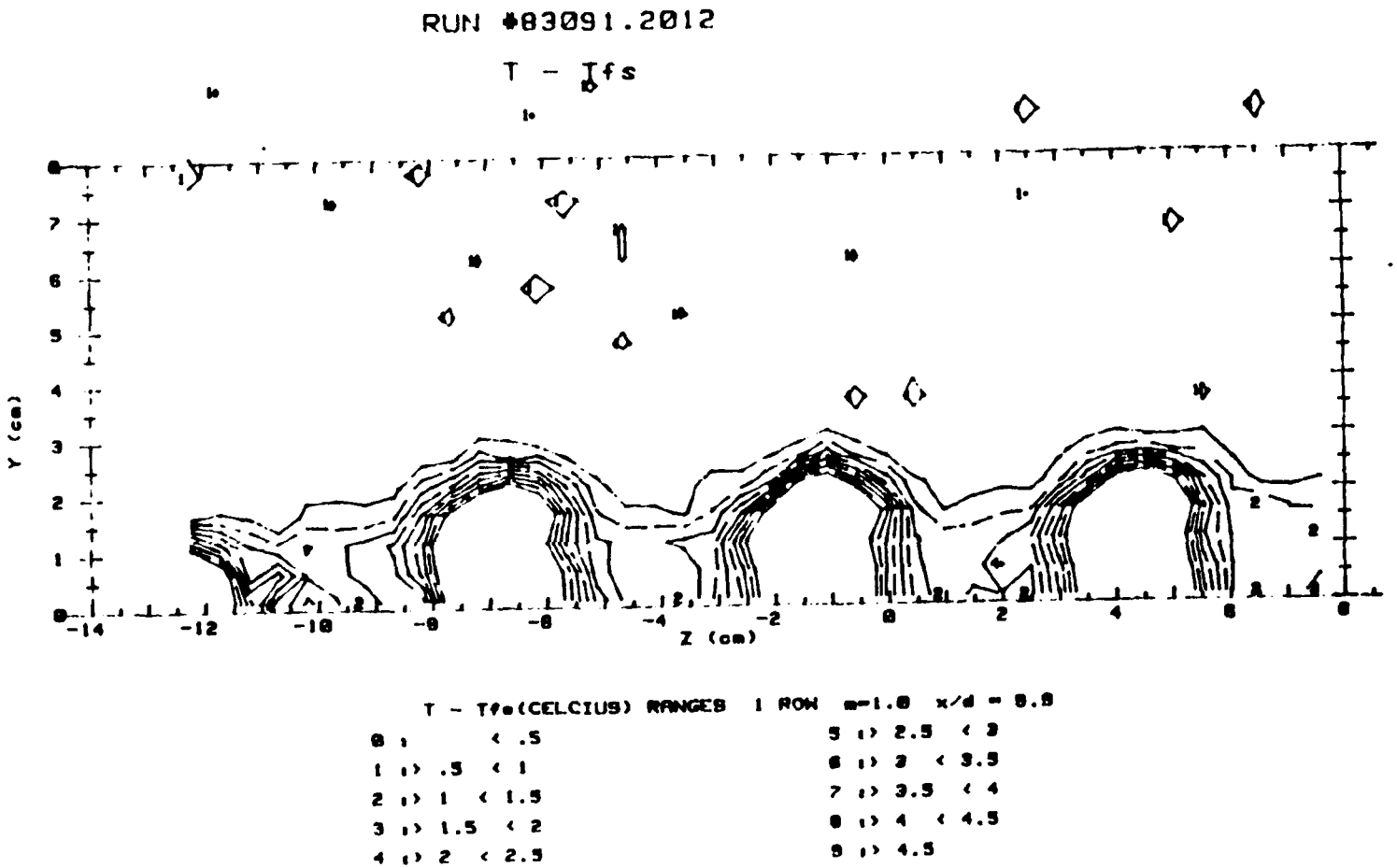


Figure 142. Streamwise Injectant Distribution, Compound Angle, 1 Row, m=1.0, x/d=9.9

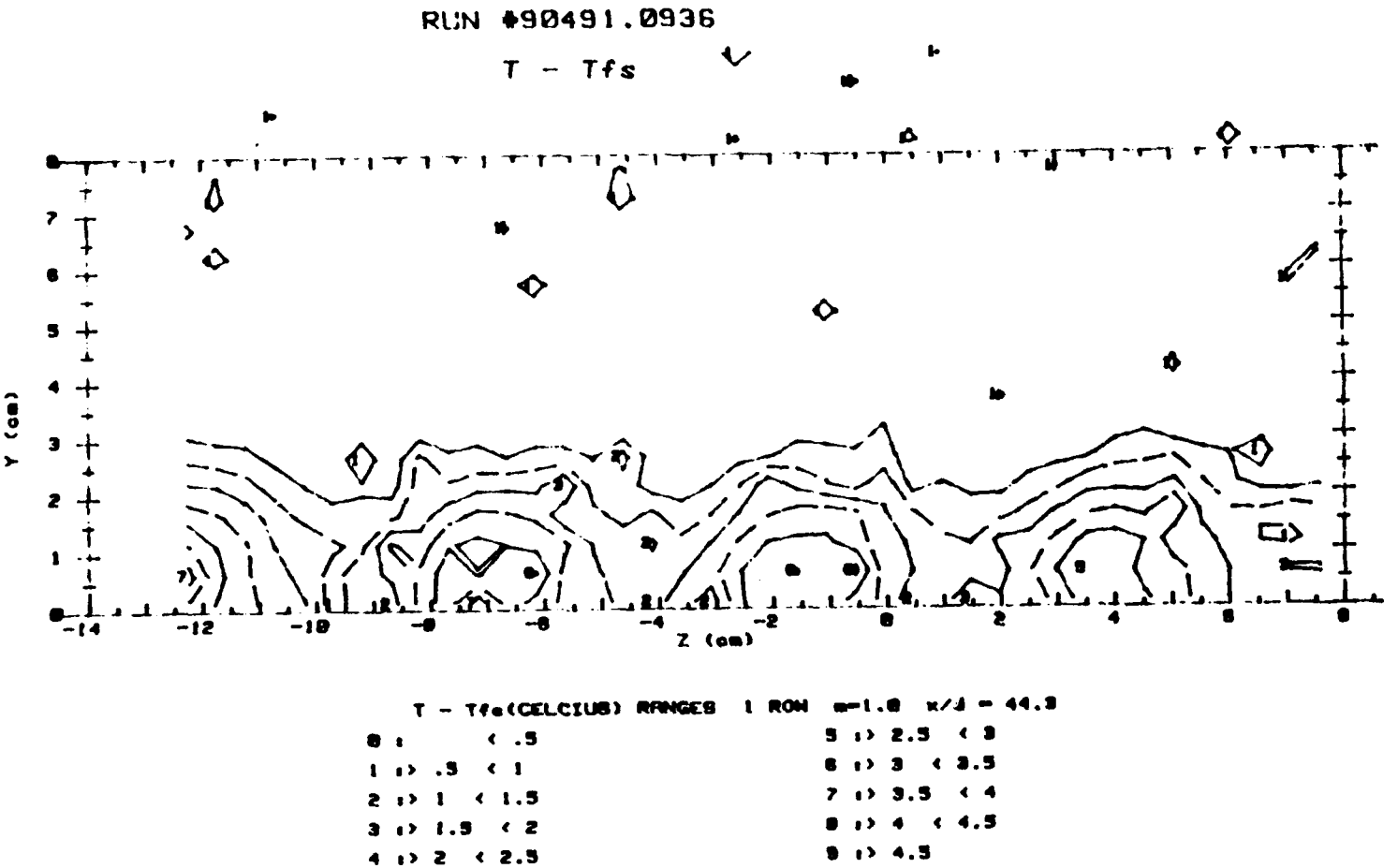


Figure 143. Streamwise Injectant Distribution, Compound Angle, 1 Row, m=1.0, x/d=44.3

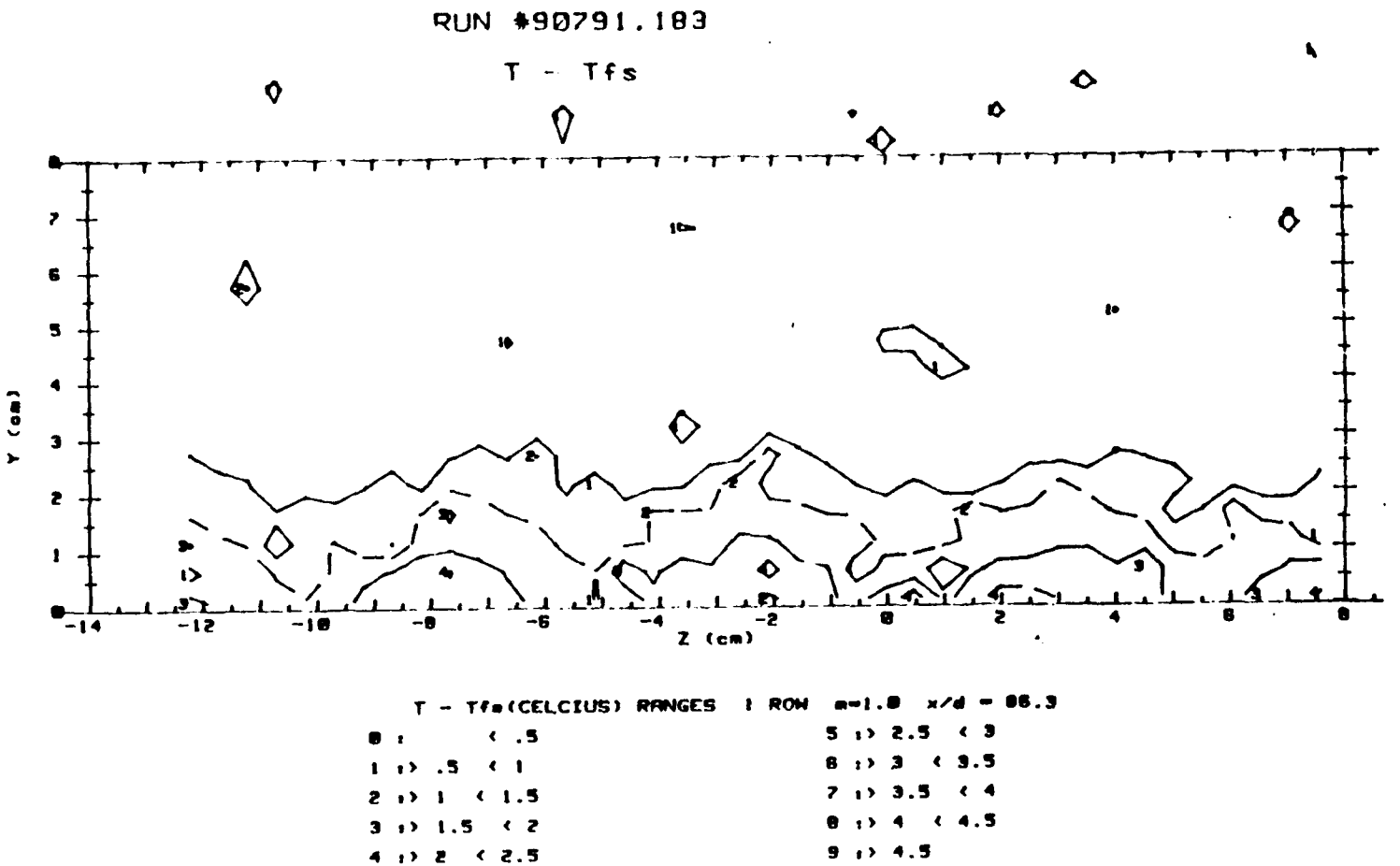


Figure 144. Streamwise Injectant Distribution, Compound Angle, 1 Row, m=1.0, x/d=86.3

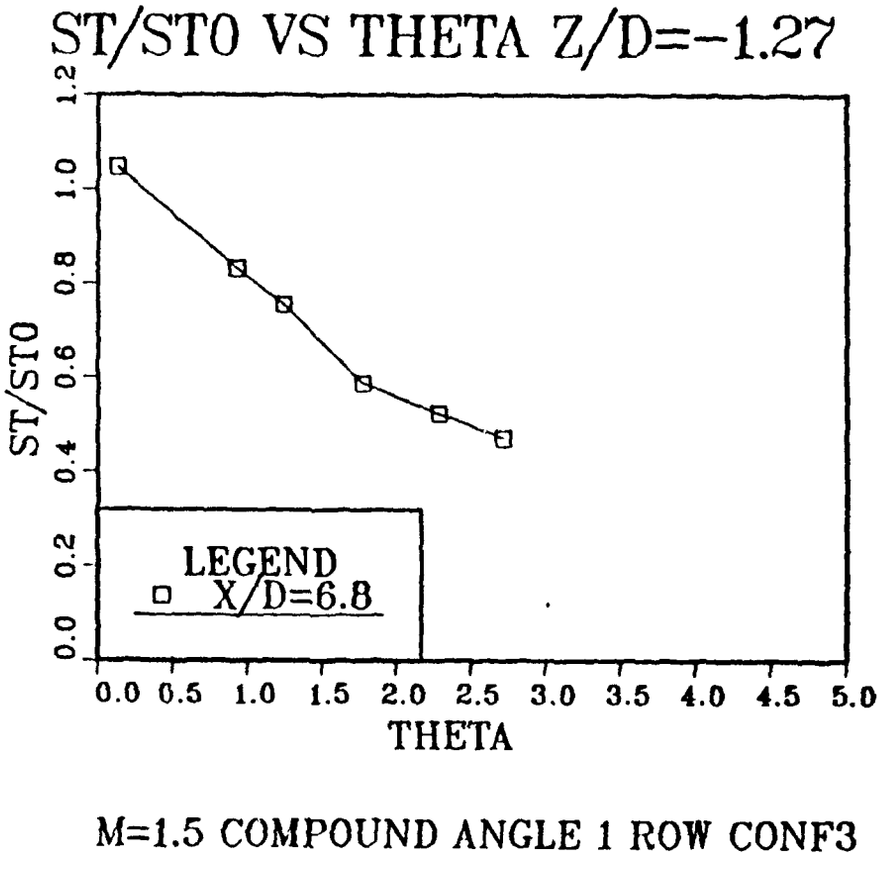


Figure 145. St/Sto Versus θ, Compound Angle, 1 Row, m=1.5, x/d=6.8, z/d=-1.27

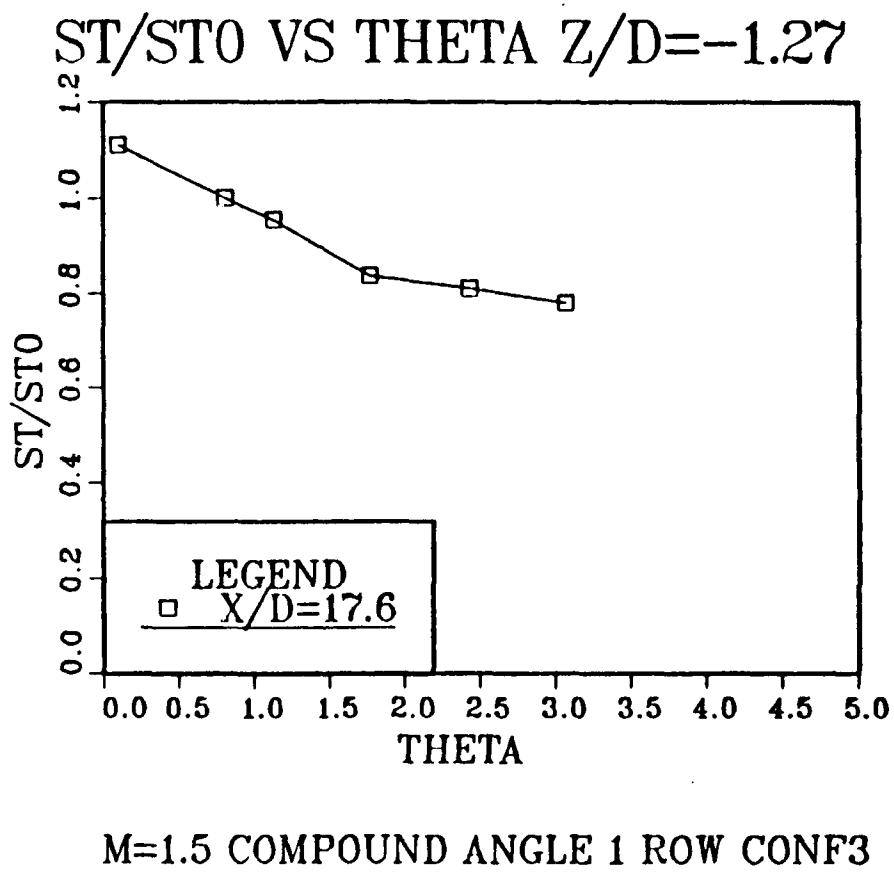


Figure 146. St/Sto Versus θ, Compound Angle, 1 Row, m=1.5, x/d=17.6, z/d=-1.27

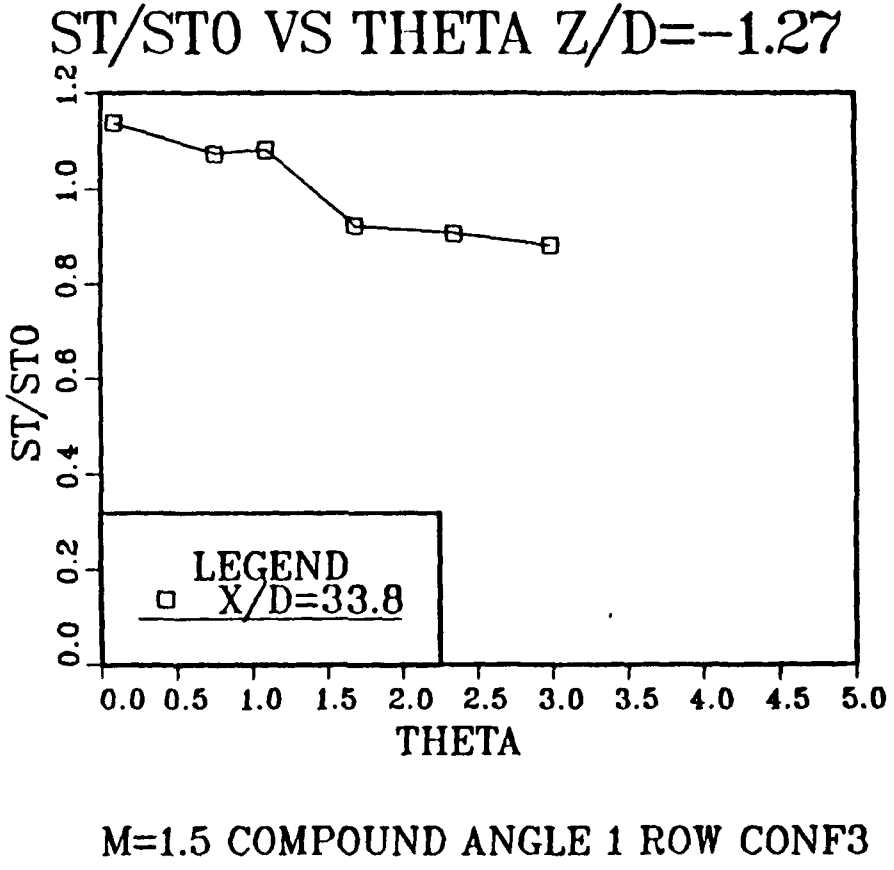


Figure 147. St/Sto Versus θ, Compound Angle, 1 Row, m=1.5, x/d=33.8, z/d=-1.27

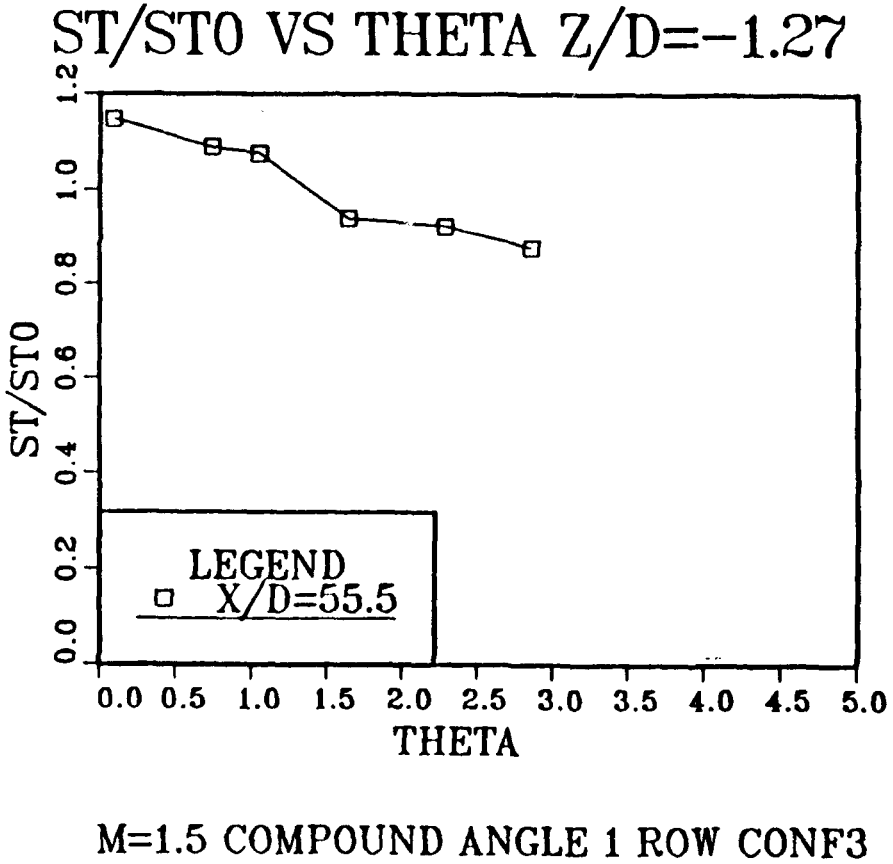


Figure 148. St/Sto Versus θ, Compound Angle, 1 Row, m=1.5, x/d=55.5, z/d=-1.27

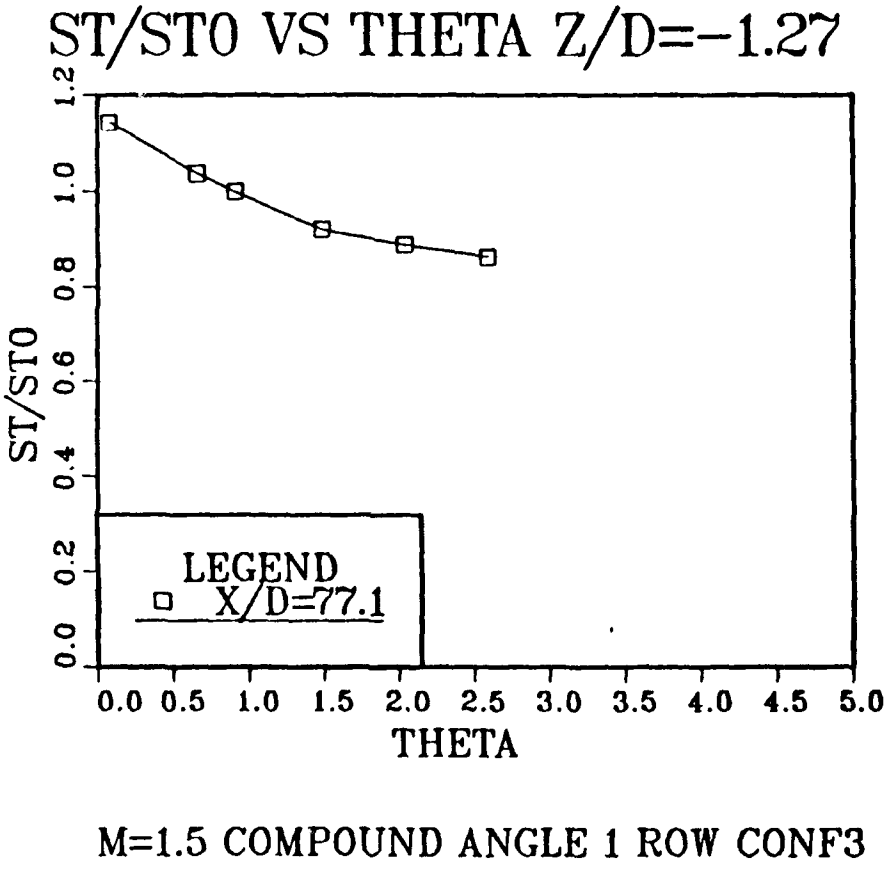


Figure 149. St/Sto Versus θ, Compound Angle, 1 Row, m=1.5, x/d=77.1, z/d=-1.27

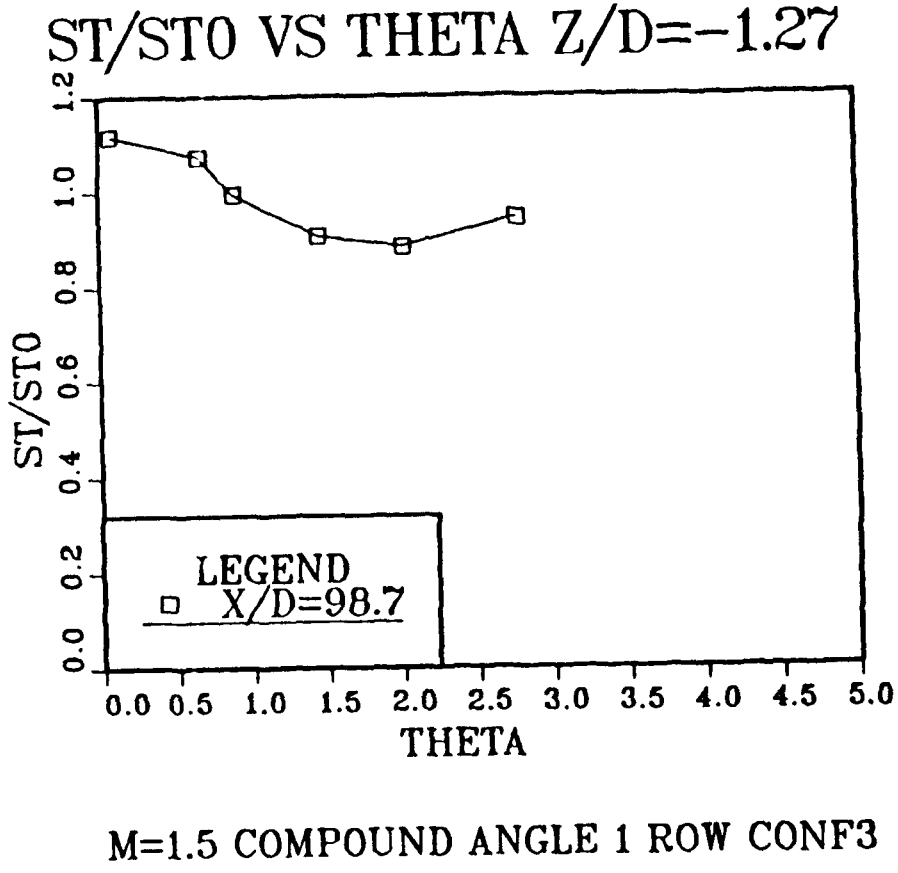


Figure 150. St/Sto Versus θ, Compound Angle, 1 Row, m=1.5, x/d=98.7, z/d=-1.27

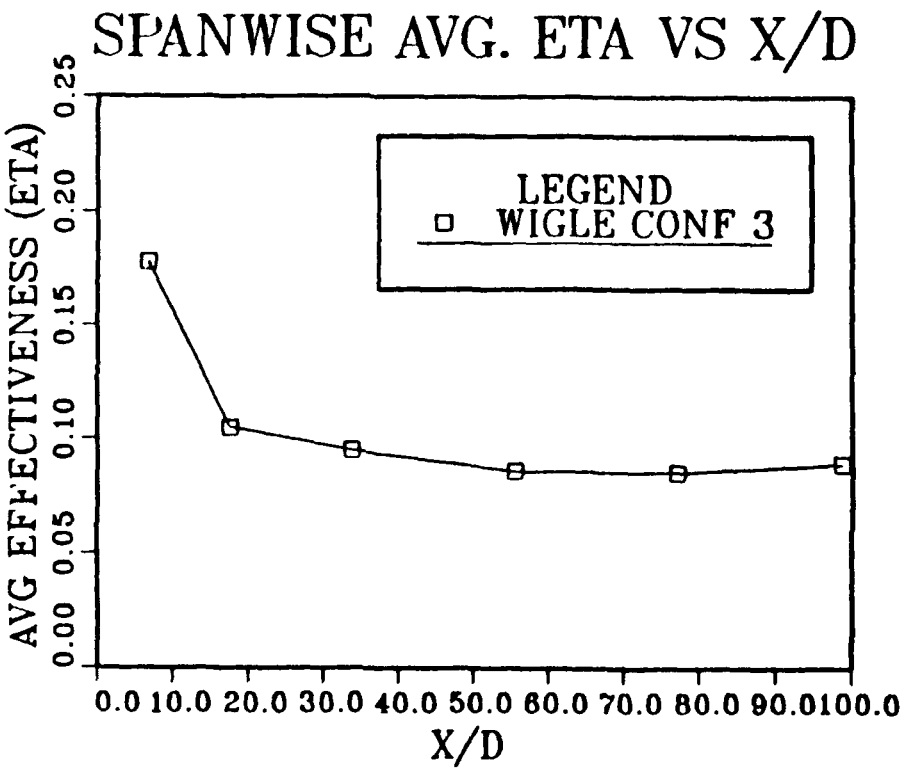


Figure 151. η Versus x/d, Compound Angle, 1 Row, m=1.5, Spanwise Average

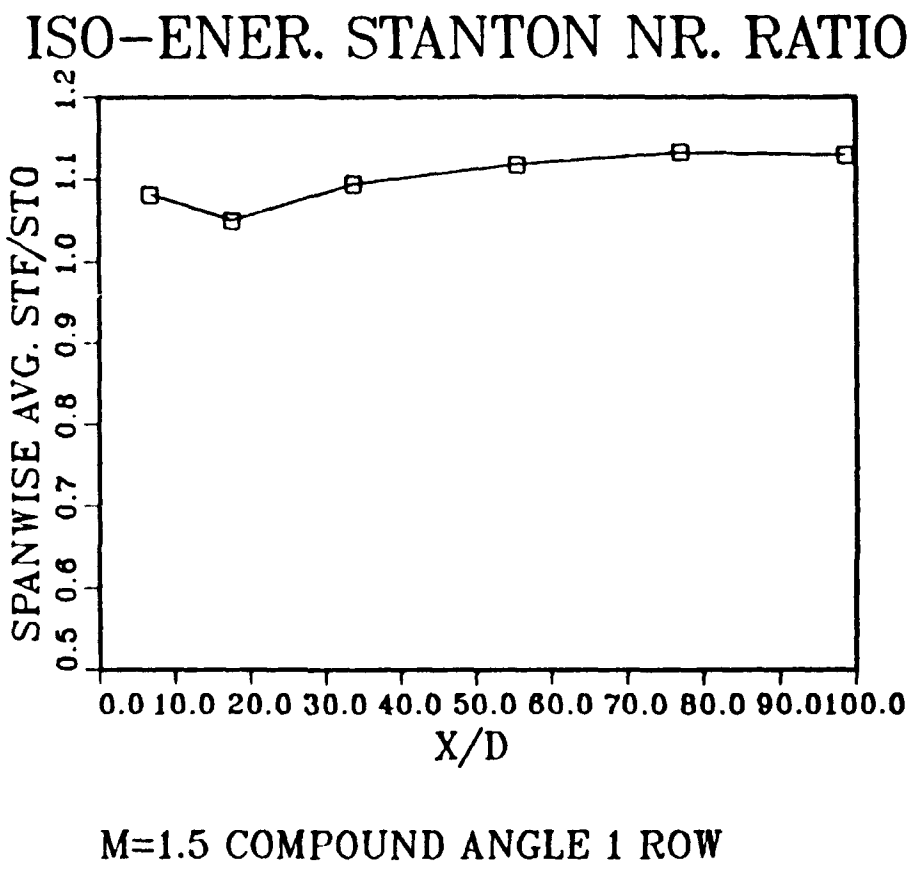


Figure 152. Stf/Sto Versus x/d, Compound Angle, 1 Row, m=1.5, Spanwise Average

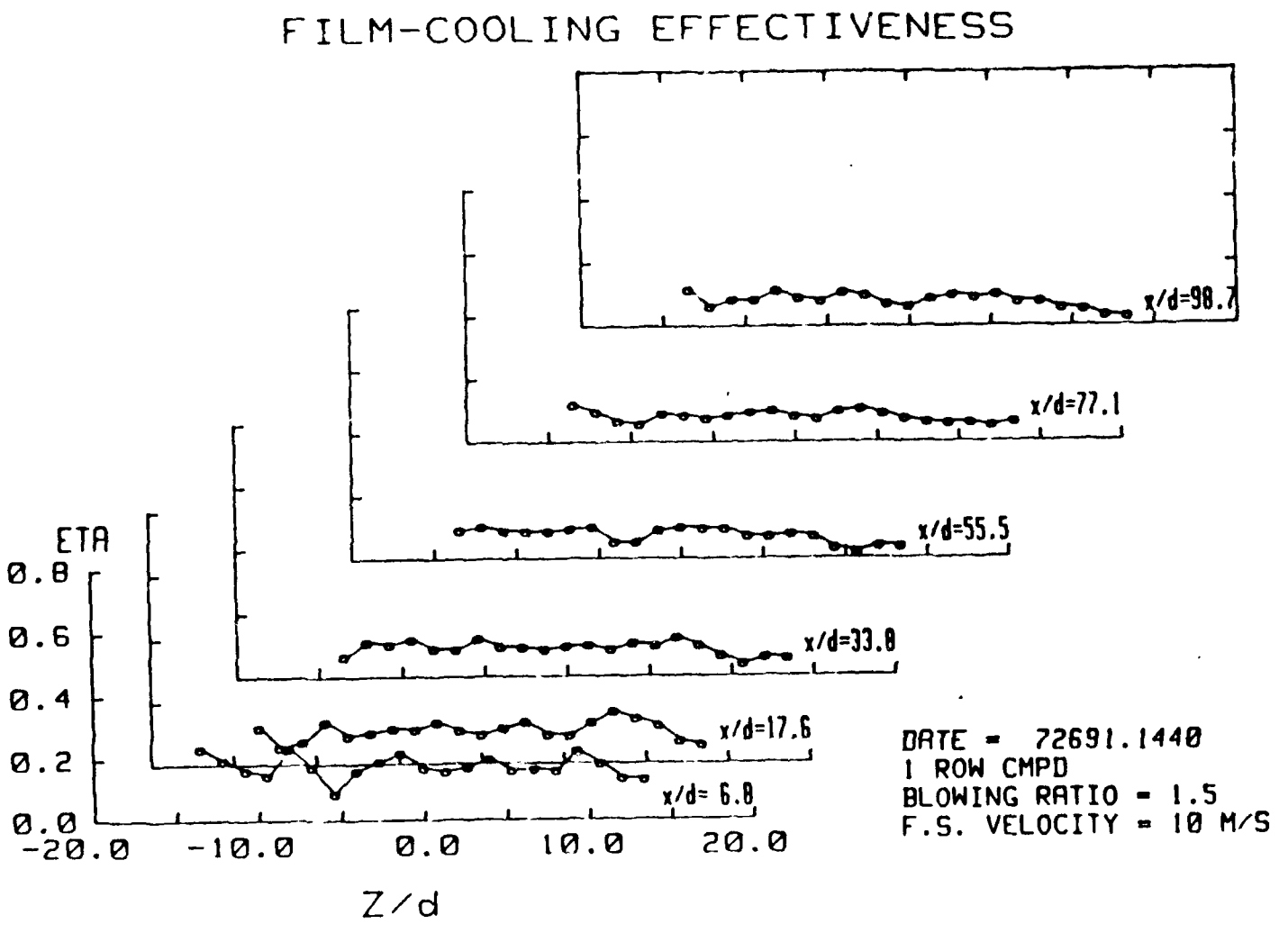


Figure 153. Spanwise Variation of η, Compound Angle, 1 Row, m=1.5

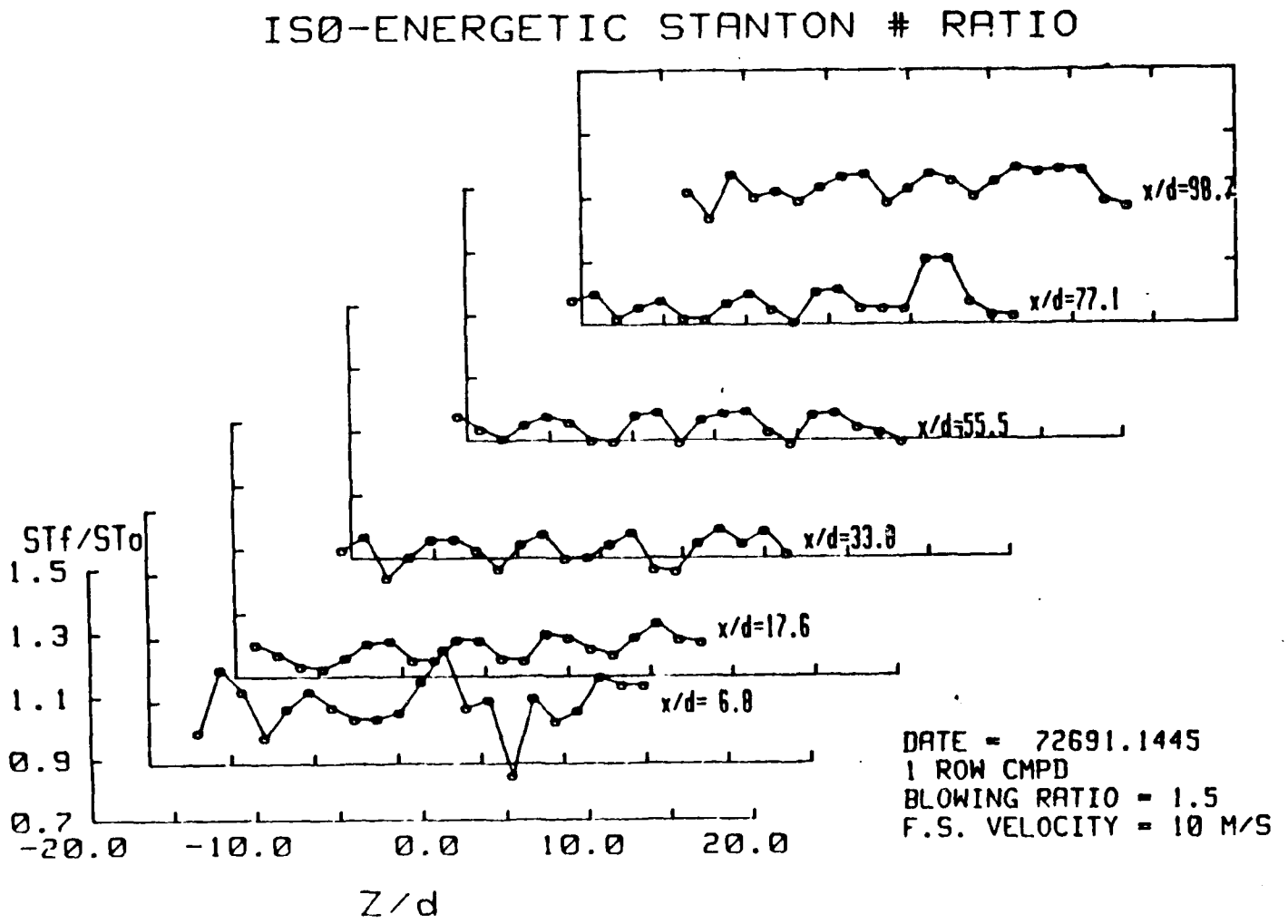


Figure 154. Spanwise Variation of Stf/Sto, Compound Angle, 1 Row, m=1.5

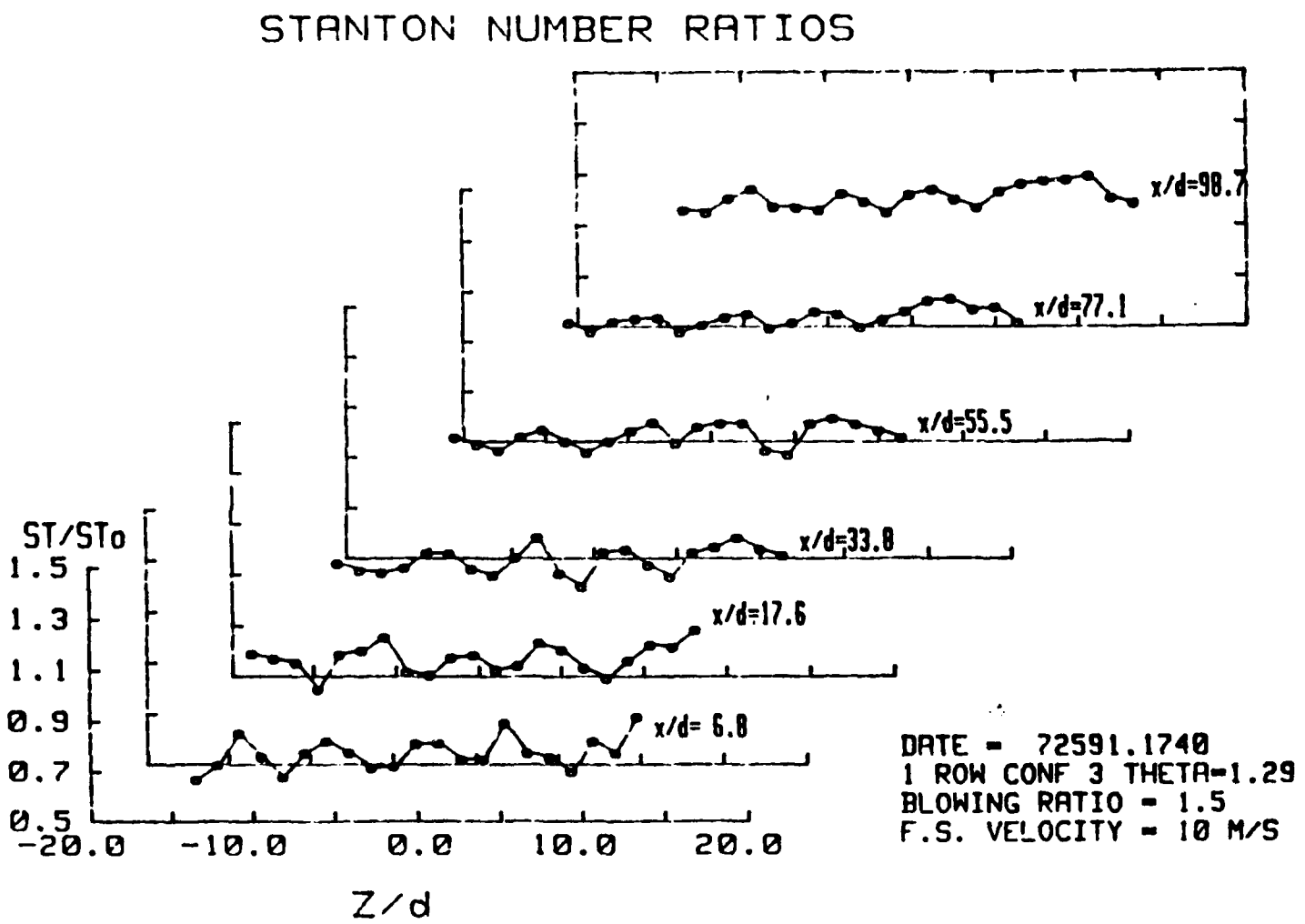


Figure 155. Spanwise Variation of St/Sto, Compound Angle, 1 Row, m=1.5, θ=1.5

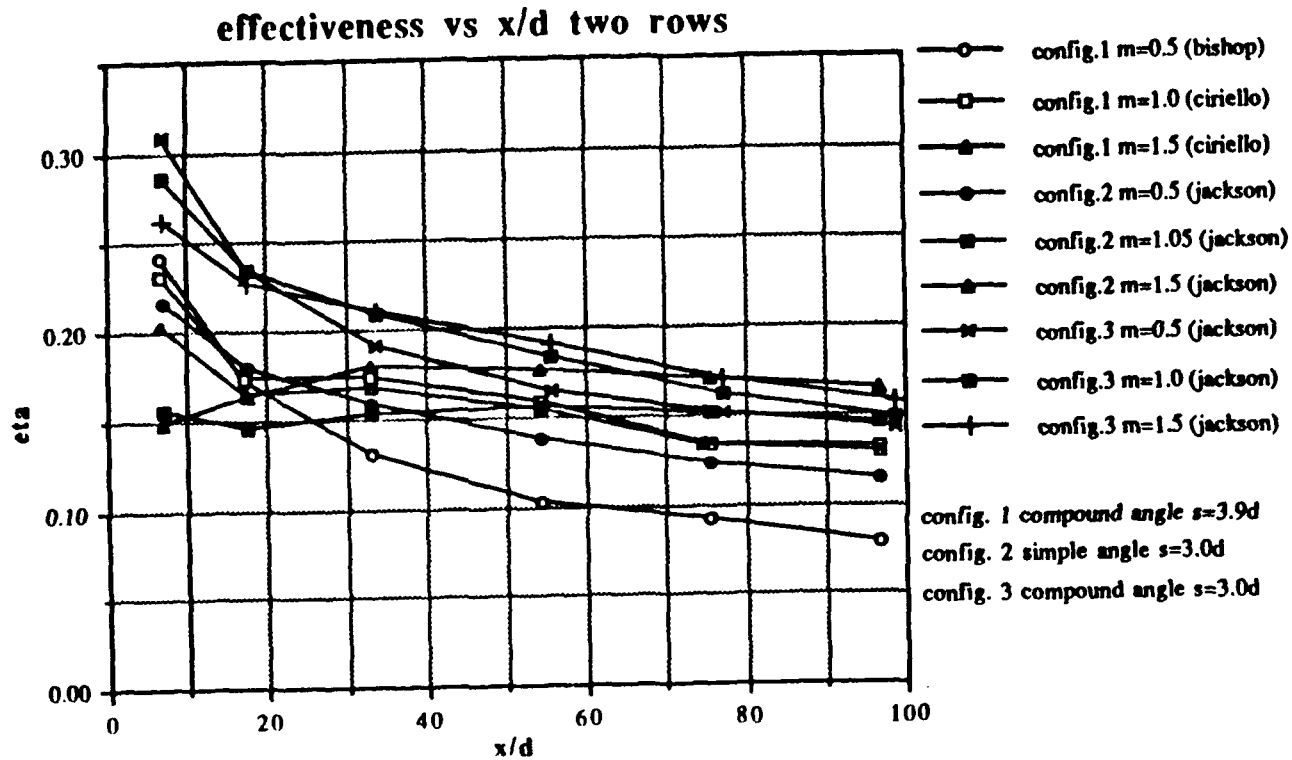


Figure 156. Comparison of Two Row Adiabatic Effectiveness as Dependent Upon x/d, for Compound and Simple Angle Configurations

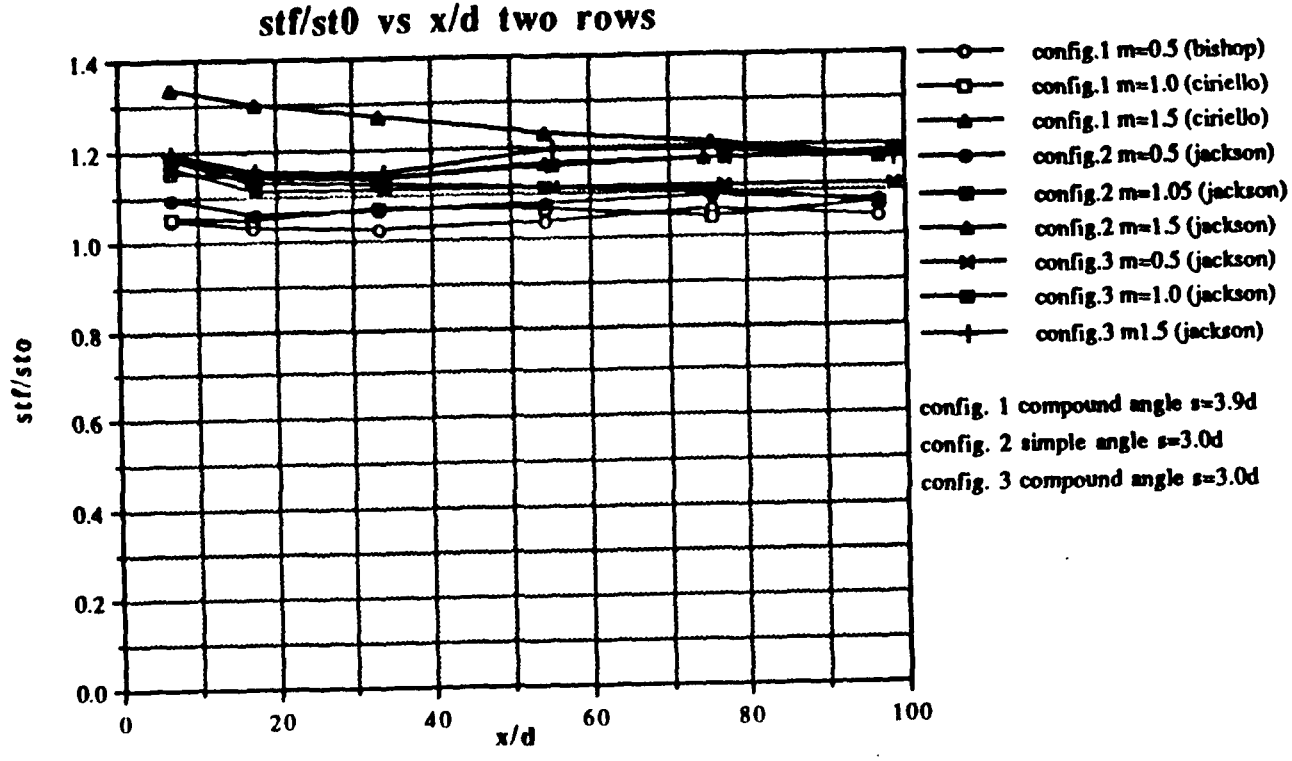


Figure 157. Comparison of Two Row Stf/Sto as Dependent Upon x/d for Compound and Simple Angle Configurations

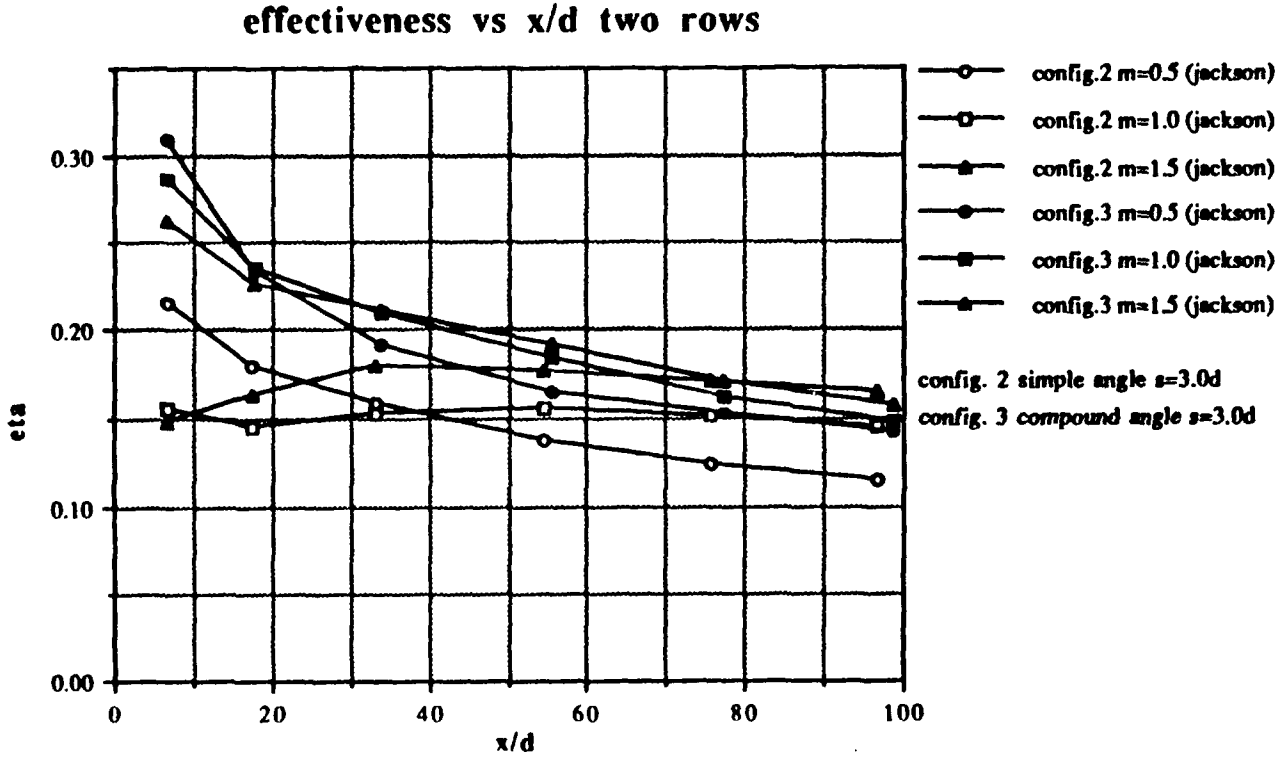


Figure 158. Comparisons of Two Row Adiabatic Effectiveness as Dependent Upon x/d for Configuration 2 (Simple Angle), and Configuration 3 (Compound Angle)

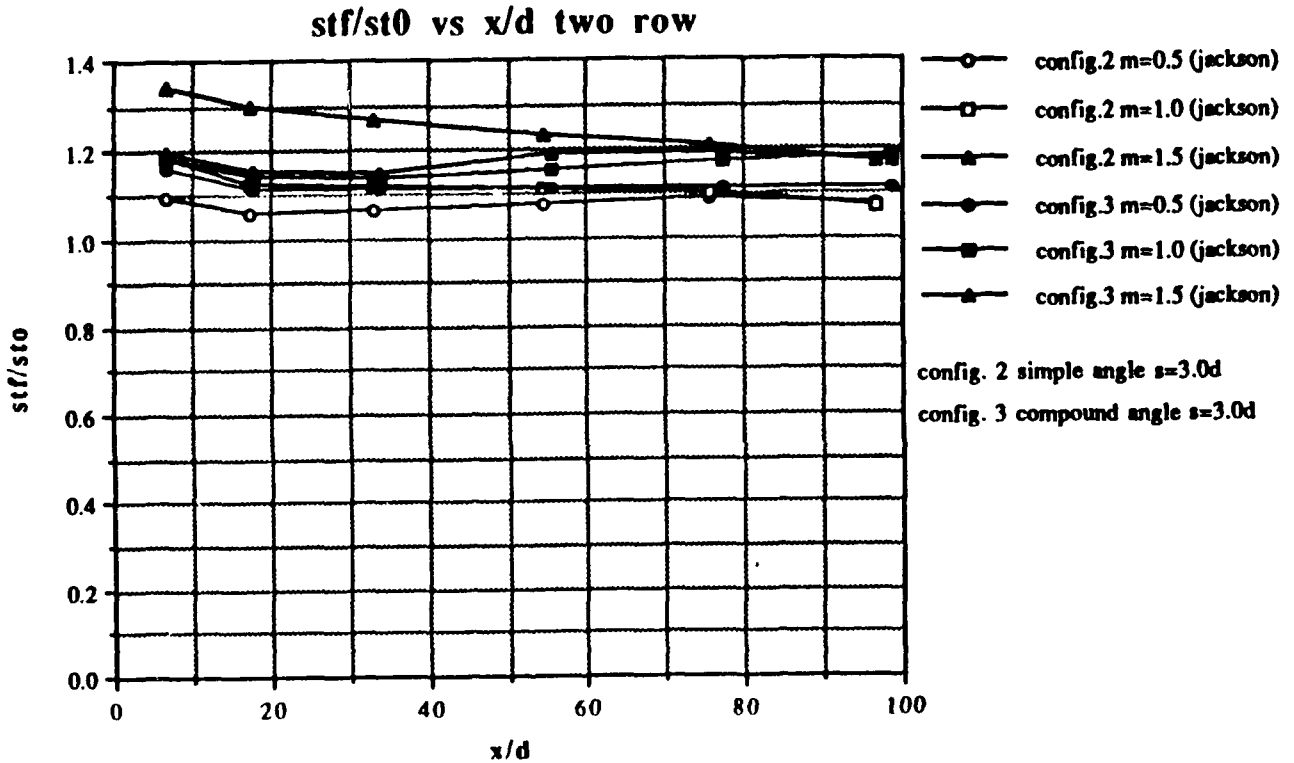


Figure 159. Comparisons of Two Row Stf/Sto as Dependent Upon x/d for Configuration 2 (Simple Angle), and Configuration 3 (Compound Angle)

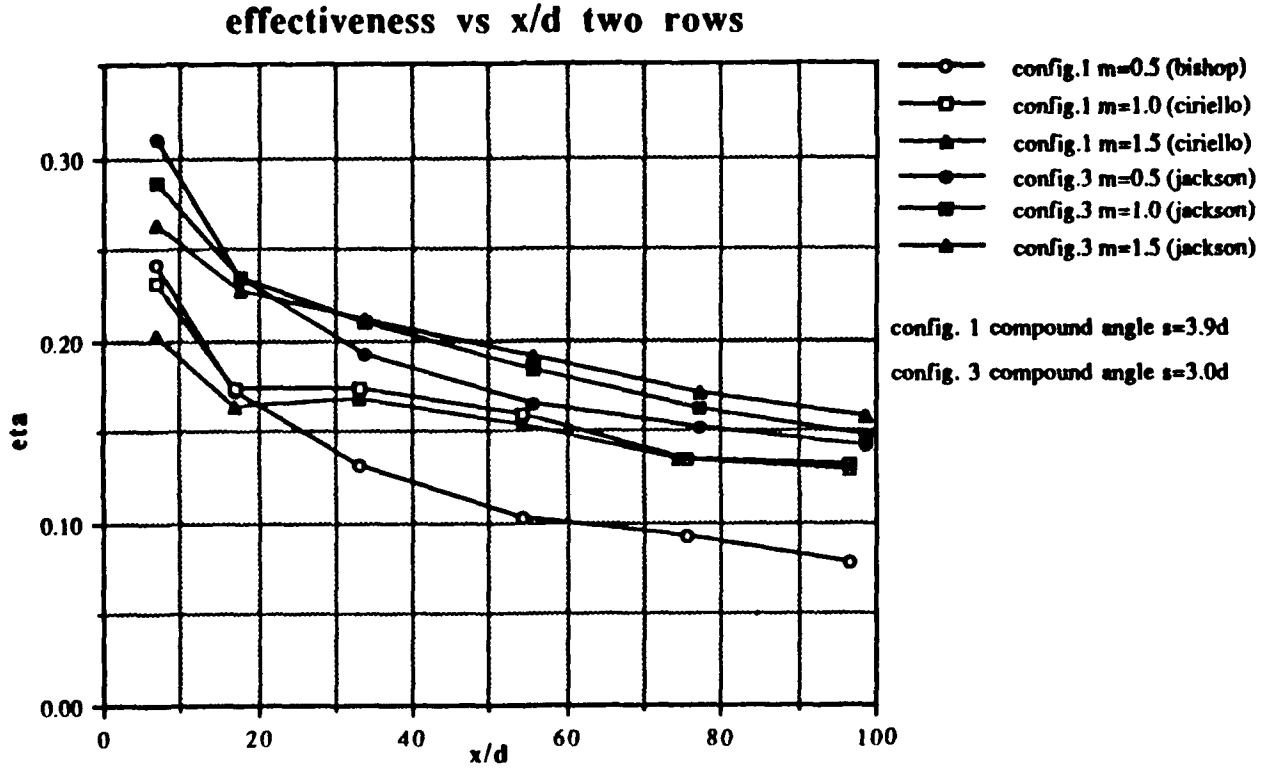


Figure 160. Comparisons of Two Row Adiabatic Effectiveness as Dependent Upon x/d for Configuration 1 (Compound Angle), and Configuration 3 (Compound Angle)

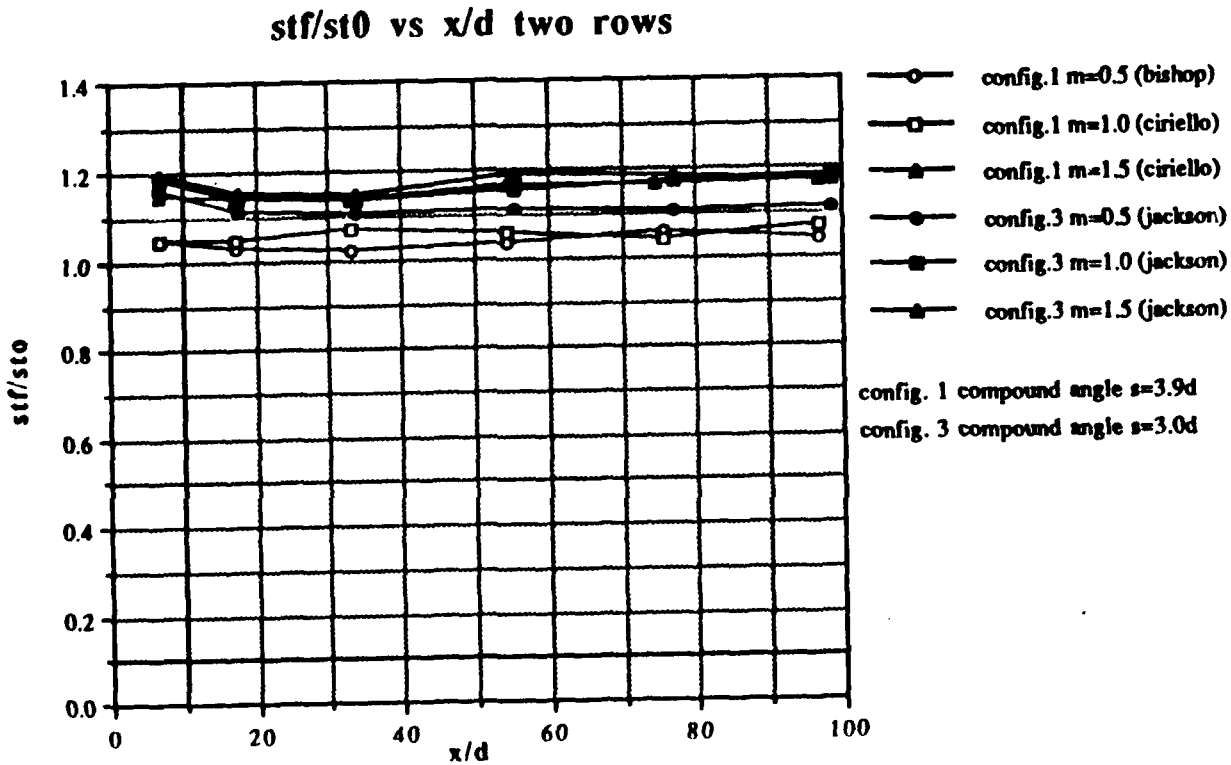


Figure 161. Comparisons of Two Row Stf/Sto as Dependent Upon x/d for Configuration 1 (Compound Angle), and Configuration 3 (Compound Angle)

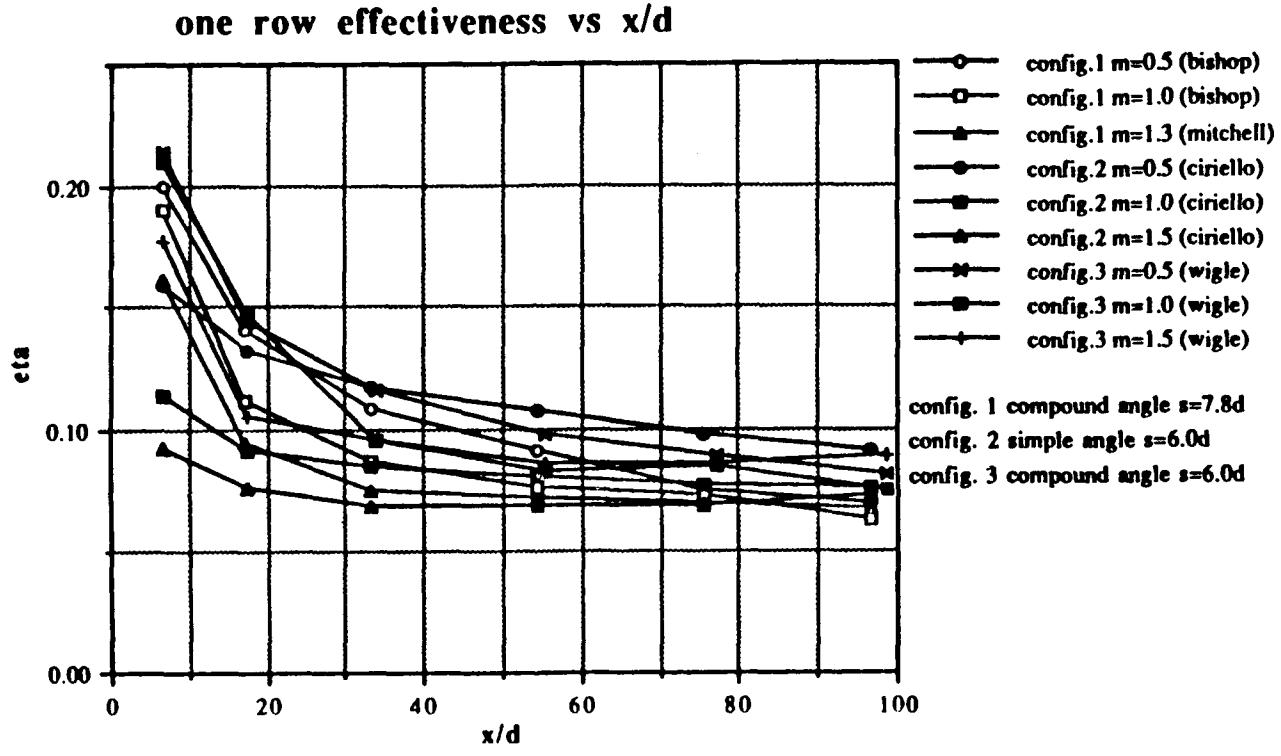


Figure 162. Comparison of One Row Adiabatic Effectiveness as Dependent Upon x/d for Compound and Simple Angle Configurations

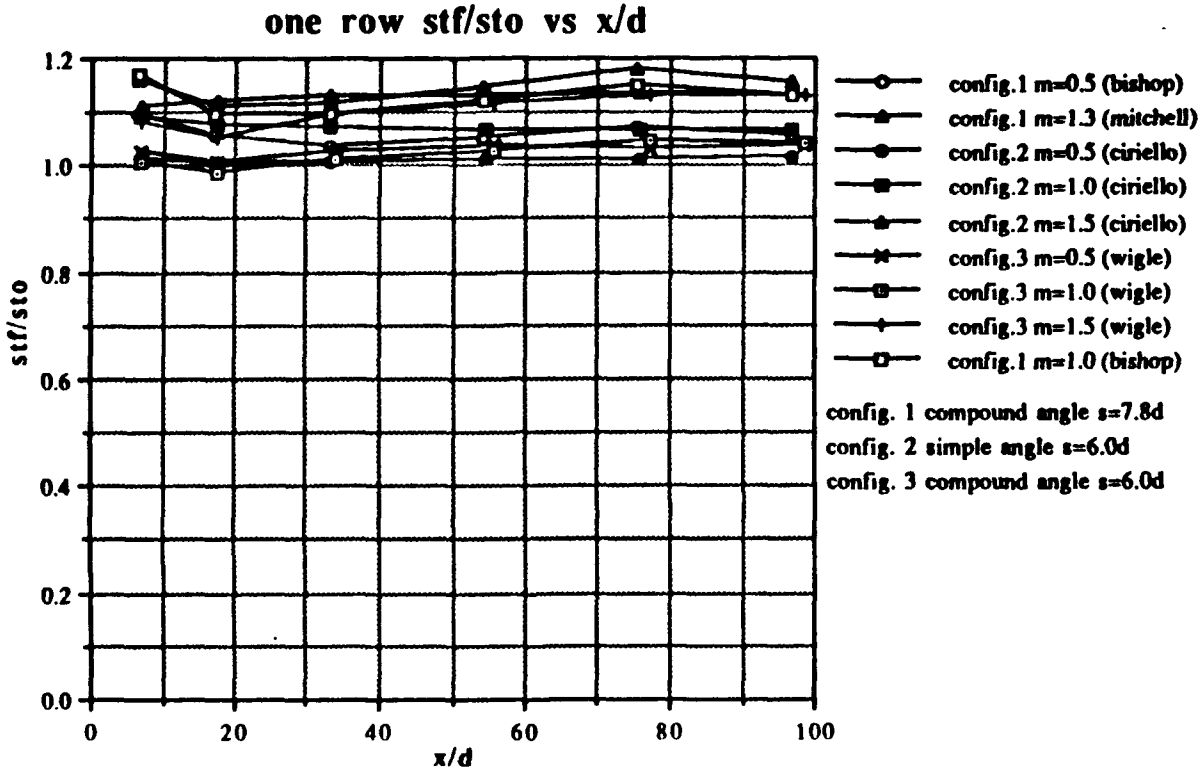


Figure 163. Comparison of One Row Stf/Sto as Dependent Upon x/d for Compound and Simple Angle Configurations

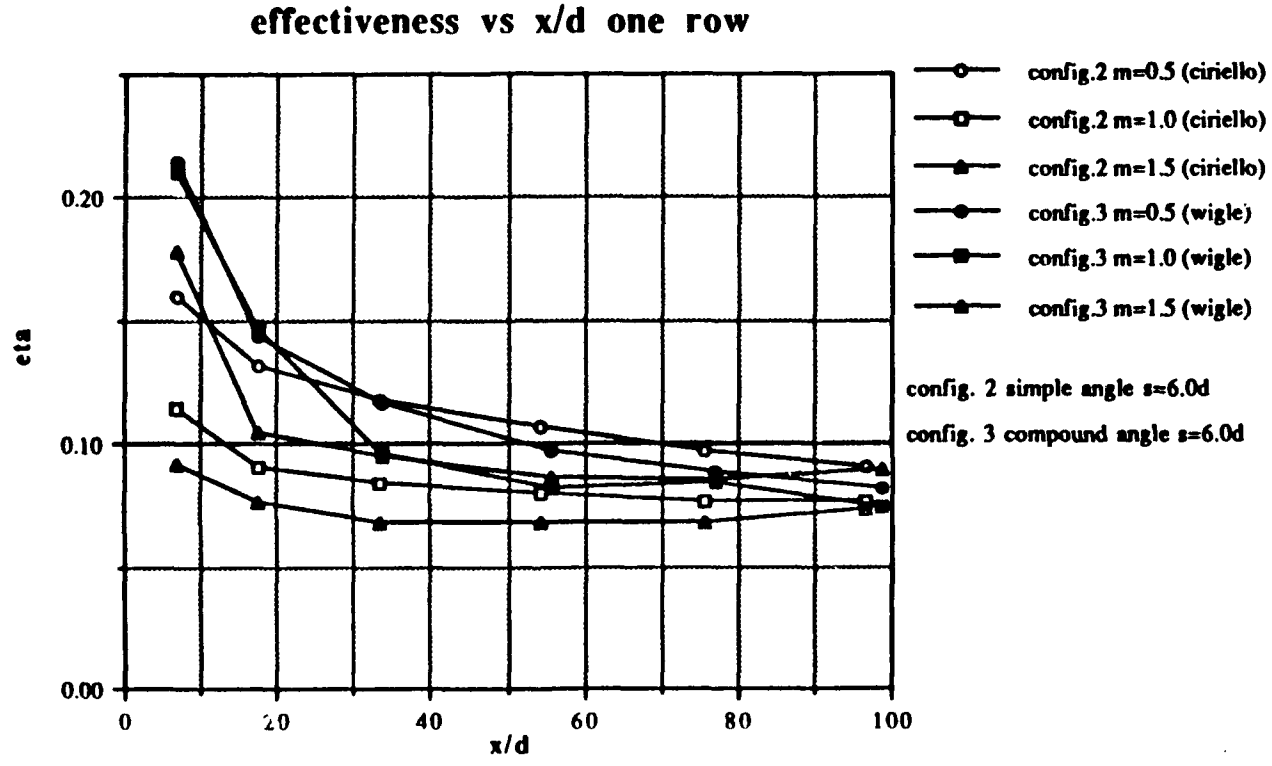


Figure 164. Comparisons of One Row Adiabatic Effectiveness as Dependent Upon x/d for Configuration 2 (Simple Angle), and Configuration 3 (Compound Angle)

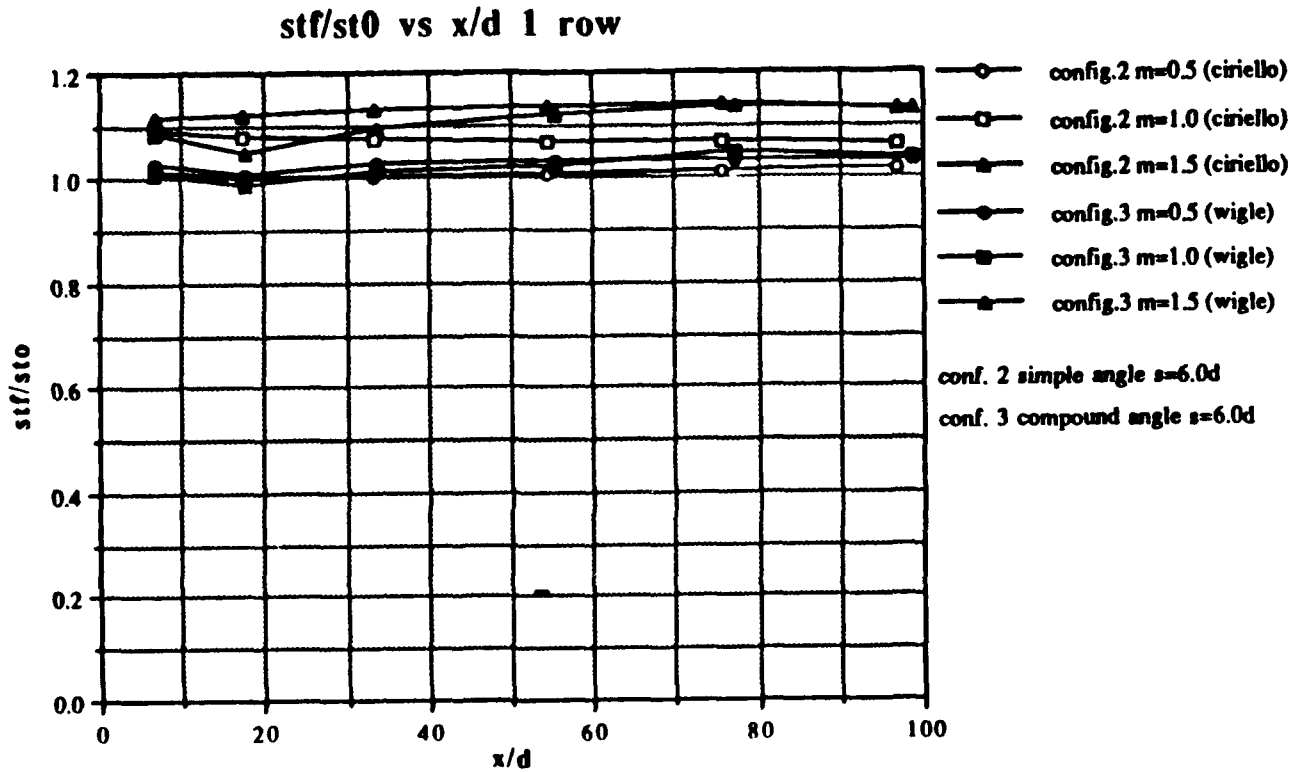


Figure 165. Comparisons of One Row Stf/Sto as Dependent Upon x/d for Configuration 2 (Simple Angle), and Configuration 3 (Compound Angle)

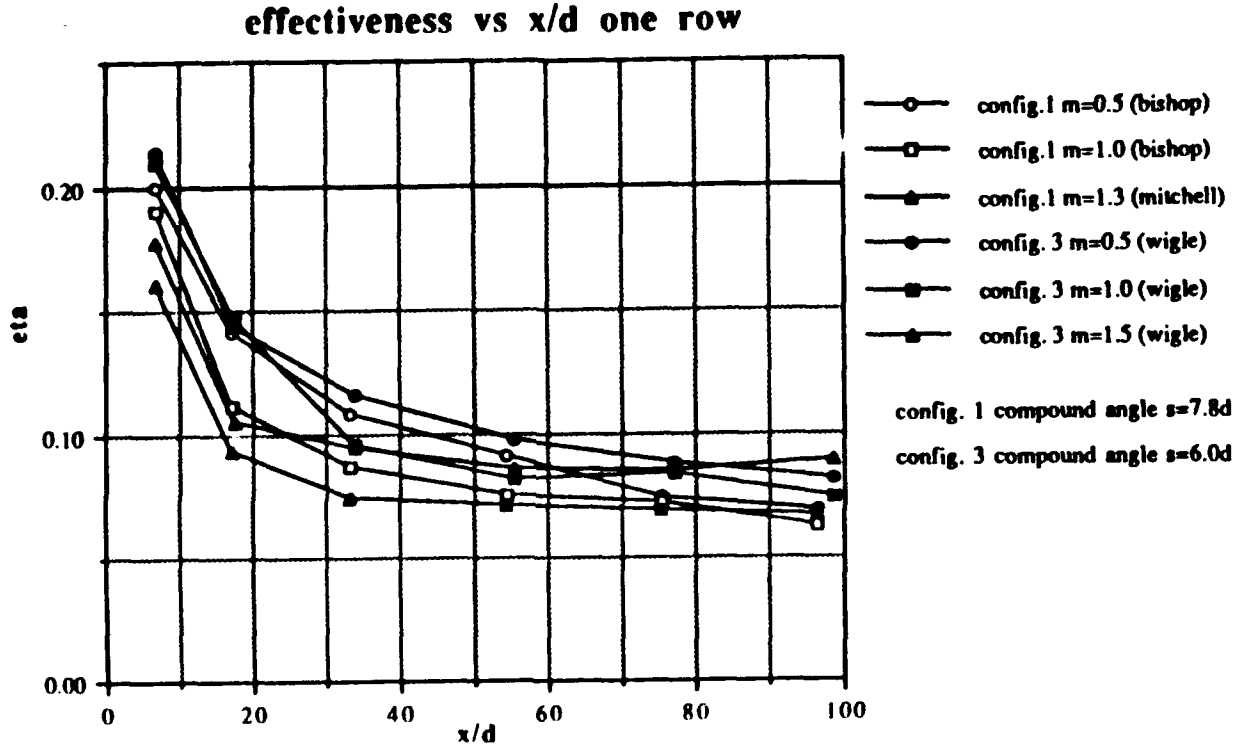


Figure 166. Comparisons of One Row Adiabatic Effectiveness as Dependent Upon x/d for Configuration 1 (Compound Angle), and Configuration 3 (Compound Angle)

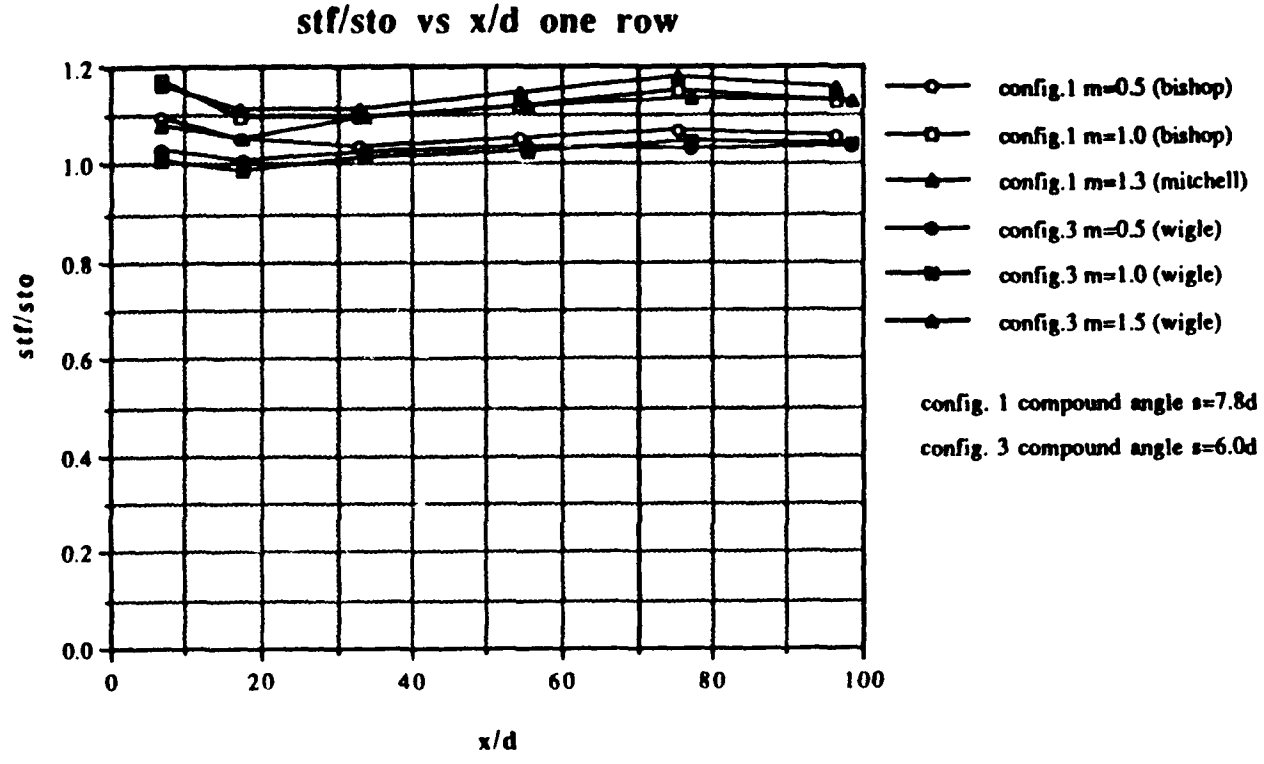


Figure 167. Comparisons of One Row Stf/Sto as Dependent Upon x/d for Configuration 1 (Compound Angle), and Configuration 3 (Compound Angle)

APPENDIX B: UNCERTAINTY ANALYSIS

An uncertainty analysis by Schwartz [Ref. 8] was accomplished on the input parameters and variablles used for this study. A 95% confidence interval was utilized. Table I contains a summary of the parameters and their uncertainties:

TABLE I. EXPERIMENTAL UNCERTAINTIES FOR MEASURED QUANTITIES

Quantity (units)	Typical Nominal Value	Experimental Uncertainty
T_∞ (°C)	18.0	0.13
T_w (°C)	40.0	0.21
$P_{ambient}$ (mm Hg)	760	0.71
ρ_∞ (kg/m^3)	1.23	0.009
U_∞ (m/s)	10.0	0.06
C_p [J/(kg K)]	1006	1
q_wA (W)	270	10.5
h [W/(m^2 K)]	24.2	1.03
St	0.00196	0.000086
St/Sto	1.05	0.058
A (m^2)	0.558	0.0065
m	0.98	0.05
x/d	54.6	0.36

APPENDIX C: DATA ACQUISITION, PROCESSING AND PLOTTING PROGRAMS

1. Mean Velocity Survey Software:

FIVEHOLE1: This program acquires pressure data from each of the five transducers associated with the probe. The FIVEHOLE1 program controls the MITAS motor controller which, in turn, controls the automatic traversing device on which the five hole probe is mounted. An 800 point pressure survey is conducted in the Y-Z plane normal to the freestream flow. Two data files, FIVx and FIVPx, are created. The FIVx data file consists of mean velocity, center port pressure, average pressure of the four peripheral ports, and the yaw and pitch coefficients for each of the 800 locations sampled. The FIVx data file consists of the pressures P1 through P5 sensed by each of the five pressure probe sensing ports, the average pressure of the four peripheral ports and the mean velocity, for each of the 800 survey locations.

PADJUST: This program accesses the FIVPx data file created by FIVEHOLE1 and adjusts the pressures to account for spatial resolution problems. Pressure correction is performed using a curve fit to move the measurement location to the center sensing port location. The output file of PADJUST is FIVxA.

VELOCITY: This program accesses FIVxA, the data file created by PADJUST, and computes Ux, Uy and Uz velocity components. The output file of VELOCITY is Vx.

UX3: This program accesses Vx, the data file created by VELOCITY, and plots streamwise velocity (Ux) contours of the Y-Z plane surveyed by the five hole pressure probe.

PTOT3: This program accesses Vx, data file created by VELOCITY, and plots total pressure contours of the surveyed Y-Z plane.

2. Mean Temperature Survey Software:

ROVER1: This program acquires flow temperature data from the "roving" thermocouple mounted on the automatic traversing device. The traversing device is controlled by the MITAS controller which is, in turn, controlled by this program. The output data file consists of differential temperatures (T_{rover} - T_{∞}) for each for the 800 survey locations in the Y-Z plane. The output file for ROVER1 is TEMx.

PLTMP3: This program uses the differential temperature file TEMx, created by ROVER1 and plots differential temperature contours of the surveyed Y-Z plane.

3. Heat Transfer Measurement Software (No Film Cooling):

STANTON3: This program acquires multiple channel thermocouple data for heat transfer measurements with no film cooling. It creates two output data files, TDATA and IDATA. The TDATA file consists of 126 test plate thermocouple temperatures. The IDATA file run number, test plate voltage and current, ambient pressure, pressure differential, ambient temperature, freestream velocity, air density and freestream temperature.

STANTON4: STANTON4 accesses TDATA and IDATA files created by STANTON3 and calculates heat transfer coefficients and Stanton numbers for each of the 126 thermocouple locations. This program also calculates the average Reynolds number for each thermocouple row. STANTON4 creates three output files. These files are HDATA, SDATA, and STAV. The HDATA file consists for the local heat transfer coefficient, the Stanton number and the X and Z coordinates for each of the 126 test plate thermocouples. The SDATA file contains only the Stanton number values calculated for each thermocouple location. STAV contains the X location and the average Reynolds and Stanton numbers for each of the six thermocouple rows.

4. Heat Transfer Measurement Software (with Film Cooling):

SETCONDV2: This program is used to set conditions for heat transfer data acquisition when film cooling is employed. SETCONDV2 determines injection velocity, Reynolds number, blowing ration (m) and non-dimensional temperature

(θ). It requires user input from the terminal of freestream conditions, rotameter percent flow and injection plenum differential pressure.

STANFC1B: This program is used when film cooling is employed to acquire multiple channel thermocouple data for heat transfer measurements. STANFC1B creates three data files: a temperature data file (Tx), a terminal input data file (Cx), and a film cooling data file (CFCx). The temperature data file consists for the 126 test plate thermocouple temperatures. The terminal input data file records the identical information contained in the IDATA file of STANTON3, as discussed earlier. The film cooling data file contains the injection rotameter percent flow and the injection plenum differential pressure.

STANFC2A: This program accesses the temperature, terminal input and film cooling data files created by STANFC1B. The program calculates Stanton number values for the 126 thermocouple locations and creates a single output file (FCx) containing these values.

EFFFC2B: This program is a modification of STANFC2A. This program accesses the temperature, terminal input and film cooling data files created by STANFC1B. In addition, it accesses an output file created by STANFC2A, (FCx), and directly calculates adiabatic effectiveness without power being applied to the test bed.

STANR1: This program reads three Stanton number data files and creates a single output file containing two Stanton number ratios for each of the 126 thermocouple locations. The required input data files are: SDATA file created by

STANTON4 containing baseline Stanton numbers for no film cooling and two FCx data files created by STANFC2A containing Stanton numbers with film cooling. The output file of STANR1 is STRx.

FLMEFFV2: This program processes Stanton number data and calculates the local and spanwise averaged film cooling effectiveness and iso-energetic Stanton number ratios. The program reads several files and creates two output files. The program reads the SDATA file created by STANTON4 which contains the baseline Stanton numbers for no film cooling, and up to six FCx, Tx and Cx files created by STANFC2A, and STANFC2B. One of the two output data files contains the local effectiveness and iso-energetic Stanton number ratios and the other output file contains the spanwise averaged effectiveness and iso-energetic Stanton number ratios.

3DSTGETA: This program accesses the files created by FLMEFFV2 and plots the spanwise variation of effectiveness in three-dimensional form.

3DSTGSTRIS: This program accesses the files created by FLMEFFV2 and plots the spanwise variation of the iso-energetic Stanton number ratio in three-dimensional form.

3DSTRST: This program accesses STRx, the Stanton number ratio file created by STANR1, and plots the spanwise variations of the Stanton number ratios in three-dimensional form.

APPENDIX D: DATA FILE DIRECTORY

1. HEAT TRANSFER DATA
 A. BASELINES
 Generating Programs: STANTON3/STANTON4
 TBNA-DATE - Temperature data file
 IBNA-DATE - User terminal input data file
 HBNA-DATE - Heat transfer coefficient data file
 SBNA-DATE - Local Stanton number data file

DATA RUN #	DATA FILE	EXPERIMENTAL CONDITIONS
31491.1345	TB6A391 IB6A391 HB6A391 SB6A391	Simple Angle T_P-T_F=20.08 °C, no film-cooling
31691.1333	TB4A391 IB4A391 HB4A391 SB4A391	Simple angle T_p-T_f=9.66 °C no film-cooling
51491.1233	TB6S591 IB6A591 HB6A591 SB6A591	Compound Angle T_p-T_f=20.83 °C, no film-cooling
51491.1649	TB4A591 IB4A591 HB4A591 SB4A591	Compound Angle T_p-T_f=9.66 °C, no film-cooling

B. STANFC1B/STANFC2A
DATA FILES - (film-cooling)
ρTxx - Temperature data file
ρCxx - User terminal input data file
ρCFCxx - Film-cooling parameters data file
ρFCxx - Local Stanton number data file

SIMPLE ANGLE, 2 ROWS

DATA RUN #	DATA FILE	EXPERIMENTAL CONDITIONS
32891.1520	2T1 2C1 2CFC 2FC1	Simple angle, 2 rows, m=1.05, 1.12
32991.1431	2T4 2C4 2CFC4 2FC4	Simple angle, 2 rows, m=1.05, θ=0.58
32991.2107	2T5 2C5 2CFC5 2FC5	Simple angle, 2 rows, m=1.05, θ=2.53
40291.0845	2T6 2C6 2CFC6 2FC6	Simple angle, 2 rows, m=1.05, θ=0.21
40891.1040	2T9 2C9 2CFC9 2FC9	Simple angle, 2 rows, m=1.05, θ=1.66
40891.1314	2T10 2C10 2CFC10 2FC10	Simple angle, 2 rows, m=1.05, θ=2.78

41391.1405	2T12 2C12 2CFC12 2FC12	Simple angle, 2 rows, m=0.5, θ=.03
41491.1042	2T13 2C13 2CFC13 2FC13	Simple angle, 2 rows, m=0.5, θ=0.77
41491.2210	2T14 2C14 2CFC14 2FC14	Simple angle, 2 rows, m=0.5, θ=1.11
41491.2255	2T15 2C15 2CFC15 2FC15	Simple angle, 2 rows, m-0.5, θ=1.60
41591.0837	2T16 2C16 2CFC16 2FC16	Simple angle, 2 rows, m=0.5, θ=2.41
41591.1032	2T17 2C17 2CFC17 2FC17	Simple angle, 2 rows, m=0.5, θ=2.95
41891.1018	2T18 2C18 2CFC18 2FC18	Simple angle, 2 rows, m=1.5, θ=0.42
41891.1137	2T19 2C19 2CFC19 2FC19	Simple angle, 2 rows, m=1.0, θ=0.89

41991.1609	2T20 2C20 2CFC20 2FC20	Simple angle, 2 rows, m=1.5, θ=1.15
41991.1352	2T22 2C22 2CFC22 2FC22	Simple angle, 2 rows, m=1.5, θ=2.57
41991.1455	2T23 2C23 2CFC23 2FC23	Simple angle, 2 rows, m=1.5, θ=2.31
42391.1515	2T24 2C24 2CFC24 2FC24	Simple angle, 2 rows, m=1.5, θ=1.34

COMPOUND ANGLE, 2 ROWS

DATA RUN #	DATA FILE	EXPERIMENTAL CONDITIONS
51591.1037	3T1 3C1 3CFC1 3FC1	Compound angle, 2 rows, m=1.0, θ=0.27
51591.1448	3T2 3C2 3CFC2 3FC2	Compound angle, 2 rows, m=1.0, θ=0.94
51591.1704	3T3 3C3 3CFC3 3FC3	Compound angle, 2 rows, m=1.0, θ=1.23

51691.1302	3T4 3C4 3CFC4 3FC4	Compound angle, 2 rows, m=1.0, θ=1.72
51691.1538	3T5 3C5 3CFC5 3FC5	Compound angle, 2 rows, m=1.0, θ=2.17
51691.1700	3T6 3C6 3CFC6 3FC6	Compound angle, 2 rows, m=1.0, θ=2.82
51791.1307	3T7 3C7 3CFC7 3FC7	Compound angle, 2 rows, m=0.5, θ=.04
51791.1700	3T8 3C8 3CFC8 3FC8	Compound angle, 2 rows, m=0.5, θ=1.15
52091.0949	3T9 3C9 3CFC9 3FC9	Compound angle, 2 rows, m=0.5, θ=1.82
52091.1211	3T10 3C10 3CFC10 3FC10	Compound angle, 2 rows, m=0.5, θ=2.32
52091.1447	3T11 3C11 3CFC10 3FC10	Compound angle, 2 rows, m=0.5, θ=2.32

52091.1447	3T11 3C11 3CFC11 3FC11	Compound angle, 2 rows, m=0.5, θ=2.96
52091.1653	3T12 3C12 3CFC12 3FC12	Compound angle, 2 rows, m=0.5, θ=1.54
52191.1520	3T13 3C13 3CFC13 3FC13	Compound angle, 2 rows, m=1.5, θ=0.48
52291.1255	3T14 3C14 3CFC14 3FC14	Compound angle, 2 rows, m=1.5, θ=0.9
52291.1645	3T15 3C15 3CFC15 3FC15	Compound angle, 2 rows, m=1.5, θ=1.24
52491.1030	3T17 3C17 3CFC17 3FC17	Compound angle, 2 rows, m=1.5, θ=2.21
52491.1332	3T18 3C18 3CFC18 3FC18	Compound angle, 2 rows, m=11.5, θ=2.44

COMPOUND ANGLE, 1 ROW

DATA RUN #	DATA FILE	EXPERIMENTAL CONDITIONS
64791.1130	3T19 3C19 3CFC19 3FC19	Compound angle, 1 row, m=1.0, θ=0.12
61991.1400	3T20 3C20 3CFC20 3FC20	Compound angle, 1 row, m=1.0, θ=1.09
61991.1047	3T21 3C21 3CFC21 3FC21	Compound angle, 1 row, m=1.0, θ=1.43
70191.1251	3T22 3C22 3CFC22 2FC22	Compound angle, 1 row, m=1.0, θ=2.52
70191.1638	3T23 3C23 3CFC23 3FC23	Compound angle, 1 row, m=1.0, θ=2.08
70991.0900	3T25 3C25 3CFC25 3FC25	Compound angle, 1 row, m=0.5, θ=.046
70991.1447	3T26 3C26 3CFC26 3FC26	Compound angle, 1 row, m=0.5, θ=1.21

70991.1540	3T27 3C27 3CFC27 3FC27	Compound angle, 1 row, m=0.5, θ=1.64
71091.1029	3T28 3C28 3CFC28 3FC28	Compound angle, 1 row, m=0.5, θ=2.75
71091.1306	3T29 3C29 3CFC29 3RFC29	Compound angle, 1 row, m=0.5, θ=1.44
71091.1456	3T30 3C30 3CFC30 3FC30	Compound angle, 1 row, m=0.5, θ=1.44
71191.1447	3T32 3C32 3CFC32 3FC32	Compound angle, 1 row, m=1.5, θ=1.095
71191.1658	3T33 3C33 3CFC33 3FC33	Compound angle, 1 row, m=1.5, θ=1.42
71791.1516	3T34 3C34 3CFC34 3FC34	Compound angle, 1 row, m=1.5, θ=2.83
71791.1615	3T35 3C35 3CFC35 3FC35	Compound angle, 1 row, m=1.5, θ=1.52

71791.1733	3T36 3C36 3CFC36 3FC36	Compound angle, 1 row, m=1.5, θ=2.62
71891.1835	3T39 3C39 3CFC39 3FC39	Compound angle, 1 row, m=1.5, θ=1.77

B. FILM EFFECTIVENESS DATA
Generation Program: FLMEFFV2, 3
ρFCxx - Local effectiveness data file
ρSTRxx - Spanwise average effectiveness data file

DATA RUN #	DATA FILE	EXPERIMENTAL CONDITIONS
32891.1520 32991.1431 32991.2109 40291.0845 40891.1314	STR1 STR1A	Simple angle, 2 rows, m=1.05
41491.1042 41391.1405 41491.2210 41491.2255 41591.0837 41591.1032	STR2 STR2A	Simple angle, 2 rows, m=0.5
41891.1018 41891.1137 41891.1609 41991.1455 42391.1550 41991.1352	STR3 STR3A	Simple angle, 2 rows, m=1.5

COMPOUND ANGLE, 2 ROW

51591.1037	3STR4_1	Compound angle, 2 row, m=1.0
51591.1448	3STR4_2	
51591.1704		
51691.1302		
51691.1538		
51691.1700		
51791.1307	3STR5_1	Compound angle, 2 row, m=0.5
51791.1700	3STR5_2	
52091.0949		
52091.1211		
52091.1653		
52091.1447		
52191.1520	3STR6_1	Compound angle, 2 row,, m=1.5
52291.1255	3STR6_2	
52291.1645		
52491.10030		
52491.1332		

COMPOUND ANGLE, 1 ROW

61791.1130	3STR1_1	Compound angle, 1 row, m=1.0
61991.1400	3STR1_2	
61991.1047		
70191.1251		
70191.1638		
70991.0900	3STR2_1	Compound angle, 1 row, m=0..5
70991.1447	3STR3_2	
70991.1540		
71091.1029		
71091.1456		

71191.1447	3STR3_1	Compound angle, 1 row, m=1.5
71191.1685	3STR3_2	
71791.1516		
71791.1615		
71791.17333		
71891.1835		

D. MEAN VELOCITY DATA:
1. COMPOUND ANGLE X/D=9.9

DATA RUN #	DATA FILE	GENERATING PROGRAM	EXPERIMENTAL CONDITIONS
80391.0755	FIV0 (disc 7)	FIVEHOLE1	2 rows, m=0.5,
	FIVP0	FIVEHOLE1	x/d=9.9
	FIVO0	PADJUST	
	V4	VELOCITY	
80491.1830	FIV1 (disc 7)	FIVEHOLE1	2 rows, m=1.0,
	FIVP1	FIVEHOLE1	x/d=9.9
	FIVO1	PADJUST	
	V5	VELOCITY	
804911.0941	FIV2 (disc 7)	FIVEHOLE1	2 rows, m=1.0,
	FIVP2	FIVEHOLE1	x/d=9.9
	FIVO1	PADJUST	
	V6	VELOCITY	
80291.0940	FIV1 (disc 8)	FIVEHOLE1	1 row, m=0.5,
	FIVP1	FIVEHOLE1	x/d=9.9
	FIVO1	PADJUST	
	V2	VELOCITY	
80191.1540	FIV2 (disc 8)	FIVEHOLE1	1 row, m=1.0,
	FIVP2	FIVEHOLE1	x/d=9.9
	FIVO2	PADJUST	
	V3	VELOCITY	

2. COMPOUND ANGLE, X/D = 44.3

DATA RUN #	DATA FILE	GENERATING PROGRAM	EXPERIMENTAL CONDITIONS
80791.1154	FIV2 (disc 9)	FIVEHOLE1	2 rows, m=0.5,
	FICP2	FIVEHOLE1	x/d=44.3
	FICO2	PADJUST	
	V7	VELOCITY	
80691.2100	FIV1 (disc 10)	FIVEHOLE1	2 rows, m=1.0,
	FIVP1	FIVEHOLE1	x/d=44.3
	FIVO1	PADJUST	
	V8	VELOCITY	
80691.0900	FIVO (disc 10)	FIVEHOLE1	2 rows, m=1.5,
	FIVP0	FIVEHOLE1	x/d=44.3
	FIVO0	PADJUST	
	V9	VELOCITY	
82991.0944	FIVO (disc 9)	FIVEHOLE1	1 row, m=0.5,
	FIVP0	FIVEHOLE1	x/d=44.3
	FIVO0	PADJUST	
	V10	VELOCITY	
81291.1110	FIV1 (disc 9)	FIVEHOLE1	1 row, m=1.0,
	FIVP1	FIVEHOLE1	x/d=44.3
	FIVO1	PADJUST	
	V11	VELOCITY	

3. COMPOUND ANGLE, X/D = 86.3

DATA RUN #	DATA FILE	GENERATING PROGRAM	EXPERIMENTAL CONDITIONS
82191.0842	FIV2 (disc 10)	FIVEHOLE1	2 rows, m=0.5,
	FIVP2	FIVEHOLE1	x/d=86.3
	FIVO2	PADJUST	
	V14	VELOCITY	

82291.0949	FIV0 (disc 11) FIVP0 FIVO0 V15	FIVEHOLE1 FIVEHOLE1 PADJUST VELOCITY	2 rows, m=1.0, x/d=86.3
82891.1100	FIV1 (disc 11) FIVP1 FIVO1 V16	FIVEHOLE1 FIVEHOLE1 PADJUST VELOCITY	2 rows, m=1.5, x/d=86.3
81491.0858	FIV0 (disk 10) FIVP0 FIVO0 V12	FIVEHOLE1 FIVEHOLE1 PADJUST VELOCITY	1 row, m=0.5, x/d=86.3
82091.1455	FIV1 FIVP1 FIVO1 V13	FIVEHOLE1 FIVEHOLE1 PADJUST VELOCITY	1 row, m=1.0, x/d=86.3

E. COMPOUND ANGLE INJECTION MEAN TEMPERATURE SURVEY DATA:
Generating Program: ROVER1

DATA RUN #	DATA FILE	EXPERIMENTAL CONDITION
83091.2012	TEM0	1 row, m=1.0, x/d=9.9
90291.1422	TEM1	2 rows, m=0.5, x/d=9.9
90291.1900	TEM2	2 rows, m=1.0, x/d=9.9
90391.0847	TEM3	2 rows, m=1.5, x/d=9.9
90391.1416	TEM4	1 row, m=0.5, x/d=9.9
90391.1952	TEM5	1 row, m=0.5, x/d=44.3
90491.0936	TEM6	1 row, m=1.0, x/d=44.3
90491.1451	TEM7	2 rows, m=1.0, x/d=44.3

90591.1000	TEM8	2 rows, m=1.0, x/d=44.3
90591.1530	TEM9	2 rows, m=1.5, x/d=44.3
90691.1500	TEM10	2 rows, m=1.0, x/d=86.3
90691.2100	TEM11	2 rows, m=0.5, x/d=86.3
90791.1000	TEM12	2 rows, m=1.5, x/d=86.3
90791.1830	TEM13	1 row, m=1.0, x/d=86.3
90791.2223	TEM14	1 row, m=0.5, x/d=86.3

LIST OF REFERENCES

1. Metzger, D.E., Carper, H.J., and Swank, L.R., "Heat Transfer with Film Cooling Near Nontangential Injection Slots," *Journal of Engineering for Power*, pp. 157-153, April 1968.

2. Ortiz, A., "The Thermal Behavior of Film Cooled Turbulent Boundary Layers as Affected by Longitudinal Vortices," Master's Thesis, Naval Postgraduate School, Monterey, California, September 1987.

3. Ligrani, P.M., Ortiz, A., Joseph, S.L., and Evans, D.L., "Effects of Embedded Vortices on Film-Cooled Turbulent Boundary layers," ASME-88-GT-170, ASME Gas Turbine and Aeroengine Congress and Exposition, Amsterdam, The Netherlands, June 1988, also *ASME Transactions — Journal of Turbomachinery*, Vol. 111, pp. 71-77, 1989.

4. Williams, W., "Effects of an Embedded Vortex on a Single Film-Cooling Jet in a Turbulent Boundary Layer," Master's Thesis, Naval Postgraduate School, Monterey, California, June 1988.

5. Craig, D.W., "Effect of Vortex Circulation on Injectant from a Single Film-Cooling Hole in a Turbulent Boundary Layer," Master's Thesis, Naval Postgraduate School, Monterey, California, September 1990.

6. Bishop, D., "Heat Transfer, Adiabatic Effectiveness and Injectant Distributions Downstream of Single and Double Rows of Film Cooling Holes with Compound Angles," Master's Thesis, Naval Postgraduate School, Monterey, California, September 1990.

7. Mitchell, S., "The Effects of Embedded Longitudinal Vortices on Heat Transfer in a Turbulent Boundary Layer with Film Cooling from Holes with Compound Angles," Master's Thesis, Naval Postgraduate School, Monterey, California, September 1990.

8. Ciriello, S., "Heat Transfeer, Adiabatic Effectiveness and Injectant Distributions Downstream of Single and Double Rows of Film-Cooling Holes with Simple and Compound Angles," Master's Thesis, Naval Postgraduate School, Monterey, California, March 1991.

9. Ligrani, P.M., Ciriello, S., Bishop, D.T., "Heat Transfer, Adiabatic Effectiveness and Injectant Distributions Downstream of a Single Row and Two Staggered Rows of Compound Angle Film-Cooling Holes," Naval Postgraduate School, Monterey, California, 1991.

10. Schwartz, G.E., "Control of Embedded Vortices Using Wall Jets," Master's Thesis, Naval Postgraduate School, Monterey, California, September 1988.

11. Joseph, S.L., "The Effects of an Embedded Vortex on a Film-Cooled Turbulent Boundary Layer," Master's Thesis, Naval Postgraduate School, Monterey, California, December 1986.

INITIAL DISTRIBUTION LIST

		No. of Copies
1.	Defense Technical Information Center Cameron Station Alexandria, Virginia 22304-6145	2
2.	Library, Code 52 Naval Postgraduate School Monterey, California 93943-5002	2
3.	Professor P.M. Ligrani, Code ME/Li Department of Mechanical Engineering Naval Postgraduate School Monterey, California 93943-5000	3
4.	Department Chairman, Code ME Department of Mechanical Engineering Naval Postgraduate School Monterey, California 93943-5000	1
5.	Dr. Dan Groghan Naval Sea Systems Command Code 56X3 Washington, D.C. 20362	4
6.	Naval Engineering Curricular Officer, Code 34 Department of Mechanical Engineering Naval Postgraduate School Monterey, California 93943-5000	1
7.	Professor C.S. Subramanian, Code ME/Su Department of Mechanical Engineering Naval Postgraduate School Monterey, California 93943-5000	1

8. LT. Stephen M. Jackson 1
264 B. Everly Ct.
Mt. Laurel, New Jersey 08054